



ISSN 1811-1165 (Print)
ISSN 2413-2179 (Online)

EURASIAN PHYSICAL TECHNICAL JOURNAL

VOLUME 20, NO. 2(44), 2023

phtj.buketov.edu.kz

EURASIAN PHYSICAL TECHNICAL JOURNAL

p - ISSN 1811-1165

e - ISSN 2413-2179

Volume 20, No. 2(44), 2023

1st issue – March, 2004

Journal Founder:

**E.A. BUKETOV KARAGANDA
UNIVERSITY**

**Е.А. БӨКЕТОВ АТЫНДАҒЫ
ҚАРАҒАНДЫ УНИВЕРСИТЕТИ**

**КАРАГАНДИНСКИЙ УНИВЕРСИТЕТ
имени Е.А. БУКЕТОВА**

<https://phtj.buketov.edu.kz>

Contact information:

Editorial board of EAPhTJ (Build. 2, room 216)
E.A. Buketov Karaganda University
Universitetskaya Str., 28, Karaganda,
Kazakhstan, 100024
Subscription index: 75240

Tel: +7(7212) 77-04-03
Fax: +7(7212) 35-63-98
E-mail: ephjt@mail.ru

Signed to print on 21.06.2023
Format 60x84 1/8. Offset paper.
Volume 18.88 p.sh. Circulation 300 copies.
Agreed price. Order No. 66.

Басуға 21.06.2023 ж. қол қойылды.
Пішімі 60×84 1/8. Офсеттік қағазы.
Көлемі 18.88 ес.-б.т. Таралымы 300 дана.
Бағасы келісім бойынша. Тапсырыс № 66.

Подписано к печати 21.06.2023 г.
Формат 60 × 84 1/8. Офсетная бумага.
Объем 18.88 печ.л. Тираж 300 экз.
Цена договорная. Заказ № 66.

Printed in the Publishing House
of the E.A.Buketov KarU

Е.А. Бөкетов атындағы ҚарУ баспасының
баспаханасында басылып шықты

Отпечатано в Издательстве
КарУ имени Е.А. Букетова

Chief EDITOR

Sakipova S.E., E.A. Buketov Karaganda University, Karaganda, Kazakhstan

EDITORIAL BOARD

Aringazin A.K., L.N. Gumilyov Eurasian National University, Astana, Kazakhstan

Dzhumanov S., Institute of Nuclear Physics, Uzbekistan Academy of Sciences, Tashkent, Uzbekistan

Ibrayev N.Kh., Institute of Molecular Nanophotonics, E.A.Buketov Karaganda University, Kazakhstan

Jakovics A., Institute of Numerical Modelling, University of Latvia, Riga, Latvia

Kadyrzhanov K.K., L.N. Gumilyov Eurasian National University, Astana, Kazakhstan

Kucherenko M.G., Director of the Laser and Information Biophysics Centre, Orenburg State University, Orenburg, Russia

Kuritnyk I.P., Department of Electronics and Automation, High school in Oswiecim, Poland

Kushpil S., Heavy Ion Group, Nuclear Physics Institute of the Czech Academy of Science, Řež near Prague, Czech Republic

Miau J.J., Department of Aeronautics and Astronautics, National Cheng Kung University, Tainan, Taiwan

Miroshnichenko A.S., Department of Physics and Astronomy, University of North Carolina at Greensboro, North Carolina, USA

Narimanova G.N., Tomsk State University of Control Systems and Radioelectronics, Tomsk, Russia

Potapov A.A., V.A. Kotelnikov Institute of Radio Engineering and Electronics of RAS, Moscow, Russia

Pribaturin N.A., Institute of Thermal Physics, SB RAS, Novosibirsk, Russia

Saulebekov A.O., Kazakhstan Branch of Lomonosov Moscow State University, Astana, Kazakhstan

Senyut V.T., Joint Institute of Mechanical Engineering of National Academy of Sciences of Belarus, Minsk, Belarus

Shrager E.R., National Research Tomsk State University, Tomsk, Russia

Stoev M., South-West University «Neofit Rilski», Blagoevgrad, Bulgaria

Suprun T., Institute of Engineering Thermophysics of NASU, Kyiv, Ukraine

Trubitsyn A.A., Ryazan State Radio Engineering University, Ryazan, Russia

Zeinidenov A.K., E.A. Buketov Karaganda University, Karaganda, Kazakhstan

Zhanabaev Z.Zh., Al-Farabi Kazakh National State University, Almaty, Kazakhstan

TECHNICAL EDITORS

Kambarova Zh.T., Akhmerova K.E., E.A. Buketov Karaganda University, Karaganda, Kazakhstan

CONTENTS

PREFACE	4
MATERIALS SCIENCE	
1. <i>Rasulov Z.N., Usanov D.N., Voinash S.A., Malikov V.N., Karnaukhov A.I., Ishkov A.V., Fadeev D.A.</i> METAL DESTRUCTION IN PROCESS OF MANUFACTURING PARTS FROM MOLYBDENUM AND NIOBIUM	5
2. <i>Khairaliyev S., Kaishubayeva N., Kapayeva S., Bergander Marek J., Dzhundibayev V.</i> COEFFICIENT OF FRICTION AT REST OF ROUGH SURFACES	12
3. <i>Narjis Zamil Abdulzahra</i> EXTRAORDINARY MAGNETORESISTANCE OF LASER ANNEALED NANO BORON DEPOSITED ON OXIDIZED POROUS SILICON	20
ENERGY	
4. <i>Alkhdery L.A., Yurchenko A.V., Mohammed J.A.-K., Neshina Y.G.</i> AUTOMATED TEMPERATURE AND HUMIDITY CONTROL AND MONITORING SYSTEM FOR IMPROVING THE PERFORMANCE IN DRYING SYSTEM.....	32
5. <i>Klimenko V.N., Suprun T.T.</i> ANALYSIS OF SYNTHETIC RENEWABLE METHANE PRODUCTION TECHNOLOGIES FOR IMPLEMENTATION IN UKRAINE.....	41
6. <i>Usenkov R.A., Kokhanova S.Ya., Trushin M.V.</i> THE USE OF ALTERNATIVE ENERGY SOURCES FOR THE OPERATION OF ENGINEERING SYSTEMS OF DETACHED CONSUMERS.....	46
7. <i>Jaddoa, Ameer A., Mahdi Mahmoud M., Hamad Karema A.</i> ON ASSESSING THE EFFECTIVENESS OF HYBRID SOLAR COLLECTORS SCHEME IN IRAQ'S ENVIRONMENT	57
8. <i>Tleubergenova A.Zh., Dyusembaeva A.N., Tanasheva N.K., Minkov L.L., Mukhamedrakhim A.R.</i> INVESTIGATION OF AERODYNAMIC THRUST FORCE WIND POWER PLANT WITH COMBINED BLADES.....	65
ENGINEERING	
9. <i>Yermakhanova A.M., Kenzhegulov A.K., Meirbekov M.N., Samsonenko A., Bayserikov B.</i> STUDY OF RADIO TRANSPARENCY AND DIELECTRIC PERMITTIVITY OF GLASS- AND ARAMID EPOXY COMPOSITES	70
10. <i>Zhanabaev Z.Zh., Ussipov N.M.</i> INFORMATION-ENTROPY METHOD FOR DETECTING GRAVITATIONAL WAVE SIGNALS.....	79
11. <i>Iwuji P.C., Okoro R.C., Idajor J.A., Amajama J., Ibrahim A.T., Echem Ch.O.</i> PERFORMANCE ANALYSIS AND DEVELOPMENT OF PATH LOSS MODEL FOR TELEVISION SIGNALS IN IMO STATE, NIGERIA	87
12. <i>Tsyganov V. V.</i> FEATURES OF MECHANICS DESTRUCTION TRIBOUNITS AT DIFFICULT DYNAMIC LOADING	99

PHYSICS AND ASTRONOMY

13.	<i>Kanapina A.E., Seliverstova E.V., Ibrayev N.Kh., Derevyanko N.A., Ishchenko A.A.</i> FEATURES OF THE DECAY OF EXCITED STATES OF IONIC DYES IN THE NEAR FIELD OF METAL NANOPARTICLES	106
14.	<i>Saulebekov A.O., Kambarova Zh.T., Omarova G.S.</i> MINIATURE HIGHLY SENSITIVE ELECTRON SPECTROMETER FOR THE ANALYSIS OF CORPUSCULAR FLUXES	112
15.	<i>Zhilgildinov Zh.S., Lisitsyn V.M., Karipbayev Zh.T., Tulegenova A., Alpyssova G.K., Mussakhanov D.A., Zhunusbekov A.M.</i> ENHANCING PHOTOMETRIC PERFORMANCE OF YAG:CE CERAMICS: INVESTIGATING THE ROLE OF ANNEALING IN RADIATION-ASSISTED SYNTHESIS	118
16.	<i>Alper Pahsa</i> MOLECULAR DYNAMIC SIMULATION OF PLASMA MATERIAL INTERACTION TO CALCULATE THEORETICAL SPUTTERING YIELD	127
	SUMMARIES	138
	INFORMATION ABOUT AUTHORS	147
	GUIDELINES FOR AUTHORS	150

Dear authors and readers!

Dear colleagues!

Traditionally, we inform our authors and readers about the most important results. We have already shared the great news that, according to the Scimago Journal & Country Rank (SJR) analytical platform of May 3, 2023, the "Eurasian Physical Technical Journal" is included in the Q3 quartile in all scientific areas!

Hirsch SJR has now reached a value of 5! The achieved indicators were obtained thanks to the authors who provided the results of scientific research on topical problems of physics and technology, as well as the qualified work of the editors and reviewers of the journal.

In 2023, the journal indexing in the Scopus database continues in four scientific areas: Energy; Engineering; Materials Science; Physics and astronomy. As of June 2023, the CiteScoreTracker Score is 0.9. This indicator value directly depends on the citations number in the articles of other editions on the articles published in the Eurasian Physical Technical Journal.

It should be noted that the percentile increased in all directions: Engineering – 25%; Physics and Astronomy – 24%, Energy – 23%, Materials Science – 17%; <https://www.scopus.com/sourceid/21100920795#>

The Materials Science section offers articles on the study of the properties of various materials, for example, the dependence of metal destruction on the type and method of their processing; the influence of the nature of the roughness of the contacting surfaces on the value of dry friction; the effect of laser annealing on the electrical and magnetic properties of the nanoboron, which causes an increase in the magnetoresistance of the material with increasing laser temperature, etc.

Articles of the section "Energy" are devoted to the problems of increasing the efficiency of thermal power plants and studying the possibilities of using alternative energy sources for the functioning of engineering systems of isolated consumers. So, for example, the development of automated control systems for the operation of a solar dryer, taking into account changes in climatic conditions; methanation technologies for the production of synthetic methane; technologies for using thermal air from an animal stall for heating or cooling rooms; development of combined blades to increase the traction force of a wind power plant, etc. The results of a study of heat removal from photovoltaic installations due to the mass flow rate of the coolant in the Baghdad agglomeration, Iraq are of practical importance.

Authors of Engineering section articles propose a solution to topical technical problems, such as the study of radio transparency and dielectric constant of glass-aramid-epoxy composites; development of a new information-entropy method for detecting gravitational wave signals, supplementing the standard matched filtering method; performance analysis and loss prediction of television signals using the example of distribution in the state of IMO, Nigeria; development of a model of the mechanics of contact destruction of tribounits during friction under conditions of complex dynamic loading, etc.

The Physics and Astronomy section presents the study results of the physics of phenomena at the micro and nano levels, such as: assessment of the effect of silver nanoparticles on intramolecular processes of deactivation of the electronically excited state in molecules of polymethine dyes of various ionicity; development of a small-sized highly sensitive electron spectrometer for analyzing the composition of corpuscular flows in a wide range of measured particle energies for space vehicles; improvement of photometric characteristics of samples of yttrium-aluminum garnet doped with cerium due to annealing in radiation synthesis; molecular dynamics simulation of plasma interaction with wall materials in a thermonuclear reactor by the Monte Carlo method.

We hope that the presented research results will be of interest and will be useful for scientists, teachers, researchers, doctoral students and undergraduates. We will be glad to see you among our readers and authors of the next issues, where it is planned to publish custom-made review articles by leading scientists on topical and priority areas of modern physics and technology.

Best regards,
Editor-in-chief, Professor Sakipova S.E.
June, 2023

METAL DESTRUCTION IN PROCESS OF MANUFACTURING PARTS FROM MOLYBDENUM AND NIOBIUM

Rasulov Z.N.¹, Usanov D.N.¹, Voinash S.A.², Malikov V.N.^{3*}, Karnaukhov A.I.⁴,
Ishkov A.V.⁵, Fadeev D.A.³

¹ Baltic State Technical University "Voenmeh" D.F. Ustinov, St. Petersburg, Russia

² Kazan Federal University, Kazan, Russia

³ Altai State University, Barnaul, Altai Territory, Russia, osys11@gmail.com

⁴ Reshetnev Siberian State University of Science and Technology, Krasnoyarsk, Russia

⁵ Altay State Agricultural University, Barnaul, Russia

The effect of coatings with surface-active properties and aerothermoacoustic treatment on Mo and Nb stampability, mechanical properties, and microdistortions of the crystal lattice is considered. An improvement in the quality of products obtained by drawing using these technologies has been established due to an increase in plasticity and a decrease in microdistortions of the crystal lattice. Modification of the surface of the tool reduces distortion in the micro-regions of the crystal lattice, reducing the stresses of the 2nd and 3rd kind of deformed Nb and improving its formability and the quality of semi-finished products and finished products. Low formability of Mo and Nb is associated with the presence of brittle phases of lamellar and sharp-edged shape, which reduce ductility and toughness. For Nb, an additional negative factor is the presence of grains up to 40–50 μm in size.

Keywords: coatings; molybdenum; niobium; microstructure; aero thermoacoustic treatment; deformability

Introduction

A variety of products are made from refractory metals (molybdenum and niobium) - honeycomb panels of spacecraft, heat exchangers, shells of rockets and capsules, thermal and other screens, wing edge trim and stabilizers in supersonic aircraft, and much more. The shaping of semi-finished products from refractory metals and alloys is carried out, among other things, by cold stamping, for example, screens - hollow axisymmetric thin-walled parts with a flange or bottom, as well as without them. The screen material must have heat resistance, heat resistance, high electrical and thermal conductivity, high-temperature long-term strength. When operating at high temperatures, an important feature is the low thermal neutron capture cross section. Materials providing a complex of these properties - niobium and molybdenum [1].

To carry out cold plastic deformation (CPD) operations, for example, drawing, which is widely used for the production of a number of products, the workpiece material must have, in addition to the required strength values, the necessary plasticity characteristics.

Molybdenum is a valuable refractory metal with a melting point of about 2610°C [2]. The strength of the interatomic bond of molybdenum is so great that at room and high temperatures its strength is always high [3]. In addition, unlike other refractory metals such as Ta, Nb, Co, W, etc., molybdenum not only has a high melting point, excellent thermal conductivity, good electrical conductivity and corrosion resistance, has a low thermal expansion coefficient and high hardness [4]. However, its use as a structural material is limited by the increased brittleness that is known to occur due to intragranular fracture. Yoshinaka [5] believed that grain boundaries with sufficiently high energy are responsible for intragranular fracture in molybdenum. Meanwhile, Watanabe and Tsurekawa [6] investigated the relationship between intragranular fracture and grain boundary microstructure in 2D polycrystalline molybdenum and pointed out that increasing the resistance of polycrystalline molybdenum to intragranular fracture can be achieved by controlling the character of grain boundaries. Moreover, molybdenum and its alloys, due to their high melting point, high hardness [4], low-temperature brittleness [7], and poor ability for high-temperature oxidation resistance [8], could hardly be obtained by casting, forging and other mechanical processing, for except for the powder metallurgy method. However, the conventional processing of molybdenum by powder metallurgy requires

long-term sintering at high temperature, which leads to excessive grain coarsening and subsequent deterioration of mechanical properties. Garg et al. [9] investigated the sintering mechanism of molybdenum powders and proposed an accurate model for calculating optimal molybdenum sintering cycles using the powder metallurgy method. On the other hand, molybdenum must be processed in a narrow range of high temperatures due to its significant resistance to deformation [10]. Microstructural analysis, mechanical behavior and testing of the properties of molybdenum and its alloys have been carried out by many researchers in recent years. For example, Laribi et al. [11] investigated the metallurgical and mechanical properties of molybdenum coating formed by flame spraying, studying its microstructure, hardness, and tribological resistance. In addition, Ciulik and Taleff [12], as well as Wang et al. [13] investigated the behavior of molybdenum sheet at temperatures from 1300 C to 1600°C, as well as its properties at elevated temperatures.

In industry, molybdenum strips of technical purity are used, obtained using the technology of cold plastic deformation (Specifications 11-90. Molybdenum strips). At the same time, blanks are obtained according to the scheme: annealing, cold rolling in two mutually perpendicular directions, which provides the required level of strength $\sigma_{\text{temporary resistance}} = 800-980 \text{ MPa}$, but at the same time the level of plasticity is low – $\delta = 1-2\%$ (Specifications 48-19-272-83 Molybdenum bands), which makes it difficult or impossible to carry out cold plastic deformation (drawing). Plasticity can be increased during vacuum annealing of workpieces up to $\delta = 3\%$, but in this case the strength decreases to $\sigma_{\text{temporary resistance}} = 685 \text{ MPa}$. (Specifications 11-90).

Niobium (Nb) is a metal with a melting point of 2468°C, a density of 8.57 g/cm³, and a cubic crystal structure [14]. Niobium is used in the chemical, nuclear and electrical industries and in the production of superconducting wire [15, 16]. Niobium is able to interact with oxygen (O₂), nitrogen (N₂), water vapor (H₂O), carbon monoxide (CO) and gases present in the environment. Because of these characteristics, niobium is produced and purified in an inert atmosphere or high vacuum.

There are three methods for producing products from Nb: powder metallurgy (PM), vacuum arc welding (VAW), and electron beam melting (EBM). The EBM process is more common and produces high purity metal, around 99.99%. During plastic deformation, the hardening process occurs due to the multiplication, interaction and distribution of dislocations, which is strongly influenced by the ESF (energy stacking fault). The evolution of the microstructure during plastic deformation is very important with respect to the deformation mechanism, mechanical properties and material formation. In addition, the deformation characteristics of the microstructure affect the behavior of the material during recrystallization [17, 18]. To conduct a qualitative microstructural analysis, niobium needs special preparation for metallography due to mechanical characteristics that can cause various surface disturbances. Niobium is supplied in the form of strips according to Specifications 48-19-264-84 in the annealed state.

However, it should be taken into account that Mo and Nb strips of the same batch according to specifications can differ significantly in deformability, which, when drawing followed by vacuum annealing, can lead to significant product defects.

One approach to improve ductility is microalloying molybdenum and niobium with aluminum, tantalum, magnesium, chromium, zirconium, or vanadium. However, the anisotropy of plastic deformation can often lead to the destruction of the material [19, 20, 21].

In this regard, it is advisable to study the possibility of using technologies that improve the deformability of metals by increasing plasticity, not only by intermediate annealing. These technologies include: aero-thermoacoustic treatment - ATAT and the application of coatings with surface-active properties - surfactants, the use of which on steels and alloys has shown the possibility of increasing plasticity and deformability.

1 Materials and methods of research

The study of the effect of ATAT and surfactant coatings was carried out on sheets of Mo and Nb with a thickness of 0.15 mm. Mo was conditionally divided into 2 subgroups: Mo1 - with good deformability and Mo2 - with poor; the result of which are defects in the workpieces (scallop, cracks, poor-quality surface). The cause of the defect in the stamping of caps from an anisotropic strip is the texture of recrystallization, which results in a wavy edge - scalloped. Scallops are the result of different metal drawing in different directions with different wall thinning (Fig. 1b).

Aerothermoacoustic treatment (ATAT) was carried out on a facility created at Baltic State Technical University "Voenmeh" D.F. Ustinov according to the developed technology [1]. The surfactant FLUORO-surfactant coating was applied according to the developed scheme using ultrasonic cleaning. Mechanical properties were determined by static tensile testing on a Shimadzu AGX-100kN machine on flat standard specimens. The microstructure of the alloy was studied using a DSX 510 OLIMPUS optical microscope with software and a scanning electron microscope.

To determine the qualitative phase composition and microdistortions of the Nb crystal lattice in the initial state, with surface modification and subsequent drawing, a Rigaku Ultima IV multifunctional X-ray diffractometer was used. The diffractometer is equipped with a complex of control programs and a processing complex PDXL (X-ray Powder Diffraction Software). X-ray diffraction was carried out in focusing geometry according to the Bragg-Brentano scheme in filtered $\text{CuK}\alpha 1$ radiation. Microdistortion calculations ($\Delta d/d$) were carried out for all peaks using the Williamson-Hall method. The Nb sample without cold plastic deformation was used as a reference.

2 Results and discussion

The results of mechanical tests of Mo and Nb in the initial state, after acoustic treatment and application of pav-coating are presented in Table 1.

Table 1. Mechanical properties of Mo and Nb in the initial state and after ATAT.

No. mode	Type of initial processing	Additional processing, processing time	Mechanical properties		
			$\sigma_{0,2}$	$\sigma_{\text{temporary resistance}}$	δ
			MPa		%
Mo					
1	annealing, cold rolling (as delivered)	-	949	986	1.5
2	annealing, cold rolling	The impact of air flow and acoustic field with a sound pressure level of 140-160 dB. within 10 min.	830	960	2.8
3	annealing, cold rolling	The impact of air flow and acoustic field with a sound pressure level of 140-160 dB. within 20 min.	935	1115	3.3
4	annealing, cold rolling	-	-	900-980	1-2*
5	annealing, cold rolling	Annealing for 30-40 min.	-	685	2,0; 3,0**
Nb					
1	delivery condition - annealed	-	151	230	8,2
2	delivery condition - annealed	The impact of air flow and acoustic field with a sound pressure level of 140-160 dB. within 15 min.	122	250	27
3	delivery condition - annealed	-	-	200	15

Mo: 4.5 – Mode TY 11-90, Specifications 48 -19 -273-91, *Nb- Mode 3 Specifications 48-4-317-74

From the above results of testing the mechanical properties of Mo samples that have undergone acoustic treatment (ATAT) according to the optimal mode No. 3, it can be seen that both σ_w (slightly) and $\delta\%$ increase simultaneously, which makes it possible to avoid the appearance of defects in the product when using cold plastic deformation technology, such as scalloping and cracks.

According to the test results of Nb samples that have undergone acoustic treatment (ATAT) according to the optimal mode No. 2, it can be seen that the strength ($\sigma_{\text{temporary resistance}}$) practically does not change, but significantly, more than 3 times, $\delta\%$ increases compared to the initial value. This allows both to use a large degree of deformation in the production of products, to reduce processing time, and to reduce the loss of expensive materials due to defects. The study of the Mo microstructure of both subgroups showed

that in the Mo1 structure with good deformability, slip lines and bands, fault bands (slip line curvature) are fixed, which indicates that during the deformation process, dislocation slip in two or more systems of planes and reactions at their intersection, which corresponds to the stage of multiple slip (Fig. 1). In this case, slip bands are formed, which are a pack of slip lines. At the stage of multiple slip, the structure of the metal becomes more complicated (Fig. 1.a), the dislocation density increases significantly.

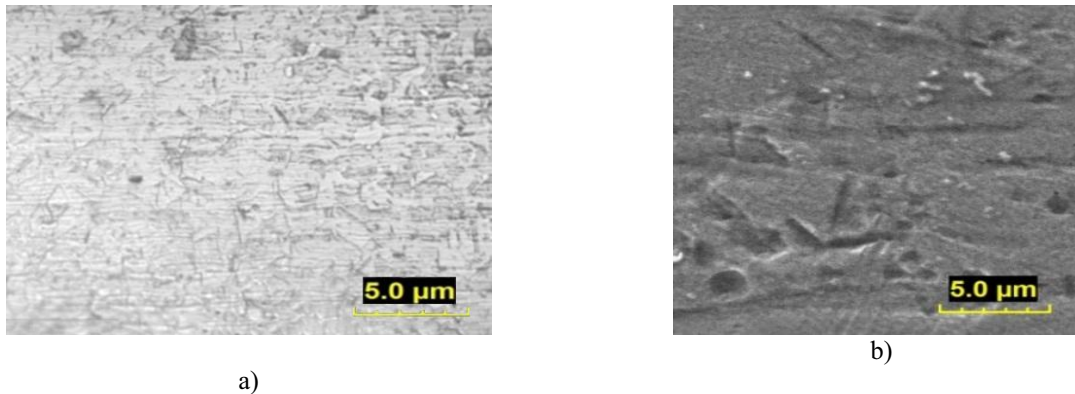


Fig.1. Mo1 microstructure with good deformability, a – slip lines are continuous stripes, a high value of Mo plasticity is noted, b – slip lines are strongly fragmented, a slight decrease in the value of Mo plasticity is noted

The structure of Mo indicates a relatively uniform distribution of dislocations. Dislocations bypass barriers (fields of elastic stresses, inclusions of different sizes) that arise during their movement due to the transverse slip of screw dislocations. The presence of blocked dislocations leads to fragmentation of slip bands (Fig. 1.b). The metal under consideration is characterized by a rather fine-grained structure with a grain size range of 3-15 μm , and the largest number of grains has sizes in the range of 4-10 μm , which allows having sufficient plasticity with the required strength.

The microstructure of a material with poor deformability - Mo2 is shown in Fig.2. It is characterized by a significant decrease, in comparison with Mo1, in the length of slip lines in slip bands. The reason may be the “jamming” of possible slip planes inside the sample by various barriers, such as inclusions, including sharp-edged ones (Fig. 2. a).

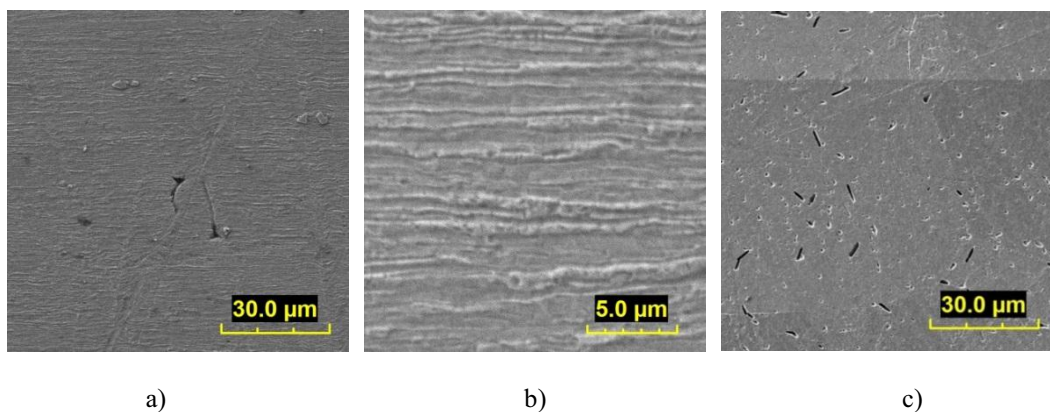


Fig.2. The microstructure of the material with poor deformability - Mo2, a - there are sharp-edged inclusions in the slip planes, the plasticity of Mo is slightly reduced, b - a cellular streaky structure is formed, where light subgrains are cells with a smaller number of dislocations, dark stripes are zones with a high density of dislocations, there is a more noticeable decrease in Mo plasticity, c - there are lamellar inclusions up to ~5-8 μm in size, which significantly reduce Mo plasticity.

In metals with a bcc lattice (Mo, Fe, Nb), during plastic deformation, the processes of formation of dislocation tangles develop in the local volumes of crystals, where they intersect, i.e. a cellular dislocation structure is formed. Due to the unevenness of the sizes of grains and cells, a cellular streaky structure is formed (Fig. 2. b). Light subgrains are cells in which there are fewer dislocations, dark stripes are zones in

which the density of dislocations is high. When the content in Mo of more than 0.1% of interstitial impurities may be the segregation of impurities along the grain boundaries, which leads to delamination of the metal in the process of plastic deformation. Stratification is a manifestation of the anisotropy of mechanical properties and the segregation of impurities. Stratification also occurs when the banded structure remains after recrystallization, which is present in Mo2, and can determine its reduced plasticity (Fig. 2. b).

In the structure of Mo2 with especially degraded deformability (Fig. 2. c), there are lamellar inclusions (or cavities formed after brittle inclusions are chipped) up to $\sim 5\text{-}8\ \mu\text{m}$ in size, as well as small inclusions, obviously reducing the plasticity of Mo. The structure of Nb in the initial state is shown in Fig.3.

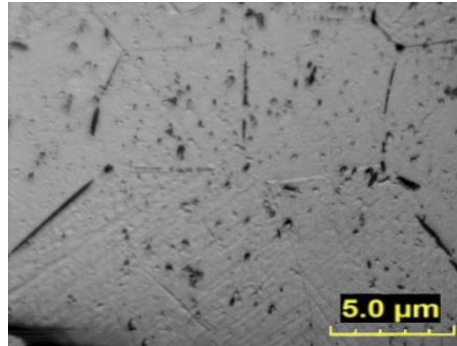


Fig.3. Microstructure of Nb, with phases of different sizes, separated along the grain boundaries and along the grain and causing a certain decrease in the plasticity of Nb.

The Nb grain size is in the range of $5\text{--}50\ \mu\text{m}$. The largest number of grains have a size of $15\text{--}40\ \mu\text{m}$. The metal is characterized by a significant uneven grain size. According to specifications, the Nb grade (Hb-1) contains 0.01% of each of the impurities (nitrogen, oxygen, carbon). In Fig. 3, one can see the presence of phases of different sizes, separated along the grain boundaries and along the grain. The grain size significantly affects the plasticity and deformability of Nb. The embrittlement of Nb with coarse grains is determined by the higher concentration of oxygen and other impurities along the grain boundaries, which is associated with its shorter length. This results in a reduced plasticity of Nb and the presence of defects, which are also characteristic of Mo. In the Nb static tension diagram (in the neck region), the deformation proceeds according to a mixed mechanism: zones of ductile and brittle fracture alternate with a large zone of brittle fracture.

An increase in the plasticity of Mo and Nb during ATAT (Table 1) is associated both with the refinement of phases, grains and their fragmentation, and with a decrease in internal stresses. deformation also proceeds through a viscous mechanism with minimal fracture.

To determine the microdistortions of the crystal lattice, X-ray diffraction analysis of 6 samples of niobium was carried out after various stretching. X-ray diffraction qualitative phase analysis of the samples revealed the following: the main phase in all samples is Nb. There is no texture in the first sample (the ratio of the peak intensities corresponds to the tabular data of the powder state (textureless)). In all other samples, some redistribution of the reflection intensities is observed, probably caused by the previous plastic deformation. Surfactant was applied to samples 3, 5, 6 before deformation. Results of microdistortion calculations crystal lattice are given in Table 2.

Defects, manifestations in the process of shaping of tissues from Nb coating with a decrease in plasticity, which in turn may be associated with damage in microregions - stresses of the second kind, i.e. accumulation of imperfections in the crystal structure. Data on the damage of the crystal lattice ($\Delta d/d$) allow us to judge the amount of elastic deformation, which is a material. The width of the diffractive paints (in terms of the magnitude of the values of $\Delta d/d$) can be produced with the growth of lattice defects. The role of growth in the reduction of plasticity in the process of plastic deformation is determined by the fact that elastically damaged microregions under external load become decomposition concentrators and turn into crack nuclei.

From the dislocation point of view, elastically distorted microregions are clusters of edge dislocations if they are located in such a way that the stress fields reinforce each other. This contributes to the appearance of microcracks and a decrease in ductility and toughness.

Table 2. Calculations of microdistortions of the crystal lattice

Calculations of microdistortions of the crystal lattice	$\Delta d/d, 10^{-3}$	(110) – (220)		
		$\cos(\theta_1)/\cos(\theta_2)$	β_2/β_1	$\text{tg}(\theta_2)/\text{tg}(\theta_1)$
1 source disk	-	1.26	1.22	2.51
2 tubule with a diameter of ~ 3 mm,	1.9	1.26	2.28	2.51
3 ----- « + surface-active substance	1.7	1.26	2.31	2.51
4 glass with a diameter of ~ 8 mm, min h=4mm	1.5	1.26	2.33	2.51
5 glass with a diameter of ~ 8 mm ,min h=8mm + surface-active substance	2.5	1.26	2.27	2.51
6 glass with a diameter of ~ 12 mm + surface-active substance	2.1	1.26	2.30	2.52

As is known, in the presence of lattice distortions in metal microregions, the width of the lines is proportional to the tangent of the reflection angle, and in the case of small crystals, to the secant of the same angle. An analysis of the values of microdistortions ($\Delta d/d$) in samples 2–6 Nb showed that the found ratios of the true linewidth at large and small reflection angles β_2/β_1 were closer to $\text{tg}(\theta_2)/\text{tg}(\theta_1)$ than to $\text{ces}(\theta_2)/\text{ces}(\theta_1)$. Therefore, distortions occur mainly due to the growth of distortions in the microregions of the crystal lattice.

The distortion in the microregions of the crystal lattice of sample 3 with surfactant is somewhat less than that of sample 2 without coating at the same degree of deformation. Consequently, the surfactant ensures greater plasticity of Nb during deformation and better product quality. With a decrease in the degree of deformation of sample 4 with respect to samples 2 and 3, the distortion of the crystal lattice decreases. In the presence of surfactants on samples 5 and 6, an increase in the degree of deformation to 30% makes it possible to obtain a sample without defects.

Conclusion

1. Low formability of Mo and Nb is associated with the presence of brittle phases of lamellar and sharp-edged shape, which reduce ductility and toughness. For Nb, an additional negative factor is the presence of grains up to 40–50 μm in size.

2. Acoustic treatment of Mo and Nb improves ductility and toughness without compromising strength, improving formability.

3. Modification of the surface of the tool reduces distortion in the micro-regions of the crystal lattice, reducing the stresses of the 2nd and 3rd kind of deformed Nb and improving its formability and the quality of semi-finished products and finished products.

4. In the technological process of obtaining products according to the Mo and Nb drawing-annealing scheme, annealing can be replaced by ATAE, which will reduce the duration and cost of the process, while improving the quality of products.

REFERENCES

- 1 Vorob'eva G.A., Remshev E.Yu. Effect of the Parameters of Aerothermoacoustic Treatment of 40Kh Steel on the Acoustic Emission Parameters. *Rus. Metall*, 2016, Vol. 3, pp. 215–218. doi: 10.1134/S0036029516030162
- 2 Pranav G., Seong J., German R.M. Effect of die compaction pressure on densification behavior of molybdenum powders. *Int. J. Refrac. Met. Hard Mater*, 2017, Vol. 25, No. 1, pp. 16–24. doi: 10.1016/j.ijrmhm.2005.10.014
- 3 Wang Y., Li F. Study on hot deformation characteristics of molybdenum based on processing map. *Xiy. Jinsh. Cail. Yu Gongce*, 2009, Vol. 38, № 8, pp. 1358–1362.
- 4 Schade P., Bartha L. Deformation and properties of PM molybdenum and tungsten. *Int. J. Ref. Metal. Hard Mater*, 2002, Vol. 20, № 4, pp.259–260. doi: 10.1016/S0263-4368(02)00071-9
- 5 Yoshinaga H. Grain-boundary structure and strength in high temperature materials. *Mater. Trans. JIM*, 1990, Vol.31, No. 4, pp. 233–248.

- 6 Watanabe T., Tsurekawa S. Control of brittleness and development of desirable mechanical properties in polycrystalline systems by grain boundary engineering. *Acta Mater*, 1990, Vol. 47, No. 15, pp. 4171–4185. doi: 10.1016/S1359-6454(99)00275-X
- 7 Shigeaki K., Sadahiro T., Tadao W. Grain boundary hardening and triple junction hardening in polycrystalline molybdenum. *Acta Mater*, 2005, Vol. 53, pp.1051–1057. doi: 10.1016/j.actamat.2004.11.002
- 8 Wang D., Yuan X., Li Z. Progress of research and applications for Mo metal and its alloys. *Rare Metal. Let*, 2006, Vol. 25, No. 12, pp.1–7. doi: 10.3390/met10020279
- 9 Garg P., Park S. German Randall M. Effect of die compaction pressure on densification behavior of molybdenum powders. *Int. J. Ref. Metal. Hard Mater*, 2007, Vol. 25, pp. 16–24. doi: 10.1016/j.ijrmhm.2005.10.014
- 10 Wang Y., Li F. Numerical simulation of radial precision forging technology for metal molybdenum. *Xiy. Jinsh. Cail. Yu Gongc*, 2009, Vol. 38, No. 12, pp. 2136–2140.
- 11 Laribi M., Vannes A.B., Treheux D. Study of mechanical behavior of molybdenum coating using sliding wear and impact tests. *Wear*, 2007, Vol. 262, No. 11–12, pp. 1330–1336. doi: 10.1016/j.wear.2007.01.018
- 12 Ciulik J., Taleff E.M. Power-law creep of powder-metallurgy grade molybdenum sheet. *Mater. Sci. Eng. A*, 2012, Vol. 463, No. 1–2, pp. 197–202. doi: 10.1016/j.msea.2006.09.113
- 13 Wang Y., Gao J., Gongming C. Properties at elevated temperature and recrystallization of molybdenum doped with potassium, silicon and aluminum. *Int. J. Ref. Metal. Hard Mater*, 2008, Vol. 26, No. 1, pp. 9–13. doi:10.1016/j.ijrmhm.2007.01.009
- 14 Hampel A.C. *Rare metals handbook, second edition*. New York. 1971, 350 p. doi: 10.1149/1.2427960
- 15 Brauner A., Nunes C.A., Bortolozzo A.D., et al. Superconductivity in the new Nb₅Si₃-xBx phase. *Sol. State Comm*, 2009, Vol. 149, No. 11-12, pp. 467-470. doi:10.1016/j.ssc.2008.12.037
- 16 Santos F.A., Ramos A.S., Santos C., et al. Obtaining and stability verification of superconducting phases of the Nb–Al and Nb–Sn systems by mechanical alloying and low-temperature heat treatments. *J. all. Comp*, 2010, Vol. 491, No. 1-2, pp. 187-195. doi:10.1016/j.jallcom.2009.11.011
- 17 Hansen N. Cold deformation microstructures. *Mater. Sci. Tech*, 1990, Vol. 6, No. 11, pp. 6 - 19. doi:10.1179/mst.1990.6.11.1039
- 18 Borges D.G., Márcia R.B. Microstructural and Mechanical Characterization of the Niobium Cold Deformed-Swage. *Mater Sci. For*, 2015, Vol. 805, pp. 362-367. doi:10.4028/www.scientific.net/MSF.805.362
- 19 Sharif A.A., Misra A., Mitchell T.E. Deformation mechanisms of polycrystalline MoSi₂ alloyed with 1494 at.% Nb. *Mater. Sci. Eng. A*, 2013, Vol. 358, No. 1-2, 279–287. doi:10.1016/S0921-5093(03)00307-1
- 20 Carolin Z., James S.K-L. Low temperature deformation of MoSi₂ and the effect of Ta, Nb and Al as alloying elements. *Acta Mater*, 2019, Vol. 181, pp. 385-398. doi:10.1016/j.actamat.2019.09.008
- 21 Volokitina I., Nayzabekov A., Volokitin A. Influence of torsion under high pressure on the change in the microstructure of microalloyed steel. *Eurasian Physical Technical Journal*, 2022, 19(4(42)), 17–21. doi:10.31489/2022No4/17-21

COEFFICIENT OF FRICTION AT REST OF ROUGH SURFACES

Khairaliyev S.^{1*}, Kaishubayeva N.², Kapayeva S.³, Bergander Marek J.⁴, Dzhundibayev V.⁵

¹ Intekko Ltd, Astana, Kazakhstan, kh.serik@gmail.com

² Rauza-PV LLP, Astana, Kazakhstan

³ East-Kazakh Technical University, Ust-Kamenogorsk, Kazakhstan

⁴ Magnetic Development INC., Madison, USA

⁵ L.N. Gumilyov Eurasian National University, Astana, Kazakhstan

At present, the process of designing dry friction units for mechanical engineering and some other structures is becoming more and more laborious, forcing designers to make more and more efforts in this work. A significant complication of the work performed gives the random nature of the roughness of both contacting surfaces and this circumstance forces the designers to look for new ways to solve existing problems. In this paper, we consider the contact interaction of two rough parts, the roughness of which is modeled by spherical surfaces. The proposed friction pair model makes it possible to estimate the interaction forces of contacting rough surfaces acting between the considered surfaces. It should be emphasized that this paper considers the interaction of contacting bodies with an applied external force capable of starting the relative movement / sliding of the considered bodies with rough surfaces.

Keywords: Rough surface; analytical modelling; static interaction of rough surfaces

Introduction

Descriptions of the various friction phenomena was attempted in numerous studies by considering the surface roughness effect. Surface topography observed in microscopic scale was proved to be extremely rough and of random nature, composed of alternating ledges and hollows of various dimensions referred to as surface heights, or asperities and micro cavities. One of the earliest models to describe surface roughness was presented by Archard. It represented the rough surfaces as spherical asperities consisting of smaller asperities in recursion, which would deform elastically at the points of contact with another surface [1]. The true area of contact then would be the summation of the areas of contact of each of the asperities [1].

On the other hand, Zhuravlev modeled roughness as spherical irregularities of the same size, located at different heights with a linear distribution [2]. Based on the Hertz solution for two contacting rough surfaces, it was concluded that the true contact area is proportional to the normal load [2]. Archard's and Zhuravlev's models were further developed by Greenwood and Williamson to incorporate Gaussian distribution of asperity heights and plastic deformation of asperities beyond the elasticity limit [3]. They showed that whether the asperities deform elastically or plastically did not depend on the normal load, and as an indication of the type of deformation plasticity index, ψ , was introduced.

Later Bush, Gibson and Thomas proposed a model (BGT model) of roughness as elastically deformed paraboloids distributed according to the random process model [4]. On the other hand, Kragelsky et al. [5] modelled roughness as elastic rods of varying heights. The authors' equation for the function of the normal force, N , with respect to rough planes' separation, a , revealed that the contact area, A_c , had linear dependence on normal load [4].

Numerical modelling is also used to describe the roughness and analyze the friction. For example, Ogilvy [6] produced a numerical model of statistically distributed elastic and plastic asperities, and estimated the friction coefficients through the adhesive force (microscale) and the overall true area of contact (macroscale). On the other hand, Karpenko and Akay [7] did computational three-dimensional modelling of elastic deformations. Ford also numerically estimated the effect of contact angle in the Greenwood and Williamson's model for elastic and plastic deformation [3]. These deformations were also addressed in [8] taking into account the control volume conservation. Statistical calculations were also performed for micro-slip [9] and fretting phenomena [10]. Serious works include the book by Kragelsky [11] and the book written

under the direction of Chichinadze [12]. In these books, the geometric parameters of rough friction surfaces are considered in detail and the processes of their contact interaction are modeled.

The contact of surfaces was considered in [13] with spherical roughness in the absence of an external horizontal force. The performed calculations made it possible to come to the conclusion about the reasonableness of using the model considered here for calculating the forces of contact interaction.

1 Friction force model

The main goal of this work is to calculate the static friction force, for which the model of a friction pair was adopted, the initial consideration of which was carried out in [13]. To calculate the forces of contact interaction, we use the model shown in Fig. 1. It is quite obvious that in real conditions not all irregularities of the contacting parts of the friction unit are in contact with each other and the calculation will be performed in this way - the most realistic case will be taken into consideration when only a part of the roughness of both parts are in contact.

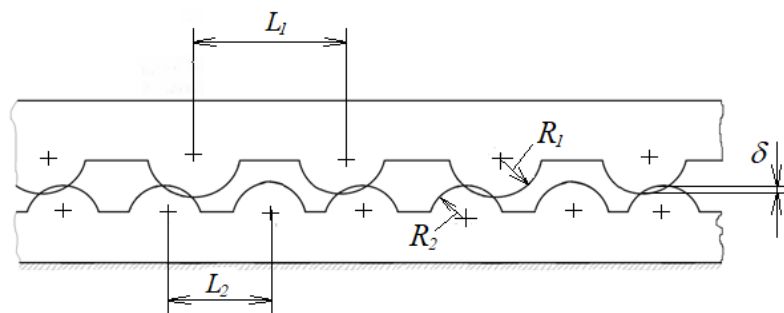


Fig1. Two rough contact surfaces (the slider and the base):

R_1 and R_2 are micro-roughness radii of the slider and the base, respectively, δ is the overlapping of the pair of contacting micro-asperities in the vertical direction, L_1 and L_2 are period of micro-roughness of the slider and the base.

The contact of the roughness of the slide and the roughness of the base is shown in Fig. 2, the irregularities shown here are interacting. The vertical force and the horizontal force are shown in Fig. 2 and we will consider how these forces can be determined. Obviously, the sum / integral of all vertical forces in each contact must be equal to the external vertical force and the sum / integral of all horizontal forces in each contact must be equal to the external horizontal force.

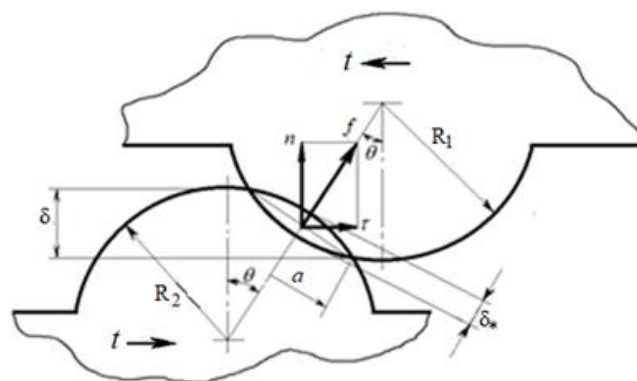


Fig. 2. Mechanical contact model between two asperities:

f is the contact reaction along the line connecting the centers of the radii of the slide and the base, n and τ are the vertical and the horizontal forces of interaction in the normal and horizontal directions, a is the radius of the contact circle of microroughness, θ is the angle between the vertical line and the line connecting the centers. t is that part of the external force that acts on the considered roughness.

Different authors approach the calculation of the friction force with different bases [11]:

- friction is explained by lifting along microroughness;
- friction is explained as the result of overcoming the forces of molecular interaction between two solids;
- friction arises as a deformation force;
- a combined approach to determining the friction force.

In this work, the forces of interaction arising from the contact of spherical roughness will be determined. During friction of rough surfaces, a rather large number of pairs of roughness come into contact, as in Fig. 2; all contacting pairs of roughness are at different angle θ . For further consideration of a real friction pair, a model will be adopted in which all contacting spheres of the base are reduced to one protrusion (part of the sphere) in Fig. 3, and the contacting protrusions of the slider, i.e. undoubtedly in different positions in relation to the base are shown in Fig. 3 as a deformable medium (here it looks like a gray mass).

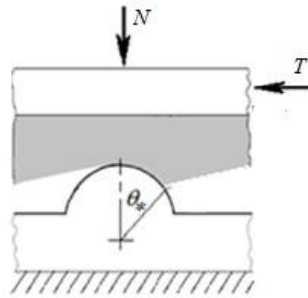


Fig. 3. Contact of the roughness of the slide, reduced to one roughness of the base. θ_* is the initial contact angle.

We consider the moment of the beginning of contact, Fig. 3 is shown somewhat simplified for such a position - in the left part of the upper body, the material allegedly "does not have time" to return to the "undeformed state", but in fact the left part of the body does not deform and the figure shows it in such a way that the process under consideration was clearer. Consider the case when an external horizontal force T is applied to the slider on the right-side side, forcing the slider to move to the left. For the slider to start sliding on the base, the magnitude of this force must reach a certain value, which is classified as the static friction force. It is quite reasonable to assume that at the moment of the beginning of sliding, the contact forces between the roughness of the slider and the base in the left half of the roughness of the base become equal to zero.

The primary consideration of the forces of contact interaction of the slider with the base without the application of an external horizontal force T was carried out in [13]. Now we must calculate the horizontal force T , and also take into account the fact that the contact of the roughness of the slider and the base occurs as shown in Fig. 3. In [13], the following formulas were derived for calculating the contact forces of the roughness of the slide and the base

$$n = c_{\theta}(\theta_*^2 - \theta^2)^{3/2} ; \tag{1}$$

$$\tau = c_{\theta}\theta(\theta_*^2 - \theta^2)^{3/2} , \tag{2}$$

where θ_* is the angle at which the beginning of contact between the roughness of the slider and the base is possible (θ_0 has the same definition, but it is used in the absence of horizontal forces including friction forces as shown in Fig.3); the following values were also taken in [13] for calculations:

$$c_{\theta} = c \left(\frac{R_1 + R_2}{2} \right)^{3/2} ; \quad c = \frac{4}{3} R^{1/2} E ,$$

and

$$\frac{1}{R} = \frac{1}{R_1} + \frac{1}{R_2} \quad R = \frac{R_1 R_2}{R_1 + R_2} , \quad E = \frac{E_1 E_2}{E_1(1 - \mu_2^2) + E_2(1 - \mu_1^2)} .$$

(1) and (2) describe the μ_l forces of interaction in a single contact. The total force of interaction of friction surfaces can be found by summing / integrating all contacts of the roughness of the slide and the base. The vertical and horizontal forces of contact of friction surfaces are:

$$N = \frac{j_a c \theta}{2\theta_L} \int_0^{\theta_*} (\theta_*^2 - \theta^2)^{3/2} d\theta. \quad (1)$$

$$T = \frac{j_a c \theta}{2\theta_L} \int_0^{\theta_*} (\theta_*^2 - \theta^2)^{3/2} \theta d\theta. \quad (4)$$

Here $\theta_L = \frac{L_1 + L_2}{2(R_1 + R_2)}$ is the greatest angle up to which it is assumed that the micro-asperity of the slider is opposed to the micro-asperity of the base, j_a is the number of contacting pairs of roughness in the contact zone; the calculations will use the value of the change Δj_a with an increase in the vertical force N and the approach of the friction surfaces under the action of an external normal force.

In the future, we will carry out calculations with the assumptions that as the slide and the base come closer under the action of an external force, the number of contacting pairs of roughness increases. The stiffness of the roughness of the slider and the base, which come into contact with an increase in the normal force and the approach of the contacting bodies, undoubtedly differs in magnitude from the stiffness of the roughness that came into contact before the considered moment. However, in the proposed primary consideration of the contacting surfaces, we will assume that the rigidity of all contacting pairs of roughness is the same.

As can be seen, in equations (3) and (4) the integral is taken within the limits different from the limits used in [13] - here it is taken from zero to θ_* on the side where the contact begins and, as can be seen, after passing the vertex roughness contact disappears. As a result of integrating formulas (3) and (4), we obtain the following expressions for calculating the normal force and horizontal (frictional) force

$$N = \frac{3\pi j_a c \theta_*^4}{32\theta_L} \quad (5)$$

$$T = \frac{j_a c \theta_*^5}{10\theta_L} \quad (6)$$

The coefficient of friction now can be calculated

$$\mu = \frac{T}{N} \quad (7)$$

The used model of two contacting bodies with a rough surface makes it possible to trace the process of the formation of the friction force at relative rest of the contacting bodies and to simulate the process of friction of rough surfaces. In our opinion, the considered model also makes it possible to explain the main reasons for the increase and decrease in the coefficient of friction. We believe that the theoretical calculation of the friction force performed in Section 2 makes sense and gives a good idea of the dependence of the friction coefficient on the normal force.

2 Results and discussion

Based on the experience of our work, we want to say that as the vertical external force increases, the slider and the base approach each other and, at the same time, the number of pairs of new microasperities entering into contact decreases. Nevertheless, we believe it is possible to perform the initial calculation of the process of increasing the external force with a constant number of pairs of roughnesses coming into contact, but this can only be done at the initial stage of modeling a contacting friction pair. Further, on the basis of the formulas presented here, graphs of the dependence of the friction coefficient on the values characterizing the considered friction pair are constructed.

Table 1. Common parameters for all systems shown in the following graphs

R_1, m	R_2, m	L_1, m	L_2, m	E_1, Pa	μ_1	E_2, Pa	μ_2
$1.5 \cdot 10^{-5}$	$2.0 \cdot 10^{-5}$	$1.6 \cdot 10^{-4}$	$2.0 \cdot 10^{-4}$	2.2000E+11	0.25	2.2000E+11	0.25

Fig. 4 shows three graphs of the dependence of the coefficient of friction of materials with the characteristics indicated in Table 1, and the radii of roughness and the number of these roughness are given in Table 2. It can be seen that with an increase in the normal force N applied to the friction pair, the coefficient μ of static friction increases.

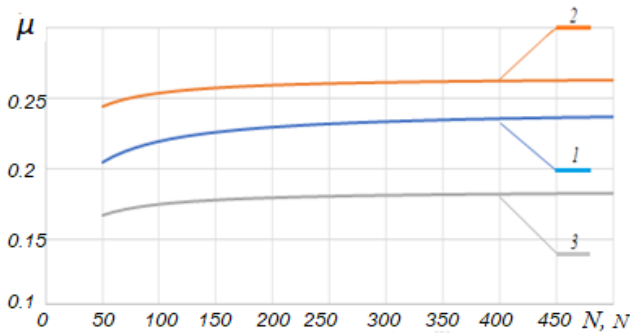


Fig. 4. The dependence of the coefficient of friction μ on the pressing force (all values are in table 2).

Table 2. The parameters of the graphs in Fig.4.

	1	2	3
j_a	10	7	15
Δj_a	1	1	2

Earlier it was said that the change in the number of contacting roughness Δj_a occurs with an increase in the vertical force N . It would be more correct to specify the change in the number of roughness depending on the increase in the depth of immersion of the slider roughness in the roughness of the base, but in this first work it is assumed in a simplified way that the number contacting roughness increases depending on the applied vertical force N .

Fig. 4 shows graphs of the coefficient of friction for three different friction surfaces. The curve constructed for friction pair 2 has the least roughness and, in our opinion, with a smaller number of roughness, the slider penetrates deeper into the roughness of the base and this creates a greater value of the friction coefficient. The friction pair, for which curve 3 is constructed, has a large number of roughness and this leads to less convergence of the bodies and a lower coefficient of friction. Friction pair number 1 has an average number of roughness and creates an average value of the friction coefficient.

On Fig. 5 graphs are constructed for materials with the same roughness parameters (radii) as those considered in Fig. 4, but the amount of roughness is different. It can be seen that in Fig. 4, the initial number of roughness is greater than in Fig. 5, but the subsequent increase in the number of contacting roughness is less than that shown in Figs. 5. As can be seen, a large initial number of roughness and their slight increase with an increase in the vertical force pressing the slider to the base leads to an increase in the friction coefficient with an increase in the vertical force pressing the slider.

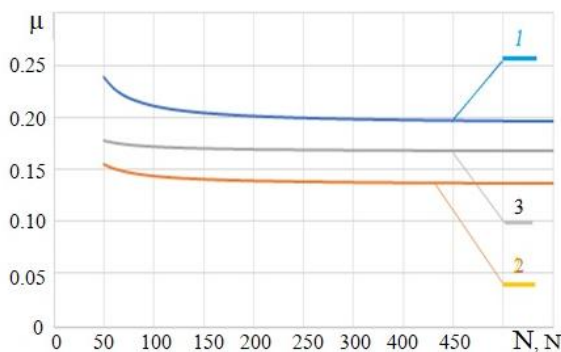


Fig. 5. The dependence of the coefficient of friction μ on the pressing force (all values are in table 3).

Table 3. The parameters of the graphs in Fig. 5.

	1	2	3
j_a	5	10	8
Δj_a	2	3	2

In the case of a smaller initial number of roughnesses and with a larger number of roughnesses that come into contact with an increase in the vertical external force, the friction coefficient decreases with an increase in the external vertical force. As becomes obvious, with a larger number of microroughnesses, the friction coefficient decreases. Why? With a larger number of roughnesses, each contacting pair has a smaller contact force and this leads to the fact that the contact angle is smaller, the contact roughnesses of both friction pairs are in contact at a smaller angle (closer to their top).

Fig. 6 shows three graphs with the same parameters at the initial moment of contact, but with a subsequent increase in force, the number of microroughnesses that come into contact again differs. The deformation turns out to be greater for the friction pair, in which the number of roughnesses is less, and if the friction pair has more microroughnesses, the friction coefficient is lower.

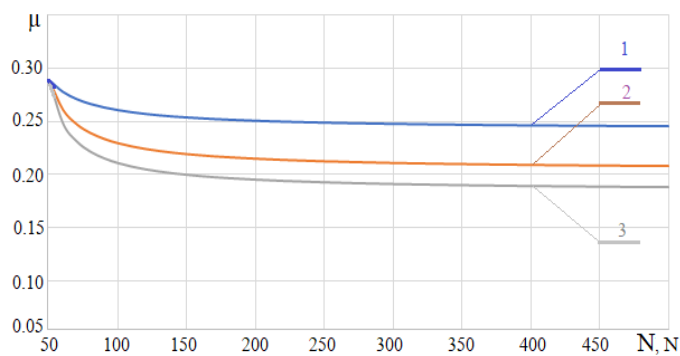


Fig. 6. The dependence of the coefficient of friction μ on the pressing force (all values are in table 4).

Table 4. The parameters of the graphs in Fig. 6.

	1	2	3
j_a	5	5	5
Δj_a	2	4	6

Thus, the chosen model of two contacting bodies with a rough surface makes it possible to trace the process of the formation of the friction force at relative rest of the bodies under consideration and, in our opinion, makes it possible to explain the main reasons for the increase and decrease in the coefficient of friction. The graphs in Fig. 7 turned out to be interesting. As can be seen from Table 5, the radii of curvature of the roughness of all three surfaces are the same, only the number of roughness differs, but an increase in the number of roughness occurs with the same ratio $j_a / \Delta j_a = 5$ with an increase in the external force by 10 N.

As can be seen in Fig. 7, while all three graphs of the friction coefficients remain constant - they do not change at any value of the vertical force. It should be said that we obtained the same effect with the same ratio ($j_a / \Delta j_a = 5$) in other systems with other values of the roughness radii. Apparently, it is worth pondering over this phenomenon and finding out how real the effect obtained here is.

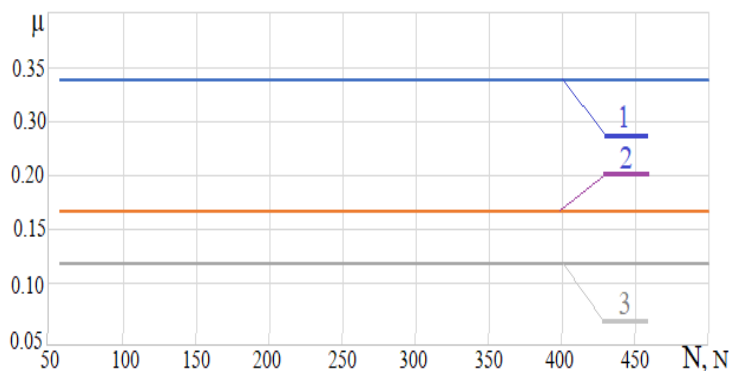


Fig. 7. The dependence of the coefficient of friction μ on the pressing force (all values are in table 5).

Table 5. The parameters of the graphs in Fig. 7.

	1	2	3
j_a	5	5	5
Δj_a	2	4	6

We find another graph of the dependence of the coefficient of friction on the force useful. On Fig. 8 four graphs of the dependence of the coefficient of friction on the number of microroughnesses are shown; we are ready to say once again that not all the graphs shown in this paper can be found in real friction pairs, but they allow us to understand the law of formation of the friction force.

Fig. 8 shows four graphs of the dependence of the coefficient of friction on the pressing force of the friction bodies. As can be seen, the fourth friction pair has the largest initial number of microroughnesses (this is unlikely), but the subsequent number of microroughnesses grows absolutely the same for all four friction pairs. The second friction pair seems to be the most realistic, because the friction coefficient shows the most frequently occurring values. It is possible to see the first and third pairs of friction in real life, but not very often; the fourth pair seems quite unrealistic.

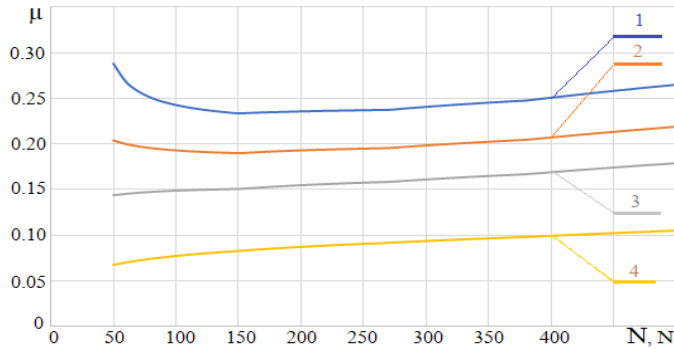


Table 6. The parameters of the graphs in Fig. 8.

	j_a	Δj_a
1	5	3210
2	10	3210
3	20	3210
4	90	3210

Fig. 8. The dependence of the coefficient of friction μ on the pressing force with different number of microroughness.

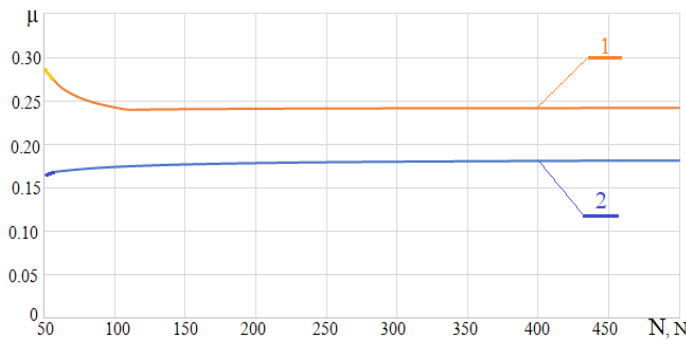


Table 7. The parameters of the graphs in Fig. 9.

	j_a	Δj_a
1	5	3210
2	15	2310

Fig. 9. The dependence of the coefficient of friction μ on the pressing force with different number of microroughness.

As can be seen in Fig. 9, the coefficient of friction of material 1 first decreases and then very slowly increases. Material 2 grows noticeably at first, but then grows very slowly (outwardly, the graph looks almost unchanged). We have chosen to include these two graphs because they seem to be quite typical and have not yet included other friction pairs in this article, since the friction model requires understanding of real contact processes.

Conclusion

We modeled many friction pairs and chose for this article those that exhibit the most characteristic and understandable friction properties, and added several other friction pairs that seem unlikely, but show quite interesting properties. This article examines the static contact of rough surfaces under the action of normal and shear (horizontal) forces on them, the action of which is resisted by the static friction force. When solving such a problem, the surface roughness is represented by spherical protrusions, the parameters of which are the same within one surface. The results obtained as a result of solving these problems allow us to consider the reaction of rubbing bodies for different characteristics of rough surfaces.

References

- 1 Archard J.F. Elastic Deformation and the Laws of Friction. *Proceedings of the Royal Society of London*, 1957, Vol. 243, pp. 190–205. doi: 10.1098/rspa.1957.0214
- 2 Zhuravlev V.A. On the question of theoretical justification of the Amontons-Coulomb law for friction of unlubricated surfaces. *Proceedings of the Institution of Mechanical Engineers, Part J - Journal of Engineering Tribology*. 2007, No. 221, pp. 893-895. doi: 10.1243/13506501JET176
- 3 Greenwood J.A., Williamson J.B.P. Contact of Nominally Flat Surfaces. *Proceedings of the Royal Society of London A*, 1966, Is. 295(1442), pp. 300–319. doi: 10.1098/rspa.1966.0242
- 4 Bush A.W., Gibson R.D., Thomas T.R. The elastic contact of a rough surface. *Wear*, 1975, 35(1), pp. 87–111. doi: 10.1016/0043-1648(75)90145-3
- 5 Kragelskii I.V., Dobyshin M.N., Kombalov V.S. *Friction and Wear. Calculation methods*. Oxford: Pergamon Press Ltd. 474 p. eBook. Available at: <https://shop.elsevier.com/books/friction-and-wear/kragelsky/978-0-08-025461-6>
- 6 Ogilvy J.A. Numerical simulation of friction between contacting rough surfaces. *J. Phys. D. Appl. Phys.*, 1991, No. 24(11), pp. 2098–2109. doi: 10.1088/0022-3727/24/11/030
- 7 Karpenko Y.A., Akay A.A numerical model of friction between rough surfaces. *Tribol. Int.*, 2001, No.34(8), pp. 531–545. doi: 10.1016/S0301-679X(01)00044-5
- 8 Chang W.R., Etsion I., Bogy D.B. An Elastic-Plastic Model for the Contact of Rough Surface. *J. Tribol.*, 1987, No. 109(2), pp. 257–263. doi: 10.1115/1.3261348
- 9 Bjorklund S.A random model for micro-slip between nominally flat surfaces. *J. Tribol.*, 1997, 119(4), pp. 726–732. doi: 10.1115/1.2833877
- 10 Eriten M., Polycarpou A.A., BergmaL.A. Physics-based modeling for fretting behavior of nominally flat rough surfaces. *Int. J. Solids Struct.*, 2011, 48(10), pp. 1436–1450. doi: 10.1016/j.ijsolstr.2011.01.028
- 11 Kragelskii I.V. *Friction and Wear*. Elmsford: Pergamon Press, 1982, 420 p.
- 12 Chichinadze A.V., Braun E.D., Bushe N.A., et al. *Fundamentals of Tribology. Friction, Wear, and Lubrication*. Moscow, Mashinostroyeniye Publ., 2001. 664 p. [in Russian]
- 13 Khairaliyev S.I., Kaishubayeva N., Spitas Ch., Dzhundibayev V. Static interaction of rough surfaces under normal force. *Eurasian Physical Technical Journal*, 2020, Vol.17, No. 2(34), pp.110-115. doi 10.31489/2020No2/110-115.

EXTRAORDINARY MAGNETORESISTANCE OF LASER ANNEALED NANO BORON DEPOSITED ON OXIDIZED POROUS SILICON

Narjis Zamil Abdulzahra

Department of Physics, College of Science, Al-Nahrain University, Jadriya, Baghdad, Iraq,
ner_ner2@yahoo.com

This study explores the impact of laser annealing on the electrical and magnetic properties of nano boron deposited on oxidized porous silicon (n-B/PSiO₂) and its potential for spintronic applications. The Nd: YAG laser was used at varying energies to anneal the n-B thin films. Increasing the laser energy increased grain size and more ordered grain structures. It also increased surface roughness due to forming new grain boundaries and secondary phases. The electrical properties of the material were also affected by the laser annealing, with an increase in forward and reverse current and an increase in electrical resistivity with increased annealing temperature. The study also found that the magnetoresistance of the material increased with increasing laser temperature, attributed to tunnel injection through the thin silicon dioxide layer, and could be up to 7 times higher than non-annealed n-B/PSiO₂ in a magnetic field. The study highlights the importance of controlling materials' grain size and structure for their physical and electrical properties. In addition, it provides insights into the electronic properties of n-B/PSiO₂ and the behavior of charge carriers in a magnetic field.

Keywords: Extraordinary Magnetoresistance, Laser Annealing, Nano Boron/ Oxidized Porous Silicon, Electrical Properties, Magnetic Properties, Spintronic Applications.

Introduction

Silicon is a material with exceptional promise for magneto electronics, thanks to its long spin coherence of up to 7 meters. However, in conventional micro- and Nanoelectronics, the functional state of a device is determined by electric current and electric field, which can lead to energy dissipation and leakage. Spintronic offers the solution to limitations by manipulating the spin degree of freedom instead of electric current [1]. The demand for non-volatile memories with high storage density, operation speed, and low power consumption has increased in recent years. One promising solution is Resistive Random-Access Memory (RRAM), which has the advantages of high integration, low power consumption, high read-write speed, and compatibility with CMOS technology. RRAM devices are resistors whose electrical resistance can be changed by an externally applied magnetic field. They operate based on the electrostatics principle of $R_{FB} = R_0 / \sin \theta$, where the resistance of material's resistance. The material is proportional to the magnetic field [2].

The Extraordinary Magneto Resistance (EMR) effect, discovered in 2000, is more effective than the Giant Magneto Resistance (GMR) effect. When a transverse magnetic field is applied, the EMR effect occurs in semiconductor-metal hybrid systems. At room temperature, it shows lower resistance in the absence of a magnetic field, and when a strong magnetic field has higher resistance, which can operate without physical contact, have many applications, including in MRAM, hard disc drives, magnetometers, ferrous detection, electronic compasses, bio-sensors, position sensors, magnetic field sensors, and for measuring electric current [3]. The conventional theory of magnetoresistance in metals and semiconductors relies on a distribution of scattering times among conducting carriers that a unique Hall field cannot compensate for. According to scientific research, materials with a fast, free electron Fermi surface and a significant charge carrier led to positive magnetoresistance that is quadratic in weak and saturates in strong magnetic fields [4].

Laser annealing is a technique used to modify the properties of a material's surface by applying intense laser pulses. While it is true that the effect of laser annealing on morphological features of the surface is an important aspect to consider, it is essential to note that the specific details regarding these effects may vary depending on the material being annealed and the parameters of the laser annealing process. The general overview of the potential effects of laser annealing on surface morphology is given by [5]; Surface Melting and Solidification: Laser annealing can induce localized melting of the surface material, followed by rapid

solidification as the laser beam moves away. This process can lead to changes in the surface topography, such as the formation of re-solidified regions, which may exhibit different morphological features compared to the original surface; Surface Roughness Modification: Laser annealing can also influence the surface roughness of a material. The energy delivered by the laser can cause material ablation, vaporization, or rearrangement, leading to the smoothing or roughening of the surface [6]. The laser energy density, pulse duration, and repetition rate are crucial parameters that determine the extent of roughness modification; Surface Crystallization: In some cases, laser annealing can induce the recrystallization of the material's surface occurs when the laser energy is sufficient to heat the material above its recrystallization temperature, allowing the atoms or molecules to rearrange into a more ordered crystal structure. This recrystallization process can result in changes in surface grain size, orientation, or texture; Surface Morphological Defects: Depending on the energy and intensity of the laser, certain morphological defects may arise on the material surface. For instance, laser-induced surface ablation can generate pits, craters, or microscale roughness. These defects may affect the material's surface properties and functionality [7].

It is important to note that the specific morphological changes induced by laser annealing will depend on the material properties, laser parameters (such as energy density, pulse duration, and repetition rate), and the desired outcome. Therefore, it is recommended that the authors provide detailed information on the material, laser parameters, and characterization techniques used to evaluate the morphological changes induced by laser annealing in their specific study [8]. The nano Boron surface temperature after laser shot given by [9-11]

$$T_{(0,t<\tau)} = T_0 + \frac{2I_0(1-R)(Nt)^{\frac{1}{2}}}{K} \quad (1)$$

where T_0 : initial surface temperature (29K), I : R: reflectivity 0.74 at 1.064 μm , K : thermal conductivity W/cm.k , N : thermal diffusivity (cm^2/s), and t : pulse duration (7ns). The thermal properties were measured by transient (frequency-domain) 3ω method (FDTR technique) by depositing cooper micro heater/sensor design as in figure (3, a).

1 Samples and Experimental Details

The crystalline wafer of p-type silicon with a resistivity of 3.5 $\Omega\cdot\text{cm}$, 508 μm thickness, and (111) orientation was used as starting substrates. The substrates were cut into a square with areas of $1 \times 1 \text{ cm}^2$. The native oxide was cleaned in a mixture of HF and H_2O (1:2). After chemical treatment, Photo-electrochemical etching was performed in a mixture of 48% (1:1) HF-Ethanol at room temperature using a Pt electrode. The schematic diagram of the electrochemical etching system is shown in Fig. 1. The porous area was 1 cm^2 , and as-prepared porous silicon was dried by rapid hot air (using a dryer) and stored in a container containing ethanol to reduce oxidization and contaminations. The current of 40 mA/cm^2 was applied for 10 min. Samples were illuminated by a semiconductor green laser 514.5 nm and powered at 100 mW. The rapid thermal oxidation (RTO) system consists of the tungsten halogen lamp type (OSRAM 64575) with a power of 1000 W based on a ceramic base. A parabolic reflector-like half circuit was put under the lamp to increase the heating efficiency. (2) A quartz tube has a 3 cm diameter opening from two sides to circulate the dry oxygen source. The quartz tube is attached to a halogen lamp to obtain the desired temperature. The RTO temperatures are $30 \text{ }^\circ\text{C}$ at an oxidation time of 60 s. They can be calibrated using a thermocouple type J with a digital reader above the sample.

The nano-boron (n-B) was deposited on the PSiO_2 surface, and n-Boron (0.3 mg/L) was dissolved in ethanol. Ethanol is a polar solvent that can dissolve nano boron if it is soluble in this solvent. Ethanol is a commonly used solvent in spin coating due to its low evaporation temperature, which makes it easy to evaporate from the substrate after spin coating. Ethanol is also a relatively safe solvent, but it is flammable and should be handled cautiously. After dissolving, the n-B was deposited by the spin coating method, using a rotation per minute of 3000 for 60 seconds. Then, ten drops of n-B were dropped on the surface of the rotated PSiO_2 . After that, the n-B thin film was dried at 150°C for 10 minutes to remove any volatile components. These processes were repeated ten times to increase the thickness of the n-B thin film.

Nd: YAG laser used in the experimental work at a wavelength of 1.06 μm . This laser is made by DELIXI and used in this work to provide pulse energy ranging from (50-500) mJ in 7ns pulse duration. A spot diameter focuses the laser beam on the target. In this work, the laser beam diameter on carbon targets is 0.08 cm. The distance between the sample and the laser is 12 cm. The LSP set up a flow chart as in Figure 2.

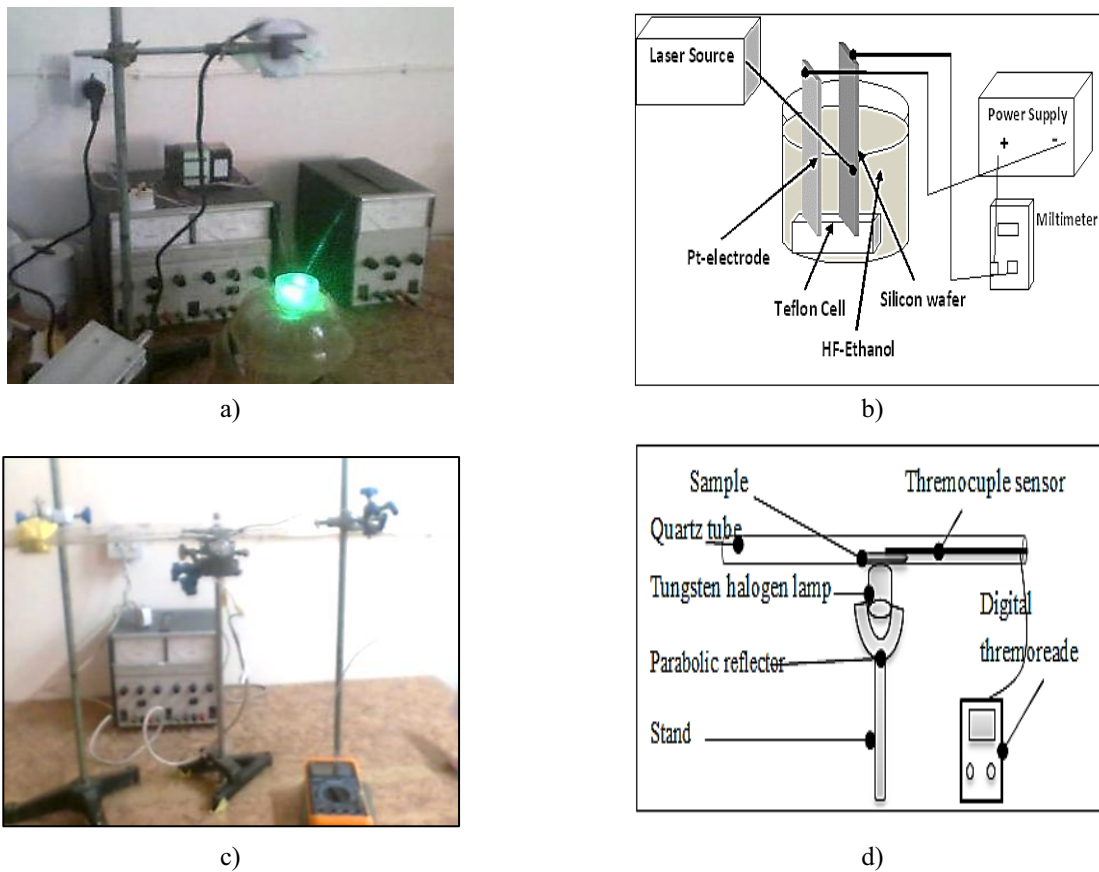


Fig.1. (a) The schematic diagram depicts the PEC process. (b) The photographic image, (c) The photographic image RTO system, (d) Schematic diagram of the RTO system.

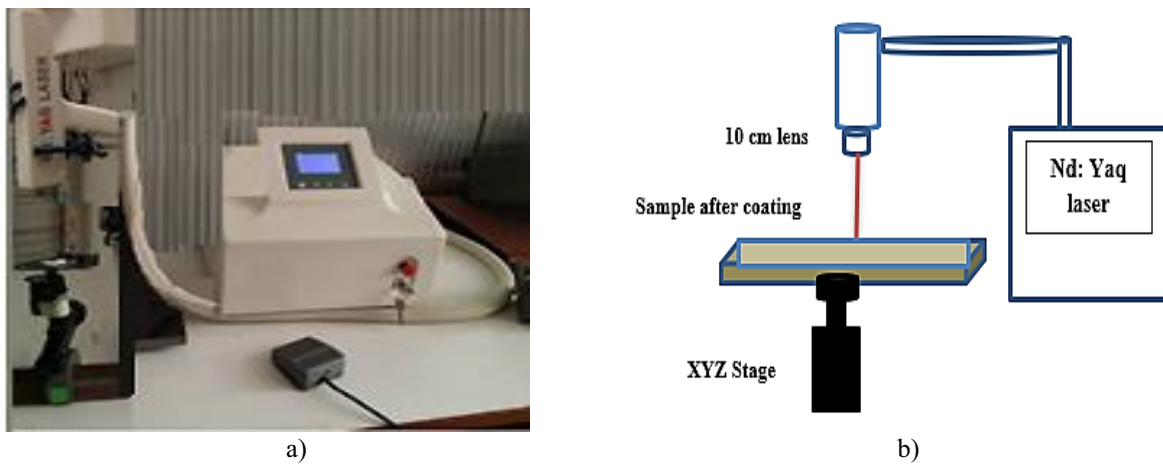


Fig.2. Laser annealing images: a) photographic image; b) Schematic diagram

Thermal properties were measured by copper deposited by the evaporation method as a heat sink, shown in Figure 3; the purpose of this measurement is to find the thermal constant used in equation 1 for a calculated surface temperature where thermal conductivity is $(113.12 \cdot 10^{-7} \text{ W/cm. k})$, and thermal diffusivity is $(0.27 \text{ cm}^2/\text{s})$. $0.1 \mu\text{m}$ -thick silver layers were deposited by one drop on the wafer

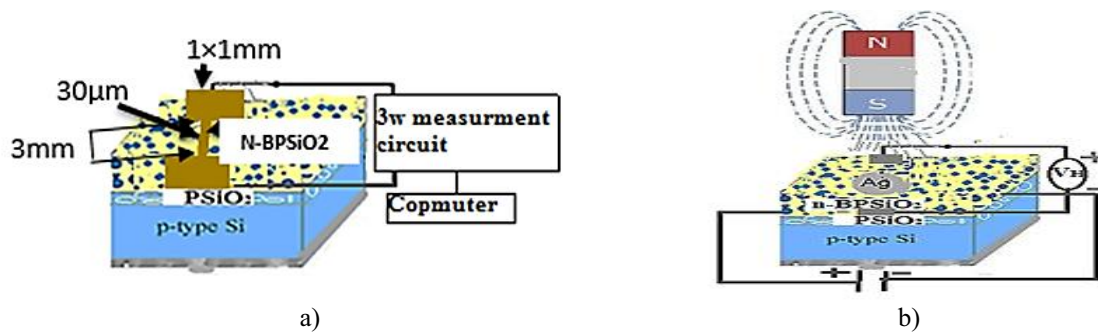


Fig. 3. (a) Chart diagram of the experimental 3ω measurement. Finally, n-B thin films were annealed at different overlapping 50:50 by Nd: YAG laser energy and study the prober energy gives the best electrical properties, (b) Hall measurement schematic diagram.

The structure properties, such as surface morphology, layer thickness, and pore diameter, were measured. AFM measured these grain size distributions and surface topography. The silver past electric contacts. Where deposited paste using one drop on samples by Aluminum mask has a circular area of about 3mm^2 and connected wire; after three days, the Aluminum mask was removed, and remain the silver with the connected wire dried; the electric circuit is shown in the figure below as a schematic diagram. The Hall Effect measurement system ECOPIA (HMS-300 VER3.5) input data temperature 300K, current (0.1mA) delay time (0.1s) applied magnetics 0.55T.

2 Results and discussion

2.1 Surface heating temperature

The surface heating temperature was determined from relation (1). Fig.4 (a, b) shows the experimental data of silicon; a photometer from PIER-ELECTRONIC measured the transmission and reflection. At $1064\ \mu\text{m}$ wavelength, the transmission and reflection values were 14% and 74%, respectively; the obtained reflectivity was used to calculate surface temperature. Figure (4, c) shows that the absorption of laser energy can cause increased surface temperature by increased laser energy on the material surface. The laser energy is absorbed by the n-B/PSiO₂, which raises its temperature. The magnitude of the temperature increase depends on various factors, such as the absorption coefficient of the material, the laser fluency, and the duration of the laser exposure. In addition, the material's thermal conductivity also plays an essential role in the magnitude of the temperature increase. Materials with low thermal conductivity will have higher temperatures, as heat is not efficiently transferred away from the surface. It's essential to consider the effects of the increased temperature on the material, as it can cause structural changes, chemical reactions, and other effects that can impact the material's properties [10 -12].

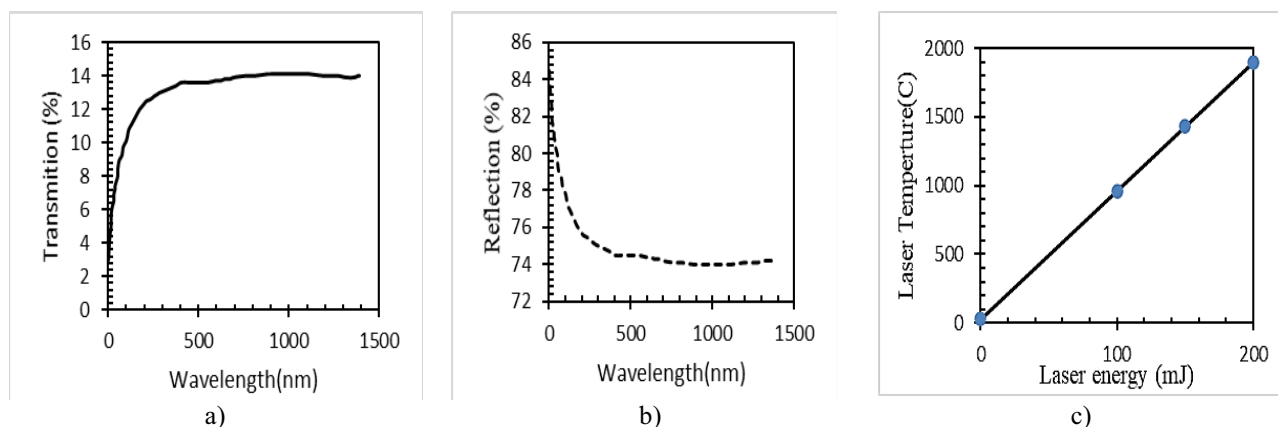


Fig.4. The (a) transmission and (b) reflection measurement of n-B deposited on OPSi, and (c) Laser temperature on the surface at different laser energies.

2.2 Atomic Force Microscopy

Atomic Force Microscopy (AFM) analysis is a powerful tool for investigating materials' surface morphology and roughness, including nano-sized boron deposited on oxide porous silicon before and after annealing it by laser. An AFM obtained high-resolution images of the surface at the nanoscale. It obtained information about the surface topography, roughness, and any parameter changes due to annealing with different laser energies. Fig.5. Show the AFM images before and after annealing samples with different laser energies, which cause changes in the surface morphology and roughness of the material.

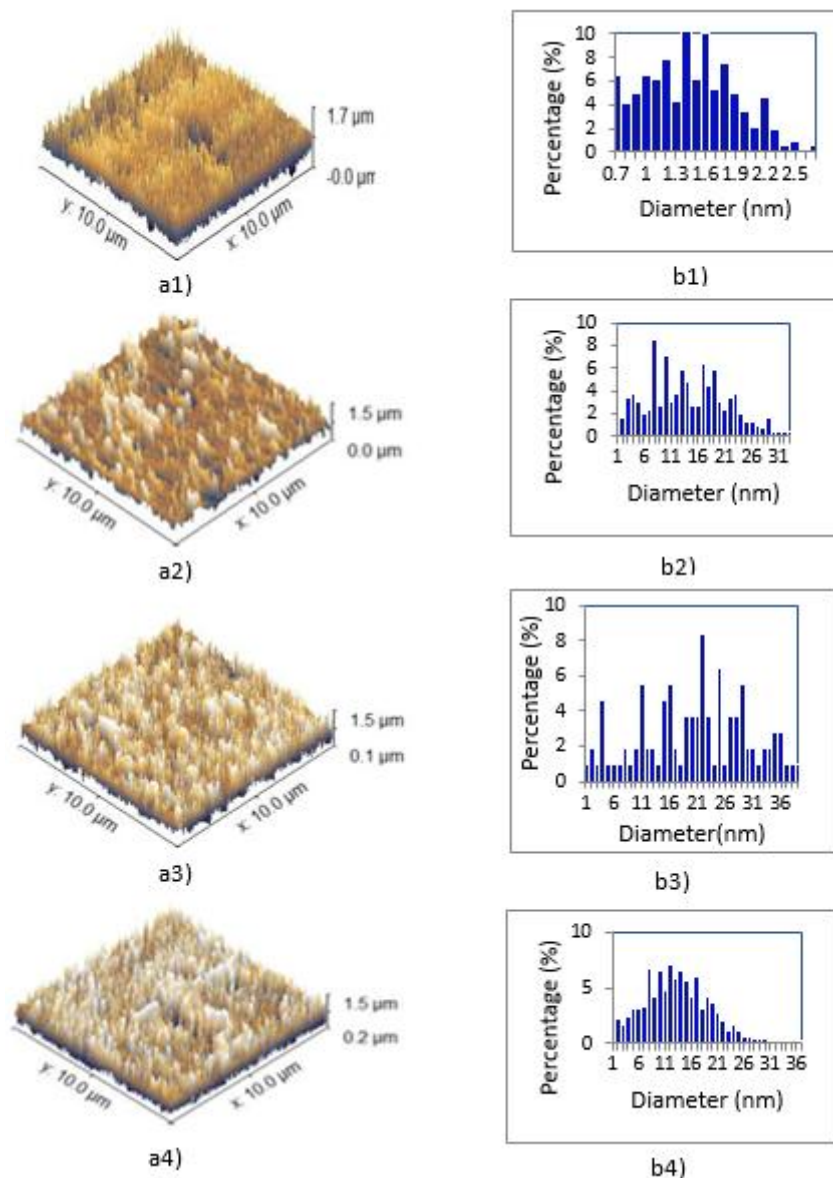


Fig.5. AFM images (a1) before laser annealing, (a2) 100mJ, (a3) 150mJ, and (a4) 200mJ laser energy, while (b1, b2, b3, and b4) represented grain size distribution.

The number of grains increased by increased laser energies after annealing being influenced by various factors, including the laser energy used during the annealing process. In the case of nano boron deposited on oxide porous silicon, increasing the laser energy can increase the number of grains. Higher laser energy can cause a higher temperature during the annealing process, leading to more rapid and intense n-B/PSiO₂ recrystallization, new grains' formation, and the growth of existing grains, increasing the number of grains [13]. Additionally, the increased laser energy can promote boron diffusion and segregation within the material, further promoting grain growth and the formation of new grains. The laser energy 100mJ generated

a heat temperature of 963°C, causing structural defects in the material to anneal and heal, leading to a more ordered and uniform grain structure; increasing laser energy decreased the maximum grain size [14].

When annealing of n-B/PSiO₂ at laser temperatures of 1430°C and 1897°C. The results show that the maximum grain size of the material decreased after the annealing process. The decrease in grain size can be attributed to several factors, such as the increased concentrations of the material's atomic structure at high temperatures, which can lead to grain boundary migration and the formation of smaller grains. The n-B may also influence the grain growth behavior of the PSiO₂ material. It is important to note that a material's grain size and structure can significantly impact its physical and mechanical properties. Understanding how to control the grain size through processes such as annealing is vital in developing advanced materials. [15, 16]

Surface roughness refers to the small-scale deviations of a surface from its average height. At the annealing temperature of 963°C, the surface roughness of the n-B/PSiO₂ decreased after the annealing process. For example, the decrease in surface roughness after annealing laser energy 100 mJ due to several factors; I. The migration of grain boundaries can lead to a more homogeneous and smooth grain structure; II. Although the recrystallization of the material can result in the formation of larger and more uniform grains, the surface roughness of the n-B/PSiO₂ increased after annealing by laser energy 150 and 200mJ that heated the surface temperatures to 1430°C and 1897°C respectively, due to several factors, such as the formation of new grain boundaries, which can lead to a more heterogeneous grain structure. In addition, the precipitation of secondary phases can result in the formation of tiny, localized rough features on the surface [17]; the grain size information and surface properties are shown in Table 1.

Table 1. The grain and surface information estimated from AFM analysis for annealing n-B/PSiO₂, (a) without laser annealing, (b) 100mJ, (c) 150mJ, and (d) 200mJ laser energies.

Sample no.	Total grain number	Avg. diameter (nm)	Maximum grain high(nm)	Surface roughness (nm) Rq	Surface area ratio $\times 10^4$
a	320	1.41	1.4	19.3	15
b	293	1.94	2.3	15.1	6
c	887	1.86	1.8	20	16
d	1227	1.51	1.4	20	21

2.3 Electrical and Magnetic Properties

2.3.1 I-V Characteristics

Both forward and reverse currents were increased after annealing by Nd: Yag laser with different energies. Figure 6 shows that increased current before annealing nano boron deposited on porous oxide silicon because of oxygen-related defects in the n-B/PSiO₂ can impact the charge transport and increase the forward and reverse currents [17]. The decrease in forward and reverse current after annealing is due to many reasons.

I. Surface morphology: The laser annealing process can alter the surface morphology of the nano boron deposited on the porous oxide silicon, decreasing the forward and reverse currents due to the nano boron particles fusing or aggregate, creating areas of high resistance that can impact charge transport [18].

II. Laser annealing can alter the interface states between the nano boron and oxide porous silicon and decrease forward and reverse currents. The formation of new interface states can increase the interface's resistance and impact the material's charge transport [19];

III. Dopant activation: laser annealing can help to activate the dopants in the nano boron, leading to improved charge transport and reduced forward and reverse current [20];

IV. Oxygen Content: The annealing process can also lead to the formation of oxygen-related defects in the n-B/PSiO₂, which can impact the charge transport and increase the forward and reverse currents [21].

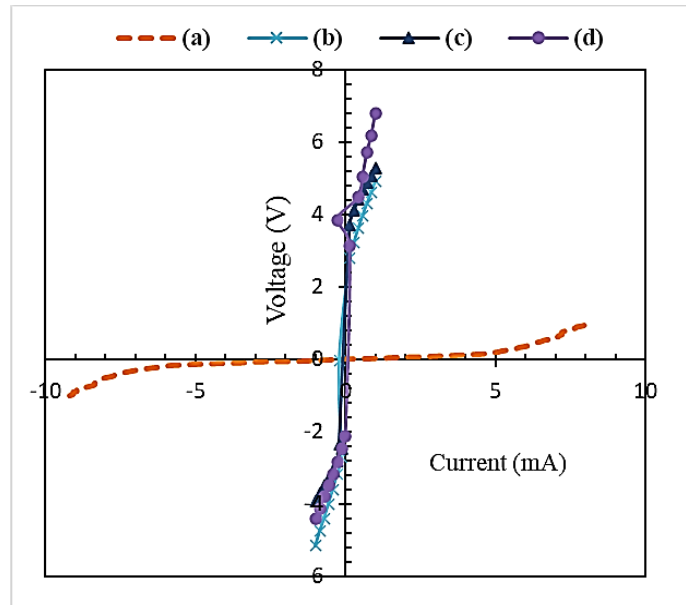


Fig.6. I-V characteristics of n-B/PSiO₂ (a) before laser annealing, (b) 100mJ, (c) 150mJ, and (d) 200mJ laser energy.

2.3.2 Electrical and Magnetic Parameters

The occurred electrical parameters like; electrical resistivity, Electron mobility, bulk concentration, and hall constant are shown in Figure 7. In the Fig. (7, a), the electrical resistivity is increased with increased laser annealing temperature, which can be attributed to several factors; Firstly, introducing high-energy laser radiation to the n-B/PSiO₂ material can cause defects in the crystal lattice structure of the material. These defects can act as scattering centers for the electrons in the material, leading to increased electrical resistivity [22]. Secondly, high-energy laser radiation can cause an increase in the concentration of impurities or dopants in the n-B/PSiO₂ material, which can also contribute to an increase in electrical resistivity because impurities or dopants can introduce additional energy levels in the band gap of the material, which can trap electrons and increase resistivity. Finally, high-energy laser radiation can cause thermal effects in the n-B/PSiO₂ material, such as localized heating or melting, altering its electronic properties and increasing resistivity [23].

Fig. (7, b) shows that the decrease in electric mobility with increasing laser annealing energy of nB deposited on OPS is due to several factors. One of the primary factors is the formation of defects in the material. The high energy of the laser beam can disrupt the crystal lattice structure of both the nB and OPS, leading to the formation of defects that act as traps for electrons. These defects can decrease the electrons' mobility and reduce the material's overall conductivity. The thermal annealing effect is another factor that can contribute to the decrease in electric mobility. When the material is subjected to high temperatures during laser annealing, there can be a reduction in the number of charge carriers, such as electrons, due to the formation of thermally activated defects, leading to a decrease in electric mobility. Overall, the decrease in electric mobility with increasing laser annealing energy of nB deposited on OPS results from the formation of defects and thermal annealing effects [21]. The authors [24] suggest the possibility of varying the change in the concentration of defects and impurities. The Defects in vacancies, interstitials, or impurities can arise during fabrication or through the interaction between boron and the underlying silicon oxide layer. Some possible defects in this system include; Boron Vacancies: Vacancies occur when boron atoms are missing from their lattice positions.

These vacancies can act as scattering centers for charge carriers and influence electrical conductivity; Silicon Vacancies: Similarly, vacancies in the silicon lattice can be introduced during the fabrication process or due to the interaction with boron. Silicon vacancies can also affect the electronic properties and conductivity of the material; Interstitials: Interstitials are atoms or ions that occupy positions between the regular lattice sites. Interstitial boron or silicon atoms can disrupt the crystal structure and influence conductivity [25]; Surface Defects: The presence of defects at the surface, such as dangling bonds or surface

states, can affect the electronic properties and charge transport at the interface between the n-B and PSiO₂ layers [23]; Regarding impurities, they can be introduced during the deposition process or originate from the starting materials. Some impurity mechanisms relevant in this system include; Contaminants in the Boron source: Impurities can be unintentionally introduced if the boron source used during the deposition process contains impurities. These impurities could be elements or compounds not desired in the final material; Diffusion from the substrate: The oxidized porous silicon (PSiO₂) substrate can release impurities through diffusion processes during the annealing step. These impurities could originate from the silicon oxide layer or underlying silicon substrate [26]; Gas contamination: If the deposition or annealing processes occur in an environment with impure gases, such as residual oxygen, moisture, or other contaminants, they can contribute to the formation of impurities in the n-B thin films

Fig. (7, c) shows increased bulk concentration with increasing laser annealing energy of n-B/PSiO₂ because the oxide on porous silicon enhances its surface area and reactivity [23]. When the laser energy is increased, it can lead to higher temperatures and more intense heating of the nano boron and porous silicon substrate resulting in various effects, such as improved crystallization of the boron and enhanced diffusion of the boron atoms into the substrate. As a result, the bulk concentration of the nano boron can increase with increasing laser annealing energy can benefit various applications, such as developing advanced electronic and optoelectronic devices. However, optimizing the laser annealing conditions is essential to achieve desired properties without causing damage or degradation to the materials.

In Fig. (7, d), The Hall coefficient is a material property that describes the behavior of charge carriers in a magnetic field and is defined as the ratio of the electric field to the product of the magnetic field and the current density. The sign of the Hall coefficient determines the type of charge carriers (electrons or holes), and the magnitude of the coefficient depends on their concentration and mobility [27]. In the case of n-B/PSiO₂, the laser annealing process can affect the Hall coefficient; when n-B/PSiO₂ is subjected to laser annealing, the Hall coefficient can show an interesting behavior with changes in laser annealing temperature. Specifically, the Hall coefficient may increase with laser annealing temperature up to a certain point of 963 °C due to enhanced diffusion of nano boron atoms into the substrate, increasing the carrier concentration. Decreasing with a further increase in laser annealing temperature. When the laser energy is increased, it can lead to higher temperatures and more intense heating of the n-B/PSiO₂, which can result in various effects, such as improved crystallization of the boron and enhanced diffusion of the boron atoms back out of the substrate, resulting in a decrease in the carrier concentration and a corresponding decrease in the Hall coefficient. Therefore, the Hall coefficient of nano boron deposited on silicon can exhibit a non-monotonic behavior with changes in laser annealing temperature, increasing to a specific temperature before decreasing with further temperature increases. This behavior can be necessary to consider when optimizing the laser annealing conditions for the desired electrical properties of the material. The nano boron is represented as a paramagnetic metal inversely proportional to applied annealing laser energy that decreases the hall coefficient; some reports talk about decreased boron magnetism susceptibility (χ_{par}) with increasing temperature [10].

Figure (7, e) shows that increased magnetoresistance with increasing laser temperature is attributed to the tunnel injection through the thin silicon dioxide layer causing a charge acceleration and providing the energy to trigger a transition to a high mobility transport regime by an autocatalytic impact ionization process [27]. A small annealing laser temperature probably causes shrinkage of the acceptor wave functions, and the overlap by the tails is reduced for an average pair of neighboring acceptors. The effective acceptor energy level increases concerning the valence band, by which the activation energy for impact ionization significantly increases, strongly suppressing the current. The quasi-neutrality breaking of the space-charge effect causes insufficient charge to compensate for the electrons injected into the device. They speculate that in the regime of electric field inhomogeneity, the motion of electrons becomes correlated and thus dependent on applying laser energy or being a component to construct spin logic [28]. The relationship between magnetoresistance and sheet concentration is shown in Figure (7, f). An increase in sheet concentration can lead to an increase in magnetoresistance because increasing the concentration of magnetic particles or impurities in a material lead to a more robust response to an applied magnetic field, resulting in a more significant change in resistance, also annealing n-B/PSiO₂ may be changed the electronic properties due to the structure of the material changes, or changes in the interaction between the material and the magnetic field [29, 30].

In the context of the relationship between the change in the concentration of defects and impurities and the change in electrical conductivity, when considering a charge transfer mechanism as ballistic, the charge

carriers (electrons or holes) move through the material without scattering or colliding with impurities or defects. In this idealized scenario, the charge carriers' concentration and mobility determine the material's electrical conductivity [31]. In the case of n-B/PSiO₂, the concentration of defects can have a twofold effect on the change in the conductive properties.

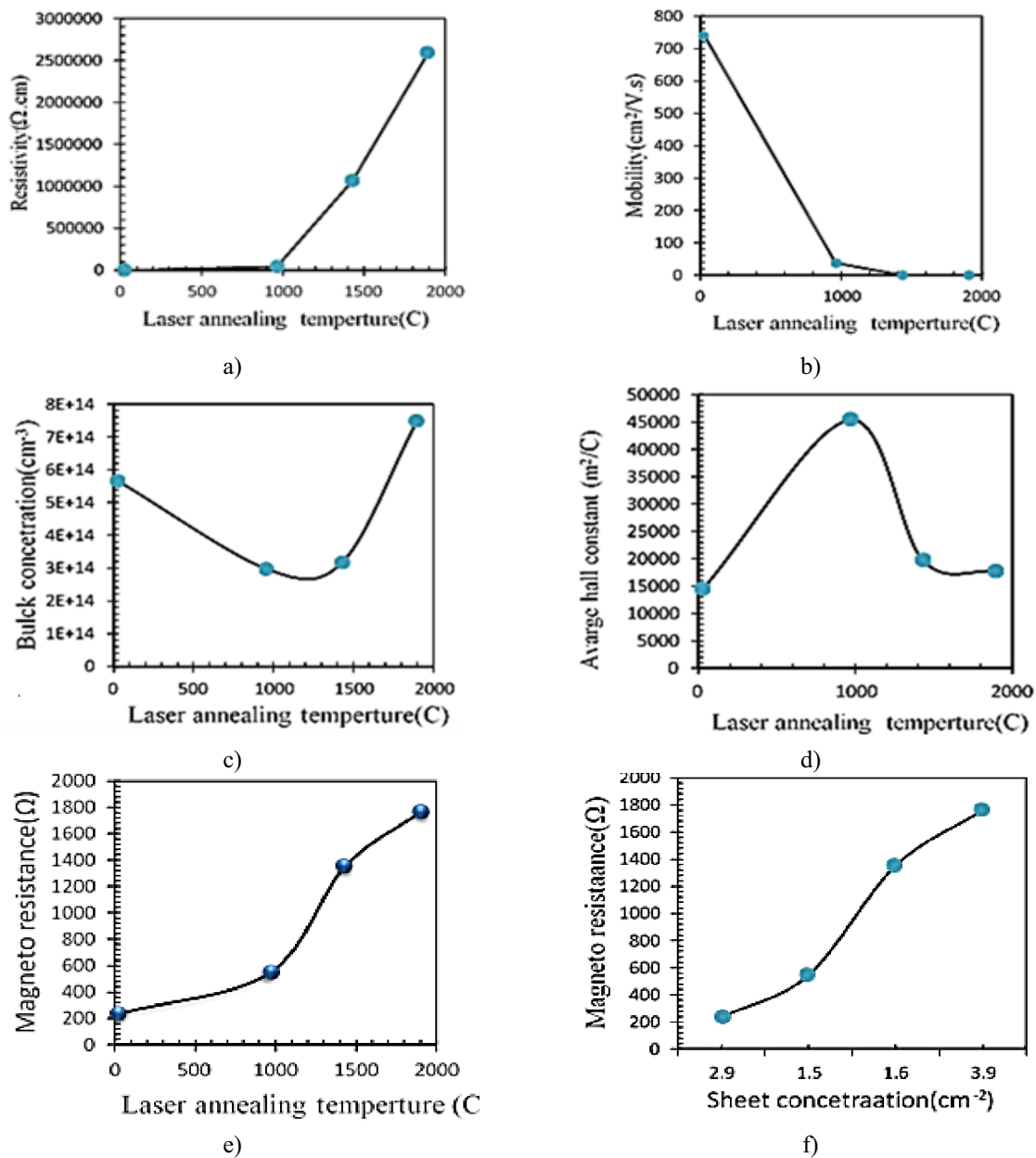


Fig.7. Electrical parameters of n-B/PSiO₂ before and after annealing at different laser energy with (a) resistivity, (b) mobility, (c) bulk concentration, (d) average Hall constant, (e) Magneto resistance Vis different laser annealing, (f) Magneto resistance Vis material sheet concentrations.

Let's break it down; Defects as scattering centers: Defects such as vacancies, interstitials, or impurities can act as scattering centers for charge carriers. When charge carriers encounter these defects, they experience scattering, reducing their mobility and decreasing electrical conductivity [32]. Higher defect concentrations would result in increased scattering, leading to a more significant decrease in conductivity; Defects as dopants: Impurities or defects can also act as dopants, introducing additional charge carriers into the material. Depending on the nature of the defects and their energy levels relative to the material's band structure, they can either contribute to the population of charge carriers (n-type doping) or create electron-hole pairs (p-type doping). This additional population of charge carriers increases the overall electrical

conductivity of the material. Therefore, higher defect concentrations can lead to a higher concentration of dopants, resulting in increased conductivity [33].

Now, when n-B thin films are annealed using an Nd: YAG laser at varying energies, the annealing process can affect the concentration and distribution of defects in the material. The laser energy can modify the arrangement of boron atoms and their interactions with the surrounding silicon and oxygen atoms, leading to changes in defect concentration. If the laser annealing process reduces the concentration of defects, it would likely result in improved crystallinity and reduced scattering of charge carriers, leading to an increase in electrical conductivity. Conversely, if the annealing process introduces additional defects or disturbs the existing defect structure, it could increase scattering and decrease electrical conductivity [34].

In the case of n-B/PSiO₂ and considering a ballistic charge transfer mechanism, the concentration of defects can influence the electrical conductivity through two mechanisms: scattering of charge carriers and introducing additional charge carriers as dopants. The annealing process using an Nd: YAG laser at varying energies can alter the defect concentration, thereby affecting the conductive properties of the n-B thin films.

The relation between the Hall coefficient and magnetoresistance is shown in Figure 8, where the average Hall coefficient increased at 545 Ω magnetoresistance and decreased at 1352 and 1764 Ω. The Hall coefficient is a material property related to the behavior of charge carriers in a magnetic field.

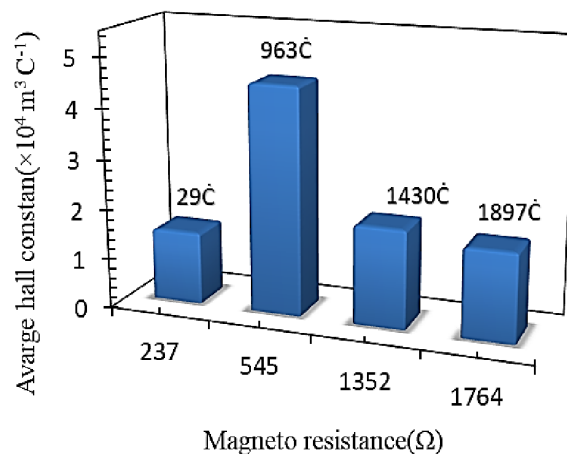


Fig. 8. Magneto resistance Vis average hall constant

When the hall coefficient increases, the material's charge carrier concentration or mobility increases in the presence of a magnetic field. Hence, n-B/PSiO₂ at an annealing temperature of 963 C generates a stronger electric field for a given magnetic field. While decreased hall coefficient at magnetoresistance 1352 and 1764 Ω suggests that the n-B/PSiO₂ is generating a weaker electric field for a given magnetic field, which could be due to a decrease in the number of charge carriers, a decrease in their mobility, or a combination of both. In general, the decrease in nano boron magnetism susceptibility (χ_{par}) with the increasing annealing temperature changes in the Hall coefficient can be used to infer information about the charge carriers in a material, such as their density and mobility. It is a helpful tool for the electronic properties studying of materials during magnetoresistance [35,36].

Conclusions

This study concludes that laser annealing is an essential technique for tailoring the electrical properties of n-B/PSiO₂. Still, the optimization of laser annealing conditions is essential to achieve the desired properties without causing damage or degradation to the material. The study found that laser annealing with different energies can affect surface morphology, electrical resistivity, electric mobility, bulk concentration, Hall coefficient, and magnetoresistance of n-B/PSiO₂. Increasing laser annealing energy can improve the material's electrical conductivity, increase surface roughness, and introduce defects and impurities. The non-monotonic behavior of the Hall coefficient with changes in laser annealing temperature is an important consideration when optimizing the laser annealing conditions for the desired electrical properties of the material. The study provides valuable insights into the impact of laser annealing on the properties of n-

B/PSiO₂ and can inform the development of new materials and applications; the increased electrical resistivity of n-B/OPSi with increasing laser annealing energy due to many factors, including the introduction of defects, an increase in impurity or dopant concentration, and thermal effects. Increasing the laser annealing temperature can generally lead to changes in the crystal structure, defect density, and carrier concentration, affecting the Hall coefficient. As I mentioned earlier, the Hall coefficient measures the electric field ratio to the magnetic field in a material. Therefore, a decrease in the Hall coefficient suggests that the material generates a weaker electric field for a given magnetic field. This could be due to a decrease in the number of charge carriers, their mobility, or a combination of both.

In summary, the increase in the number of grains observed with increasing laser energy of nano boron deposited on porous oxide silicon can be attributed to the influence of laser energy on the recrystallization and grain growth processes in the material. The grain size reduction, in this case, may result in improved mechanical, electrical, or thermal properties of the material. The application prospects strongly motivate this research and show huge magnetoresistances in n-B/PSiO₂ after Nd: YAG laser annealing at energy 200mJ. The device could be suitable as a magneto-resistive sensor for high-density data storage, forming the basis of an avalanche spin-valve transistor. Furthermore, this behavior can be necessary to consider when optimizing the laser annealing conditions for the desired electrical properties of the material.

Acknowledgments

In this paper, we would like to thank the people who assisted in completing this work.

REFERENCES

- 1 Seliverstova E.V., Ibrayev N. Kh., Alikhaidarova E.Zh. The Effect of Laser Energy Density on the Properties of Graphene Dots. *Eurasian Physical Technical Journal*, 2022, 19, No.2 (40), pp.30-34.
- 2 Chen A.A review of emerging non-volatile memory (NVM) technologies and applications. *Solid-State Electronics*, 2016, 125, pp.25-38.
- 3 Sun J., Kosel J. Extraordinary Magnetoresistance in Semiconductor. Metal Hybrids: A Review. *Materials*, 2013, 6, pp. 500-516.
- 4 Porter N., Marrows C. Linear magnetoresistance in n-type silicon due to doping density fluctuations. *Scientific Reports*. 2012, 2, 565 p.
- 5 Narjis Z. Non-Distractive Testing by Nanosecond Nd: Yag Laser Technique as Alternative Method to Find Nano -ZnO/Al Properties. *Laser manufacturing and material processing*. Accepted. 2023. doi:10.21203/rs.3.rs-2625199/v1
- 6 Alwan M.A. , Abdalzahra N.Z. The influence of heating treatment on physical properties of porous silicon. *Al-Nahrain Journal of Science*, 2009, 12, 2, pp.76-81.
- 7 Mahbubur M.R., et. al. Effects of annealing temperatures on the morphological, mechanical, surface chemical bonding, and solar selectivity properties of sputtered TiAlSiN. *Thin films. Journal of Alloys and Compounds*, 2016, 671, pp. 254-266.
- 8 Zamil N. Ultrasonic shock wave generated by laser as an alternative method to find different bone properties. *Lasers in Medical Science*, 2023, 38:138, pp.1-15.
- 9 Theerthagiri J., Karuppusamy K., Lee S.J., et al. Fundamentals and comprehensive insights on pulsed laser synthesis of advanced materials for diverse photo- and electrocatalytic applications. *Light: Science & Applications*, 2022, 11, 250 p.
- 10 Zamil N. Ultrasonic shock wave generated by laser as an alternative method to find different bone properties. *Lasers in Medical Science*, 2023, 38:138, pp.1-15.
- 11 Sands D. Pulsed laser heating and melting, heat transfer. *Engineering Applications*, 2011, pp. 47-70.
- 12 Zamil N. Assessment of Surface Modification by Laser Studies of Polymer Material before and after M.B. Doping. *New Trends in Physical Science Research*, 2022, 1, pp. 123-132.
- 13 Chaurasia S., et al. *Simultaneous measurement of particle velocity and shock velocity for megabar laser-driven shock studies. Barc Newsletter*, 2010, 317 p.
- 14 Colvin J., Larsen J. Extreme Physics Properties and Behavior of Matter at Extreme Conditions. *Cambridge University Press*, 2013.
- 15 Zamil N. Laser-Driven Acoustic Waves: Physical Properties of Paramagnetic Metal. *Research & Reviews. Journal of Pure and Applied Physics*, 2022, 10, 6, pp.1-6.
- 16 Khudhair W.A., Zamil N. Laser Nanosecond Technique, FTIR and AFM Application to Find Physical Properties of PVA Doped with Dye. *New Trends in Physical Science Research*, 2022, Vol. 7, pp.73-85.

- 17 Cristiano F., La Magna A. Laser Annealing Processes in Semiconductor Technology Theory, Modeling, and Applications in Nanoelectronics, *A volume in Woodhead Publishing Series in Electronic and Optical Materials*, 2021, 200, 210p.
- 18 Wang Y., *et al.* Laser spike annealing and its application to leading-edge logic devices. *Conference: Advanced Thermal Processing of Semiconductors. 16th IEEE International Conference* (2008).
- 19 Liu X., *et al.* Aggregation and deposition behavior of boron nanoparticles in porous media. *Journal of Colloid and Interface Science*, 2009, 330, 1, pp. 90-96.
- 20 Zizi A., *et al.* The effect of ND-YAG laser surface treatment on mechanical properties of carburizing steel AISI 1006. *Journal of Engineering Science and Technology*, 2020, 15, 6, pp. 3891 - 3902.
- 21 Hamoudi W.K., Raouf D.N., Zamil N. Laser-Induced Shock Wave Studies of Para and Ferro Magnetic Materials. *J Material Sci Eng.*, 2017, 6, 3, pp. 1000349.
- 22 Alwan M.A., Narges Z.A., Halim N.H.A. Influence of rapid thermal oxidation process on the optoelectronic characteristics of PSI devices. *Int. J. Nanoelectronics and Materials*, 2009, 2, pp. 157 – 161.
- 23 Zamil N. Porous Silicon on Insulator Technology. *Journal of Scientific Research and Reports*. 2022, 28, 1, pp. 98-106.
- 24 Zamil N. The Structure and Electrical Properties of Porous Silicon Prepared by Electrochemical Etching. *Iraqi Journal of Physics*, 2011, 9, 15, pp. 94-101.
- 25 Zamil N. Electrical Properties of Oxidized Porous Silicon. *Al- Mustansiriya J. Sci.*, 2009, 20, 4, pp. 59-68.
- 26 Paul A., Laurila T., Divinski S. Handbook of Solid State Diffusion. *Diffusion Fundamentals and Techniques*, 2017, Vol. 1, pp. 1-54.
- 27 Zamil N. The Effect of Laser Wavelength on Porous Silicon formation mechanism, *NUCEJ*. 2011, 14, pp.197-101.
- 28 Alberi K., Scarpulla M.A. Suppression of compensating native defect formation during semiconductor processing via excess carriers. *Scientific Reports*, 2016,6, 27954.
- 29 Zeena M.A., Narges Z., Hammood I.H. Optical Properties of Tap Water Purity using He-Ne Laser with Different Power Density. *Al-Nahrain Journal of Science*, 2014, 17, 3, pp.99-107.
- 30 Schoonus J., *et al.* Unraveling the mechanism of sizeable room-temperature magnetoresistance in silicon. *J. Phys. D: Appl. Phys.*, 2009, 42, 185011.
- 31 Nicholas A., *et al.* Linear magnetoresistance in n-type silicon due to doping density fluctuations. *Scientific Reports*, 2012, 2, 565p.
- 32 Silva A., *et al.* Magnetoresistance of doped silicon”, *Physical Review B.*, 2015, 91, pp. 214414.
- 33 Zhao Y., Tripathi M., *et al.* Electrical spectroscopy of defect states and their hybridization in monolayer MoS₂. *Nature Communications*, 2023, 14, pp. 44.
- 34 Komsa H.P., Krashennnikov A.V. Defects in Two-Dimensional Materials. Chapter 2 - Physics and theory of defects in 2D materials: the role of reduced dimensionality. *Materials Today*, 2022, pp. 7 – 41.
- 35 Alwan M.A., Khalaf W.K., Abdulzahra N.Z. Physical Properties of MOS Porous Silicon Detector Fabricated under RTO Method. *Eng. & Tech. Journal*, 2009, 27, 11, pp. 2286 – 2290.
- 36 Gupta M., *et al.* *Handbook of Laser Micro- and Nano-Engineering*, 2020, 31 p.
- 37 Saraswati V., Paulose P. Magnetic susceptibility and magnetic resonance in boron and boron carbides. *Journal of the Less Common Metals*, 1987, 128, pp. 185-193.

AUTOMATED TEMPERATURE AND HUMIDITY CONTROL AND MONITORING SYSTEM FOR IMPROVING THE PERFORMANCE IN DRYING SYSTEM

Alkhdery L.A.¹, Yurchenko A.V.², Mohammed J.A.-K.³, Neshina Y.G.^{4*}

¹National Research Tomsk Polytechnic University, Tomsk, Russia

²National Research Tomsk State University, Tomsk, Russia

³Electromechanical Engineering Dept., University of Technology, Baghdad, Iraq

⁴A. Saginov Karaganda Technical University, Karaganda, Kazakhstan, 1_neg@mail.ru

Temperature and relative humidity are the key control parameters in drying processes for preserving and improving food quality. To achieve this goal, an automatic control system has been designed and built to provide adequate heat and drying streams according to the ambient requirements of various climatic zones and the kind of dried product. The control system combined with sensors allows the temperature and humidity of the drying chamber to be adjusted online by predetermined parameters. When there is little or no radiation present or when rapid drying rates are required, the heated air stream may be produced utilizing an electric motor fan in addition to an electrical backup heater. The fan automatically modifies its speed using the Pulse Width Modulation technique for energy efficiency depending on the required temperature of the drying chamber. The control system based on Arduino Uno board is built within the solar dryer, after which tests are carried out. The test results are displayed on a display. The management system was set up to maintain an ambient temperature between 40 and 60 °C and relative humidity between 10 and 20 %. The system is a flexible solution for different climatic zones and dried products, according to experimental findings demonstrating its efficiency in managing the drying environment. Finally, this paper can conserve energy because it only works when the temperature around the food is below 60 °C.

Keywords: Solar dryer; temperature and humidity control; Arduino UNO; electric fan; backup heater; monitoring system, printed circuit boards

Introduction

Controlling the temperature of any room as a result of solar radiation is an essential responsibility in many automated activities. One of the important activities of the solar dryer is food applications [1,2]. Specialized sensors, ranging from simple to intelligent sensors, as well as the application of environmental monitoring, are used to detect the temperature in the room. There are several research publications on controlling room temperature, but few of them have used Arduino to autonomously manage room temperature and humidity, especially for monitoring purposes. We looked at several publications and have highlighted a few key points.

Abed [3] designed and evaluated the performance of a solar dryer, which is made of three basic parts, a drying solar collector, solar dryer chamber, and chimney. To improve the drying efficiency, a fan was installed at the chimney outlet to manually exhaust the hot air outside the solar dryer. A developed computational and experimental setup of a hybrid PV Thermal double-pass counterflow system coupled with a mixed-mode solar dryer system was suggested by Jadallah et al. [4]. The temperature of the solar cells was reduced by manually pumping air into the PVT system via a fan created by the PV module, hence increasing the PV module's electrical efficiency. The air is passed from the fan to the PVT solar system, then into the drying chamber, using the forced convection mode.

Some studies used different controllers and techniques to manage the climate inside the room. Abdullah et al. [5] presented a temperature control system concept that may be implemented on the Tudung Saji microcontroller. Both the hardware implementation and software simulation were tried and results were achieved. The goal of this study is to guard against bacteria when a particular temperature has been reached. The program appears to be quite excellent at managing and rather preventing bacteria, as bacteria may be

destroyed at a particular temperature. This might also be tried using the Arduino IDE. Widhiada et al. [6] recommended the introduction and designed a control system for temperature distribution for use in a newborn incubator. To ensure a baby's optimum health, it is critical to maintain a specified temperature within the room in this system. The experimental setup employed a microcontroller-based incubator system for temperature sensing and control including humidity as well. This has proven to be a very beneficial tool for baby care and wellness. Humidity was also taken into consideration in the experiment, which used a microcontroller-based system for measuring and controlling temperature. This was a critical application for the well-being and care of children.

Kesarwani et al. [7] produced a case study to control the temperature in systems using microcontrollers, bridge rectifiers, and TRIACs. To adapt temperature measurement, Bhatia, V. and G. Bhatia [8] developed a speed control system that relies on temperature fluctuations. To build the hardware and simulate it on the computer, PWM and simulation tools were utilized. Wellem et al. [9] used an Atmel Atmega 8385 system and an LM35 temperature sensor to evaluate a temperature monitoring technique. Asraf [10] developed a PID controller and implemented it using National Instruments' LabVIEW virtual laboratory environment. It was proposed that an Arduino-based hardware implementation would yield far more related and acceptable temperature management results. Sami et al. [11] used the PWM principle and utilized LCD monitors to display temperature readings. Okpagu and Nwosu [12] constructed a temperature control system for egg incubators with the aid of PID controllers, DC motors, sensors, a fan control system, and LCDs. This is a critical sort of incubator system since it is necessary to monitor the embryo's growth and development; hence control and monitoring of temperature values were crucial in this system. Devi and Kalnar [13] employed temperature sensors to manage the drying chamber's atmosphere. The exhaust fan began to run based on the chosen temperature, controlling the drying atmosphere.

In summarizing the previous literature, automatic temperature and humidity control, particularly autonomous monitoring, has not been addressed by researchers, focusing primarily on the temperature and humidity in question. We recommend an Arduino-controlled and hardware-based temperature and humidity control system, with online monitoring and measuring as the primary focus. The goal of this work is to design an autonomous system for managing fan speed and switching the auxiliary source (backup heater). The control system is integrated into the solar dryer and tested using an Arduino Uno board. The test findings are shown on an LCD screen. To control and ease the display of temperature and relative humidity, the control software is built-in Arduino IDE. This design is regarded as a user-friendly automatic temperature-controlled fan regulator that decreases energy consumption while also assisting in improving the drying rate, hence enhancing the solar dryer's efficiency and getting a nutritionally valuable output. This will certainly be reflected in maintaining the quality and freshness of the drying food. Finally, this paper can save power energy which only functions when the temperature around the food is below 60 °C.

1 Problem identification for the drying process

The most common errors made in solar drying are related to ignoring the factors that are critical in most drying operations; time, air temperature, air velocity (and air exchange). However, certain renewable energies, such as solar and wind have the drawback of only being available for a limited time. Because renewable energy is reliant on weather-related natural events such as wind, rain, and solar energy, it is difficult to manage. These sources are external factors that depend on weather conditions and are not controlled by them. Increasing or decreasing energy leads to:

1.1 Overheating

During normal drying, water is continuously removed from near the material's surface. As depicted in Figure 1, we will begin with moisture inside a slice of the material, then blast warm air over the surface moisture that is traveling to the surface of the material, which will subsequently be removed by evaporation and exit the drier as wet exhaust air.

Some sun dryers generate enough heat inside the drying chamber to cause harden the material being dried. This is due to insufficient ventilation and excessive warmth. Extremely high temperatures can quickly evaporate surface moisture. This dries the surface and prevents moisture from the inside of the material from diffusing outwards to it. As a result, a dry, sometimes leathery covering forms surrounding the substance. This layer then functions as a moisture barrier, preventing the moisture from escaping.

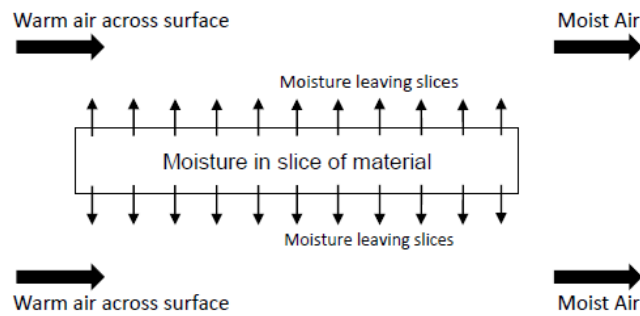


Fig.1. Normal drying process

After a period, the material will feel dry to the touch and have a leathery texture, giving the impression that it is completely dried. However, as seen in the figure, moisture trapped inside the material will eventually make its way to the top of the leathery layer, which will reverse the process as shown in Figure 2. Mold formation is a common side effect of storage or packing, and it can lead to major problems. Don't give in to the temptation to use too much heat to hasten the drying process.

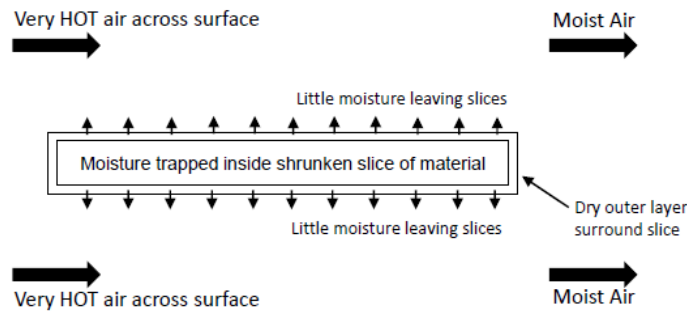


Fig.2. Excessive heating in the drying process

1.2 Poor heating

In the sun drying process of several agro-commodities, two separate transfer processes occur simultaneously, including heating the product and air and the mass transfer from the inside to the outside of the product, as well as drying medium through evaporation. Temperature, air velocity, and concentration differential all impact the passage of water and heat between the product and the drying air.

Heat and mass exchange between the material slice and the air is crucial throughout the drying process. As a result, there is no thermal transfer when the temperature of the air surrounding the product drops since there is no temperature differential between the product and the air. The mass diffuses down from a greater concentration to a lower concentration. As the temperature rises, moisture vaporizes off the material's surface and is released into the atmosphere. Low sun radiation and low air temperature within the drying chamber result in high relative humidity, which stops the drying process and causes the product to rot. As a result, to address the aforementioned problems, care should be made to preserve consistent drying air circulation and maintain a proper temperature within the dryer. This is accomplished via designing and constructing an automated system that online controls the temperature and humidity within the drying chamber, which is ideal for all weather conditions and the type of agricultural goods to be dried.

2 Hardware implementation

The system is divided into three stages. The first detects humidity and temperature using the DHT11 humidity and temperature sensor. The second component receives the output of the DHT sensor module and converts temperature and humidity readings into a useful percentage and Celsius scale number. The third portion of the system uses an LCD to display humidity and temperature. Single-wire serial communication is used to link the system. The Arduino first transmits a start signal to the DHT module, which is followed by a

response signal including temperature and humidity data from the DHT. The hardware system comprises the following components:

- [Arduino](#), Uno
- Motor Driver, L293D IC
- Sensor, DHT22
- Display, 16×2 [LCD](#)
- Fan motor, 12 V DC
- Battery, 12V
- Potentiometer, 2.2k Ω
- Relay, 5V DC
- Breadboard
- Back-up heater

Figure 3 displays the block diagram for the hardware implementation.

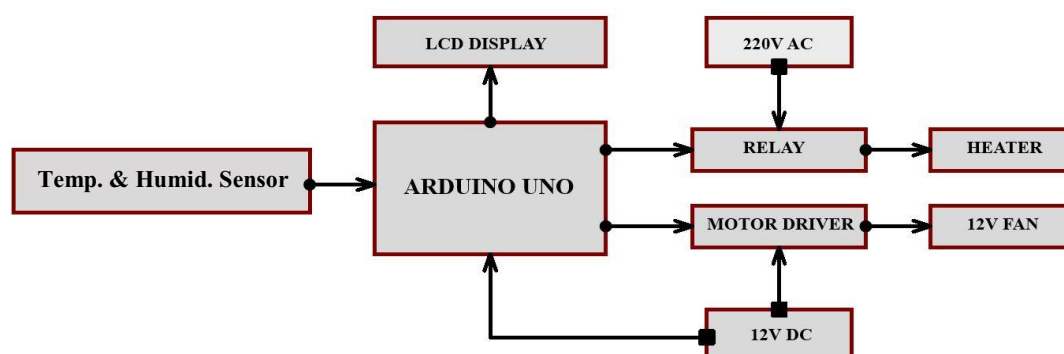


Fig.3. Block diagram of temperature and humidity control

2.1 Arduino UNO Board

Using Arduino UNO to collect the data from the sensors efficiently enables the system to control the indoor environment of the solar dryer based on the measured parameters. Arduino boards come in a variety of shapes and sizes, including the Arduino Yun, Arduino Mega, Arduino Nano, Pro Mini, and others. However, the Arduino Uno is the most well-known. It is used to regulate the entire solar dryer operation. The microcontroller board called UNO uses the ATmega328P. On this board, there are six analog inputs, a 16 MHz quartz crystal, six analog outputs, a USB connection, an ICSP header, a power connector, and a reset button. There are also 14 pins for digital input and output (six of which may be utilized as PWM outputs). Everything required for getting started with the microcontroller is included; all you have to do is connect it to a computer using the USB port or power it using a battery or an AC-to-DC converter.

2.2 DHT22 Temperature and Humidity sensor

A DHT22 sensor measures the temperature, which is used to control the fan speed. Relative humidity can also be detected, which is used to control the fan speed. Relative humidity can also be detected. This sensor comes in a 4-pin single-row device and has an integrated resistive-type humidity measuring component, an NTC-type temperature measurement element, and an 8-bit microcontroller with a quick reaction time. The serial communication method used by the DHT22 module is also referred to as "single-wire communication." As contrasted with other sensors, this one is incredibly user-friendly and extremely accurate. This module transmits data as a pulse train for a predetermined period. It requires certain initialization commands with a time delay before transferring data to the Arduino. And the entire procedure takes roughly 4 milliseconds. To begin, the Arduino sends high to low start signals with an 18 sec delay to DHT22 to assure DHT detection. The Arduino then pulls up the data line and waits for the DHT to respond for 20-40 sec. When the DHT receives the start signal, it sends a low voltage level response signal to Arduino with an 80sec time delay.

DHT22 sensors are used in the dryer system to detect humidity and temperature inside the chambers. This data is received and interpreted by an Arduino MEGA microcontroller. When the exhaust fan eliminates extra moisture within the dryer chamber and the parameters do not reach the desired temperature limit, it

signals to regulate the temperature. The storage chamber's humidity is controlled by adjusting the fan speed based on the sensor's measurement.

2.3 L293D fan motor driver

An L293D motor driver IC combined with Arduino is used for controlling the exhausted DC fan motor. Two DC motors can be driven by this IC. The motor speed is controlled by providing signals according to the PWM technique [14]. The minimum and maximum temperature values can be adjusted in the program code according to the fan speed requirement. The fan speed is automatically the PWM controlled according to the chamber and that gives a lot more accuracy than the manual manner. To operate the DC motor fan, the suggested program adjusts five distinct parameters. If the temperature value is below 40°C, the fan will be turned off and information on the LCD will be shown. The DC fan will begin functioning at low speed if the temperature is between 40 and 45 °C (25 % duty cycle). The fan will also spin at a medium speed if the temperature becomes in the range of 45-50°C (50 % duty cycle). The fan will operate at high speed if the temperature is between 50°C and 55°C (75 % duty cycle). The fan will speed up to the maximum value if the temperature is more than or equal to 55°C (100 % duty cycle).

2.4 Liquid Crystal Display LCD

The information on temperature and humidity for the solar drying chamber is monitored using an LCD, which offers information while managing the temperature and humidity values inside the chamber. The temperature and humidity are displayed on the display, which is directly linked to Arduino in 4-bit mode, as shown in Figure 4. RS, EN, D4, D5, D6, and D7 pins of the LCD are linked to Arduino digital pins 2-7. A 5k pull-up resistor is also used to link a DHT11 sensor module to Arduino's digital pin 12.

2.5 Heating temperature controller

This Arduino is a good example of making an on-off type controller. The most basic type of temperature control device is an on-off controller. The device's output is either on or off, with no in-between condition. When the temperature exceeds the set point, an on-off controller will change the output. On-off control is commonly employed in systems that require precise control and can tolerate having the energy switched on.

3 Circuit Diagram

Figure 4 shows how to connect all of the essential components using Arduino and DHT22, as shown in the circuit design for temperature-based DC fan speed control and monitoring. The Arduino is the brain of the system, controlling all functions. An output voltage corresponding to the temperature in Celsius (centigrade) is provided by the precision IC DHT22. The operational humidity and temperature ranges are 0–100% relative humidity and 40–80 degrees Celsius, respectively. A digital signal is calibrated using the DHT22 sensor output. Its stability and dependability are guaranteed by a patented digital signal-gathering method, as well as temperature and humidity monitoring technology. The sensing devices are connected to the 8-bit single-chip microprocessor.

4 System Flowchart

The system flowchart depicts the device workflow in the drying system. Figure 5 shows the system flowchart for temperature and humidity monitoring. The backup heater and electric fan begin to run at the preset temperature and humidity, controlling the drying environment. The electric fan is automatically controlled to change the speed level according to temperature changes compared to the traditional dryer.

At first, when the temperature is less than 40°C, the fan will stop and the backup heater will work on, also when the temperature is higher than 40°C, the fan speed will rotate at a slow value, and at the same time the backup heater will turn off and when the temperature reaches 45°C, the fan will rotate at medium speed. When the temperature reaches 50°C, the fan speed will be high, and if the temperature increases to 55°C, the fan will rotate at the maximum speed. The same thing in the process of the temperature gradient downward, the fan will work according to the temperatures received from the sensor until the temperature is less than 40°C, the fan will turn off and the heating coil will turn on again.

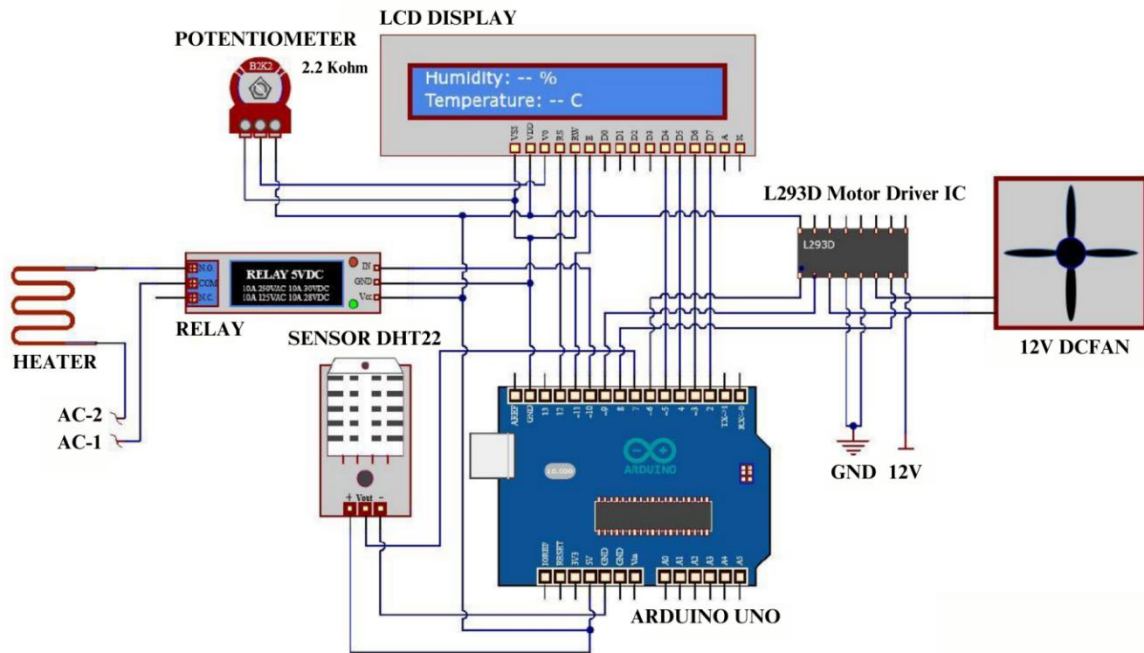


Fig.4. Circuit schematic of the proposed temperature-based DC fan speed control & backup heater

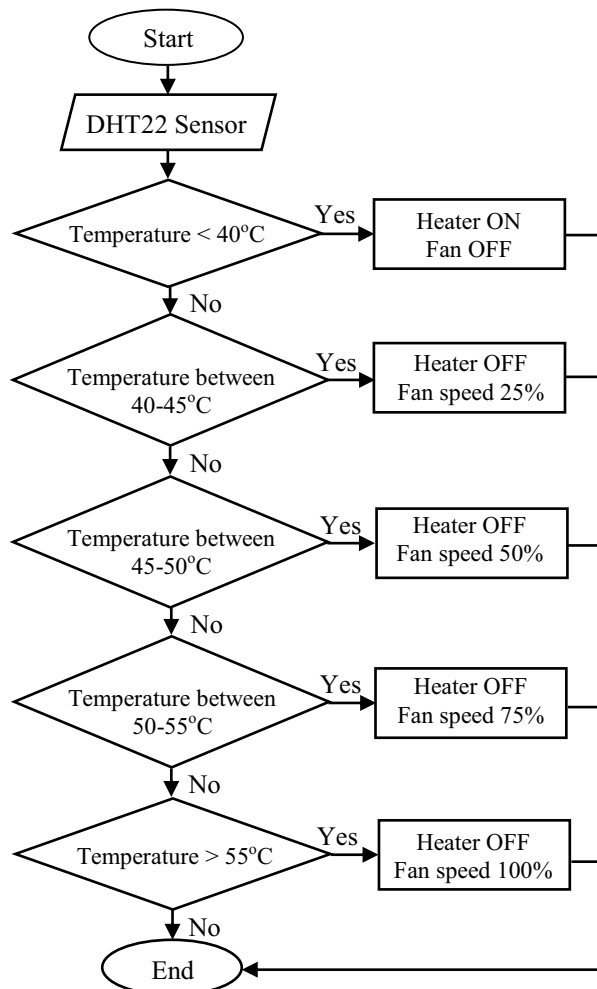


Fig.5. Monitoring system flowchart for temperature and humidity

The rotational speed of the fan depends on the rotational speed of the fan detected by the DHT22 sensor. The increase and decrease of temperatures depend on the intensity of the radiation when there is little or no solar radiation

5 Results and discussion

In the exhaust, a temperature sensor is fitted. The fan speed is controlled by the microcontroller via the temperature sensor, based on the specified desired temperature on the exhaust side. As a result, the temperature within the drying chamber is kept under control. The experimental setup was completed, and a large number of temperature measurements were recorded using the appropriate displays depicted in Figure 6. The illustration depicts how to connect the display to the board and Arduino hardware. In this work, the LCD online produces four readings: two of them are for automatically showing the temperature and humidity on the display. The third reading is for the duty cycle value of the PWM voltage to drive the DC motor fan at a suitable speed, and the fourth reading is for automatically switching ON/OFF the heater. The fan's operating state is determined by the pre-set threshold.

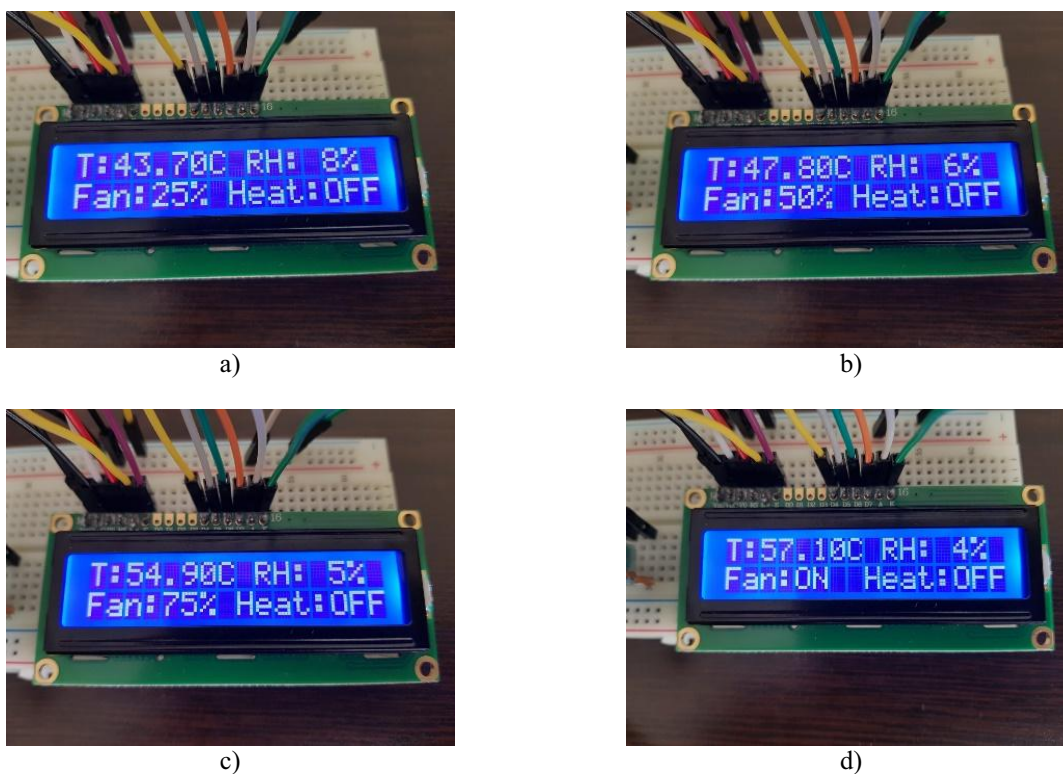


Fig.6. Display the temperature, relative humidity, and status of the DC fan in automatic control:
 a) lower range (40 – 45) °C; b) medium range (45 – 50) °C;
 c) high range (50 – 55) °C; d) highest range more or equal 55°C.

The operational ranges for temperature and relative humidity are 40–60 °C and 0–100%, respectively. The management system was set up to maintain an ambient temperature between 40 and 60 °C and relative humidity between 10 and 20 %. In the first picture of Figure 6, the LCD demonstrates a temperature of 43.7 °C in the lower range of temperature which is between 40 °C and 45 °C at a relative humidity of 8% causing the controller to send a PWM voltage with a 25 % duty cycle to make the DC fan runs with low speed. Secondly, the LCD demonstrates a temperature of 47.8°C in the medium range of temperature between 45°C and 50°C at a relative humidity of 6% causing a 50 % duty cycle to make the DC fan run at medium speed. Thirdly, the LCD demonstrates a temperature of 54.9 °C in the high range of temperature, between 50°C and 55°C at a relative humidity of 5% causing a 75 % duty cycle to make the DC fan run at high speed.

The final picture of the figure shows the LCD findings temperature of 57.10 °C in the highest range which is more than or equal to 55 °C at a relative humidity of 4% causing a 100 % duty cycle to make the DC fan run at maximum speed.

The results of temperature and humidity and corresponding motor fan speeds can be demonstrated according to the following Table 1. From the findings, it can be deduced that the fan speed increases with dryer temperature and decreases with relative humidity in the chamber.

Table 1. Temperature and relative humidity monitoring and corresponding fan speed

Readings	Temperature (°C)	Relative humidity (%)	Duty cycle (%)	Fan speed
1	43.70	8	25	Low
2	47.80	6	50	Medium
3	54.90	5	75	High
4	57.10	4	100	Highest

Conclusions

The proposed developed system overcomes the defects of the traditional approach in the process of drying and managing products and maintains their quality and prevents spoilage. The key characteristics of this system include cost-effectiveness, portability, robustness, quick usage, and satisfactory performance under various circumstances.

The proposed design is seen as a built-in dryer with an easy-to-use automated fan regulator that is temperature controlled to reduce energy consumption while also aiding in speeding up the drying process, hence increasing the efficiency of the solar dryer and obtaining a nutritionally useful product. The food that is being dried will undoubtedly retain its quality and freshness as a result. As a last measure to save energy, this paper only works when the temperature around the product is 40-60°C.

Using an online monitoring system would improve the efficiency of drying and storing grains. The entire drying time, storage temperature, humidity, and real-time sensor data may all be noted by the observer.

This study contributes to the creation of automated methods for enhancing drying system performance, with the possibility of its use in agricultural products and medicinal herbs. It has been verified how this system works and how to encode a temperature-controlled fan. This method of managing simply temperature control automatically seems to be reliable. It might be made more reliable, and fuzzy regulated by using soft computing technologies.

The given theoretical analysis can be used to create a mathematical model of thermal heating of printed circuit boards (PCBs) in electronic devices and to analyze the heat emission from them caused by convection and radiation. During the operation of PCBs, when heating occurs, it may lead to some deformations such as twisting, bending, and delamination, which can be analyzed and predicted using the simulation results.

Funding

The study was supported by a grant from the Russian Science Foundation No. 22-19-00389, <https://rscf.ru/project/22-19-00389/>.

REFERENCES

- 1 Mohana Y., Mohanapriya R., Anukiruthika T., Yoha K.S., Moses J.A., Anandharamakrishnan C. Solar dryers for food applications: Concepts, designs, and recent advances. *Solar Energy*, 2020, Vol. 208, pp. 321–344. doi: 10.1016/j.solener.2020.07.098
- 2 Alkahdery L.A., Yurchenko A.V., Mohammed J.A.-K., Mekhtiyev A.D., Neshina Y.G. Performance Improvement of Solar Dryer using an Auxiliary Heat Source under Different Values of Airflow Rates. *Eurasian Physical Technical Journal*, 2023, Vol. 20, No. 1(43), pp. 42–50. doi:10.31489/2023No1/42-50
- 3 Abed E.M. Design and Testing Solar Dryer Performance. *Eng. and Tech. J.*, 2013, Vol. 31, No. 12, pp. 169-184. doi: 10.30684/etj.31.12A.14
- 4 Jadallah A.A., Alsaadi M.K., Hussien S.A. The Hybrid (PVT) Double-Pass System with a Mixed-Mode Solar Dryer for Drying Banana. *Eng. and Tech. J.*, 2020, Vol. 38, No. 8, pp. 1214–1225. doi: 10.30684/etj.v38i8A.535
- 5 Abdullah R., Rizman Z.I., Dzulkefli N.N.S.N., Ismail S., Shafie R., Jusoh M.H. Design an Automatic Temperature Control System for Smart Tudung Saji Using Arduino Microcontroller. *ARPJ Journal of Engineering and Applied Sciences*, 2016, Vol. 11, No. 16, pp. 9578–9581.

- 6 Widhiada W., Negara D.N.K.P., Suryawanm P.A. Temperature Distribution Control for Baby Incubator System Using Arduino ATmega 2560. *Bali Indonesia*, 2017, Vol. 19, No. 10 part xv, pp. 1748–1751.
- 7 Kesarwani K., Pranav S.M., Noah T.N., Kavitha K.V.N. Design of Temperature Based Speed Control System Using Arduino Microcontroller. *Int. J. Chem. Sci.*, 2016, Vol. 14 (S3), pp. 753–760.
- 8 Bhatia V., Bhatia G. Room Temperature based Fan Speed Control System using Pulse Width Modulation Technique. *International Journal of Computer Applications*, 2013, Vol. 81, No. 5, pp. 35–40. doi:10.5120/14011-2067
- 9 Wellem T., Setiawan B.A Microcontroller—Based Room Temperature Monitoring System. *International Journal of Computer Applications*, 2012, Vol. 53, No. 1, pp. 7–10. doi:10.5120/8383-1984
- 10 Asraf H.M., Dalila K.A.N., Hakim A.W.M., Hon R.H.M.F. Development of Experimental Simulator via Arduino-based PID Temperature Control System using LabVIEW. *Journal of Telecommunication, Electronic and Computer Engineering*, 2017, Vol. 9, No. 1–5, pp. 53–57.
- 11 Sami K., Lavanya M., Arivalagan M., Harsha Y.S. Temperature Controlled Based Cooler Pad Using Arduino. *Journal of Chemical and Pharmaceutical Sciences*, 2016, No. 5, pp. 216–220.
- 12 Okpagu P.E., Nwosu A.W. Development and temperature control of smart egg incubator system for various types of egg. *European J. of Eng. and Tech.*, 2016, Vol. 4, No. 2, pp. 13-21.
- 13 Devi T.H.B., Kalnar Y.B. Design Consideration of Smart Solar Dryer for Precision Drying. *Journal of AgriSearch.*, 2021, Vol. 8, No. 2, pp. 135-138. doi:10.21921/jas.v8i2.7297
- 14 Mohammed, J.A.-K. Pulse Width Modulation for DC Motor Control Based on LM324. *Eng. and Tech. J.*, 2013, Vol. 31, No. 10, pp. 1882-1896. doi:10.30684/etj.31.10A6

ANALYSIS OF SYNTHETIC RENEWABLE METHANE PRODUCTION TECHNOLOGIES FOR IMPLEMENTATION IN UKRAINE

Klimenko V.N., Suprun T.T.

Institute of Engineering Thermophysics, National Academy of Sciences of Ukraine, Kyiv, suprun@secbiomass.com

Methanation technologies for the production of synthetic renewable methane are considered. The possibilities of applying the methods of catalytic and biological methanation are analyzed. The implementation of methanation technologies is carried out with the efficient use of renewable energy sources. The Power to Gas concept for the generation of synthetic renewable methane in different countries are considered. Some results of studies of methanation processes, obtained in ongoing projects, are presented. World experience in the implementation of methanation technologies for the production of synthetic renewable methane can be an example for Ukraine.

Keywords: synthetic renewable methane, methanation processes, the concept of Power to Gas, renewable energy sources

Introduction

There is a growing interest in renewable energy sources in the modern world energy industry. These are solar energy, wind energy and biomass energy, which are an alternative to traditional energy sources - coal, natural gas and oil. However, a number of factors hinder the practical use of these sources. For solar and wind power plants that operate unstably in time (day-night, summer-winter, the influence of weather conditions), there are difficulties in coordinating their operating modes with electric networks. For biogas plants, direct transfer of the resulting biogas to existing gas networks is not possible due to the high (up to 50%) carbon dioxide content in biogas. Therefore, it is necessary to transform these types of renewable energy into a form that is compatible with the possibilities of their use. For solar and wind power plants, this is the accumulation of excess generated unstable electricity by generating synthetic methane - the so-called Power-to-Gas (PtG) process [1, 2].

The PtG technological chain is a three-stage energy conversion process. The first stage is to convert the primary energy from the sun, wind or biomass into electricity or biogas. The second stage uses renewable electricity and biogas to produce carbon dioxide and hydrogen. The methanation process, which converts CO₂ and H₂ into synthetic renewable methane, is the third final stage. Thus, synthetic renewable methane is an accumulator of used renewable energy.

The purpose of the publication is to analyze the experience of foreign countries in obtaining synthetic renewable methane and to determine the most effective technologies for implementation in Ukraine.

Research methods include the study and analysis of literature and other data, in particular, methanation projects. Ukraine has great potential and prospects for the development of biomethane production [3], so the use of world experience in the implementation of the PtG concept is an important issue for our country.

1 Methanation process

There are two methods of methanation technology as the basis of PtG processes:

- in catalytic reactors in which the Sabatier chemical reaction is implemented;
- in biological reactors, where the methanation process occurs with the participation of methanogenic microorganisms, the so-called archaea.

Studies of methanation processes in both of these directions are carried out in many countries: the USA, Switzerland, Denmark, Germany, France, Japan, and others. Laboratory, pilot and demonstration installations that implement the ideas of PtG are already known.

1.1 Catalytic methanation

Catalytic methanation – is a chemical reaction in which hydrogen and carbon dioxide are synthesized into methane. The production of methane through the Sabatier reaction (1) is an exothermic catalytic reaction and usually takes place at temperatures from 200°C to 550°C:



To improve the efficiency of methanation, numerous studies have been carried out to develop catalysts with high activity, CH₄ selectivity and stability under conditions of heat release during the reaction. Such catalysts as Nickel, Ruthenium, Rhodium, Palladium, Cobalt, Iron were considered [4].

Reaction (1) is highly exothermic, so the adiabatic temperature rise associated with the reaction is quite high. This increase in temperature leads to a decrease in the proportion of H₂ and CO₂ that have reacted (i.e., to a decrease in the amount of methane generated or the rate of methanation). To increase the yield of methane, it is necessary to lower the temperature of the methanation process, as well as to increase the pressure in the reactor. The search for economically feasible ways to lower the operating temperatures of the methanation process is one of the main issues in creating an acceptable technology for the PtG process.

For catalytic methanation various types of reactors are used. In cooled fixed-bed reactors [1] the working process takes place in cylindrical tubes with a catalyst, which are washed on the outer surface with a coolant of a given temperature. In this case, water can be used as a coolant, but its main drawback is the dependence of the boiling point on pressure, i.e. high temperatures require high pressure. Other concepts are based on the use of three-phase reactors for methanation [5]. In suspension reactors, the working zone is filled with heat-transfer liquids, in which small particles of the catalyst go into a state of suspension due to the gas flow. The high heat capacity fluid allows almost complete removal of the heat of the reaction, ensuring practically isothermal operation of the methanator.

A disadvantage of fixed bed adiabatic reactors is the appearance of high temperature and high pressure drop zones. To overcome these shortcomings, structured reactors such as monolithic reactors have been developed [6]. The use of an internal metal structure made it possible to increase heat transfer in the working area by two to three orders of magnitude.

Microchannel reactors [7] are a modification of structured reactors. The advantages of such reactors are compactness and good thermal control. Compactness is ensured by an increased ratio of the surface of the metal microstructure to its volume. Ru-TiO₂ in powder form was used as a catalyst. The application of a catalyst to a metal structure, as well as the removal of the used catalyst, make it difficult to operate such reactors.

1.2 Biological methanation

The process of biological methanation is carried out using archaea of the genus *Methanothermobacter* as catalysts capable of converting hydrogen and carbon dioxide into synthetic methane. Biological methanation takes place in anaerobic conditions at atmospheric pressure and temperatures from 20 to 65°C. There are two concepts of the biological methanation process:

- *In situ* methanation, i.e. in a biogas reactor, where hydrogen is directly supplied from some external source;
- *Ex-situ* methanation in a special reactor - a methanator, where biogas (a mixture of 50-60% methane and 40-50% carbon dioxide), hydrogenotrophic methanogens, and hydrogen are supplied separately. Alternative CO₂ can also be supplied here.

During *in-situ* methanation, hydrogen from an external source (electrolyzer) is fed into the lower part (bottom) of the reactor, blown through the fermentation liquid, where with the help of archaea, it methanizes CO₂, which is released in the process of anaerobic fermentation of biomass. Intensive stirring of the fermentation liquid activates the process. As the conducted studies have shown, it is extremely difficult to achieve complete conversion of CO₂ released during the fermentation process.

Within the framework of the BTU-FESPE project of the Brandenburg University of Technology, the process of biocatalytic methanation in an anaerobic trickled-bed reactor was investigated [8]. Such a reactor contains a packed bed as a surface on which microorganisms can be immobilized. A three-phase system is formed on the carrier surface (biofilm–liquid–gas). Thus, in the anaerobic trickle-bed process, methane with a concentration above 98% can be obtained [8].

An article by research organizations in Ireland [9] published the results of studies on *in-situ* and *ex-situ* biological methanation to produce synthetic renewable methane that can be fed into existing gas networks. The work [9] proposes a sequential combination of several *ex-situ* blocks, as well as a hybrid model for combining *in-situ* and *ex-situ* blocks, taking into account the advantages and disadvantages of each of these concepts. The paper [10] also considers various systems and technologies for biological methanation, such as *in-situ* and *ex-situ*. The main parameters that determine the cost-effectiveness of each technology, as well as ways to optimize them, are noted.

1.3 Comparison of biological and catalytic methanation

Comparison of biological and catalytic methanation technologies was carried out in many works. In particular, in a review [2] these comparisons were made according to the following indicators:

- The volume of the reactor required to ensure the same productivity;
- Resistance to the influence of impurities;
- Dependence of the methanation process on the load;
- Energy efficiency.

The results of these studies showed that:

- The volume of the catalytic methanation reactor is less than the volume of the biological methanation reactor required to provide the same productivity;
- Biological methanation is more resistant to impurities. Contaminants such as sulfur and oxygen do not affect biological methanation, while in catalytic methanators sulfur and its compounds are harmful to nickel catalysts;
- Fixed-bed reactors are the most sensitive to load changes due to catalyst temperature fluctuations. The liquid phase present in biological and three-phase methanation buffers the effect of load changes;
- Considering that catalytic methanation does not require a stirrer and can use waste heat, this technology is more efficient.

2 Implementation of the PtG concept in pilot, demonstration and laboratory plants

In [11], a detailed review of PtG projects implemented in different countries is made. The largest number of projects during 2009-2019 was carried out in Germany and concerned both catalytic and biological methanation. Among other countries, the leadership is held by Great Britain, Denmark, Switzerland, the USA, Austria, Japan and others.

2.1 PtG projects with catalytic methanation

One of the largest PtG plants in Germany with a capacity of 5 MW Audi e-gas uses catalytic methanation technology in one isothermal fixed-bed reactor [12]. Renewable electricity for electrolysis comes from four wind turbines and CO₂ is generated in upgrading process at nearby biogas plant. The efficiency of the PtG process is 54% without taking into account additional thermal energy produced. The wind power plant itself, unlike a biogas plant, is not used permanently, but according to the power supply scheme. The plant is now qualified for participating in what is known as the electricity balancing market [13].

The idea of increasing the efficiency of PtG technology by thermally integration of high-temperature electrolysis with catalytic methanation at high pressure was implemented in the project HELMETH [14] (Fig.1). The project brings together partners from Germany, Italy, Greece and Belgium.

The efficiency of the PtG process was expected to be increased from 61% (using conventional electrolyzers and low-pressure catalytic methanation) to 85% and higher at pressures up to 30 bar and a high-temperature electrolyzer on the base of SOECs. The heat of the exothermic methanation reaction was used in the process of high-temperature electrolysis under pressure, which increased the efficiency of the PtG process. To achieve a high methane yield, the HELMETH project tested and optimized various nickel and ruthenium catalysts, which ensured the content CH₄ in the methanation product at a level of more than 97 vol.-%, and hydrogen concentrations below 2 vol.-%.

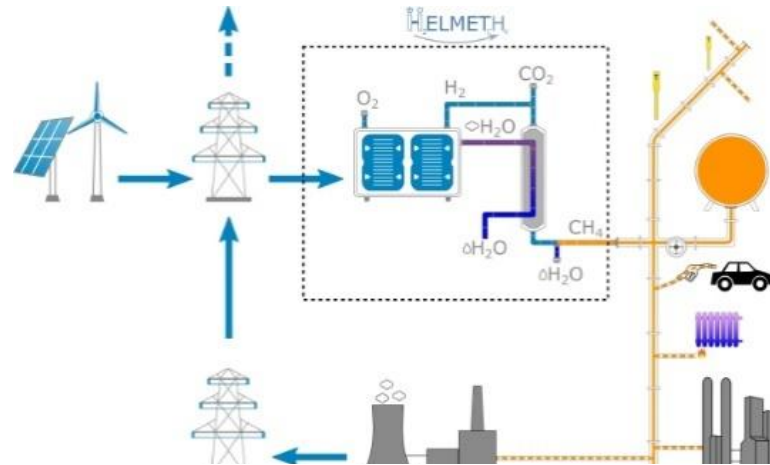


Fig.1. HELMETH PtG concept [14]

2.2 PtG projects with biological methanation

The first biomethanation-based PtG concept to reach commercial status in the world is the Bio Power 2 Gas project. It was started in 2013 and implemented in 2015 in Allendorf (Germany). Viessmann group subsidiaries provided equipment for this plant [15]. Before the implementation of the project, laboratory studies were carried out that confirmed the viability of the concept of biological methanation (the methane content in biogas increased from 60 to 95%). Thus, biological methanation of pure CO_2 and H_2 was realized in this project.

A significant recent event (April 28-29, 2022) was the official inauguration of Europe's first industrial PtG plant in Switzerland. Based on biological methanation, this plant is the first in Europe and is an important milestone both for its owner and operator Limeco and for HZI Schmack (a subsidiary of Hitachi Zosen Inova AG), which proposed the innovative technology [16]. The new PtG plant uses renewable electricity from a wastewater treatment plant to split water into oxygen and hydrogen using electrolysis. In the second stage of the process, this hydrogen is fed to the HZI Schmack methanation reactor together with the waste water gas. In the "BiON" process the microorganisms in this bioreactor convert hydrogen and CO_2 contained in wastewater gases into biomethane under anaerobic conditions. The biomethane is then purified and can be fed into the local gas network as a CO_2 -neutral substitute for natural gas.

Conclusion

In modern conditions, the production of synthetic renewable methane, which are an alternative to expensive and sometimes scarce natural gas, is of great importance. The current PtG system can be considered as a main generator of synthetic renewable methane. Today, in many countries of the world (Germany, Great Britain, Denmark, Switzerland, USA, Austria, Japan, the Netherlands and others), active work is underway to create technologies that implement the concept of PtG. Numerous laboratory, pilot and demonstration projects have already been carried out, confirming the viability and promise of the PtG concept.

The main efforts of researchers are aimed at increasing the efficiency of hydrogen generation and methanation processes, as well as increasing the productivity of electrolyzers and methanators. For example, for adiabatic catalytic methanation reactors, the main problem is ensuring the optimal reaction temperature due to cooling. However, for instance, a three-phase reactor is devoid of this disadvantage. For biological methanation reactors, the main problem remains the low level of mass transfer of hydrogen, which limits the productivity of the process.

The PtG concept involves the production of synthetic renewable methane by catalytic or biological methanation, i.e., combining hydrogen with carbon dioxide using surplus energy from renewable energy sources to generate hydrogen in certain electrolyzers.

Comparing the results of the implemented PtG projects with catalytic and biological methanation processes, we can draw the following conclusions:

– Medium to large PtG projects (over 1MW) are being implemented using catalytic methanation technology due to their scalability and the ability to increase process efficiency by using the heat of methanation.

– Small-capacity projects should be implemented using biological methanation, because biomethanation requires the use of reactors with a large specific volume. However, its increased resistance to such harmful impurities as sulfur and oxygen compensates this direction of biomethanation.

– Both biomethanation concepts of PtG – *in-situ* and *ex-situ* – have found their practical implementation. The hybrid model *in-situ* + *ex-situ* takes advantage of each of these concepts.

The world experience of implementing the PtG concept should become an example for Ukraine. A separate task of this study was to determine the most appropriate methanation technologies for the production of synthetic renewable methane in Ukraine. It should be noted that in recent years there has been an increased interest in biogas technologies in Ukraine. To date, more than 70 biogas plants have already been built in the country. Therefore, it is quite logical and economically justified to use biomethane technologies for the production of synthetic renewable methane. For example, such a plant may combine a biogas reactor as a source of carbon dioxide, which is an integral part of the resulting biogas, with an *ex-situ* methanation process, where either biological or catalytic methanation is used. This way of developing bioenergy can be a powerful incentive for the construction of solar and wind power plants as sources of electricity for producing renewable hydrogen used in the methanation process. However, to get a final answer to the question - which of the technologies can be recommended for implementation in Ukraine, is possible only based on a feasibility study of synthetic renewable methane production technologies.

REFERENCES

- 1 Schaaf T., Grünig J., Schuster M.R., et al. Methanation of CO₂ - storage of renewable energy in a gas distribution system. *Energ Sustain Soc.*, 2014, 4. doi: 10.1186/s13705-014-0029-1
- 2 Gotz M., Lefebvre J., Mors F., et al. Renewable power-to-gas: A technological and economic review. *Renewable Energy*, 2016. 85, pp. 1371-1390. doi:10.1016/j.renene.2015.07.066
- 3 Geletukha G., Kucheruk P., Matveev Yu. Prospects and potential for biomethane production in Ukraine. *Ecological Engineering & Environmental Technology*. ISSN 2719-7050. 2022, Vol. 23, Is. 4, pp. 67–80. <http://www.ecoet.com/Prospects-and-Potential-for-Biomethane-Production-in-Ukraine,149995,0,2.html>
- 4 Tan C.H., Nomanbhay S., Shamsuddin A.H., et al. Current Developments in Catalytic Methanation of Carbon Dioxide – A Review. *Front. Energy Res.*, 2022. Vol. 9:795423. doi:10.3389/fenrg.2021.795423
- 5 Lefebvre J., Gotz M., Bajohr S., et al. Improvement of three-phase methanation reactor performance for steady-state and transient operation. *Fuel Proces. Technol.*, 2015, 132, pp. 83 – 90. doi:[10.1016/j.fuproc.2014.10.040](https://doi.org/10.1016/j.fuproc.2014.10.040)
- 6 Janke C., Duyar M.S., Hoskins M., et al. Catalytic and adsorption studies for the hydrogenation of CO₂ to methane. *Appl. Catal. B Environ.*, 2014. 152-153, pp. 184-191. doi:10.1016/j.apcatb.2014.01.016
- 7 Brooks K.P., Hu J., Zhu H., et al. Methanation of carbon dioxide by hydrogen reduction using the Sabatier process in microchannel reactors. *Chem. Eng. Sci.*, 2007. 62, pp. 1161-1170. doi:10.1016/j.ces.2006.11.020
- 8 Burkhardt M., Koschack T., Busch G. Biocatalytic methanation of hydrogen and carbon dioxide in an anaerobic three-phase system. *Bioresour. Technol.*, 2014. 178, pp. 330-333. doi: 10.1016/j.biortech.2014.08.023
- 9 Voelklein M.A., Rusmanis D., Murphy J.D. Biological methanation: Strategies for in-situ and ex-situ upgrading in anaerobic digestion. *Applied Energy*, 2019, 235, pp.1061-1071. doi: 10.1016/j.apenergy.2018.11.006
- 10 Rusmanis D., O’Shea R., Wall D.M., et al. Biological hydrogen methanation systems – an overview of design and efficiency. *Bioengineered*, 2019, 10:1, pp. 604-634. doi: 10.1080/21655979.2019.1684607
- 11 Bailera M., Lisbona P., Romeo L.M., et al. Power-to-gas projects review: Lab, pilot and demo plants for storing renewable energy and CO₂. *Renewable and Sustainable Energy Reviews*, 2017, Vol. 69, pp. 292-312. doi.org/10.1016/j.rser.2016.11.13
- 12 Rieke S. Catalytic methanation – the Audi e-gas project as an example of industrialized technology for Power to gas. *REGATEC, 2015*, Barcelona, Spain, 2015.
- 13 Strohbach O. Audi e-gas plant stabilizes electrical grid. *Press Release - Audi MediaInfo - Technology and Innovation Communications*; 2015. <https://www.automobilsport.com/audi-e-gas-stabilizes-electrical-grid---138930.html>
- 14 Project HELMETH. <http://www.helmeth.eu/index.php/project>
- 15 Heller T. Thomas Heller, Power-to-Methane Joint Workshop - Renewable Energy House, Brussels, 06.09.2017. [https://www.gie.eu/wp-content/uploads/filr/3234/4.%20Thomas%20Heller-Microb Energy.pdf](https://www.gie.eu/wp-content/uploads/filr/3234/4.%20Thomas%20Heller-Microb%20Energy.pdf)
- 16 <https://bioenergyinternational.com/europes-first-industrial-biological-methanation-ptg-plant-inaugurated>

THE USE OF ALTERNATIVE ENERGY SOURCES FOR THE OPERATION OF ENGINEERING SYSTEMS OF DETACHED CONSUMERS

Usenkov R.A.¹, Kokhanova S.Ya.¹, Trushin M.V.²

¹ Kazan National Research Technical University named after A.N. Tupolev, Kazan, Russia, RAUsenkov@kai.ru

² Kazan (Volga Region) Federal University, Kazan, Russia, mtrushin@mail.ru

The operation of many of the engineering systems that are necessary for the functioning of a detached residential building depends on specific sources of alternative energy, the use of which can significantly reduce the consumption of traditional fossil energy resources. A review of scientific works devoted to the operation of engineering systems using alternative energy sources is given. Several schemes of power equipment have been developed to obtain thermal and electrical energy supplied to isolated consumers. When designing a fixed technical solar system using solar radiation for operation, the locations of all power equipment, the solar receiver pitch on the roof of the building and the values of its optimal angle of inclination to the horizon were determined. A scheme of a small transportable hydroelectric power plant has been developed, which generates electric energy using the pressure created by the flow of water. A thermal refrigeration unit is designed, which uses the heat of the air removed from the animal stall to heat the heated medium.

Keywords: alternative energy sources, hydropower, heat, thermal refrigeration unit, temperature, heated medium

Introduction

The growth of energy capacities for industrial needs is increasingly raising the issue of saving energy resources, finding reliable alternative energy sources and creating energy saving, environmentally friendly technologies. Alternative energy sources can substitute traditional energy sources. Among the alternative energy sources, the most promising ones are solar energy and water energy.

The sun emits energy as radiation and about 30 % of its total amount is reflected back into space, and about 70 % reaches the Earth's surface [1,2]. This energy can be captured and converted into electricity or heat. That is why the issue of the efficient use of solar energy is receiving more and more attention.

The density of monochromatic radiation flux propagation in the form of solar radiation light depends on a number of factors, including geographic location, season and time of day. When the Sun is low, the rays go through a longer path in the atmosphere and they become more and more scattered, which results in a higher percentage of scattered radiation. The seasons determine the amount of sunshine on any given day: up to 18 hours in the summer and only 8 hours in the winter. According to [3,4], a string of regions of the Russian Federation with the number of sunny hours in the range from 2000 to 3000 per year can be determined.

There are technical systems that can be: 1) stationary devices oriented at a certain angle to the horizon; 2) devices that are able to change their position throughout the day and be under the constant influence of solar radiation. Mobile technical solar systems are environmentally friendly power plants designed to heat water and air, where a working medium is pumped through a circulation pump to a predetermined temperature. These devices can work at both low and medium ambient temperatures.

In [5], a numerical study was carried out to determine the amount of daily solar energy consumed by a mobile technical solar system with an evacuated "water in glass" tube collector for various angles of inclination, azimuthal angles of the collector, and geometric parameters under changing mass flow rate of the heated medium. The optimal inclination angles were obtained, at which the power plant works most efficiently.

The authors of [6] compared the efficiency and performance characteristics of stationary technical solar systems with tubes made of unglazed transparent material and ordinary glass under local conditions. The controlled parameters were the inlet and outlet temperatures of the tubes, solar radiation intensity, ambient temperature, wind speed and ambient relative humidity. In [7], a design of a stationary technical solar system with tubes made of stainless steel was developed, which is a tube with a closed stainless steel thermosyphon, which consists of evaporative and condensing parts. The developed parabolic grooved design of a stationary

technical solar system, consisting of evaporative and condensing parts provides higher thermal efficiency compared to other existing technical systems.

The authors of [8] examined the influence of various nanomaterials and nanofluids on the efficiency of various types of technical solar systems. In the paper [9] a comparison was made between the technical solar systems made of metal and polymer materials with free convection under environmental conditions. A number of advantages of using polymeric materials in the manufacture of solar technical systems was discovered in comparison with metal structures. The thermal refrigeration plant takes energy in the form of heat from a low temperature source, increases the thermal potential of the taken energy and transfers the heat to a consumer.

The implementation of the thermodynamic cycle of a thermal refrigeration plant assumes that in order to increase the temperature of the heated medium, it is necessary to take heat from a low temperature source. As a source of low temperature, the following can be used: humid air, soil, sewage, heat of the air removed from the stall of animals, heat removed from cooled bodies in refrigeration units, etc. In a thermal refrigeration plant, a condenser is a heat exchanger that pumps heat to a heated medium with the purpose of its subsequent beneficial use in various engineering systems, and an evaporator is a heat exchanger that takes heat from a low temperature source. Thermal refrigeration units are used to heat humid air.

The authors of [10] carried out a comparative analysis of the economic costs of converting the heating system of private houses from oil boiler units to thermal refrigeration units. The authors of [11] conducted a numerical experiment and formulated recommendations for the selection of heat pumps in relation to various production processes. It was found that due to the recovery and modernization of removed heat, thermal refrigeration units can save 15-78 % of the consumed hot water, depending on the specific process. In [12], recommendations are given for choosing a specific type of thermal refrigeration units from several suitable combinations. In [13], based on the developed simulation model, energy and economic characteristics were analyzed and compared for four types of thermal refrigeration units operating at low-temperature waste heat recovery. Recommendations are given on the choice of a thermal refrigeration unit depending on the specific conditions of their operation. The authors of [14] described the operation of a refrigeration unit for cooling milk with simultaneous heating of water (Fig. 1).

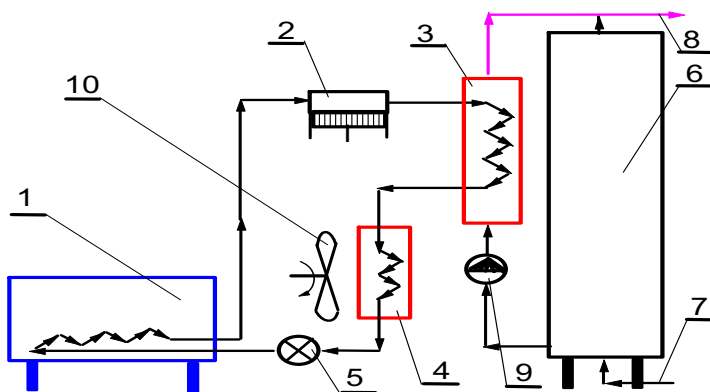


Fig.1. Layout of the refrigeration unit [14]: an evaporator in the milk tank; 2 - a compressor; 3 - condenser for water heating; 4 - an air condenser; 5 - a throttle; 6 is a water tank; 7 - the cold water inlet; 8 the hot water outlet; 9 is a centrifugal pump; 10 - a fan

Freon R12 is used as a working fluid circulating in the refrigeration unit. The pressure in condenser 3 is 1.73 MPa, and the temperature is 45 °C. The pressure in the evaporator 1 is 0.34 MPa, and the temperature is -3 °C. The refrigerant circulation circuit has an additional heat exchanger-condenser 4, which makes it possible to increase the temperature of a small part of hot water from 40 °C to 70 °C due to the superheat of the Freon in the reverse thermodynamic cycle. The total power of electric drives is 35 kW. The condenser 4 can be placed directly in the water heat storage tank 6.

The heat that is removed by fresh milk during its cooling, and the "waste" heat from the compressor 2 can be taken using the evaporator 1 and transferred to the heated medium by the condensers 3 and 4 of the refrigeration unit. Figure 2 shows a diagram of the operation of a refrigeration unit on a dairy farm [15]. Fresh milk with an initial temperature of 37 °C enters the plate heat exchanger 7. A pipeline is installed in

the first section of the heat exchanger, through which tap water with a temperature of 10°C is supplied, moving in the opposite direction (countercurrent).

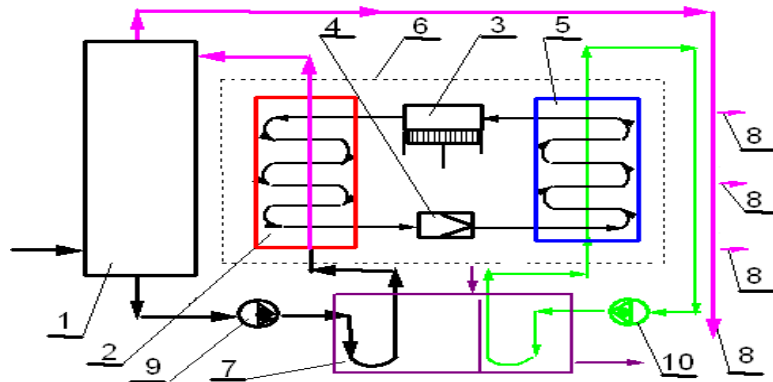


Fig.2. Layout of a refrigeration unit on a dairy farm [15]: 1 is a hydraulic accumulator; 2 is a condenser; 3 is a compressor; 4 is a pressure reducing valve; 5 is an evaporator in a tank with "ice" water; 6 is a body of the refrigeration unit; 7 is a plate heat exchanger; 8 is a consumer of hot water; 9 is a centrifugal pump for forced circulation of cold water; 10 is a centrifugal pump for forced circulation of "ice" water

At the same time, the temperature of the water rises to 28°C , and the temperature of the milk drops to about 20°C . Then the heated water through the pipeline enters the condenser 2 of the refrigeration unit, where the freon vapor (Freon R22), condensing, heats the water up to 55°C . Warm water enters the upper part of the accumulator 1, from which it is used as needed for household needs. Milk from the first section of the plate heat exchanger 7 with a temperature of about 20°C enters the second section, where "ice" water with a temperature of 1°C is supplied in a countercurrent from the refrigeration unit through the built-in pipeline. Cooled to 4°C , milk is pumped into vehicles or into storage containers.

Water, having heated up to 7°C , enters the tank 5 with the "ice" water of the refrigeration unit, where the boiling freon passing through the evaporator takes heat from the water and reduces its temperature to 1°C .

Thus, by recuperating the "waste" heat of milk and the compressor unit of the refrigeration unit, without additional energy costs, heated water is obtained for household purposes with a temperature of 55°C in the amount of 1.1 liters per liter of cooled milk. The scheme of operation of the thermal refrigeration unit TRU-14 for a dairy farm [16] is shown in fig. 3.

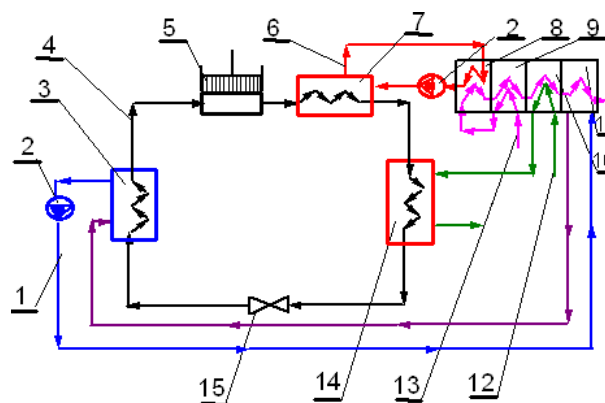


Fig.3. Layout of thermal refrigeration unit TRU-14 for a dairy farm [16]: 1 is an "ice" water line; 2 is centrifugal pumps; 3 is an evaporator; 4 is a freon line; 5 is a compressor; 6 is a hot water line; 7 is a heat exchanger; 8 is a pasteurization section; 9 is a regeneration section; 10 is a pre-cooling section; 11 is a final cooling section; 12 is a tap water line; 13 is a milk line; 14 is a condenser; 15 is a thermostatic expansion valve TEV

The thermal refrigeration unit is designed to cool water used as an intermediate coolant in tanks, and simultaneously heat it to meet sanitary and technological needs on livestock farms.

The freon (Freon R22) boiling in the evaporator 3 removes heat from the water in line 1 and lowers the water temperature to 0 °C. Then the freon vapor is compressed by the compressor 5 and fed into the heat exchanger 7, where R22 freon is condensed due to heat exchange with water. Further, water, heated to 85...90 °C, from the heat exchanger 7 enters the milk pasteurization section 8.

In the condenser 14, freon R22 transfers all the heat obtained by compressing freon vapor in the compressor 5 to running water, which is heated to 50 °C and used on a dairy farm for sanitary and hygienic purposes. As shown by theoretical calculations, the use of a 75kW thermal refrigeration unit TRU-14 on a dairy farm for 1,000 heads saves up to 100 tons of liquid fuel and 350,000 kW· h electricity per year on the farm. The technological scheme of operation of the thermal refrigeration unit TRU-14 for a dairy farm is shown in Fig. 4.

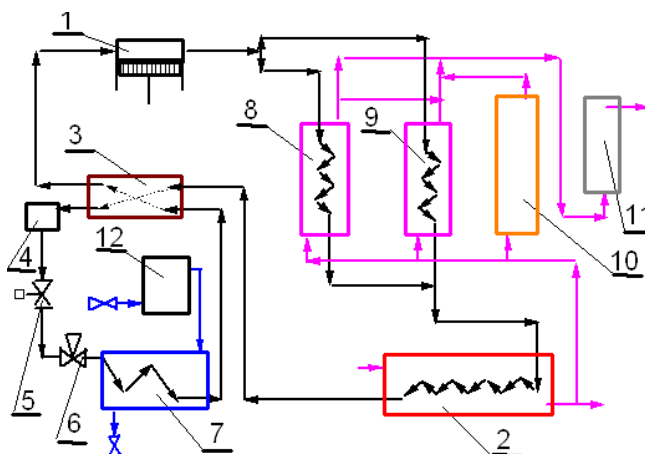


Fig.4. Technological scheme of thermal refrigeration unit TRU-14 for a dairy farm [16]: 1 is a compressor; 2 is a condenser; 3 is a regenerative heat exchanger; 4 is a filter-drier; 5 is a membrane solenoid valve; 6 is a thermostatic expansion valve; 7 is an evaporator; 8 is a heat exchanger; 9 is a heat exchanger; 10 is a capacitive water heater; 11 is an electric heater; 12 is a cold water tank

Freon R22 vapors are compressed by the compressor 1 and fed into the condenser 2, where they are cooled and condensed, giving off the heat to running water. From the condenser 2, liquid freon enters the regenerative heat exchanger 3, and then moves into the filter-drier 4, where it gets dried and cleaned from impurities. Further, passing through the solenoid valve 5, freon R22 is fed into the thermostatic valve 6, where the freon is throttled to the boiling pressure, and enters the evaporator 7. In the evaporator 7, the freon boils, absorbing heat and cooling the coolant (water). Vapors of freon R22 are pumped out by the compressor 1 from the evaporator 7 through the regenerative heat exchanger 3, and then the refrigeration cycle is repeated. Cold water (refrigerant) makes a closed cycle in the milk cooling system. Warm water at the outlet of the condenser 2 is divided into two streams. Part of it enters the heat exchangers 8, 9 and 10 for further heating, and its amount is set using a water control valve.

The water in the heat exchangers is heated by heat exchange with hot freon vapor moving in countercurrent. The flow heat exchanger provides heating of water to a temperature of 40 °C in 10...15 minutes after turning on the refrigerating unit. The heat exchanger of the convective circuit heats water in the amount of 150 liters to a temperature of 60 ... 65 °C in a cycle of 3.25 hours. If it is necessary to withdraw hot water before the completion of the full cycle of the thermal refrigeration unit, the water temperature can be brought to a predetermined level using the electric water heater 11.

At present, the use of alternative energy sources in the energy industry, which includes the energy of water resources of rivers (hydropower), is becoming an urgent task. This type of energy owes its origin to solar energy. The sun evaporates the water of rivers, seas and oceans, and then it rains over the entire territory of the globe.

It has been estimated that the planet Earth has 10^{18} tons of water reserves, and only 1/2000 of it is annually involved in the cycle. Hydropower provides around 2,600 TW· h of the world's electricity generation per year, which is about 20 % of the world's total electricity demand, making it one of the most reliable and cost-effective renewable energy sources. In 2001, the largest hydropower producing countries were Canada (333.0 TW· h), the US (201.2 TW· h) and Norway (120.4 TW· h). Hydropower consumption

in the EU countries grew by almost 27 % between 1991 and 2001. In 2001, hydropower accounted for approximately 5 % of total electricity consumption in the EU countries. France is the largest producer of hydropower in the EU. In 2001, the generating capacity of hydropower plants in France was about 25,000 MW [17].

As of 2015, over 47,000 small hydropower plants under 50,000 kW have been built in China. Most hydropower plants are located in the mountainous regions of southern China, where there are large reserves of water resources (rivers) [18]. According to [1], the average capacity of one small hydropower station was 143 kW. These small-scale hydropower plants (SHPPs) generated up to 0.01 % of the entire produced electricity.

Lately, scientists and researchers have been looking for progressive and economically sound technical solutions for small hydropower plants (SHPPs). HPPs and SHPPs can serve as a reliable reserve of electricity for remote consumers. The authors of [19] describe the operation of the HPP as a power plant for generating electricity from renewable energy sources and evaluate the possibility of building a HPP in the Republic of Macedonia. The paper describes the possibility of using HPPs of low power (up to 10 MW).

In [20], the possibility of extracting energy from water resources is estimated using the example of the Alviela River in Portugal using three types of turbines: two propeller turbines (with and without adjustable blades) and an Archimedes screw turbine. The results showed that with an available head of 2.5 m, the most acceptable solution is to use an Archimedes screw turbine with a nominal flow of 3 m³/s and a nominal power of 55 kW. The further development of the world energy industry is connected with a more rational use of energy.

Thus, it can be stated that:

- modernization of the existing structures of stationary and mobile technical solar systems, hydroelectric power plants and refrigeration unit is required;
- there is a strong need for new information that will make it possible to study the issue of the development and design of the simplest structures of technical solar systems, transportable small-scale hydropower plants and thermal refrigeration units.

The purpose of the study is to develop specific recommendations and select design solutions for power equipment for remote consumers, which will allow converting the energy potential of alternative sources into other types of energy for their subsequent beneficial use.

1 Experimental technique

To assess the possible use of three experimental power plants by remote consumers, the design calculation of power plants based on algebraic equations describing their operation was chosen as a research method. As experimental power plant No. 1, the authors propose a layout of a stationary technical solar system that can be used to ensure the operation of engineering systems for a residential building of a detached consumer. The layout of the power plant is shown in fig. 5.

Experimental power plant No. 1 consists of a solar receiver, which is an aluminum corrugated pipeline with a diameter of $d = 0.08$ m and a length of $l = 10$ m, which receives the energy of solar rays, a centrifugal fan and an accumulator. Humid air with a temperature of $t_{f_1} = 17$ °C is taken from the environment through the air intake grille and fed into the pipeline by a fan. Aluminum corrugated pipeline is mounted on the south side of the roof of the building, which is inclined to the horizon at an angle of 30 °.

Owing to the centrifugal fan 2, air moves through the pipeline with a mass flow rate varying in the range of $G = 0.05 \dots 0.054$ kg/s and a corresponding volumetric flow rate of $Q = 0.0417 \dots 0.045$ m³/s, and at the same time at the outlet its temperature becomes turns $t_{f_2} = 39 \dots 41$ °C. Heated air is supplied either to the room or to the accumulator 3, which is located under the building. The design of the stationary technical solar system provides for the use of recirculated air from the room and the supply of outside air directly to the accumulator 3 in the case when the solar receiver 1 is not working (at night or in cold weather).

The design calculation of the power plant is performed in the following sequence.

1. Initial and final parameters of coolants are set.
2. Using the literature recommendations, the speeds of the coolant moving through the pipeline are set.
3. The values of the volumetric and mass flow rates of the coolant are determined by the value of the velocity.

4. The power of the heat flow is determined, which is transmitted with the help of solar radiation to the cold coolant (air).

5. The efficiency of a stationary technical solar system is calculated.

Useful heat flow, which is transferred to the coolant through the pipeline wall, W

$$\Phi_e = Gc_p(t_{f_2} - t_{f_1}), \quad (1)$$

where G is the mass flow rate of the coolant, kg/s;

c_p is the specific isobaric heat capacity of air, which in this case does not depend on temperature, $c_p = 1004 \text{ J}/(\text{kg} \cdot \text{K})$;

t_{f_1} is the humid air temperature at the inlet of the pipeline, $t_{f_1} = 17 \text{ }^\circ\text{C}$;

t_{f_2} is the humid air temperature at the outlet of the pipeline, $t_{f_2} = 39 \dots 41 \text{ }^\circ\text{C}$.

It was determined that the values of the useful heat flux vary in the range of $\Phi_e = 1104 \dots 1301 \text{ W}$.

The efficiency of a stationary technical solar system is the following:

$$\eta = \frac{\Phi_e}{\pi dl \cdot J_C}, \quad (2)$$

where πdl is the pipeline side surface area, m^2 ;

J_C is the total flux density of solar radiation incident on the surface of the pipeline, $J_C = 600 \text{ W}/\text{m}^2$.

It was found that the values of the efficiency of a stationary technical solar system varied in the range of $\eta = 0.59 \dots 0.7$. As an experimental power plant No. 2, the authors propose a layout for a transportable small hydroelectric power station, which can be used to produce electrical energy. The layout of the power plant is shown in fig. 6. Experimental power plant No. 2 consists of a water intake device, a pressure hose, which is a polyethylene pipe with a diameter of $d = 0.025 \text{ m}$ and a length of $l = 5 \text{ m}$, a hydraulic turbine and an electric current generator.

Water enters the intake device 1 and then, moving along the pressure hose 2, through the inlet pipe enters the spiral chamber 3 of the hydraulic turbine. The flow of water inside the chamber spins the turbine impeller and transmits torque to the electric current generator 4, which, during rotation, generates electrical energy used for the needs of consumers.

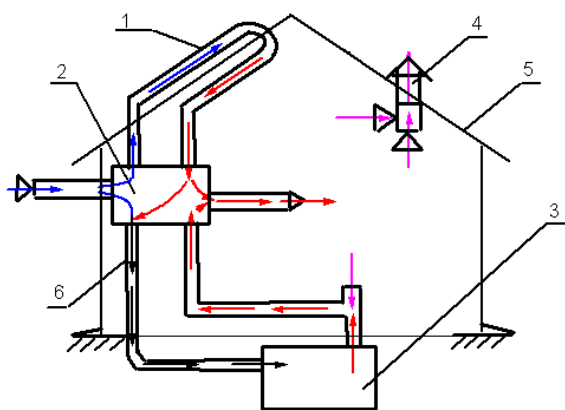


Fig. 5. Layout of a stationary technical solar system in a residential building: 1 is a solar receiver for solar rays; 2 is a centrifugal fan; 3 is an accumulator (water, granite, pebbles); 4 is an exhaust hood; 5 is a gable roof of the building; 6 is an air duct.

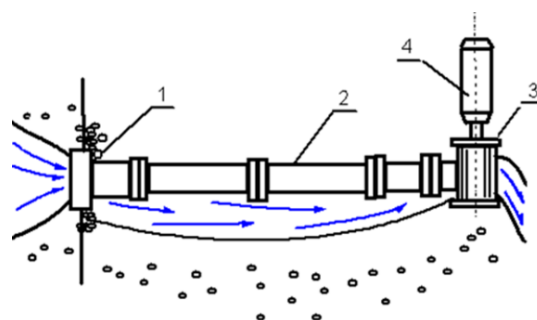


Fig. 6. Layout of a transportable hydropower station: 1 is a water intake device; 2 is a pressure hose; 3 is a spiral chamber of the hydraulic turbine; 4 is an electric current generator

Water moves along the pressure hose with a volumetric flow rate, which varies in the range of $Q = 0.01 \dots 0.03 \text{ m}^3/\text{s}$. We assume the available water head to be constant at $H = 3 \text{ m}$, the efficiency of the turbine is $\eta_{\text{turb}} = 0.55 \dots 0.95$ and the efficiency of the generator is $\eta_{\text{gen}} = 0.96 \dots 0.97$. A small hydroelectric

power station is operated for 6 months a year due to the freezing of the reservoir in the autumn-winter period, that is, the time is $t = 4320$ h.

The design calculation of the power plant is performed in the following sequence:

1. The variety range of the volumetric flow rate Q is set.
2. The available head H is taken as a constant value.
3. Using the literature recommendations for small hydroelectric power plants, the efficiency of the turbine η_{turb} and the efficiency of the generator η_{gen} are determined.
4. The operating time is determined for a small hydroelectric power station (in hours) during the year.
5. Calculate the power of a transportable HPP N at a specific point in time, W .
6. The maximum power is calculated for a transportable hydroelectric power station N_{max} , called installed power, W .
7. The amount of electricity E generated by a transportable hydroelectric power station for the entire time of operation is determined, $kW \cdot h$.

It was determined that the amount of electricity generated by the transportable hydroelectric power station for a fixed period of time varied in the range of $E = 740 \dots 2220$ $kW \cdot h$. As an experimental power plant No. 3, the authors propose a layout of a stall thermal refrigeration unit, which allows preparing and supplying hot water and heated air to a residential building of a detached consumer. A diagram of the thermal refrigeration unit that uses the heat of the air removed from the animal stall to heat the coolant is shown in fig. 7.

The experimental power plant No.3 consists of an evaporator 1, which is located in the animal stall (room No. 1), a primary heat exchanger 5, a condenser 3, located in a residential building (room No. 2), a compressor 2 and a throttle 4. A primary recuperative heat exchanger 5 is mounted in the animal stall, which transfers heat from the air to an intermediate heat carrier (water), which is sent through the pipes to the evaporator 1 and gives off its heat to freon R12. In the evaporator, freon R12 circulating in the refrigeration unit boils and enters compressor 2 in the state of dry saturated steam. In the compressor, freon R12 is compressed and enters condenser 3 in the form of superheated steam.

As a result of the condensation process, freon flows in the form of a liquid into throttle 4 and then it enters the evaporator 1, and the processes occurring in the thermal refrigeration unit are repeated. The condensation process is accompanied by the release of heat, which, with the help of an intermediate coolant, can be used to ensure the operation of an engineering system that replenishes the heat losses of a residential building. If an engineering system with a working medium "dry air – saturated water vapor" is used in a residential building, the air must be heated to the specified parameters in a water heater before being supplied to the working area and then delivered to the room using the air distribution grille 6.

The design calculation of the power plant is performed in the following sequence:

1. The variation range of the volumetric flow rate of R12 freon circulating in the thermal refrigeration unit is set to be $M = 0.1 \dots 0.3$ kg/s .
2. Using the thermal Ts - diagrams of the refrigeration unit for difluoro-dichloro-methane (freon R12) the thermodynamic parameters of the state at the characteristic points of the cycle are determined.
3. Values of the specific removed q_1 and supplied q_2 heat are determined.
4. The specific work of the refrigeration cycle l_c is calculated.
5. The adiabatic power of the compressor drive N is determined.
6. The cooling ε and heating φ coefficients are calculated.
7. The theoretical volume V , described by the compressor piston in 1 s, is determined.

The stall thermal refrigeration unit operates on a throttling cycle. The boiling point of freon R12 in the evaporator is t_0 , the condensation temperature is t_c . Freon R12 enters the compressor in the form of dry saturated steam with a temperature t_0 . Before entering the throttle, the working fluid is supercooled to a temperature of $t_H = t_c - 10^\circ C$. Freon R12 mass flow rate is $M = 0.1$ kg/s . Let us build a cycle of operation of a stall thermal refrigeration unit in a thermal Ts - diagram for difluoro-dichloromethane (Fig. 8). The presented thermal Ts - diagram for freon R12 allows you to determine the thermodynamic parameters of the state at the characteristic points of the cycle of a thermal refrigeration unit. The results of the Ts - diagram are summarized in Table 1.

It was found that the heating coefficient remained unchanged at $\varphi = 5.25$. To implement the reverse thermodynamic cycle, it is necessary to expend work on the compressor drive. The compressor is driven by

an electric motor. The main task in this case is the selection of an electric motor with the smallest power to ensure the economical operation of a thermal refrigeration unit.

To ensure the circulation of freon R12 with a mass flow rate of $M = 0.1$ kg/s, a piston compressor with a 2.8 kW drive is required. To analyze the possible use of a stall thermal refrigeration unit the compressor for a throttling cycle was calculated, results are summarized in the Table 2.

Table 1. State parameters of a cycle of a thermal refrigeration unit

Point number	Working fluid parameters				
	$t_i, ^\circ\text{C}$	p_i, MPa	$v_i, \text{m}^3/\text{kg}$	$h_i, \text{kJ/kg}$	$s_i, \text{kJ}/(\text{kg} \cdot \text{K})$
1	-30	0.1	0.149	559	4.77
2	45	0.75	0.025	596	4.77
3	30	0.75	0.025	587	4.75
4	30	0.75	0.0025	449	4.28
5	20	0.58	0.0025	440	4.25
6	-30	0.1	0.05	440	4.29

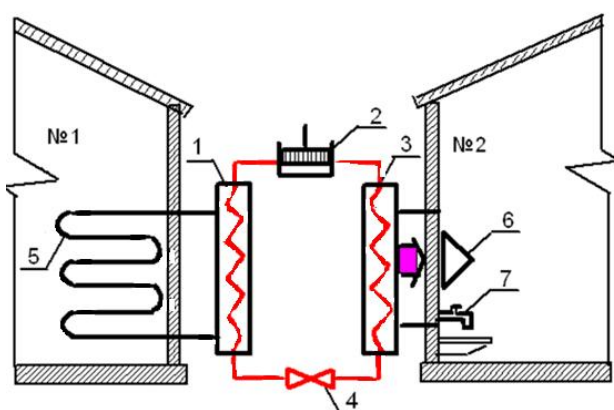


Fig. 7. Layout of a house with a thermal refrigeration unit and an animal stall: 1 - an evaporator; 2 - a compressor; 3 - a condenser; 4 - a throttle; 5 - a primary heat exchanger; 6 - a supply grille for supplying heated air to the room; 7 - a hot water mixer.

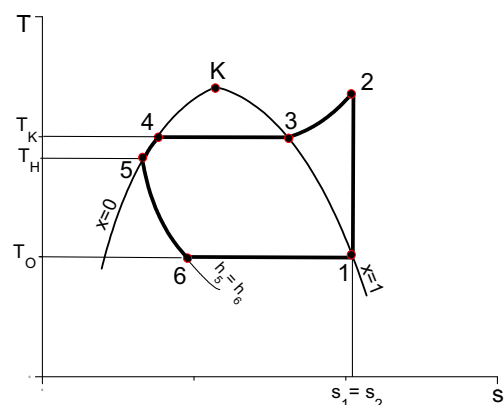


Fig. 8. Operation cycle of a thermal refrigeration unit in thermal Ts - diagram for difluoro-dichloro-methane (freon R12)

Table 2. Compressor characteristics of a thermal refrigeration unit

No.	Throttled cycle characteristics	Values	No.	Throttled cycle characteristics	Values
1	$G, \text{kg/h}$	360	8	N'_a, kW	5.46
2	$V_D, \text{m}^3/\text{h}$	53.64	9	η	0.725
3	G'	7.5	10	N'_{ib}, kW	7.53
4	λ_i	0.66	11	N_{fr}, kW	2.45
5	λ_W	0.8	12	N_e, kW	9.98
6	λ	0.528	13	$q_v, \text{kW}/\text{m}^3$	798.65
7	$V_h, \text{m}^3/\text{h}$	101.59	14	K_e	1.19

2 Results and discussions

For the experimental power plant No. 1, which consists of an aluminum corrugated pipeline with a diameter of $d = 0.08$ m and a length of $l = 10$ m, which is placed on the roof of a building to receive the energy of solar rays, a centrifugal fan and an accumulator, a design calculation was carried out based on algebraic equations. It was assumed that the temperature of humid air at the inlet to the pipeline was $t_{f1} = 17$ °C, and the temperature of humid air at the outlet of the pipeline varied in the range of $t_{f2} = 39 \dots 41$ °C.

According to the accepted value of the velocity in the pipeline, it was found that the volumetric flow rate per second varied in the range of $L = 0.0417 \dots 0.045 \text{ m}^3/\text{s}$.

The influence of the volume flow (velocity) of air moving through the pipeline on the efficiency of a stationary technical solar system was studied. The dependence of the efficiency of a stationary technical solar system on the volume flow (velocity) of air is shown in fig. 9. An analysis of the presented graph allows us to establish that with an increase in the volume flow (velocity) of air, the efficiency of a stationary technical solar system increases. This is due to the fact that with an increase in the coolant velocity, the heat transfer coefficient of radiative-convective heat transfer increases and the intensity of heat and mass transfer processes increases.

For experimental power plant No. 2, which consists of a water intake device, a pressure hose, which is a polyethylene pipe with a diameter of $d = 0.025 \text{ m}$ and a length of $l = 5 \text{ m}$, a hydraulic turbine and an electric current generator, a design calculation was carried out based on algebraic equations.

It was assumed that water moves along the pressure hose with a volumetric flow rate, which varies in the range of $Q = 0.01 \dots 0.03 \text{ m}^3/\text{s}$. The available water head is assumed to be unchanged at $H = 3 \text{ m}$, the efficiency of the turbine is $\eta_{\text{turb}} = 0.55 \dots 0.95$ and the efficiency of the generator is $\eta_{\text{gen}} = 0.96 \dots 0.97$. A small hydroelectric power station is operated for 6 months a year due to the freezing of the reservoir in the autumn-winter period, that is, the time is 4320 h. The influence of the volumetric flow rate of water Q supplied to a small hydroelectric power station on the amount of electricity generated by the generator was studied.

The dependence of the volume of electricity E generated by the generator on the volumetric flow rate of water Q is shown in fig. 10.

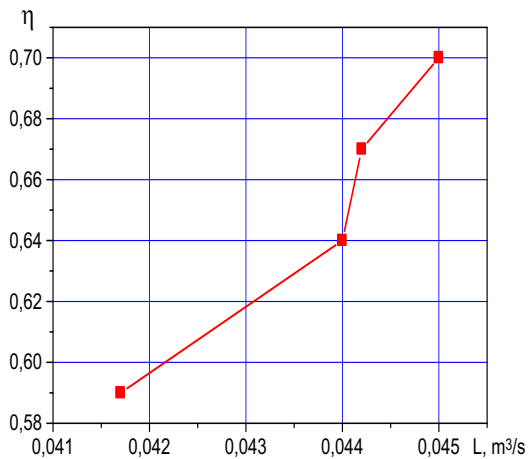


Fig. 9. Efficiency of a stationary technical solar system versus the volume flow (velocity) of air

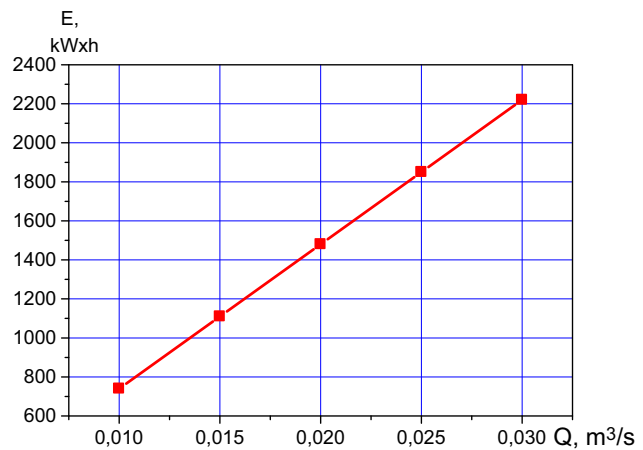


Fig. 10. Volume of electricity generated by the generator versus the volumetric flow rate of water

An analysis of the presented graph allows us to establish that with an increase in the volumetric flow of water entering the small hydroelectric power station, the generation of electric energy by the generator will increase. For the experimental power plant No. 3, consisting of an evaporator located in the animal stall, a primary heat exchanger, a condenser located in a residential building, a compressor and a throttle, a design calculation was carried out based on algebraic equations. It was accepted that the variation range in the volumetric flow rate of R12 freon circulating in the thermal refrigeration unit is $M = 0.1 \dots 0.3 \text{ kg/s}$. Using the thermal Ts -diagram for freon R12, the thermodynamic parameters of the state at the characteristic points of the cycle of the thermal refrigeration unit are determined. It was found that the total cooling capacity varied in the range of $Q_0 = 11.9 \dots 35.7 \text{ kW}$, and the specific work of the cycle remained unchanged at $l_c = 28 \text{ kJ/kg}$. The theoretical power of the compressor drive of the thermal refrigerating unit varied in the range of $N = 2.8 \dots 8.4 \text{ kW}$. It is established that the cooling coefficient is $\varepsilon = 4.25$, and the heating coefficient is $\varphi = 5.25$.

The effect of the volumetric flow rate of R12 freon circulating in a thermal refrigeration unit on the compressor drive power of a thermal refrigeration unit was studied. The dependence of the compressor drive power on the volume flow rate per second is shown in fig. 11. An analysis of the presented graph allows us to establish that with an increase in the volumetric second flow rate of freon R12, the power to drive the compressor increases. To ensure the circulation of freon R12 in a thermal refrigeration unit with a mass flow rate of $M = 0.1 \text{ kg/s}$, it is most economical to use a piston compressor with a 2.8 kW drive, since the cost of electrical energy in this case will be minimal.

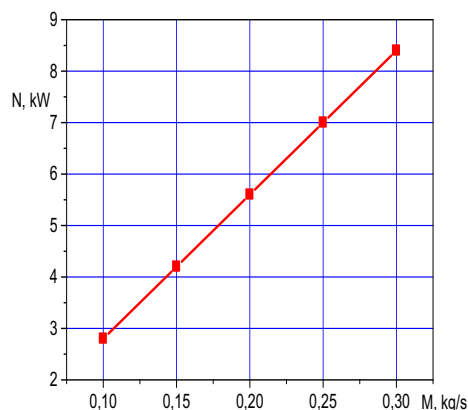


Fig. 11. The compressor drive power on the volume flow rate per second.

Conclusion

1. For the power plant No. 1, using the proposed research method, the variation ranges in the main operating parameters were determined, namely, the volumetric flow rate of the cold coolant is $L = 0.0417 \dots 0.045 \text{ m}^3/\text{s}$, the mass flow rate of air is $G = 0.05 \dots 0.054$. It is recommended to operate a stationary technical solar system at these parameters in order to obtain a coolant temperature at the pipeline outlet of $t_{f2} = 39 \dots 41 \text{ }^\circ\text{C}$.

2. The temperature range for the air obtained at the outlet of the pipeline is quite sufficient to ensure the operation of the engineering system that compensates for heat losses in the building.

3. The variation range of the efficiency of a stationary technical solar system for given operating conditions was determined to be $\eta = 0.59 \dots 0.7$.

4. The temperature of the air at the outlet of the pipeline can be maintained around the clock by using an accumulator (water, granite, pebbles) during those periods of time when there is no solar radiation (at night or in cold weather).

5. The design calculation of the power plant made it possible to establish the operating ranges for changing the main operating parameters. When conducting full-scale experiments using experimental power plant No. 1, it is possible to expand the program of experiments by organizing a developed discretely rough outer surface of an aluminum corrugated pipeline using rings that must be installed on it at the same distance from each other. Periodic destruction of the boundary layer and turbulence of the flow in the region between the ridges is an additional way to increase the heat transfer coefficient, which can be used to increase the efficiency of the power plant No. 1.

6. For the power plant No. 2, using the proposed research method, the variation ranges in the main operating parameters of a small hydroelectric power station were determined, at which it is recommended to operate the power plant: the volumetric second flow rate varied in the range of $Q = 0.01 \dots 0.03 \text{ m}^3/\text{s}$, the set power varied in the range of $N_{\max} = 171.3 \dots 513.9 \text{ W}$, the amount of electricity generated by a transportable hydropower plant for $t = 4320 \text{ h}$ varied in the range of $E = 740 \dots 2220 \text{ kW}\cdot\text{h}$.

7. A direct relationship was established between the volumetric flow of water entering a small hydroelectric power station and the generation of electrical energy by a generator.

8. The main advantages of a small hydropower plant are mobility, relatively low cost and ease of maintenance. In this regard, if necessary, the electric current generator can be upgraded into a power unit for converting hydraulic energy into mechanical energy, or this power plant can be used to supply water to remote consumers.

9. For the plant No. 3, using the proposed research method, the thermodynamic parameters of the state were determined at characteristic points of the cycle of the thermal refrigeration plant. It was found that the total cooling capacity varied in the range $Q_0 = 11.9 \dots 35.7 \text{ kW}$, the specific work of the cycle remained unchanged $l_c = 28 \text{ kJ/kg}$. The cooling coefficient $\varepsilon = 4.25$, and the heating coefficient $\phi = 5.25$.

10. A direct relationship was established between the change in the volumetric second flow rate of freon R12 and the power to drive the compressor.

11. It was found that the change in the volumetric second flow of freon R12 does not affect the values of the cooling and heating coefficients.

12. The values of the cooling and heating coefficients depend only on the nature of the working fluid circulating in the thermal refrigeration plant.

13. The main advantage of a thermal refrigeration machine with an animal stall is that the use of physiological heat of animals as low-grade heat saves significant costs during construction and operation compared to power plants that use geothermal heat from the earth and the heat of rivers, lakes and rivers as a low-temperature source.

14. The results of the calculation showed that a thermal refrigeration unit with a 10 kW drive with a heating coefficient of $\varphi = 5.25$ can provide 52.5 kW of heat. If the animal stall contains 300 pigs or cows, it is recommended to operate the thermal refrigeration unit without an additional energy source.

15. A stall thermal refrigeration plant does not generate thermal energy, but "pumps" it from the environment. At the same time, less electrical energy is spent on the "pumping" of heat than on the generation of thermal energy. Thus, 1 kW of electrical energy gives 5.25 kW of thermal energy.

16. It has been established that for each paid 1 kW of electrical energy, we will receive 4.25 kW of free thermal energy.

REFERENCES

- 1 Berkovsky B.M. *Renewable energy sources at the service of man*, Moscow, Science Publ. 1987, 125 p. [in Russian]
- 2 Deliagin G.I. *Heat generating installations*, Moscow, Stroyizdat Publ. 1986, 559 p. [in Russian]
- 3 Building regulations 2.01.01 – 82. Building climatology and geophysics, Moscow. 1996, 140 p. [in Russian]
- 4 Troiskiy A.A. *Technical progress of the energy USSR*, Moscow, Energoatomizdat Publ., 1986. – 221 p.
- 5 Kabeel A.E., Khalil A., Elsayed S.S., Alatyar A.M. Modified mathematical model for evaluating the performance of water-in-glass evacuated tube solar collector considering tube shading effect. *Energy*, 2015, Vol. 32, pp. 24-34. doi: 10.1016/j.energy.2015.06.072
- 6 Bandara A.C., et al. Assessment of the possibility of unglazed transpired type solar collector to be used for drying purposes: a comparative assessment of efficiency of unglazed transpired type solar collector with glazed type solar collector. *Procedia Engineering*, 2018, Vol. 212, pp. 1295-1302. doi: 10.1016/j.proeng.2018.01.167
- 7 Hassan Fathabadi. Novel low-cost parabolic trough solar collector with TPCT heat pipe and solar tracker: Performance and comparing with commercial flat-plate and evacuated tube solar collectors. *Solar Energy*, 2020, Vol. 195, pp. 210-222. doi: 10.1016/j.solener.2019.11.057
- 8 Ifeoluwa Wole-osho, Eric C. Okonkwo, Serkan Abbasoglu, Doga Kavaz. Nanofluids in Solar Thermal Collectors: Review and Limitations. *International Journal of Thermophysics*, 2020, Vol. 41, Article number: 157
- 9 Guangming Chen, Doroshenko A., Paul Koltun, et al. Comparative field experimental investigations of different flat plate solar collectors. *Solar Energy*, 2015, Vol. 115, pp. 577-588. doi: 10.1016/j.solener.
- 10 Sankelo P., Ahmed K., Mikola A., Kurnitski J. Renovation Results of Finnish Single-Family Renovation Subsidies: Oil Boiler Replacement with Heat Pumps. *Energies*, 2022, Vol. 15(20):7620. doi: 10.3390/en15207620
- 11 Gai L., Varbanov P.S., Walmsley T.G.; Klemesš J.J. Critical Analysis of Process Integration Options for Joule-Cycle and Conventional Heat Pumps. *Energies*, 2020, Vol. 13, 635. doi: 10.3390/en13030635
- 12 Jiatong Jiang, Bin Hu, Tianshu Ge, R.Z. Wang Comprehensive selection and assessment methodology of compression heat pump system. *Energy*, 2022, Vol. 241, Article 122831. doi: 10.1016/j.energy.2021.122831
- 13 Zhimin Tan, Xiao Feng, Yufei Wang Performance comparison of different heat pumps in low-temperature waste heat recovery. *Renewable and Sustainable Energy Reviews*, 2021, Vol. 152: 111634. doi: 10.1016/j.rser.2021.111634
- 14 Danilov R.D. Heat pumping unit for milk cooling. *Refrigeration technology*, 1979, No. 11, pp. 27-29.
- 15 Kokorin O.Ja. Energy-saving microclimate system for livestock premises. *Mechanization and electrification of agriculture*, 1986, No. 6, pp. 37-39.
- 16 Demin A.V. Improving the efficiency of use of fuel and energy resources in animal husbandry and fodder production, *Collection of scientific papers All-Russian Research Institute of Agricultural Economics VIESKH*, Moscow, VIESKH, 1982, pp. 45-49.
- 17 Mustafa Balat. Hydropower Systems and Hydropower Potential in the European Union Countries. *Energy Sources, Part A: Recovery, Utilization, and Environmental Effects*. 2006, Vol. 28. pp. 965-978. doi: 10.1080/00908310600718833
- 18 Weihua Zhao, et al. Influence of Different Types of Small Hydropower Stations on Macroinvertebrate Communities in the Changjiang River Basin, China. *Water*, 2019, Vol. 11(9), 1892. doi: 10.3390/w11091892
- 19 Panovski S., Janevska G. Hydroenergy in Macedonia. *Biomass Energy Europe*, 2010. No. 4. pp. 140–154.
- 20 Martins N.M.C., Fontes P., Covas D. Hydroenergy Harvesting Assessment: The Case Study of Alviela River. *Water*, 2021, No. 13. Article No.1764.

ON ASSESSING THE EFFECTIVENESS OF HYBRID SOLAR COLLECTORS SCHEME IN IRAQ'S ENVIRONMENT

Jaddoa, Ameer A.*, Mahdi Mahmoud M., Hamad Karema A.

Electromechanical Engineering Department, University of Technology, Baghdad, Iraq
ameer.a.jaddoa@uotechnology.edu.iq

An evaluation of the performance of the Iraqi environments in terms of electrical, thermal and exergy efficiency is introduced in this study. The research is carried out in May 2022, in the Baghdad metropolis. The extraction process of heat from the photovoltaic units which arises from the coolant liquid mass flow rate deem as an essential point. The experimental studies were implemented by absorbing heat energy behind from the photovoltaic cell's surface in insulated conditions and using a cooled water unit. The results indicated that at a mass inflow rate of 0.2 kg/sec, the maximum average total efficiency of the system was recorded 22%. As a result, it is advised that to reduce the payback interval, it is possible to design efficient solar photovoltaic-thermal systems to promote the whole system's efficiency and lower the payback interval.

Keywords: Solar Energy, Energy and Exergy, Hybrid Solar PV/T Collector.

Introduction

Renewable energy become an indispensable resource due to several challenges represented by increasing energy cost production, the population rising comes with increases in the power demand notably the limitation of fossil fuel resources. All of these reasons motivated the researchers to search on finding for alternating energy resources. Renewable energy is characterized by low cost. One of the outstanding sustainable energy resources is solar power. In this vein, it can be classified into two kinds of resources thermal and photovoltaic energies in other words conversion of solar power into thermal and electric energy, respectively. Generally, in energy applications, these systems PV and thermal are applied separately; however, it can adopt both simultaneously. It is noteworthy that such schemes (PV/T) have an energy efficiency greater than that of PV and solar thermal techniques as endorsed in the literature by several scholars. In this regard, the authors in [1] presented a new technique called BIPV/T aiming to drop the power consumption in the facilities. In accordance with the results, the authors claimed that an efficiency of 7.6% could be administered in terms of passive cooling in the summer, while about 12.5% was provided in winter. Previous studies have reported that to improve a PV system efficiency cooled with nano-fluids employing an adaptation technique called neuro-fuzzy inference system (ANFIS), the factors of solar irradiation, the nano-fluid inflow rate, and various parameters of nano-fluids were investigated [2]. More recent attention has focused on a BIPV/T approach comprising the phase alternating of material or so-called phase change material (PCM). Such a study was conducted based in Tehran, the capital of Iran. The research reported that the optimal thickness of PCM was measured to be 77.2 mm. Much of the available literature on the payback period deals with the question of period reduction. Renewable energy resources can reduce the annually emitted of CO₂ by 3.3 years of energy payback period. Besides that, a controlling load technique could apply by load OFF-ON according to energy demand along with energy storage unit aiming to expense operation reduction. On the other hand, the micro-grid could control the energy between the power network and the upstream grid, wherein several approaches were proposed to model energy management toward declining the expense operation [4-7]. More recent attention has focused on the light into electricity conversion unit combined with the airflow as a coolant system [8]. In addition to geometrical design, the work emphasised cell temperature, solar intensity, and mass inflow rate (MFR). The primary object was to enhance energy production. Various parameters were studied to investigate the hybrid schemes behavior based on different approaches applied in the simulation processes [9,10]. In this context, the author in [11] used Matlab simulation to validate the water-cooled unit with the outdoor conditions model. In transient conditions, the system PV/T provided an acceptable performance regarding the outlet temperature data. According to the

results, the system response was quick to the change in wind speed. The RMSD for outlet temperature and P_{el} were 2.07%, and 4.15%, respectively as recorded in May.

Previous studies in [12] have reported introducing a novel method of a water-cooled PV/T strategy composed of a Toddler layer mounted with water tubes organized in parallel form. In conclusion, the research revealed that thermal efficiency dropped to 40% out of 70% upon the increase in wind speed. Based on a 3-dimensional prototype applied to a polymer (3-hexylthiophene), the authors in [13] introduced an analytical module for a hybrid solar collector utilizing Matlab software and Comsol v.5.4. In comparison between polymer-based PV/T prototype monocrystalline-silicon-based PV/T collector units it is found that the first module has 6.57% lower and 85.77% higher for electrical efficiency and thermal efficiency, respectively. In this context, for PV/T systems, a development was introduced based on physical quasi-Steady thermal and transient thermal. The results appeared that both modules achieved identical results. Further, the systems were greatly influenced by the temperature.

The scholars considered that the TRNSYS tool might be the most suitable instrument for the simulation of energy systems. The reason is that it has the capability to simulate transient and dynamic processes [15,16]. For example, Klein [17] has formed a PV/T design in the TRNSYS software called type 50. In the literature, several types were exhibited to illustrate were introduced on how the product transmissivity τ – absorptivity α was applied besides the calculation of thermal losses [18-22]. Also, these studies have emphasized the thermal behavior of the PV/T unit, on the other side; researchers have not treated electrical behavior in much detail. Therefore, this work highlighted the general behavior aiming to increase the electrical-power output of the photo-voltage unit.

1 Experimental Strategy and Mathematical model of PV/T Unit.

The unit contains one identical separated pair of PV solar photovoltaic panels. The highest power at the output is 60W with rated current and voltage 2.61A, and 23V, respectively, and the panel's dimensions of 0.44m². Regarding the design, the first panel is composed of two systems. The first was manufactured so that a film of water ran over its top shell made with no front glass, while the other system was utilized to exploit the generated heat by the panel. On the other hand, the second-panel work as a traditional unit. Figures 1a and b show the system under investigation and showing the water tube comes with a slit at the top of the PV panel, pumping system and the heat exchanger.

The next paragraph shows an illustration of how the system works. The water is distributed in a thin film after being pumped through the slit by a pump machine working with 0.25 HP, the inflow velocity is 1 lit/min. Another tiny tube comes with fins that work as a heat interchanger and consumer of heat acquired by the water and also operates as heat dispersion maintaining the heat degree at a constant level. Note that the water will be at the required temperature upon inflow to the panel surface.

In this work, the load of (8.7 Ω) was adopted aiming to obtain the highest value of power at the output. Next, using an Omega-type millimeter device the current and voltage were recorded with the accuracy of 1 mill ampere and 1 millivolt, respectively. The angle degree of panels is mounted to face the south direction at 45°. At the same slop of panels, the Kimo SL100 solar meter device (use for measuring the irradiance) was mounted at the corner of one of two panels. Additionally, the ambient heat was recorded in the shaded area over a systematic time. Also, to measure the upper/lower heat of the panels, Patch-model thermocouples (k-model) were employed. For more convenience, it used a surface probe to measure the upper side heat degree of the panel. The recorded heat value was 1.5 °C, which was higher than that of the back of the panel.

Thus, was adopted 1.5 °C was a heat value difference between them. Using thermocouples (k type) fixed at the finned tube end, the heat degree of the water prior to moving over the panel and the water heat degree is sticking out of the heat interchanger. Every 10 minutes, the data was collected over the period of 30 days in Baghdad, May 2022 (latitude 33.34° and longitude 44.1°). The next hypotheses were adopted to form the energy balance equation based on each PV/T solar collector element. The first is ignoring the heat capacity of the PV/T collector, and the second, owing to the constrained condition of the procedure, heat stratification in the water of the reservoir was excluded, third, the thermal distribution was considered to be constant over the entire system.

The losses due to the resistance were ignored as it was very small. Also, we used η_0 as an indication of total efficiency as this symbol is communally utilized in the literature upon calculation of the PV/T performance [19].

$$\eta_0 = \eta_t + \eta_e \quad (1)$$

F represents the fin competence, and it takes the formula below

$$F = \frac{\tanh\left(\frac{(W-D)\sqrt{U_L/K\sigma}}{2}\right)}{\frac{(W-D)\sqrt{U_L/K\sigma}}{2}} \quad (4)$$

The general heat-losing parameter (U_L) and thermal competency of the PV/T unit (η_t) take the expression below:

$$U_L = \frac{\eta_c I_c + I_c \alpha \tau}{T_a + T_c} \quad (5)$$

According to the defined variables

$$\eta_c = F_R \tau \alpha - F_R U_L \frac{T_a - T_{fi}}{I(t)} \quad (6)$$

The electric competency relies on the heat degree of the PV unit and the cell heat degree (T_c) is given in the expression below.

$$\eta_e = \eta_h (1 - \beta_o T_h - 25 \beta_o) \quad (7)$$

$$T_c = T_a + \left(\frac{I(t) \tau \alpha}{U_L}\right) \left(\frac{1 - \eta_c}{\tau \alpha}\right) \quad (8)$$

Where the transmission-absorption parameter $\tau \alpha$ and the general HT factor U take the expression below 0.86 and 0.8 W/m²°C, respectively [19].

2 Results and Discussions

This section explains the outcome of these discussions. As it was mentioned earlier, the data were collected in May 2022. Figure 2 presents the variation in solar intensity gathered by the panels' surface. The greater the solar intensity, the higher the heat level, as illustrated in Figure 3.

In Figure 3, red curve shows radiation, blue curve presents cell temperature of PV, and green curve presents cell temperature of PVT. It was noted that the increase in radiation quantity from PV/T and PV units led to increasing the heat degree by 1.2°C and 5.4°C for the photovoltaic/thermal and photovoltaic units, respectively. Furthermore, it was discovered that on May 25, at 12:00, the highest point of the temperature of the photovoltaic module was 65 °C, while it was 32 °C for the photovoltaic/thermal module, and that it then decreased. And the cell temperature has been maintained in the range of 20–30 °C.

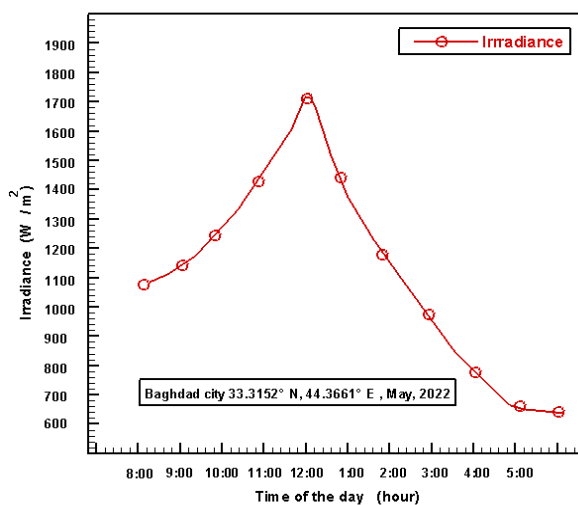


Fig. 2. Variation of irradiance over 24 hours.

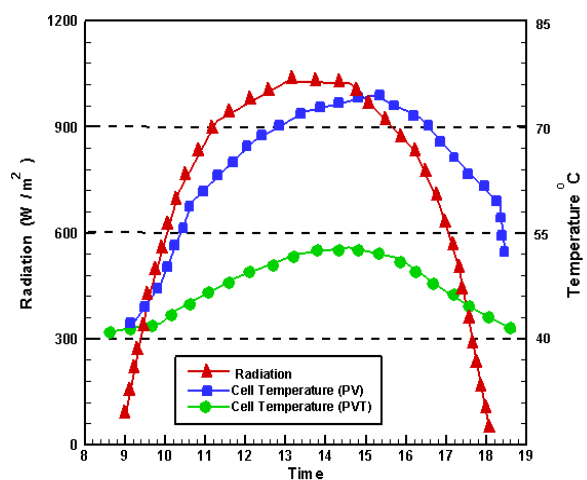


Fig. 3. Solar intensity and cell heat level of PV and PV/T

Furthermore, the results indicated that photovoltaic or thermal systems provided approximately 0.09% of the energy savings for various MFRs. This indicates that such a system has greater efficiency than traditional solar energy modules. In general, several factors can influence PV/T performance. For example, electrical and thermal transformation is influenced by parameters such as MFR, inlet and outlet water heat degrees, solar irradiance, the surrounding temperature, wind acceleration, and system orientation concerning the solar ray. On the other hand, the higher the temperature, the greater the decrease in unit efficiency. For instance, increasing the temperature by 3C led to a 0.2% decrease in efficiency. Even more, the experimental results demonstrated that higher electric conversion occurred at 55 °C and 1700 W/m², as shown in figure 4.

Furthermore, for various inflow rates, the electric efficiency ranges between 7 and 9 per cent. For instance, when the inflow rate is 0.004 kg/sec, the efficiency of the model is between 6 and 8 per cent, as shown in Figure 5. Regarding thermal efficiency, for various inflow rates, the value ranges from 20.67% to 110.67%. For example, the thermal efficiency was 60.67% and the average was 63.43%, while the lowest average efficiency was 50.03% for the MFR of 0.8 kg/sec.

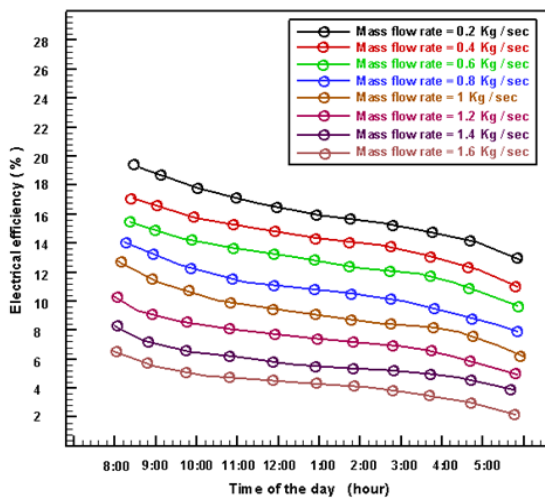


Fig. 4. Differentiation of Electrical Efficiency for different mass inflow rate for PV/T.

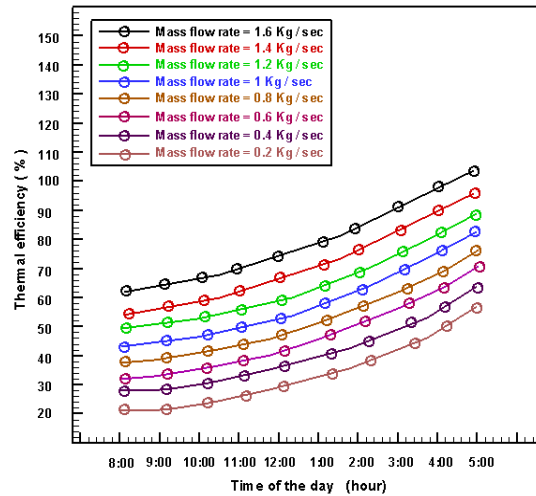


Fig. 5. Differentiation of thermal Efficiency for different mass inflow rate for PV/T

Concerning the entire efficiency, which represents the total electrical and thermal efficiency, Figure 6 depicts the photovoltaic/thermal performance. As can be seen, the range is 60.39% to 80.95% for different inflow velocities. In this context, the highest value exceeded 78.45% for a MFR of 0.8 kg/sec, and the lowest average overall efficiency was seen to be 59.67%.

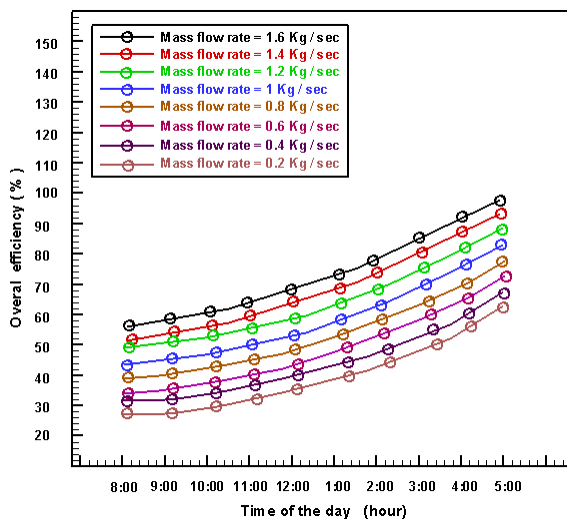


Fig. 6. Differentiation of Overall Efficiency for various mass inflow speeds for PV/T

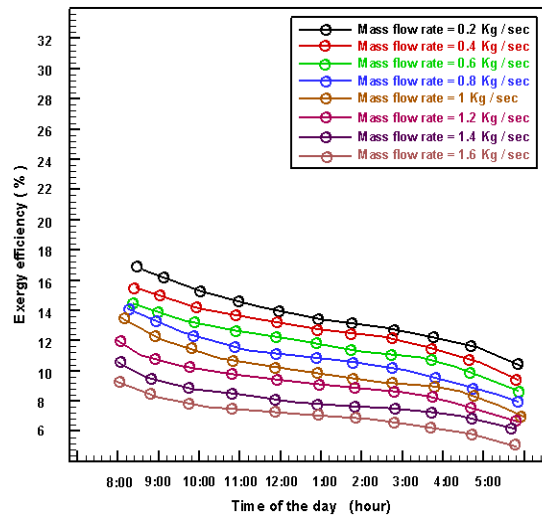


Fig. 7. Differentiation of Exergy Efficiency for various mass inflow speeds for PV/T

The difference in energy competency of photovoltaic and thermal for various MFRs of water. For different MFRs, the energy competency of photovoltaic and thermal systems ranges from 6.34% to 17.65%. The highest exergy efficiency was seen at 11.13% for a MFR of 0.8 kg/sec, as shown in Figure 7.

Figure 8 provides a comparison between different inflow rates in terms of energy-saving savings from solar PV/T. From the figure, it can be observed that the efficiency ranges from 30.35% to 90.45%, with the highest energy-saving efficiency reaching 50.34% for a MFR of 1 kg/sec. Figure 9 depicts the different heat degrees between the photovoltaic/thermal unit's inlet and outlet water temperatures ($T_{fi}-T_{fo}$) and for MFRs ranging from 0.2 kg/s to 1.6 kg/s various solar intensity quantities.

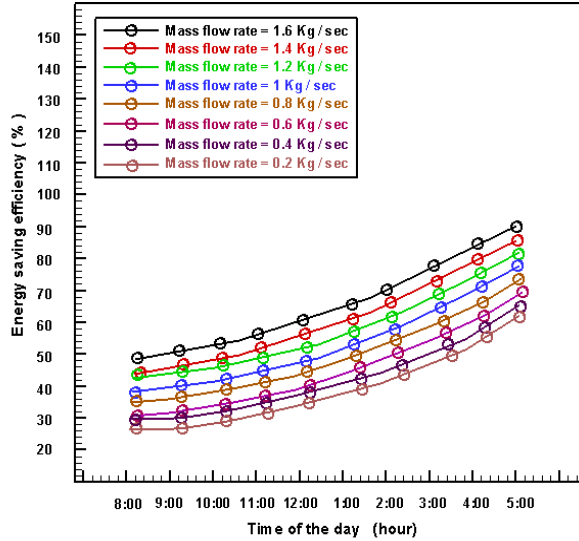


Fig. 8. Differentiation of Energy Saving Efficiency for different mass inflow rates for PV/T.

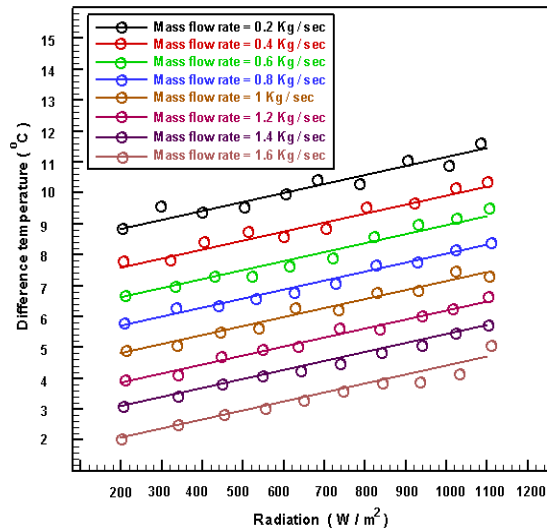


Fig. 9. Temperature variation of PV/T water collector with various inflow rates and irradiance

Further, the change in temperature of solar radiation temperature from 2 °C to 4 °C caused a change in the inlet and outlet temperatures, consequently causing a change in MFRs from 0.2 kg/s to 1.6 kg/s, respectively, at each 100 W/m². As can be observed, the higher the radion intensity, the higher the difference in temperature, and the higher the average inflow rate. Table 1 depicts the relationship between radiation intensity and temperature differences.

It is worth mentioning that the photovoltaic heat degree ranges between 50°C and 66°C, and for photovoltaic/thermal units, ranges between 40°C and 70°C at the solar intensity of 1700 W/m².

Table 1. Thermal competency expression of PV/T collector.

Mass inflow rate (kg/s)	Expression
0.2	$\eta_t = 0.32 - 2.362 \times \Delta T / I_t$
0.4	$\eta_t = 0.42 - 3.652 \times \Delta T / I_t$
0.6	$\eta_t = 0.51 - 4.821 \times \Delta T / I_t$
0.8	$\eta_t = 0.63 - 5.345 \times \Delta T / I_t$
1	$\eta_t = 0.72 - 6.23 \times \Delta T / I_t$
1.2	$\eta_t = 0.81 - 7.341 \times \Delta T / I_t$
1.4	$\eta_t = 0.93 - 8.589 \times \Delta T / I_t$
1.6	$\eta_t = 1.23 - 9.912 \times \Delta T / I_t$

As depicted in Figure 10, the efficiency of these two systems was 10.64% and 18.75%, respectively. In this vein, it can be concluded that PV/T efficiency outperforms the PV unit by 23.36%. The total electric product of both modules was 1300 W/m² and 1700 W/m², respectively. On the other hand, the entire solar intensity was 7450 W/m² on the test day. Figure 11 presents the whole electric efficiency produced by these two modules, which was 18.2% and 12.5%, respectively. In Figure 11, red curve shows electricity generated (PVT), blue curve presents radiation, and green curve presents electricity generated (PV). In comparison, 6% of energy production by PV/T is higher than that by PV module. The same scenario has been recorded at

13:00 for both modules. Finally, good agreement was found between the theoretical and experimental results; the differentiation could only be attributed to the losses in the cable and device errors.

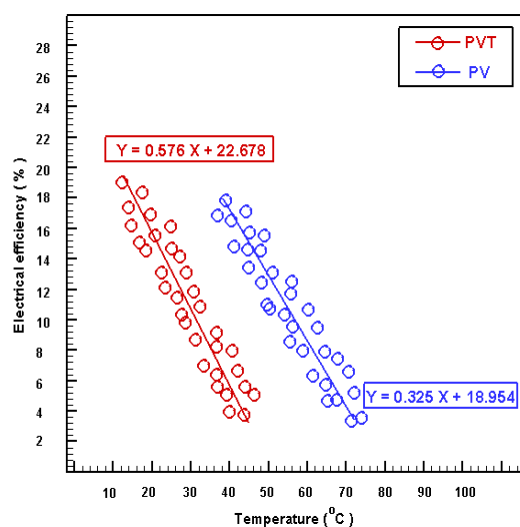


Fig.10. Differentiation of electrical competency against cell heat point for PV and PV/T at 1700 W/m² solar radiation hypothesis scenario.

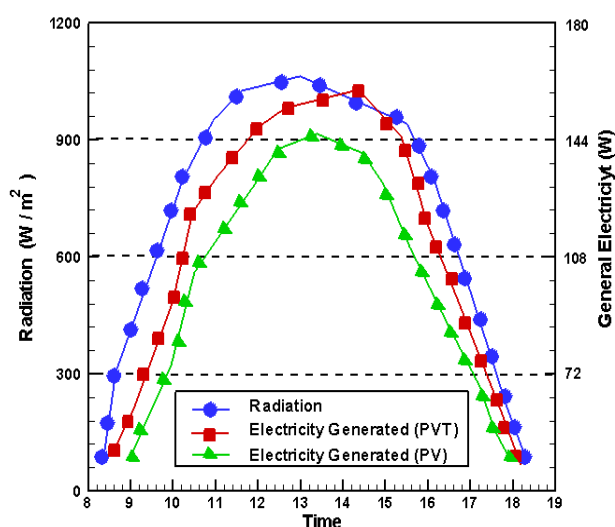


Fig.11. Electric production by PV and PV/T modules.

Conclusion

The most obvious finding to emerge from this study is that the module PV/T provides better-performing PV units, where the highest efficiency of the electrical system was 18.2%. This is demonstrated by the whole efficiency that arose from the PV/T system: 50–80% for the MFR of 0.2 kg/s with an efficiency of 22%. Also, with an MFR of 1 kg/s, the exergy efficiency ranges from 8% to 22%. The highest average exergy efficiency measured for the MFR of 0.8 kg/s was 10.64%. Concerning thermal performance, it was found that the highest value of thermal efficiency was 60%. The average efficiency increases as the MFR increases compared to the PV unit. Using the active cooling method, the PV efficiency is 12.5 per cent; thus, it provides an indication of promising results at 70 °C and the MFR of 0.2 kg/s. Both modules have similar behaviour in terms of electric generation. Finally, the amount of PV/T was 11300 W/m² compared to 1700 W/m² for the PV module, and the whole solar intensity was 7450 W/m² per 24 hours on May 25, 2022.

REFERENCES

- Xu, L., Luo K., Ji J., Yu B., Li Z., Huang S. Study of a hybrid BIPV/T solar wall system. *Energy*, 2020, Vol.193, pp.116578. doi:10.1016/j.energy.2019.116578
- Cao Y., Kamrani E., Mirzaei S., Khandakar A., Vaferi B. Electrical efficiency of the photovoltaic/thermal collectors cooled by nanofluids: Machine learning simulation and optimization by evolutionary algorithm. *Energy Rep.*, 2022, Vol.8, pp. 24–36. doi:10.1016/j.energy.2019.116578
- Sohani, A., Dehnavi, A., Sayyaadi, H., Hoseinzadeh, S., Goodarzi, E., Garcia, D.A., Groppi, D. The real-time dynamic multiobjective optimization of a building integrated photovoltaic thermal (BIPV/T) system enhanced by phase change materials. *J. Energy Storage*, 2022, Vol.46, 103777. doi:10.1016/j.solener.2022.01.036
- Jabber, Kadhim M., AL-Saadi, Mohammed K., Jaddoa Ameer A., Economic Operation of Smart Distribution Microgrid, *AIP Conference Proceedings*, 2022, 2415, 020027. doi:10.1063/5.0092301
- Mahdi, Mahmoud M., Jaddoa, Ameer A., Al Ezzi Amged. Impact of pumping head on a solar pumping system with an optimal pv array configuration: solar water heater application, *Journal of Engineering Science and Technology*, 2022, Vol. 17, No. 3, pp. 2035 – 2048. doi:10.1007/978-981-15-2780-7_78
- Mahdi, Mahmoud M., Jaddoa, Ameer A.. An experimental optimization study of a photovoltaic solar pumping system used for solar domestic hot water system under iraqi climate, *Journal of Thermal Engineering*, 2021, Vol. 7, No. 2, Special Is. 13, pp. 162-173. doi: 10.18186/thermal.871296.
- Jabber, Kadhim M., AL-Saadi, Mohammed K., Jaddoa Ameer A., Economic Operation of Low Voltage Smart Micro-grid with Integration of Renewable Energy, *Engineering and Technology Journal*, 2022. Vol.40, No.07. doi:10.30684/etj.2022.131063.1000

- 8 Sattar M., Rehman A. Ahmad N., Mohammad A., Al Ahmadi A.A., Ullah N. Performance Analysis and Optimization of a Cooling System for Hybrid Solar Panels Based on Climatic Conditions of Islamabad, Pakistan. *Energies*, 2022, Vol. 15, 6278. doi:10.3390/en15176278
- 9 Hengel F., Heschl C., Inschlag F., Klanatsky P. System efficiency of pvt collector-driven heat pumps *Int. J. Thermofluids.*, 2020, pp. 5–6, Article 100034, doi: [10.1016/j.ijft.2020.100034](https://doi.org/10.1016/j.ijft.2020.100034)
- 10 Alshibil A.M.A., Víg P., Farkas I. Performance evaluation of a hybrid solar collector in two different climates *Eur. J. Energy Res.*, 2021, pp. 17-20. doi:10.24018/ejenergy.2021.1.2.11
- 11 Sakellariou, Axaopoulos, E.P. An experimentally validated, transient model for sheet and tube PVT collector *Sol. Energy*, 2018, Vol.174 pp. 709-718, doi:10.1016/j.solener.2018.09.058
- 12 Ul Abidin, Rachid Z.A., Bond graph modeling of a water-based photovoltaic thermal (PV/T) collector *Sol. Energy*, 2021, Vol. 220, pp. 571-577. doi:10.1016/j.solener.2021.03.028
- 13 Haloui H., Touafek K., Khelifa A. Modeling of a hybrid thermal photovoltaic (PVT) collector based on thin film organic solar cells *Electr. Power Syst. Res.*, 210 2022, Article 108131. doi:10.1016/j.epsr.2022.108131
- 14 Chaibi Y., El Rhafiki T., Simón-Allué R., I. Guedea, Luaces C., Charro Gajate O., Kousksou T., Zeraoui Y. Physical models for the design of photovoltaic/thermal collector systems. *Sol. Energy*, 2021, Vol. 226, pp. 134-146. doi:10.1016/j.solener.2021.08.048
- 15 Rashad M., Żabnieńska-Góra A., Norman L., Jouhara H., Analysis of energy demand in a residential building using TRNSYS. *Energy*, 2022, Vol. 254, 124357. doi:10.1016/j.energy.2022.124357
- 16 Davidsson H., Perers B., Karlsson B., System analysis of a multifunctional PV/T hybrid solar window *Sol. Energy*, 2012, Vol.86 , pp. 903-910. doi:10.1016/j.solener.2011.12.020
- 17 Klein S.A. Calculation of flat-plate collector loss coefficients *Sol. Energy*, 1975, Vol.17, pp. 79-80. doi:10.1016/0038-092X(75)90020-1
- 18 Klein SA, et al. TRNSYS reference manual, standard component library overview in: TRNSYS 16, a TRaNsient Syst. Simul. Progr., *University of Wisconsin*, Madison, 2006, pp. 3-93. <http://sel.me.wisc.edu/trnsys>
- 19 Ozgoren M., M. Aksoy H., Bakir C., Dogan S. Experimental Performance Investigation of Photovoltaic/Thermal (PV-T) System. *Conferences 1106*, 2013. 45, published by EDP Sciences. doi:10.1051/epjconf/20134501106
- 20 Omarova Zh., et al., Performance Simulation of Eco-Friendly Solar Cells Based On $\text{CH}_3\text{nh}_3\text{sn}_3$. *Eurasian Physical Technical Journal*, 2022, Vol.19, No. 2(40). doi: 10.31489/2022No2/58-64
- 21 Aimukhanov A.K., et al., Influence of Phthalocyanine Nanostructures on Optical and Photovoltaic Characteristics of a Polymer Solar Cell. *Eurasian Physical Technical Journal*, 2022, Vol.19, No.1 (39), doi:10.31489/2022No1/26-33
- 22 Syzdykov A.B., et al. Algorithm For Finding Maximum Power Point Tracking when shadowing or failure of solar panel photo cells on satellites using low orbits. *Eurasian Physical Technical Journal*, 2023, Vol.20, No.1 (43), doi:10.31489/2023No1/65-72.

Nomenclature

A_m	Area of PV module	U_L	Overall heat loss coefficient ($\text{W/m}^2 \text{ }^\circ\text{C}$)
C_f	Fluid specific heat ($\text{kcal/kg }^\circ\text{C}$)	W	Width of the tube spacing (m)
D	Diameter of copper tube (m)	α	Absorptivity of glass
F	Fin efficiency factor	β_0	PV temperature coefficient ($^\circ\text{C}^{-1}$)
F'	Flat plate collector efficiency factor	δ	Plate thickness (m)
F_R	Flow rate factor	ΔT	Temperature difference ($^\circ\text{C}$)
\dot{m}	Fluid flow rate (kg/m^3)	η_t	Thermal efficiency of PV/T collector
T_{fi}	Fluid inlet temperature ($^\circ\text{C}$)	η_0	Overall efficiency of PV/T collector
T_{fo}	Fluid outlet temperature ($^\circ\text{C}$)	η_e	Electrical efficiency
T_c	PV cell temperature ($^\circ\text{C}$)	η_c	PV cell efficiency
T_a	Ambient temperature ($^\circ\text{C}$)	τ	Transmissivity of glass

DOI: 10.31489/2022NO2/65-69
UDC 620.92; 533.697.6; 004.94

INVESTIGATION OF AERODYNAMIC THRUST FORCE OF THE WIND POWER PLANT WITH COMBINED BLADES

Tleubergenova A.Zh.¹, Dyusembaeva A.N.¹, Tanasheva N.K.¹, Minkov L.L.²,
Mukhamedrakhim A.R.¹

¹E.A. Buketov Karaganda University, Karaganda, Kazakhstan, shymkent.a7@mail.ru

²National Research Tomsk State University, Tomsk, Russia

In this article, a wind power plant with a horizontal axis of rotation operating under conditions of variable wind speeds is considered. For this purpose, a mock-up of a wind power plant with rotating combined blades was made. During the experiments, the angle of the fixed blade relative to the cylinder changed from 0° to 60°, in increments of 15°. The air flow rate varied, from 3 to 12 m/s. The analysis of the results of the experiment on the change of the rotation frequency from the air flow velocity of the wind power plant is carried out. When changing the position of the fixed blade (0°, 15°, 30°, 45°, 60°) the value of the thrust force changes relative to the air flow in direct proportion. As the air flow velocity increases, the rotation frequency of the wind wheel increases linearly. It was found that when the fixed blade was positioned at an angle of 60 degrees, with a maximum air flow velocity of 12 m/s, the thrust force reached 2.06 N. Due to the combined use of two lifting forces, such as a cylinder and a fixed blade, increased thrust values are observed. The results obtained are useful when creating prototypes of a wind power plant with combined blades.

Keywords: wind power plant, flow velocity, combined blade, wind tunnel T-1-M, thrust force, rotational speed.

Introduction

Central Asia belongs to the regions where there are favorable conditions for the use of wind energy. The republics located in this region have huge, almost inexhaustible reserves of wind energy [1]. Wind power industry of Kazakhstan continues its dynamic development. Our country, following the global trend, is systematically working to increase the number of renewable energy power plants. Therefore, it faces the same challenges as other types of power plants using alternative energy sources. First of all, it is currency risk, stabilization of legislation, development of local content and small generation [2].

The use of wind turbines for electricity generation is the most efficient way to utilize wind energy. The efficiency of converting mechanical energy into electrical energy in an electric generator is usually up to 95%, and the loss of electrical energy during its transmission does not exceed 10%. The requirements for the frequency and voltage of the generated electricity depend on the characteristics of consumers of this energy [3]. The use of installations and devices using renewable and other new energy sources is now becoming especially important due to the problems caused by the so-called energy crisis, the shortage of hydrocarbon fuel, the tasks of saving it and environmental degradation [1-3].

Wind turbines are divided into installations with a horizontal or vertical axis of rotation. It is necessary to find out which of these wind turbines are most adapted to work in the conditions of the wind regime of the Republic of Kazakhstan. It should be noted that in most of the leading countries in the field of wind energy, wind turbines with a horizontal axis of rotation are used, which, as a rule, are a tall tower with long thin blades and a large diameter of the wind turbine. The blades have a flat convex or other similar profile, and the lifting force effect (the pressure difference on the opposite surfaces of the blades) is used as the basis of their operation [4]. The main problem that one has to face when using wind energy for energy supply to consumers is the variability of wind speed [5]. In recent years, there has been a growing demand for the development of renewable energy sources, the use of which minimizes environmental problems. Among alternative energy sources, wind generators are one of the most common. [6].

Of particular interest are rotating cylindrical combined wind turbines that operate efficiently at low wind speeds [7]. To improve the efficiency of such a wind turbine, it is necessary to study the aerodynamic characteristics of its elements, i.e., the system of transverse rotating cylinders, ways of optimization.

Accordingly, this work is relevant from a scientific point of view, in practical application. Previously, reviews of scientific research on the development and creation of wind turbines with horizontal and vertical axes of rotation were studied in detail. Works of domestic scientists were studied. A diffuser-type wind power plant is known, developed by the Doctor of Technical Sciences, professor Baishagirov H.Zh. [8].

At the Institute of Mining named after Kunaev D.A., under the leadership of Buktukov N.S. a promising design of the «Buktukov WPP» was developed [9], in which the change in the area of the swept surface occurs not by shifting the half-cylinders, but by turning, which allows a significant increase in power (many other domestic studies on the development of wind turbines were also studied in detail). As a prototype of the aerodynamic element that creates the Magnus effect on the blades of a wind turbine, the aerodynamic element described in [10] was adopted. The disadvantage of this wind turbine is the huge consumption of electricity for the operation of the drive. A distinctive feature in this work from the previous ones is the mutual combination of two different blades (rotating cylinders and fixed blades), which ensures high aerodynamic quality of the wind turbine.

Comparisons were made with experimental data with other authors of papers that describe studies with wind turbines with a horizontal axis of rotation. This wind turbine is unique compared to others, since the rotation of the wind wheel and the generation of wind energy starts from 3 m/s of air flow.

1 Experimental methodology

The purpose of this work is to analyze experimental studies of the aerodynamic characteristics of the movement of a horizontally-axial rotating cylindrical combined wind turbine in a variable flow. The research work was carried out in the laboratory «Aerodynamic Measurements» of the research Center «Alternative Energy» of the Faculty of Physics and Technology. A model of a rotating cylindrical combined wind turbine was developed, which was subsequently studied at different wind speeds in a transverse air flow.

Figure 1 shows an image of the location of the experimental installation on the working part of the wind tunnel, where the fixed blade is located at an angle in different directions relative to the axis of rotation of the cylinder.

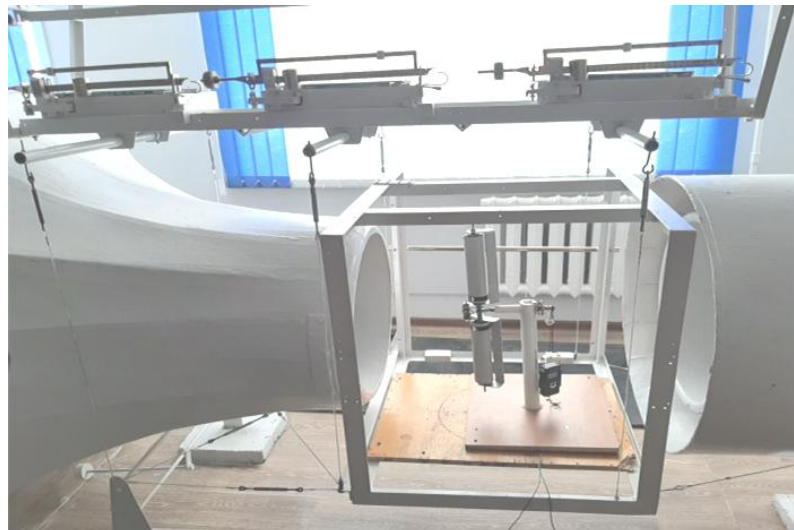


Fig.1. The location of the experimental installation on the working part of the wind tunnel

The test sample is placed in the working part of the wind tunnel and attached to the aerodynamic scales using a thin metal tensioner to reduce the resistance of auxiliary elements. Figure 2 shows how a fixed blade forms an angle (0° , 15° , 30° , 45° , 60°) relative to the distance of the axis of rotation of the cylinder. The tests were carried out with a horizontal axial combined wind turbine with a flat cylindrical rotation.

The air flow velocity varied from 3 to 12 m/s, the total diameter of the wind wheel $D = 50$ sm, the diameter of the cylinders $d = 0.5$ sm, the length of the cylinders 21 sm, the length of the fixed blade 23 sm.

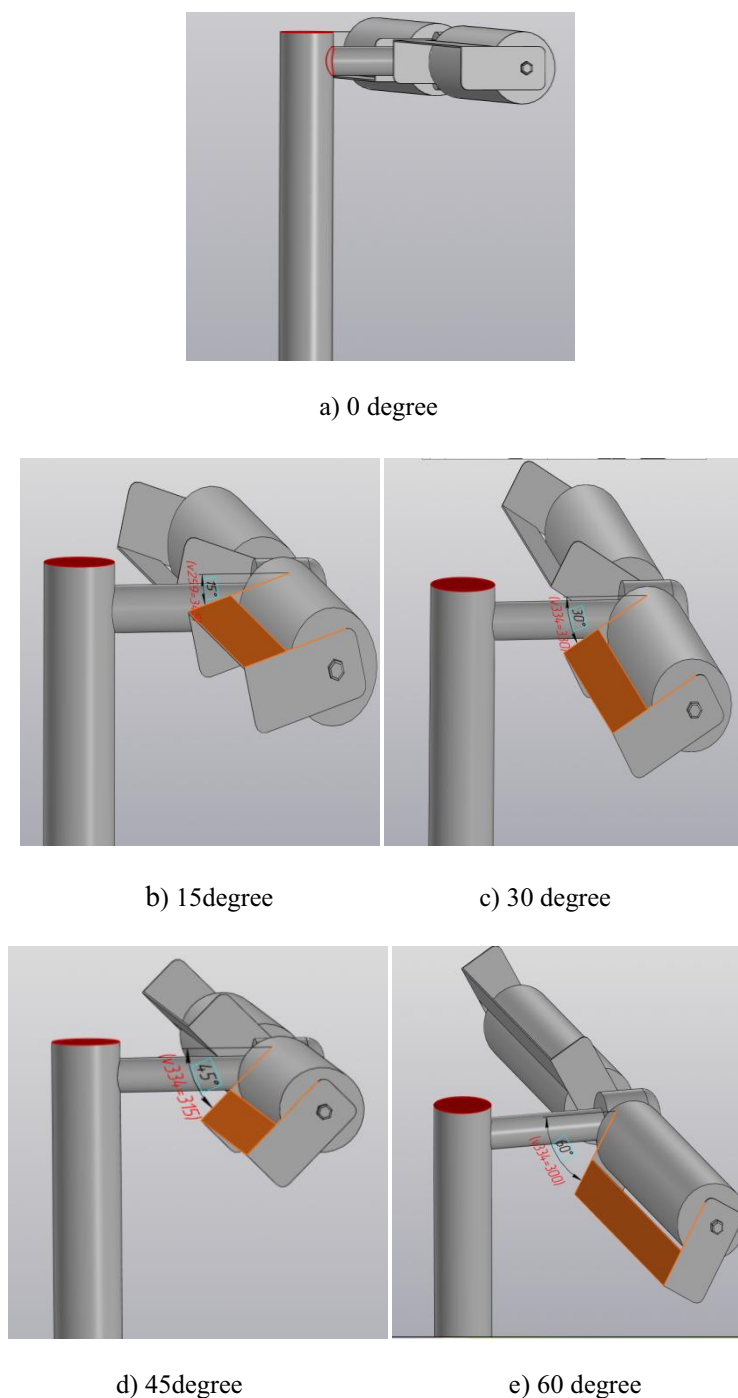


Fig. 2. Two-bladed cylinders with fixed blades

2 Research results

The aerodynamic characteristics of this model are determined - the thrust force and the rotational speed of a rotating cylindrical combined wind turbine at flow rates from 3 m/s to 12 m/s. As the wind speed increases, we see that the rotation frequency of our wind turbine also increases, which can be seen in the graph below. We determine the speed of rotation using a contactless tachometer (Fig 3).

Figure 4 shows a graph of the dependence of the thrust force of the layout on the wind speed. In Figure 4, we see an increase in the thrust force as the flow velocity increases from 3 m/s to 12 m/s. As can be seen from the dependence, with a maximum air flow velocity of 12 m/s, the thrust force values reached 0.9 N at 0

degrees, 0.97 N at 15 degrees, 1.29 N at 30 degrees, 1.09 N at 45 degrees, 2.06 N at 60 degrees, then the thrust force stabilizes, i.e. no increase is observed.

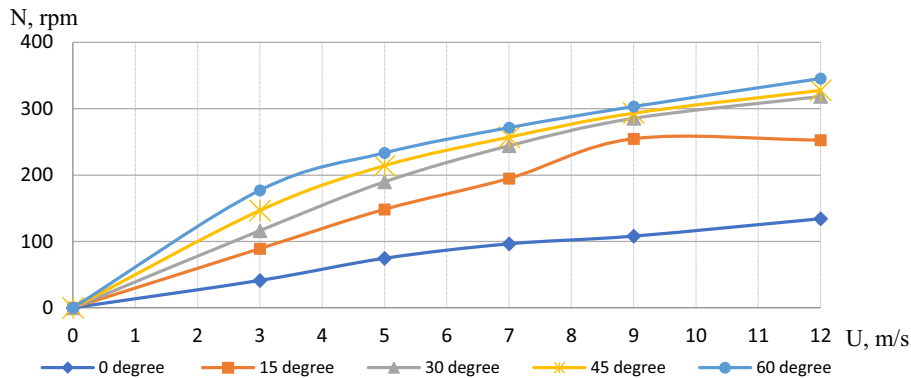


Fig. 3. Dependence of the rotation frequency of the layout on the wind speed

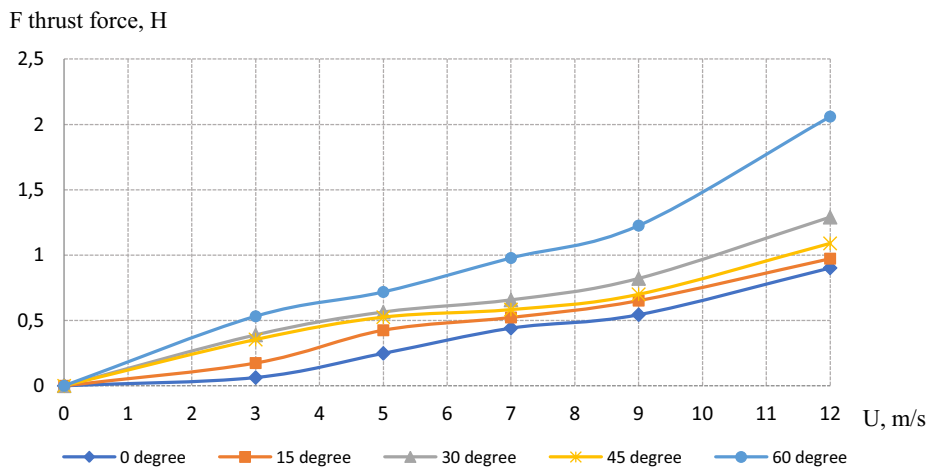


Fig.4. Dependence of the thrust force of the layout on the wind speed

Changing the angle of inclination of the fixed blade changes the curvature of the profile. Thus, it becomes possible to increase the traction force in an effective way. In the frontal part of the cylinder up to the point of separation of the boundary layer, there is a gradual delamination of the experimental data for different aspect ratios and inclination of the fixed blade. With an increase in the length of the cylinder, the value of dimensionless pressure at a fixed angle decreases, a gradual transition from the pressure distribution characteristic of spatial motion – flow around the cylinder to the pressure distribution characteristic of plane motion – flow around an infinitely long cylinder is manifested. In this case, this angle where there is a deterioration in the rotation of the blades is 45 degrees, where the thrust force decreases.

Further, with a change in the angle of inclination of 30 and 60 degrees, a gradual increase in the thrust force is observed, which is a positive result for the rotation of the blades.

Since we know that when the wind speed increases, the lifting force also increases, we can conclude that when the wind speed increases, the thrust force also increases, since the thrust force manifests itself in the pressure drop over the cylinder. The lower part of the cylinder operates at high pressure, while the upper part operates at low pressure. The pressure difference from above and below causes the thrust force.

Conclusion

Based on the results of experimental studies, the following conclusions can be drawn:

- A mock-up of a wind power plant with combined blades, in the form of a rotating cylinder and fixed blades, has been developed and created in order to increase the thrust force of the wind turbine.
- The novelty of this work is the optimal choice of operating and geometric parameters in the form of rotating cylinders and fixed blades, as well as the angle of inclination of the non-rotating blade (optimal degree of inclination).
- Experiments were carried out to study the thrust force and rotation frequency of the wind wheel depending on the change in wind speed, at different angles of the fixed blade relative to the cylinder.
- It is determined that at the set angle of inclination of the fixed blade of 60 degrees and at a wind speed of 12 m/s, the maximum values of the rotation speed of the wind wheel of 350 rpm and the thrust force of 2.06 N are obtained.

The practical application of the work is that due to the addition of fixed blades by the wind wheel, a more complete use of wind energy is provided during rotation. The proposed wind turbine with combined blades is effective because it starts the rotation of the wind wheel from 3 m/s. This wind turbine is suitable for autonomous alternative power supply in the field.

Funding

The work was carried out with the financial support of the Science Committee of the Ministry of Science and Higher Education of the Republic of Kazakhstan (IRN AP14972704 "Numerical study of a new design of wind turbine blades with a horizontal axis of rotation").

REFERENCES

- 1 Yuan Z., Liang F., Zhang H., Liang X. Seismic analysis of a monopile-supported offshore wind turbine considering the effect of scour-hole dimensions: Insights from centrifuge testing and numerical modelling. *Ocean Engineering*, 2023, 283, pp. 115067. doi:10.1016/j.oceaneng.2023.115067
- 2 Karatayev M., Clarke M.L. Current energy resources in Kazakhstan and the future potential of renewables: A review. *Energy Procedia*, 2014, 59, pp. 97-104. doi: 10.1016/j.egypro.2014.10.354
- 3 del Campo V., Ragni D., Micallef D., Diez F. J., Ferreira C. S. Estimation of loads on a horizontal axis wind turbine operating in yawed flow conditions. *Wind Energy*, 2015, 18(11), pp.1875-1891. doi: 10.1002/we.1794
- 4 Lotfi R., Mardani N., Weber G.W. Robust bi- level programming for renewable energy location. *International journal of energy research*, 2021, 45(5), pp. 7521-7534. doi: 10.1002/er.6332
- 5 Tanasheva N.K., Sakipova S.E., Minkov L.L., Bakhtybekova A.R., Shuyushbaeva N.N., Burkov M.A. Study of aerodynamic characteristics of a cylindrical blade with deflector. *Eurasian Physical Technical Journal*, 2021, 18(3 (37)), pp.48-52. doi: 10.31489/2021No3/48-52
- 6 Manyonge A.W., Ochieng R.M., Onyango F.N., Shichikha J.M. Mathematical Modelling of Wind Turbine in a Wind Energy Conversion System. *Applied Mathematical Sciences*, 2012, Vol. 6 (91), pp. 4527–4536.
- 7 Tanasheva N.K., Kunakbaev T.O., Dyusembaeva A.N., Shuyushbayeva N.N., Damekova S.K. Effect of a rough surface on the aerodynamic characteristics of a two-bladed wind-powered engine with cylindrical blades. *Technical Physics*, 2017, 62 (11). pp. 1631-1633. doi: 10.1134/S1063784217110299
- 8 Baishagirov H.J. *Wind power plant*. Publ. 2012, 4, 4p. [in Russian]
- 9 Bukatov N.S., Buktukov B.J., Moldybaeva G.J., Iakov A.K. *Wind farm Butukova 6 (option)*. Publ. 2013, 12, 4p. [in Russian]
- 10 Bychkov N.M. Wind turbine with Magnus effect: 1 Results of model studies. *Thermophysics and aeromechanics*. 2004, –11 (4), pp. 583-596.

STUDY OF RADIO TRANSPARENCY AND DIELECTRIC PERMITTIVITY OF GLASS- AND ARAMID EPOXY COMPOSITES

Yermakhanova A.M.¹, Kenzhegulov A.K.^{1,2}, Meirbekov M.N.^{1,3},
Samsonenko A. I.⁴, Baiserikov B.M.^{1,3}

¹JSC "National Center of Space Research and Technology", Almaty, Kazakhstan

²Satbayev University, JSC Institute of Metallurgy and Ore Beneficiation, Almaty, Kazakhstan

³Satbayev University, Almaty, Kazakhstan

⁴SLLP "Institute of Space Engineering and Technology", Almaty, Kazakhstan

Aramide- epoxy-filled composites are widely used for manufacturing in the structures of modern aerospace vehicles. Not only do they have excellent mechanical properties, but they are also radio-transparent materials for wave transmission. In this work, an epoxy-filled composite and a fibreglass were made by vacuum infusion for a comparative study on radio transparency and dielectric permittivity. The radio transparency of the materials analyzed has been evaluated by measuring in free space in the frequency ranges of 1-6 GHz. According to the results of radio transparency, aramide- epoxy-filled composite suffers less electromagnetic wave losses than in fibreglass. When measuring the dielectric permittivity of the aramide- epoxy-filled composites, a low average value of 2.874 has been set, whereas for the fibreglass is defined at 4.

Keywords: aramide-epoxy-filled composites, fibreglass, epoxide resin, radio transparency, frequency, dielectric permittivity.

Introduction

Radio transparency is the low loss capacity of radio materials to transmit radio waves across a broad frequency range [1]. The radio-transparent materials include organic and inorganic dielectrics that allow transmission of electromagnetic radiation of the radiofrequency range of $10^5 - 10^{12}$ Hz. [2]. The transparency of these materials for radio waves is ensured by choosing dielectrics with small values of dielectric characteristics (dielectric dissipation factor $\text{tg}\delta \leq 0.02$, dielectric permittivity $\epsilon = 1.1-9.0$) and relevant electrodynamic calculation of layer thicknesses [3]. In other words, the lower the dielectric permittivity, the more radiotransparent the material is. The reducing the dielectric permittivity and dielectric dissipation factor can reduce the capacitance and time delay of a signal to improve signal transmission in antenna, fairing. The selection of materials for manufacturing the fairing makes necessary the maximum optimization of mechanical and electrical properties for the effective functioning of radar systems of supersonic aircraft [4].

The polymer composites with fibers, which have low extended defects [5], are very promising as radio-transparent materials. One such material is polymer composites reinforced with aramid fiber that is the aramide epoxy-filled composite (AEC). They have low dielectric permittivity, low dielectric absorption losses, and outstanding mechanical characteristics, this is why they are widely used for manufacturing of fairings, stabilizers and vertical fins in the modern airplane industry [6-8]. The dielectric properties of AEC are important parameters since they directly affect the speed and loss of the wireless power during signal transmission. The precise measurements of the dielectric properties of AECs can provide engineers and researchers with valuable information that can be used to optimize the performance and characteristics of its designs [9-11].

Over the years, numerous papers [12-18], have been reported on the study of the dielectric properties of AEC. The authors' efforts apply various methods to improve the radio transparency of composites (dielectric performance degradation). According to the authors of the review paper [12], there are two simple ways to reduce the dielectric permittivity (DP) of composites. The first is to reduce the number density of the dipole by inclusion of air, and the second - to alloy with fluorine element in order to reduce the polarizability of the dipole in the composite material.

A group of several researchers believe that combining aramid fiber (AF) with fibreglass results in lower dielectric characteristics. L. Yao et al. [13,14] have investigated the dielectric properties of composites, reinforced AF, and three-dimensional hybrid composites by the rectangular waveguide method. They found that the hybrid composite 5A7C5A (A – aramid fiber and C – fibreglass) had the lowest DP, which is even lower than 17A pure aramid composite. Under the charge of Choi and Chin [15,16], authors have used the free space method, to characterize the effect of a damaged faceplate from the AEC on the wave transmission characteristics of the fairings. The hybrid composite nearly invisible fairings were designed as a composite sandwich construction consisting of E-glass/aramid/epoxy. The hybrid composite low-visibility fairing with HF2 face has met the requirements for transmission characteristics of electromagnetic waves with transmission coefficient of 81 % at the resonance frequency of 8.50 GHz and bandwidth of 0.84 GHz. The following article [17] has considered a combined dielectromechanical test method based on the free-space method and a mechanical testing machine. DPC of aramid/epoxy, epoxide resin (ER) and fibreglass/epoxy composites were measured under different deformation conditions. It was found that the DP of composites increases with increasing strain, while the tangent of the angle of dielectric losses remains unchanged. In [18] paper, nearly invisible fairing was made with an AEC face and a foamed core for low-observability. The dielectric constant and AEC dielectric dissipation measured by free space measurement were 3.742 and 0.018, respectively. The maximum transmission rate was 83 % at a bandwidth of 0.99 GHz for the transmission rate greater than 80 %. As it turned out, the composite with aramid fiber was superior in dielectric characteristics. Despite these and other high-quality studies, hardly anything is known about the dielectric properties and radio transparency of AEC, and more experimental research in this area is required.

The purpose of this work is a comparative study of radio transparency and dielectric permittivity (DP) of aramid epoxy-filled composite and fibreglass (FG) samples obtained by measuring in free space.

1 Materials and methods

For the manufacture of AEC and FG, ER of L grade was used as a binding substance (PoxySystems, Germany) with EPH hardening agent. The 3300 dtex aramid fabric has been used as reinforcing filler (Teijin, Netherlands) and Ortex 360 - 300 g/m² fibreglass (OOO Altair M, Russia). AEC and FG has been made by vacuum infusion method. The detailed description of the methodology is presented in our previous paper [19]. The dimensions of the AEC and FG have been designed specifically for measuring radio transparency in the approximate A3 format, which is shown in Figure 1.



Fig.1. Sample of AEC with A3 size

The dielectric properties of AEC and FG samples were measured using measuring equipment of the SLLP “Institute of Space Engineering and Technology” (ISET) in an anechoic shielded chamber (ASC) by free-space measurements. The measurements of radio transparency of the material sample (electromagnetic wave transmission coefficient) have been performed by comparing the levels of electromagnetic radiation between the transmitting and receiving horn antennas in the presence of sample and without it according to Figure 2. The configuration of equipment used to measure the radio transparency of a material sample: N9010B Keysight spectral analyzer with measuring receiver of electromagnetic radiation, Signal Generator type waveform generator, P6-23M/2 horn antenna. The measurements were taken in the anechoic screened chamber.

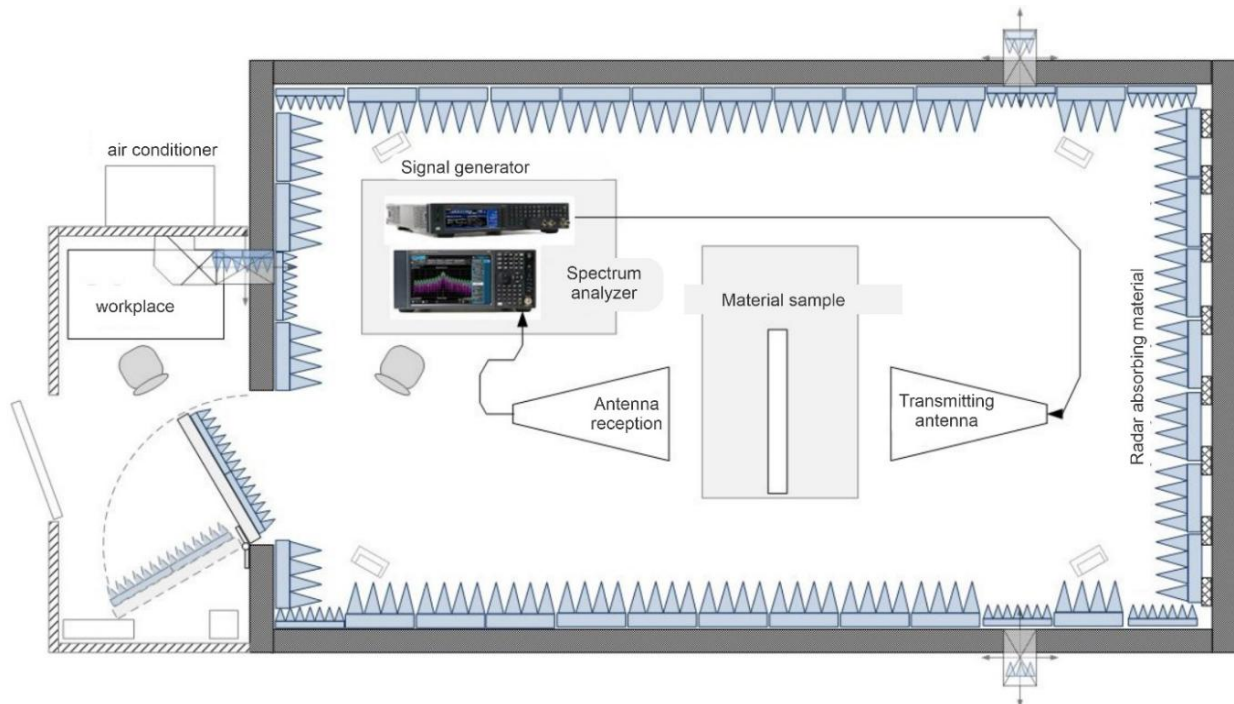


Fig.2. Diagram of measuring the material sample radio transparency in the ASC

The radio transparency is measured in the frequency band of measuring horn antenna and devices 1÷6 GHz. The measured material sample in the diagram has no contact with the antennas. A3 format sample area exceeds the aperture area of horn antenna by 20-25 %, which is in good agreement with measurement method, when the maximum electromagnetic energy in the antenna directivity diagram passes through the sample, rather than flowing between the antennas by passing the sample. When measured in the frequency range from 1 to 6 GHz, there was unevenness in the intrinsic transmission characteristic of the horn antennas in the range from 4.5 to 6 GHz approximately. In this respect, during measurements the whole range was divided into two sections: 1÷4 GHz and 4÷6 GHz, for a more accurate presentation of the results. For each section, measurements were taken three times.

2 Results and discussions

2.1 Results of materials radio transparency measurements

Figure 3 demonstrates one of the three measurements of the electromagnetic field attenuation of the AEC sample in the 1÷4 GHz band - trace 2 in blue, against the background of the antenna transmission coefficient in air (without sample) – trace 1 in yellow. 1, 3, and 5 markers correspond to yellow trace 1, and markers 2, 4, and 6 correspond to blue trace 2 with the pattern. The numerical values of frequencies and attenuations are given in the Marker Table at the bottom of the pictures (screenshot).

The comparison should be made by markers located at the same or close frequency: 1 and 2, 3 and 4, 5 and 6. For example, in Figure 2, marker 1 corresponds to the frequency $f=1.230$ GHz and attenuation 23.18 dB/mW, and marker 2 has a frequency of 1.240 GHz and attenuation – 23.53 dB/mW. The difference in attenuation due to losses in the material: $23.53 - 23.18 = 0.35$ dB/mW. Therefore, electromagnetic energy loss in the AEC at this frequency was 0.35 dB/mW. For the other frequencies, the calculation was performed in the same way. According to the results of averaging of three measurements of AEC radio transparency, it was determined that in the 1÷4 GHz range the attenuation is ~ 0.201 dB. Table 1 demonstrates the results of calculations for determination of attenuation, followed by subtracting the average value.

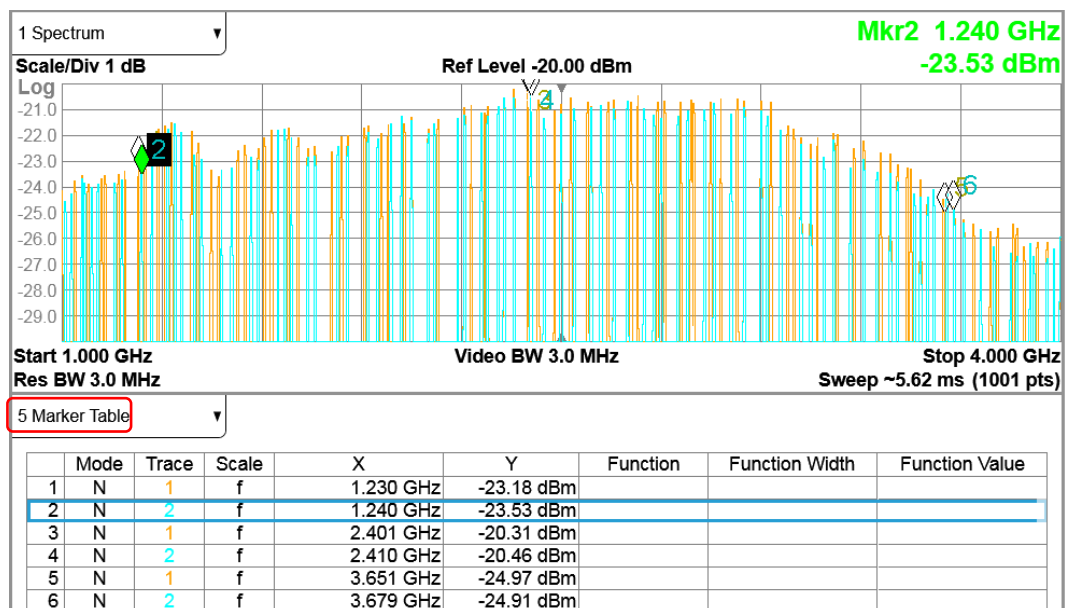


Fig.3. Measurement 1, field attenuation in the AEC

Table 1. Indicators of field attenuation in AEC in the 1÷4 GHz frequency range

Measurement	Blue marker frequency, dB/mW	Yellow marker frequency, dB/mW	Difference of attenuation, dB/mW	Averaging, dB/mW	Total loss of electromagnetic energy, dB/mW
1	23.53	23.18	0.35	0.147	0.21 (at 1÷4 GHz range frequency)
	20.46	20.31	0.15		
	24.91	24.97	-0.06		
2	23.47	23.18	0.29	0.103	
	20.40	20.31	0.09		
	24.90	24.97	-0.07		
3	23.49	23.18	0.31	0.353	
	21.12	20.31	0.81		
	24.91	24.97	-0.06		

The resulting average attenuation value of (minus) 0.21 dB can be converted to times using the decibel table [20]. Since decibels can be added (times - multiplied), then: $0.21 \text{ dB} = 0.2 \text{ dB} + 0.01 \text{ dB}$. According to the voltage, current, power conversion table, 0.2 dB corresponds to a power ratio of 0.955 (part of the power that has passed through the material), 0.01 dB corresponds to a power ratio of 0.9977. As a result $0.955 \times 0.9977 = 0.9528$ is that part of the power that has passed through the material (95.28 %). Therefore, capacity loss in the material in the 1÷4 GHz range is defined as follows: $100\% - 95.28\% = 4.72\%$.

Figure 4 below demonstrates one of the three measurements of the electromagnetic field attenuation of the AEC sample in the 4÷6 GHz range. Table 2 demonstrates the results of calculations for determination of attenuations, followed by subtracting the average value.

The capacity loss of 0.73 dB can be represented as $0.7 + 0.03 \text{ dB}$. Then 0.7 dB corresponds to power ratio of 0.8511 (part of the power that has passed through the material), 0.03 dB corresponds to a power ratio of 0.9931. As a result $0.8511 \times 0.9931 = 0.8452$ is that part of the power that went through the material is 84.52 %. Therefore, capacity loss in the material – 15.48 % in the 4÷6 GHz range.

Figure 5 below demonstrates one of the three measurements of the electromagnetic field attenuation of the FG (A3 format, H=1.5 mm). Table 3 demonstrates the results of calculations for determination of attenuations, followed by subtracting the average value of the FG sample.

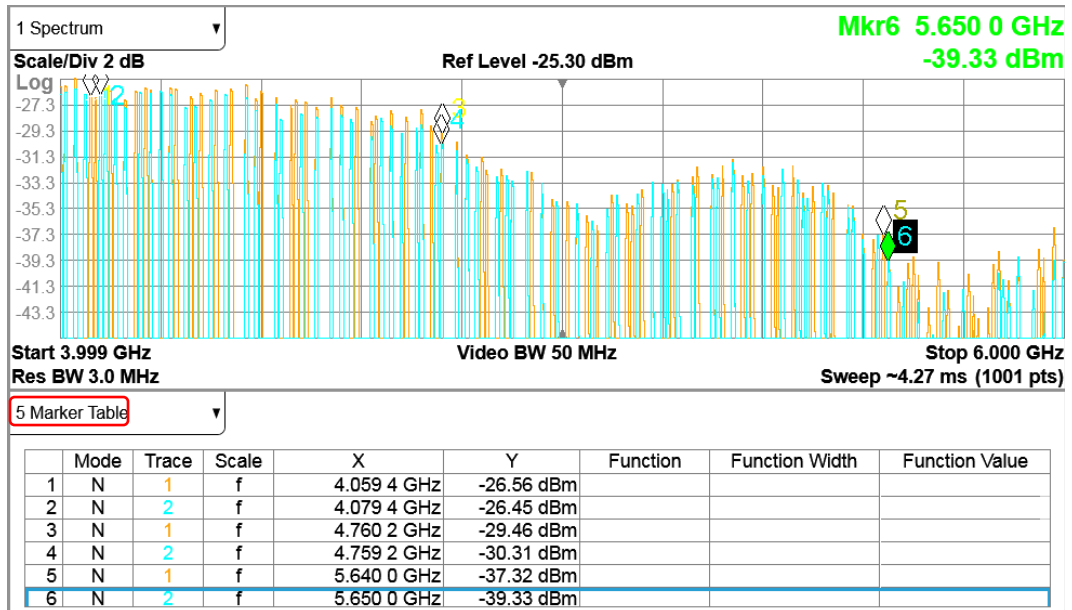


Fig.4. Measurement of 1 field attenuation in AEC in the 4÷6 GHz range

Table 2. Indicators of field attenuation in AEC in the 4÷6 GHz frequency range

Measurement	Blue marker frequency, dB/mW	Yellow marker frequency, dB/mW	Difference of attenuation, dB/mW	Averaging, dB/mW	Total loss of electromagnetic energy, dB/mW
1	26.45	26.56	-0.11	0.917	0.73 (at 4÷6 GHz range frequency)
	30.31	29.46	0.85		
	39.33	37.32	2.0		
2	26.74	26.56	0.18	0.36	
	29.81	29.46	0.09		
	37.87	37.32	0.55		
3	26.64	26.56	0.08	0.917	
	30.21	29.46	0.75		
	39.24	37.32	1.92		

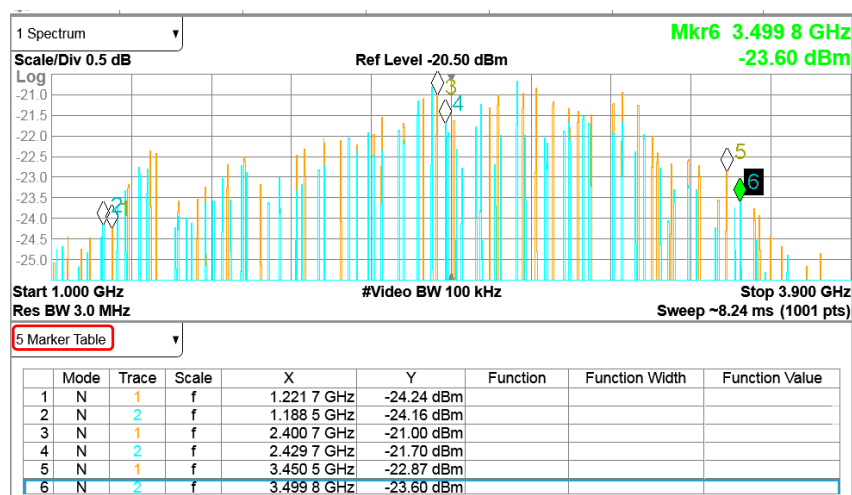


Fig.5. Measurement of 1 field attenuation in FG in the 1÷4 GHz frequency range

Table 3. Indicators of field attenuation in the FG in the 1÷4 GHz frequency range

Measurement	Difference of attenuation, dB/mW	Averaging, dB/mW	Total loss of electromagnetic energy, dB/mW
1	-0.08	0.45	0.173 (at a frequency range of 1÷4 GHz)
	0.70		
	-0.73		
2	0.01	0.25	
	0.13		
	0.65		
3	-0.24	-0.18	
	-0.70		
	0.40		

The average value of radio wave attenuation in FG in the 1÷4 GHz frequency band $(+0.45+0.25-0.18)/3 = 0.173$ dB. Therefore, in the FG capacity loss – 2.51 % in the 1÷4 GHz range. Figure 6 demonstrates a similar measurement only in the 4÷6 GHz range. Table 4 shows the results of calculations to determine the attenuations, followed by subtracting the mean value of the FG sample.

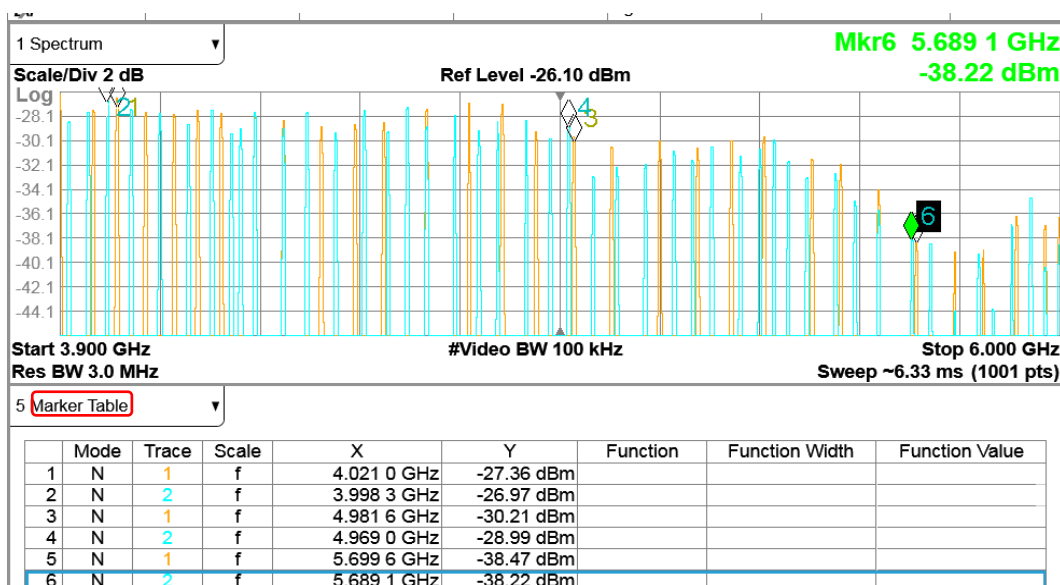


Fig.6. Measurement of 1 field attenuation in the 4÷6 GHz frequency band in FG

Table 4. Indicators of field attenuation in the FG in the 4÷6 GHz frequency range

Measurement	Difference of attenuation, dB/mW	Averaging, dB/mW	Total loss of electromagnetic energy, dB/mW
1	-0.39	-0.36	0.94 (at the range frequency 4÷6 GHz)
	-1.22		
	-0.25		
2	1.82	1.67	
	0.40		
	2.81		
3	0.87	1.53	
	1.23		
	-0.57		

The average value of radio wave attenuation in FG in the frequency range 4÷6 GHz $(-0.36 + 1.67 + 1.53)/3 = 0.94$ dB. Therefore, in the FG capacity loss – 19.47 % in the 4÷6 GHz range.

Summarizing the above results of the analysis of radio transparency of AEC and FG, final comparative table 5 demonstrates the comparative data on the radio transparency of samples. As the Table shows, average values of electromagnetic wave attenuation in the 1÷6 GHz range for AEC and FG are very close. According to the averaged values, transmission coefficient for AEC was 89.9 % and for FG 89.01 %. A possible reason for the fact that the transparency of the AEC is higher than the FG may be the low DP of the AEC compared to the FG. Since it is known that the wave transmission characteristics of wave-transparent composites with a polymer matrix are usually estimated by DP [21-22]. In contrast to the AEC, FG is made of glass fiber, which has a higher dielectric constant than the polymers used in AEC. This means that FG absorbs more radio waves, which results in decrease of its radio transparency compared to the AEC. AEC sample was close to the FG - 0.17 dB at the beginning of the 1÷4 GHz section in attenuation values - 0.21 dB, and at the end of the section it was even better. Therefore, based on the results of radio transparency, it may be concluded that the losses in AEC are less than in the FG.

Table 5. Comparison of radio transparency of AEC and FG samples

Material	Deamplification, dB/% 1÷4 GHz	Deamplification, dB/% 4÷6 GHz	Averaging
AEC	0.210 dB / 4.72 %	0.73 dB / 15.48 %	0.47 dB / 10.1 %
FG	0.173 dB / 2.51 %	0.94 dB / 19.47 %	0.55 dB / 10.99 %

2.2 Measurements of dielectric permittivity of samples

The dielectric permittivity of the samples is measured using the condenser-type method since the dielectric permittivity of the insulator material affects the capacitance of low-profile capacitor.

For the mechanical clamp of AEC and FG sheet between the plates (electrodes) of the capacitor, a stand was made with D16 aluminum electrodes (170 × 138 mm) on the basis of precision milling machine vise with minimum microcrew backlash according to Fig. 7. The capacitor capacitance in the presence of organic plastic and without it is measured with APPA701 LCR-meter. In the stand the electrode insulators from the vise mechanism are made of caprolon material with a small intrinsic DP, to minimize the stray capacitance of the stand that affects the result. The dielectric permittivity was measured according to the methods set out in [23].



Fig.7. Mechanical clamp of the AEC sheet between the plates (electrodes) of the capacitor

Table 6 shows the results of three measurements of the AEC and FG sample. As shown by the results, AEC has average DP 2.874, whereas the FG - 4. The obtained results of the FG measurement coincide with the reference data given in [23-24]. Due to the lower DP of aramide fibre than the DP of fiberglass, AEC indicates a low value. One of the reasons for the difference in DP between the AEC and FG is its structure.

Table 6. Results of DP of the AEC and FG materials

Sample 1	C diel, pF	C	d_0 , mm	ε	Averaged value ε
AEC	273	99.1	2	2.754	2.874
AEC	286	97.6	2	2.930	
AEC	289	98.3	2	2.939	
FG	600	150	1.5	4	4

FG consists of the fibreglass, which have a higher DP than the polymeric materials used in AEC. Furthermore, an important factor affecting the DP is the content of moisture and other impurities in the material. FG can be more sensitive to moisture than AEC, which can lead to an increase in its DP. However, it should be realized that DP depends on many factors and can vary over a wide range depending on the specific material and operating conditions.

Conclusion

In this work an aramid-epoxy-filled composite and fiberglass are produced by vacuum infusion method. The comparative studies of radio-transparency and dielectric permittivity of the listed composites have been performed. The radio transparency of the studied materials was evaluated by measuring in free space in the frequency ranges of 1-6 GHz. According to the results of radio transparency, it may be concluded that the losses in the aramid epoxy-filled composite are less than in the fiberglass due to the high dielectric permittivity of the latter with the previous one. According to the averaged values, the transmittance for the aramid epoxy-filled composite was 89.9 %, and for fiberglass it was 89.01 %. When measuring the dielectric permittivity, the aramid epoxy-filled composite has demonstrated a low average DP value of 2.874 due to the lower dielectric constant of the aramid fiber, whereas fiberglass is defined at 4. Our results suggest that the differences in the composition and structure of the aramid-epoxy-filled composite and fiberglass result in different physical properties, including its radio transparency.

Funding

This study is funded by the Science Committee of the Ministry of Education and Science of the Republic of Kazakhstan (grant No. AR09058225), where AR09058225 is the URN of the project.

REFERENCES

- 1 Nevdyayev L.M. *Telecommunication technologies. English-Russian explanatory dictionary-reference book*. Moscow, ICSTI, 2002, 592 p. [in Russian]
- 2 Dyadenko M.V., Gelai A.I. Radiotransparent materials based on titanosilicate glasses. *Steklo i keramika*, 2017, Vol. 90, No. 8, pp. 15-20. [in Russian]
- 3 Khatavkar N., Balasubramanian K. Composite materials for supersonic aircraft radomes with ameliorated radio frequency transmission-a review. *RSC advances*, 2016, Vol. 6, No. 8, pp. 6709-6718. doi:10.1039/c5ra18712e
- 4 Yermakhanova A.M., Sanin A.F., Meirbekov M.N., Baiserikov B.M. Investigation of dielectric and strength properties of composite materials. Review. *Kompleksnoe Ispol'zovanie Mineral'nogo Syr'a = Complex Use of Mineral Resources*, 2022, Vol. 322, No. 3, pp. 89-102. doi:10.31643/2022/6445.33
- 5 Ospanali A.T., Kenzhegulov A.K., Zhumadilov B.E., Suyundykova G.S., Medyanova B.S., Partizan G., Aliev B.A. Obtaining of carbon nanofibers based on polyacrylonitrile by the method of electrospinning. *Eurasian Physical Technical Journal*, 2020, Vol. 33, No. 1, pp. 35-38. doi:10.31489/2020No1/35-38
- 6 Chio I., Kim J.G., Lee D.G., et al. Aramid/epoxy composites sandwich structures for low-observable radomes. *Compos. Sci. Technol.*, 2011, Vol. 71, No. 14, pp. 1632-1638. doi:10.1016/j.compscitech.2011.07.008
- 7 Ismailov M.B., Yermakhanova A.M. Characterization of the epoxy resin and carbon fiber reinforced plastic stress-strain state by modified carbon nanotubes. *Eurasian Chemico-Technological Journal*, 2018, Vol. 2, No. 2, pp.137-145. doi:10.18321/ectj698
- 8 Singha A.S., Rana A.K., Jarial P.K. Mechanical, dielectric and thermal properties of Grewia optiva, fibers reinforced unsaturated polyester matrix based composites. *Mater. Des.*, 2013, Vol. 51, No. 5, pp. 924-934. doi:10.1016/j.matdes.2013.04.035
- 9 Nguyen V.H., Hoang M.H., Phan H.P., et al. Measurement of complex permittivity by rectangular waveguide method with simple specimen preparation. *International Conference on Advanced Technologies for Communications*, Hanoi, Vietnam, 2015, pp. 397-400. doi:1109/ATC.2014.7043419

- 10 Meyirbekov M.N., Ismailov M.B., Manko T.A., Koziy K.V. Study of the influence of rubber on strength properties of carbon plastic. *Space Sci. & Technol.*, 2022, Vol. 28, No. 5, pp. 07-07. doi:10.15407/knit2022.05
- 11 Jyoti J., Kumar A., Dhakate S.R., Singh B.P. Dielectric and impedance properties of three dimension graphene oxide/carbon nanotube acrylonitrile butadiene styrene hybrid composites. *Polym. Test.*, 2018, Vol. 68, pp. 454-466. doi:10.1016/j.polymertesting.2018.04.003
- 12 Li R., Yang X., Li J., et al. Review on polymer composites with high thermal conductivity and low dielectric properties for electronic packaging. *Materials Today Physics*, 2022, Vol. 22, pp. 100594. doi:10.1016/j.mtphys.2021.100594
- 13 Yao L., Wang X., Liang F., et al. Modeling and experimental verification of dielectric constant for three-dimensional woven composites. *Compos. Sci. Technol.*, 2008, Vol. 68, pp. 1794-1799. doi:10.1016/j.compscitech.2008.01.014
- 14 Yao L., Li W., Wang N., et al. Tensile impact and dielectric properties of three dimensional orthogonal aramid/glass fiber hybrid composites. *J. Mater. Sci.*, 2007, Vol. 42, pp. 6494-6500. doi:10.1007/s10853-007-1534-9
- 15 Choi I., Lee D., Lee D.G. Hybrid composite low-observable radome composed of E-glass/aramid/epoxy composite sandwich construction and frequency selective surface. *Compos. Struct.*, 2014, Vol. 117, pp. 98-104. doi:10.1016/j.compstruct.2014.06.031
- 16 Chin W.S., Lee D.G. Binary mixture rule for predicting the dielectric properties of unidirectional E-glass/epoxy composite. *Compos. Struct.*, 2006, Vol. 74, pp. 153-162. doi:10.1016/j.compstruct.2005.04.008
- 17 Xu X., et al. Measurements and analysis of the dielectric properties of aramid/epoxy composites based on free space method under stress conditions. *Polym. Test.*, 2018, Vol. 72, pp. 55-62. doi:10.1016/j.polymertesting.2018.09.029
- 18 Choi I., et al. Aramid/epoxy composites sandwich structures for low-observable radomes. *Composites Science and Technology*, 2011, Vol. 71, No. 14, pp. 1632-1638. doi:10.1016/j.compscitech.2011.07.008
- 19 Yermakhanova A.M., Baiserikov B.M., Kenzhegulov A.K., Meirbekov M.N., Zhumadilov B.Y. Study on methods to improve the mechanical properties of aramid/epoxy composites. *Journal of Elastomers & Plastics*, 2023, Vol. 55, No. 2, pp. 331-346. doi:10.1177/0095244322114764
- 20 Ginkin G. *Handbook of Radio Engineering*. Moscow, State Energy Publishing House, 1948, 362 p. [in Russian]
- 21 Li X., Liu T., Jiao Y., Dong J., Gan F., Zhao X., Zhang Q. Novel high-performance poly(benzoxazole-co-imide) resins with low dielectric constants and superior thermal stability derived from thermal rearrangement of ortho-hydroxy polyimide oligomers. *Chem. Eng. J.*, 2019, Vol. 359, pp. 641-651. doi:10.1016/j.cej.2018.11.175
- 22 Zhao K., Cheng L., Ye F., Cheng S., Cui X. Preparation and performance of Si₃N₄ hollow microspheres by the template method and carbothermal reduction nitridation. *ACS Appl. Mater. Inter.*, 2019, Vol. 11, pp. 39054-39061. doi:10.1021/acsami.9b11336
- 23 Determination of the permittivity of a substance. Available at: http://bog5.in.ua/lection/labrab/electrics/lr3_4.html (Feb14, 2023) [in Russian]
- 24 What is a Dielectric Constant of Plastic Materials? Available at: <https://passive-components.eu/what-is-dielectric-constant-of-plastic-materials/> (June15, 2023)

INFORMATION-ENTROPY METHOD FOR DETECTING GRAVITATIONAL WAVE SIGNALS

Zhanabaev Z.Zh., Ussipov N.M.*

Al-Farabi Kazakh National University, Department of Physics and Technology, Almaty, Kazakhstan
ussipov.nurzhan@kaznu.kz

The detection of gravitational waves came from a pair of merging black holes marked the beginning of the era of GW astronomy. Traditionally, to extract gravitational wave signals from experimental data, the scientific collaborations use the standard matched filtering technique. The matched filtering technique relies on the existing waveform templates, that makes it difficult to find gravitational wave signals that go beyond theoretical expectations. Moreover, the computational cost of matched filter is very high, as it depends on the number of templates used. In this article, we propose a new information-entropy method for gravitational waves detection that does not require a theoretical bank of signal templates. To demonstrate the reliability of our method we conducted an analysis using simulated and real data. Through this study, we revealed that our measure of conditional information detects the gravitational wave signals and can be used along with the matched filtering method.

Keywords: gravitational waves, information-entropy, detection, nonlinear process.

Introduction

The first direct detection of gravitational waves (GWs) by the advanced LIGO observatory proved the fundamental predictions of Einstein's theory of General Relativity and started the era of GW astronomy. The registration of first GW, the so-called GW150914, was realized due to the merger of two binary black holes with estimated masses of $29 M_{\odot}$ and $36 M_{\odot}$ [1]. During three observing sessions (O1, O2, O3) the LIGO and VIRGO collaborations recorded 90 GW signals produced by the coalescence of compact objects, mainly pairs of black holes with a small fraction of neutron star [1-7].

The detection of GWs is one of the most difficult tasks faced in fundamental science since the GW signal is much weaker compared to typical noise levels. To detect GW signals from the experimental data, the LIGO and Virgo collaborations mainly use the matched filtering method [8-10]. This method convolves a set of precalculated template waveforms with the measured data, where each template represents a source with different components such as masses, spins, etc. For each template waveform, a signal-to-noise ratio (SNR) time series is calculated, and candidates are determined according to the peak of the SNR time series. The matched filtering method is optimal for signal detection in Gaussian noise, where it yields the most statistically significant detection candidates [11]. However, this method, in order to match the signal, does a full search in the bank of templates, which in turn can slow down the data processing speed [12]. Furthermore, the premise of matched filtering method requires an accurate theoretical template. If GWs are beyond theoretical expectations, this may lead to the fact that gravitational wave signals not being detected [10].

Currently, information-theoretic approaches have found wide application in modern signal processing problems. Information-entropy technique quantifies the degree of complexity and irregularity of a signal. It is known that information is a measure of certainty, and entropy is a measure of uncertainty or disorder (noise). These two characteristics are analytically related and can provide a theoretical basis for describing signal characteristics. In papers [13-15], information entropy detection methods have been successfully applied to signal recognition. In this paper, we propose a new information-entropy method for gravitational-wave data analysis. The novelty of the method lies in the use of conditional information, defined as the difference between the joint and conditional entropy. In addition, this method does not require the construction of a theoretical bank of signal templates.

The contents of this paper are structured as follows. In section 1, we introduce our measure of conditional information by comparing it with the usual definition of Shannon's mutual information. In

section 2, we present the data generation for testing our method and describe our algorithm for determining the difference in conditional information. In Section 3, we present a result of numerical analysis of model and real gravitational wave signals. In section 4, we make a conclusion.

1 Conditional information defined through the entropy difference

Let us consider discrete time series of signals $X = \{x[n]\}$, $Y = \{y[n]\}$ given through samples with numbers n , which have a statistical relationship, forming an ensemble (X, Y) . Assume that X is the received signal, $Y = \{\Delta x[n]\}$ is the signal interference. By the signal interference we mean pulsed, chaotic and noise disturbances of the signal $\Delta x[n]$ caused by nonlinear distortions of the signal itself and external influences.

Let us take the notation $\Delta x[n]$, $n = 1, 2, 3$ – numbers of the samples, $y[n] = \Delta x[n]$ – the interval of deviation from $x[n]$ caused by interference. The deviation interval is defined by the central (symmetric) difference $\Delta x[n] = (x[n+1] + x[n-1])/2 - x[n]$. Using this form of $\Delta x[n]$ instead of the one-sided difference $x[n+1] - x[n]$ allows us to consider the second derivative of X , i. e. the wave shape. The second derivative of any nonlinear function is nonzero except for its zero value at the inflection point. Near the inflection point, the function changes impulsively, which gives a reason to use a neutral difference to detect GW in the form of nonlinear bursts of the signal disturbances. At the point of inflection, the required information will be minimal.

Further, we consider the general concepts of mutual information and entropy, followed by the introduction of our measure. It is known that mutual information measures the nonlinear relationship between two random variables. Moreover, mutual information can show us how much information can be obtained from one random variable by observing a second random variable. Mutual information has a close relationship with the concept of entropy. Because in some cases, when one of the variables is known, mutual information to some extent can reduce the uncertainty of another random variable. Thus, this means that a high value of mutual information indicates a large reduction of uncertainty, and a small reduction if the value is low. In cases where the mutual information is zero, this means that the two random variables are independent [16-18].

The commonly used mutual information $I(Y; X)$ transmitted over the communication channel X is determined by the difference between the one-dimensional and conditional Shannon entropies $H(Y)$, $H(Y|X)$ [18-20]. The relationship between these values is shown in the following formula:

$$I(Y; X) = H(Y) - H(Y|X), \quad (1)$$

As explained before, mutual information $I(Y; X)$ is related to entropy and to understand what $I(Y; X)$ actually means, we need to define entropy and conditional entropy. It is known that entropy of a random variable is the average level of “uncertainty” inherent to the variable’s possible outcomes. For example, if we have a discrete random variable Y , with possible outcomes x_1, x_2, x_n which happen with probability p_1, p_2 , the entropy of Y is defined as following:

$$H(Y) = - \sum_{i=1}^N \sum_{j=1}^M p(x[i], y[j]) \log_2 p(y[j]). \quad (2)$$

Entropy $H(Y)$ can measure the level of expected uncertainty in a random variable. This means that $H(Y)$ is roughly how much information can be learned of the random variable Y by observing just one sample. Conditional entropy can measure how much uncertainty has the random variable Y , when we know the value X . And we can define conditional entropy according to the following formula:

$$H(Y|X) = - \sum_{i=1}^N \sum_{j=1}^M p(x[i], y[j]) \log_2 p(y[j]|x[i]), \quad (3)$$

where,

$$p(y[j]|x[i]) = p(x[i], y[j]) / p(x[i]). \quad (4)$$

And $p(x[i], y[j])$, $p(y[j])$, $p(y[j]|x[i])$ are the joint, one-dimensional, and conditional probabilities of the points of the phase space $(X; Y)$ falling into squares with a relative size $\delta \ll 1$. In formula (2), the equal to 1 sum over i is left for convenience of further analysis [21-23].

From formulas (1)-(3) follows

$$I(Y; X) = \sum_{i=1}^N \sum_{j=1}^M p(x[i], y[j]) \log_2 \frac{p(x[i], y[j])}{p(x[i])p(y[j])}. \quad (5)$$

In the absence of a mutual correlation between $x[i], y[j]$, there is $p(x[i], y[j]) = p(x[i])$, hence, $I(Y; X) = 0$. From the structure of formula (5), mutual information is symmetric with respect to permutation of variables $X \rightleftharpoons Y: I(Y; X) = I(X; Y)$, the roles of the signal interference are not different. For these reasons, for the set goal (X and Y should be different variables), it is necessary to use another measure of certainty - conditional information, which we will determine through the difference of the entropies.

$$I(Y|X) = H(X, Y) - H(Y|X). \quad (6)$$

In formula (6) $H(X, Y)$ is a joint entropy of the ensemble [24-26]:

$$H(X, Y) = \sum_{i=1}^N \sum_{j=1}^M p(x[i], y[j]) \log_2 p(x[i], y[j]) \quad (7)$$

When we consider together two random variables the joint entropy measures the uncertainty. In contrast to mutual information, conditional information is asymmetric with respect to the permutation of the variables $X \rightleftharpoons Y$ since $H(Y|X) \neq H(X|Y)$. Dividing formula (6) by (7), we derive a kind of well-known conservation law for the normalized values of conditional information and entropy.

$$\tilde{I}(Y|X) + \tilde{H}(Y|X) = 1, \quad \tilde{H} = H/H(X, Y) \quad \tilde{I} = I/H(X, Y). \quad (8)$$

The relationship between information and entropy in the form of formula (8) is known for the Boltzmann entropy for an equilibrium state, or in the case of choosing Y as constant parameters. We choose the condition Y in the form of characteristic features of the desired signal determined from the experimental data.

From formula (8) we get the difference of conditional information

$$\Delta \tilde{I} = \tilde{I}(Y|X) - \tilde{I}(X|Y) = \tilde{H}(X|Y) - \tilde{H}(Y|X). \quad (9)$$

When the variables $X \rightleftharpoons Y$ are permuted, conditional information and entropy acquire different meanings. For example, $\tilde{I}(Y|X)$ determines information about a burst of nonlinear disturbances Y (about the presence of GW) in a known noise signal X . The corresponding decrease in entropy describes $H(Y(X)) - H(Y|X)$. The decrease in information corresponds to an increase in entropy $\tilde{H}(X|Y)$. If $\Delta \tilde{I} > 0$, the signal is detected, while if $\Delta \tilde{I} < 0$ there is no signal. This criterion can also have positive values in cases with rearranged variables ($X; Y$). These cases correspond to a sharp decline in Y near the inflection point. The use of $\Delta \tilde{I}$ increases the reliability of signal analysis.

Assume that the calculated variable Y has a systematic error $\Delta Y (Y = Y[0] + \Delta Y)$. Limiting ourselves to the first term of the Taylor series expansion at the point $Y[0]$, we get the function $\Delta \tilde{I}$

$$\Delta \tilde{I} = \Delta \tilde{I}(Y[0]) + \left. \frac{d\Delta \tilde{I}}{dY} \right|_{Y=Y[0]} \Delta Y \quad (10)$$

When calculating the derivative in (10) through finite differences, ΔY falls out. For weak signals with a signal-to-noise ratio of the order of one, a small increment from $\Delta \tilde{I}$ may not arise as a signal. Thus, a weak signal with a systematic error ΔY of the individual terms in (9) may be absent when calculating $\Delta \tilde{I}$.

2 Algorithm for determining the difference of conditional information

2.1 Data generation

To thoroughly test our algorithm, we use PyCBC package [27] to generate the GW signals. The parameters of the model signals are selected according to the article [9]. The GW signal is determined by the component masses m_1, m_2 randomly selected in the range from 10 to $50M_{\odot}$ and phases in the range φ_0 from 0 to 2 pi. In accordance with the selected target SNR, the amplitude and distance of the source are determined. We assume the presence of one LIGO Hanford detector, whose inclination and polarization

parameters are equal to 0, since any change in these parameters can be completely absorbed by changes in the amplitude and phase of the signal. The signals are whitened by dividing the Fourier transformed signal by the square root of the power spectral density (PSD) to reduce power at frequencies within the sensitivity of the detector. Noise modeling and whitening is also done using the same PSD that was used to whiten the signals. The colored noise whitening eliminates error sources, and it is applicable to real noise. The simulated signals are randomly placed in a time series (-16:16 s) with the condition that the peak amplitude of each signal is randomly located in the time series range from 0.75 to 0.95. After that, to achieve the optimal signal-to-noise ratio (SNR), the signal amplitude is scaled. And the optimal SNR ρ_{opt} can be determined by [9]

$$\rho_{opt}^2 = 4Re \left[\int df \frac{\tilde{h}(f)\tilde{h}^*(f)}{S_n(f)} \right], \quad (11)$$

where \tilde{h} is the frequency domain representation of the GW strain, \tilde{h}^* is its conjugate, S_n is the PSD and Re extracts the real part of the complex number. A data set was generated for each predefined optimal SNR value in the range from 2 to 10 with integer steps.

2.2 Algorithm realization

From the discrete signal of the GW, ΔX is calculated by the formula:

$$\Delta x[n] = \frac{x[n+1] + x[n-1]}{2} - x[n] \quad (12)$$

Using the well-known Sliding Window algorithm, we divide a given discrete time series $x[n]$ and $\Delta x[n]$ into windows with a length of L points. If we assume that the time delay parameter of the analysis window is 1, then the signal sequence $X[n]$ can be divided into segments with the number $N-L$, which form the following matrices $x[n] \rightarrow X$ and $\Delta x[n] \rightarrow \Delta X$.

$$X = \begin{bmatrix} x[1] & x[2], \dots & X[L] \\ x[2] & x[3], \dots & x[L+1] \\ X[N-L] & \dots & x[N] \end{bmatrix}$$

and

$$\Delta X = \begin{bmatrix} \Delta x[1] & \Delta x[2], \dots & \Delta x[L] \\ \Delta x[2] & \Delta x[3], \dots & \Delta x[L+1] \\ \Delta x[N-L] & \dots & \Delta x[N] \end{bmatrix}$$

To determine the difference of conditional information, the plane $X[n]$ and $\Delta X[n]$ is constructed and divided into cells ($i \times j$). Next, the probability of each cell is determined and the probability matrix $P(x_i, y_j)$ is obtained. From the probability matrix, we determine the difference of conditional information by the (9).

3 Results of numerical analysis of gravitational wave signals

In our method, when we detect the GW signal, the difference of conditional information $\Delta \tilde{I}$ increases, while the noise fluctuates around zero. In order to define the window size and threshold value of conditional information $\Delta \tilde{I}$, we calculate the *false positive ratio* (FPR) (Fig. 1).

The FPR is one of the important standard metrics, that is used to evaluate the detection of GWs. The FPR can be defined as follows

$$FPR = \frac{FP}{FP + TN}, \quad (13)$$

where FP is the number of false positive predictions, TN is the number of true negatives.

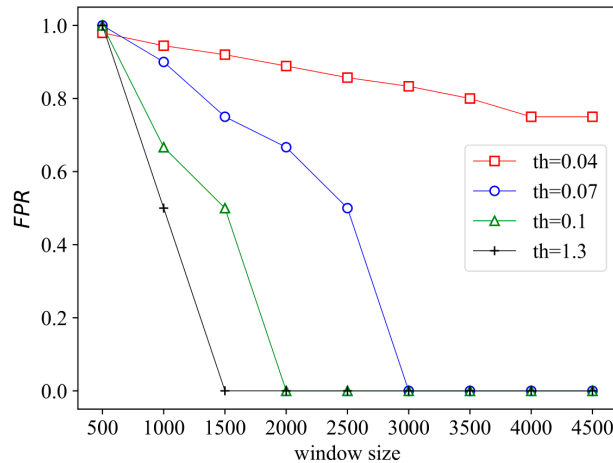


Fig. 1. The plot shows the dependence of the FPR on the window size, where, the threshold (th) value changes in the range from 0.04 to 0.1 with a step of 0.02. We calculated the FPR for the one GW model signal, whose SNR=10.

According to the figure 1, when the window size is $L > 2000$ and the threshold value is $th > 0.1$, the signal is detected without any errors. From a data set consisting of 10 000 signals at each SNR, the number of detected signals was calculated using our method. Further, to calculate the efficiency (fig.2), we choose the window size of 3000 and a threshold value of 0.1 for the validation accuracy.

The efficiency is then determined by

$$efficiency = \frac{N_{\Delta\tilde{I} > th}}{N_s}, \quad (14)$$

where $N_{\Delta\tilde{I} > th}$ is the number of detected signals, N_s is the total number of signals.

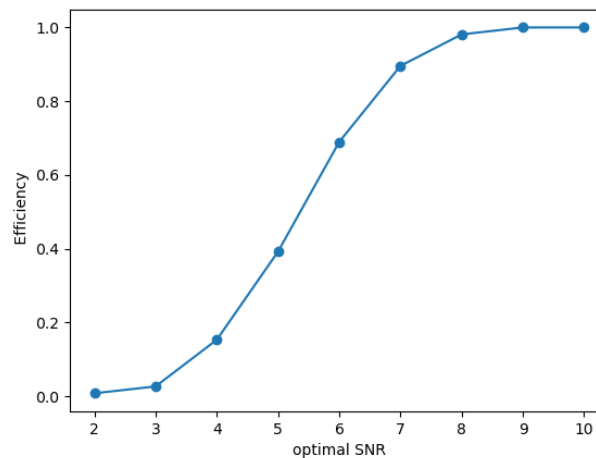


Fig. 2. The efficiency as a function of optimal SNR

The results in Fig. 2 show that the efficiency increases with the optimal SNR and achieves 100 % at an SNR of 9. To demonstrate the feasibility of our method, we conducted analysis using real LIGO data. Fig. 3 (b, c, d, e) shows the values $\tilde{I}(Y;X), \tilde{I}(Y|X), \tilde{I}(X|Y), \Delta\tilde{I}$ for the GW150914 event, calculated by formulas (1), (8), (9), correspondingly.

From Fig. 3 (b) it can be seen that the value of mutual information $\tilde{I}(Y;X)$ fluctuates around the same level and does not changed over the entire time interval and shows nearly 0.19. While the value of conditional information $\tilde{I}(Y|X)$ and the difference of conditional information $\Delta\tilde{I}$ increased at the time of detection of the desired signal nearly from 0.7 to 0.9 and from 0 to 0.6, respectively. As for the value of conditional information $\tilde{I}(X|Y)$, it decreased at the time of detection of the gravitational wave from 0.75 to 0.25 approximately.

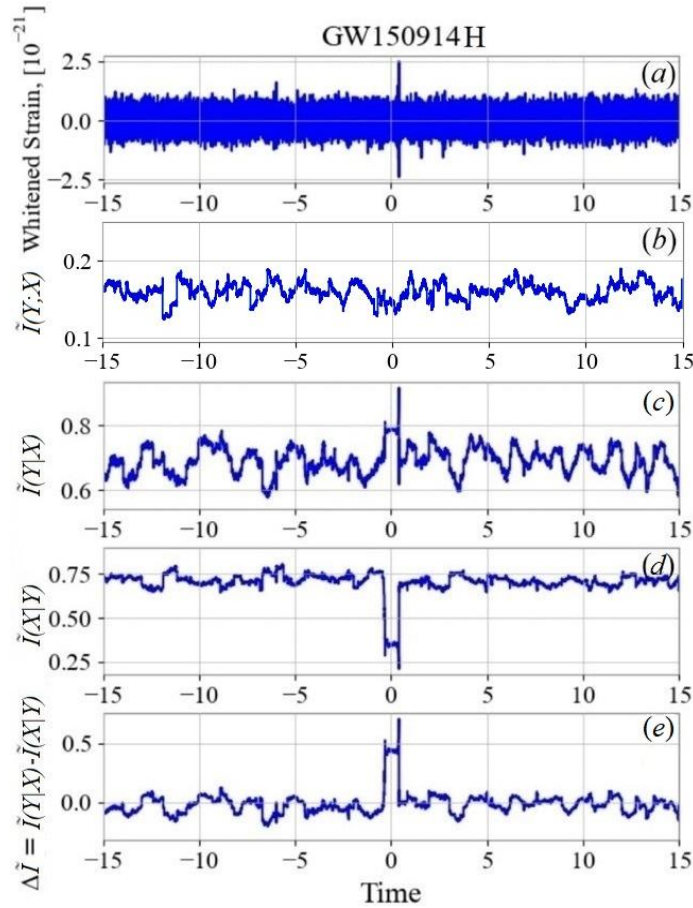


Fig. 3. Event GW150914H: whiteness signal GW (a), mutual information $\tilde{I}(Y;X)$ (b), conditional information $\tilde{I}(Y|X)$ (c), conditional information $\tilde{I}(X|Y)$ (d), difference of conditional information $\Delta\tilde{I}$ (e), where number of samples $L=3000$

The validity of using the information-entropy method proposed by us is shown in Table 1.

Table 1. Results of information-entropy analysis of GW signals from the Handford (H) and Livingston (L) detectors. M/M_{\odot} is the total mass of black holes relative to the mass of the Sun, SNR is the signal-to-noise ratio, R is the distance to the source according to [1-5, 28].

Event	$\tilde{I}(Y X)$	$\tilde{I}(X Y)$	$\Delta\tilde{I}$	SNR	M/M_{\odot}	R
[1], GW150914H GW150914L	+ +	+ +	+ +	24.4	62	410 Mpc
[2], GW151226H GW151226L	+ (minimum) -	- F-	+ (Y X → X Y) -	13.1	21.4	4292 Mpc
[3], GW170104H GW170104L	+ +	+ +	+ +	13.0	51.1	880 Mpc
[4], GW170608H GW170608L	- -	- -	- -	14.9	18.5	340 Mpc
[5], GW170814H GW170814L	+ +	+ +	+ +	15.9	56.0	5518 Mpc
[6], GW170817H GW170817L	+ +	+ +	+ +	33.0	2.73	40 Mpc

The following Table 1 presents an analysis of the mutual $\tilde{I}(Y;X)$, conditional information $\tilde{I}(Y|X)$ of six gravitational wave (GW) events recorded by the Hanford (H) and Livingston (L) detectors. The plus (+) symbols mean the detection of a signal with highlighted positive values $\tilde{I}(Y|X)$, $\tilde{I}(X|Y)$, $\Delta\tilde{I}$. Minus (-) symbols mean that there is no highlighted maximum or minimum in the difference of conditional information. The GW151226, GW170608L signals have a low signal-to-noise ratio and total masses of black holes relative to other signals (Table 1).

Conclusion

From the above study, it can be seen that the proposed information-entropy method demonstrates the good performance in GW data recognition. According to the obtained results, in all six GW events the values of mutual information $\tilde{I}(Y;X)$ do not changed over the entire time interval, while the difference of conditional information $\Delta\tilde{I}$ increases sharply at the time of gravitational waves detection. It clear that the new measure introduced by us – conditional information $\Delta\tilde{I}$ detects a signal, and the known measure – mutual information $\tilde{I}(Y;X)$ does not reveal a signal. According to the results obtained, the method can serve as an addition to the existing methods for analyzing GW signals.

Furthermore, this method in comparison with the well-known matched filtering method can discover signals beyond the existing templates. We believe that this method will undoubtedly play an important role in searching GW signals beyond what we have in the existing template bank.

Acknowledgements

This research has been funded by the Science Committee of the Ministry of Science and Higher Education of the Republic of Kazakhstan (Grant No. AP14872061).

We would like to thank Al-Farabi Kazakh National University, Department of Physics and Technology and LIGO Open Science Center for making the data and Python scripts available online.

REFERENCES

- 1 Abbott Benjamin P., et al. Observation of gravitational waves from a binary black hole merger. *Physical review letters*, 2016, 116.6: 061102. doi:10.1103/PhysRevLett.116.061102
- 2 Scientific L.I.G.O., et al. GW170104: observation of a 50-solar-mass binary black hole coalescence at redshift 0.2. *Physical review letters*, 2017, 118.22, 221101. doi:10.1103/PhysRevLett.118.221101
- 3 Abbott Benjamin P., et al. GW170608: observation of a 19 solar-mass binary black hole coalescence. *The Astrophysical Journal Letters*, 2017, 851.2, L35. doi: 10.3847/2041-8213/aa9f0c
- 4 Abbott Benjamin P., et al. GW170817: observation of gravitational waves from a binary neutron star inspiral." *Physical review letters*, 2017, 119.16, 161101. doi: 10.1103/PhysRevLett.119.161101
- 5 Abbott Benjamin P., et al. GW170814: a three-detector observation of gravitational waves from a binary black hole coalescence. *Physical review letters*, 2017, 119.14, 141101. doi: 10.1103/PhysRevLett.119.141101
- 6 Abbott R., et al. GWTC-3: compact binary coalescences observed by LIGO and Virgo during the second part of the third observing run. *arXiv preprint arXiv:2111.03606* (2021). doi: 10.48550/arXiv.2111.03606
- 7 Arnaud Nicolas. LIGO and Virgo detector characterization and data quality: Contributions to the O3 run and preparation for O4. *Nuclear Instruments and Methods in Physics Research Section A: Accelerators, Spectrometers, Detectors and Associated Equipment*, 2023, 1048, 167945. doi: 10.1016/j.nima.2022.167945
- 8 Razzano Massimiliano, et al. GWitchHunters: Machine learning and citizen science to improve the performance of gravitational wave detector. *Nuclear Instruments and Methods in Physics Research Section A: Accelerators, Spectrometers, Detectors and Associated Equipment*, 2023, 1048, 167959. doi: 10.1016/j.nima.2022.167959
- 9 Schäfer Marlin B., et al. Training strategies for deep learning gravitational-wave searches. *Physical Review D*, 2022, 105.4, 043002. doi: 10.1103/PhysRevD.105.043002
- 10 Xia H., Shao L., Zhao J., Cao Z. Improved deep learning techniques in gravitational-wave data analysis. *Physical Review D*, 2021, 103(2), 024040. doi: 10.1103/PhysRevD.103.024040
- 11 Gabbard Hunter, et al. Matching matched filtering with deep networks for gravitational-wave astronomy. *Physical review letters*, 2018, 120.14, 141103. doi: 10.1103/PhysRevLett.120.141103
- 12 Aveiro João, et al. Identification of binary neutron star mergers in gravitational-wave data using object-detection machine learning models. *Physical Review D*, 2022, 106.8, 084059. doi: 10.1103/PhysRevD.106.084059
- 13 Zhang Zhen, et al. Modulation signal recognition based on information entropy and ensemble learning. *Entropy*, 2018, 20.3, 198. doi: 10.3390/e20030198
- 14 Wang, Hui, et al. A new method of cognitive signal recognition based on hybrid information entropy and DS evidence theory. *Mobile Networks and Applications*, 2018, 23, 677-685. doi: 10.1007/s11036-018-1000-8

- 15 Li Han, Yanzhu Hu, Song Wang. A novel blind signal detector based on the entropy of the power spectrum subband energy ratio. *Entropy*, 2021, 23.4, 448. doi: 10.3390/e23040448
- 16 Kraskov A., Stögbauer H., Grassberger P. Estimating mutual information. *Physical review*, 2004, E 69.6, 066138. doi: 10.1103/PhysRevE.69.066138
- 17 Li Wentian. Mutual information functions versus correlation functions. *Journal of statistical physics*, 1990, 60, 823-837. doi: 10.1007/BF01025996
- 18 Jun Xie, et al. Conditional entropy based classifier chains for multi-label classification. *Neurocomputing*, 2019, 335, 185-194. doi: 10.1016/j.neucom.2019.01.039
- 19 Gu Rongbao. Multiscale Shannon entropy and its application in the stock market. *Physica A: Statistical Mechanics and its Applications*, 2017, 484, 215-224. doi: 10.1016/j.physa.2017.04.164
- 20 Liu Jerry, et al. Conditional entropy coding for efficient video compression. *Computer Vision–ECCV 2020: 16th European Conference, Glasgow, UK, August 23–28, 2020, Proceedings, Part XVII. Cham: Springer International Publishing*, 2020. doi: 10.1007/978-3-030-58520-4_27
- 21 Mentzer Fabian, et al. Conditional probability models for deep image compression. *Proceedings of the IEEE Conference on Computer Vision and Pattern Recognition*, 2018. doi: 10.48550/arXiv.1801.04260
- 22 Holodinsky Jessalyn K., et al. Drip and ship versus direct to endovascular thrombectomy: the impact of treatment times on transport decision-making. *European Stroke Journal*, 2018, 3.2, 126-135. doi: 10.1177/2396987318759362
- 23 Ackerman Nathanael L., Cameron E. Freer, Daniel M. Roy. On the computability of conditional probability. *Journal of the ACM (JACM)*, 2019, 66.3, 1-40. doi: 10.1145/3321699
- 24 Berlin S. Jeba, Mala John. Spiking neural network based on joint entropy of optical flow features for human action recognition. *The Visual Computer*, 2022, 38.1, 223-237. doi: 10.1007/s00371-020-02012-2
- 25 Zhang Gengxi, et al. Modeling NDVI using Joint Entropy method considering hydro-meteorological driving factors in the middle reaches of Hei river basin. *Entropy*, 2017, 19.9, 502. doi: 10.3390/e19090502
- 26 Safarihamid Kimia, Alireza Pourafzal, Alireza Fereidunian. A joint-entropy approach to time-series classification. *2021 7th International Conference on Signal Processing and Intelligent Systems (ICSPIS)*. IEEE, 2021. doi: 10.1109/ICSPIS54653.2021.9729371
- 27 itz A.H., Harry I.W., Willis J.L., Biber C.M., Brown D.A., Pekowsky L.P., Dal Canton T., Williamson A.R., Dent T., Capano C.D., et al. Pycbc software, *GitHub repository*, 2017.
- 28 Abbott Benjamin P., et al. GW151226: observation of gravitational waves from a 22-solar-mass binary black hole coalescence. *Physical review letters*, 2016, 116.24, 241103. doi: 10.1103/PhysRevLett.116.241103

DOI 10.31489/2023NO2/87-98

UDC 62; 654

PERFORMANCE ANALYSIS AND DEVELOPMENT OF PATH LOSS MODEL FOR TELEVISION SIGNALS IN IMO STATE, NIGERIA

Iwuji P.C.^{1*}, Okoro R.C.¹, Idajor J.A.², Amajama J.¹, Ibrahim A.T.¹, Echem C.O.¹

¹ Department of Physics, University of Calabar, Calabar, Nigeria, pciwuji@unical.edu.ng

² Department of Electrical and Electronic, University of Calabar, Calabar, Nigeria

It is impossible to overstate the importance of propagation models in wireless network planning, frequency assignment, and television parameter evaluation. The fact that no two locations are identical in terms of climatic conditions, building patterns, terrain, etc. makes using path loss predicting models for any area extremely challenging. Therefore, it is impossible to develop a single path loss model that applies to all environmental settings. The main aim of this study is to develop a path loss model for NTA channel 12 Owerri and evaluate its performance based on received signal strength values along five selected routes in Imo State, Nigeria. A suitable path loss model was developed by critically analyzing the measured path loss values of each base station, which were retrieved from the signal strength data received. The values of the developed path loss model were compared to those of other empirical path loss models developed by other researchers as well as the measured path loss values. The results show that the proposed path loss model is well suited for predicting the path loss of NTA channel 12 Owerri signals in the study environment, while the other conventional empirical models taken into consideration in this study overestimated the path loss of NTA channel 12 Owerri signals with Root Mean Square Error and Mean Error of 63.65 and above. Additionally, the findings indicate that NTA Owerri performs poorly at a distance of 18 kilometers from the base transmitting station. The overall findings are helpful for designing prospective television network channels in the study location and other similar environments.

Keywords: Path loss; Television; Path loss model; Received signal strength; Wireless network

Introduction

In today's world, the importance of wireless communications, particularly television (TV), cannot be overstated. According to data, more people than expected already use mobile devices to watch television in several nations [1]. Customers want a strong signal and good signal coverage for better viewing in these locations so they may obtain better information and other benefits of television. These television systems are utilized everywhere, both indoors and outdoors [2]. When designing the channel capacity, it is critical to take into consideration the environment in which the service will be provided to provide superior television services. Radio frequency barriers, scattering, and undulating terrain factors all contribute to the inconsistency of terrestrial television propagation in spread spectrum situations. The radio channel has an impact on how well television communication systems perform, and the propagation path between the transmitter and receiver might be anything from a normal line-of-sight (LOS) to a direction that is substantially impeded by nearby structures and vegetation [3]. In an urban setting, where most television systems are used, there is no direct signal arriving at the receiver. Instead, an integrated signal is created by diffraction, reflection, and scattering off numerous obstacles, such as buildings and moving objects.

The development of a transmission pattern that would improve coverage and reduce latency and interference is the primary design tenet for every wireless television broadcasting system. Any television system designed to operate in a specific setting must function the way a radio propagation channel behaves in that environment in order to be effective and be implementable [4]. Signal attenuation, or path loss occurs at all operating frequencies and gets worse with distance. Different signals may enter the detector in a subtractive or additive manner. This will result in minor signal fluctuation or multipath fading. Multipath fading is caused by the signal being reflected, scattered, and diffracted by environmental physical objects [5]. Amongst the most critical components of the television transmission environment is propagation path loss. Path loss is the term used to describe the decline in radio signal power caused by multipath fading, shadowing, and signal fluctuation on any radio signal path [6]. Path loss in wireless communication

reception can be caused by a number of factors, such as television units, diffraction, refraction, and reflection [7]. Path loss features and models are employed to compute wireless network coverage and received signal strength (RSS) of electromagnetic waves that are broadcast at various locations inside a specific transmission perimeter. These models are a useful substitute for real-field measurements, which can take a lot of time and resources. Deterministic, semi-deterministic, and empirical path loss models are the three most common types of path loss models. Because they are straightforward, user-friendly, and require less computing efficiency than deterministic models, empirical models are frequently employed for path loss predictions [8].

In order to effectively plan and optimize radio networks in various propagation settings, a variety of research-based path loss models have been created. In general, no single path loss prediction model is regarded as the best or universally accepted as the most accurate; rather, the precision of a prediction model depends on how well the parameters required in the model correspond to those present in the measured field data [9]. Field measured data and predicted path loss values are made openly accessible to the public in this research article. In this study, the measured data was used to create a path loss model for NTA Owerri in South-East Nigeria and to evaluate signal quality in terms of efficiency. Additionally, the datasets are fully defined to aid future work by professionals in the engineering area, radio network engineers, research institutions, and other researchers. The path loss exponent, whose value varies according to the transmission conditions and environment, can be used to represent path loss. The path loss exponent may be higher in some environments, such as structures, public parks, and other urban locations, than it is in a free-space environment or a relatively scattered environment [10]. These values rely on the transmission environment and system and are affected by geographical features, settlement types, the transceiver distance, as well as the position, height, and type of antennas. The path loss notation, or proponent, is one of the most important features in all propagation loss and Rayleigh fading models, and understanding it for a specific environment simplifies signal coverage and propagation analysis [11].

The development of social and human interactions in society today is greatly enhanced by television network technology. Due to a dearth of knowledge about how television operations function in large-scale, concentrated, and constrained environments, particularly in urban areas, recent applications are quite limited. In an ideal arrangement, the total signal power transmitted is what is intended to be received at the receiving head. However, this is not always the case due to some common transmission issues [12; 13]. A plethora of man-made and natural factors, including mountains, tall buildings, atmospheric pressure, temperature, and relative humidity of the specific transmission environment, contribute to some of the technical difficulties with terrestrial television broadcasting and reception, in addition to the technical shortcomings of the transmitting stations. Like all other television transmitting stations, the Nigeria Television Authority (NTA) Owerri is not exempt from these adverse difficulties [3]. There has been lots of research conducted in the past to estimate and address the problems of terrestrial television signal attenuation. Some of these studies involved the development of models or modifications of existing models to aid in the prediction of the quality of television signals at specific locations. However, none of these studies were conducted for NTA channel 12 Owerri to evaluate the television station's signal attenuation level. Additionally, no one has been able to develop a path loss model that could help to some extent in describing the signal intensity generated by NTA Owerri. As a result, NTA Owerri operators need to perform field measurements on a regular basis to obtain the necessary signal data, which lowers the frequency and level of maintenance on their broadcasting systems. This has also caused a decrease in the level of routine checks on the performance of the NTA Owerri signal strength by the television operators. This is the rationale for our research, which we conducted to develop a path loss model for NTA channel 12, Owerri and evaluate its performance in Imo State, Nigeria.

1 Methodology

1.1 Study location

Imo State is a state in the South-Eastern geopolitical region of Nigeria. It is bordered to the west by Abia State, to the south and east by Rivers State, and to the north by Anambra State. It gets its name from the Imo River, which runs along the state's eastern border. Imo State has Owerri as its capital and is known as the "Eastern Heartland" due to its location in the Eastern part of Nigeria and the fact that it is the most economically successful state in the area. Imo state is the fourteenth (14th) most populated state out of the 36 states in Nigeria, with an estimated population of more than 5.4 million as of 2016 [14]. The state has an area of around 5,100 sq km and is located between latitudes 4° 45' N and 7° 15' N, and longitudes 6° 50' E and 7° 25' E. The annual rainfall ranges from 1,500 mm to 2,200 mm, with a thickness of 60 to 80 inches, during the

rainy season, which starts in April and lasts until October. Its average yearly temperature is over 20 °C, resulting in a relative humidity that is typically 75%, though it can get as high as 95% during the rainy season.

Imo state is the third smallest state in terms of area. Geographically, the state is divided between the drier Cross-Niger transition woods in the center and the swamp forests of the Niger Delta in the extreme east. The state's lakes and rivers, including the Oguta Lake in western Imo State and the Orashi, Otamiri, Imo, and Awbana Rivers, are additional significant geographical features. Tropical rain forest is the predominant kind of vegetation in Imo State [15].

1.2 Measurement campaign

The goal of this research is to examine the signal strength generated by NTA channel 12, Owerri, and to develop a suitable path-loss prediction model for forecasting the path loss of the NTA channel 12, Owerri, signals. To do this, the NTA channel 12 Owerri signal strength was monitored along five different routes, starting from the broadcasting base station, using a cable television (CATV) signal analyzer. The RSS levels were measured along the various signal strength measurement routes, starting from 2 km to 24 km, at intervals of 2 km. The average received signal at each measurement site was used to average out inconsistent signals.

Table 1 shows the routes description where signal strength measurements were taken, which was properly considered based on their accessibility and road network. When the field measurements were being taken, a number of variables that could affect the signal quality before it reaches the intended customers were taken into account. These variables include atmospheric pressure, temperature, relative humidity, complex multi-channel environments, radio frequency generating equipment, tall structures, etc. Signal strength measurements were made during different hours of the day and months, from October 2021 to May 2022. The average field strength measurement results for the research period were taken in order to determine how well the signal strength produced by the NTA channel 12 Owerri transmitters performed along the chosen routes. The given data was then analyzed using Mat lab and the Python programming language.

Table 1. Routes description

Routes	Route A	Route B	Route C	Route D	Route E
Description(s)	Owerri-Onitsha	Owerri-Aba	Owerri-Umuahia	Owerri-Orlu	Owerri-Okigwe

An S110/S110D 5-870 MHz handheld analog cable TV radio frequency (RF) signal level meter was employed in this study as the CATV meter. The signal strength produced by any terrestrial television transmitter can be measured using a cable or community television (CATV) signal strength analyzer. It is a typical receiver that can measure the signal intensity produced by a signal generator in decibel microvolts (dBuV), and it is mostly used in TV signal level construction, repair, maintenance, and measurement. This S110/S110D CATV signal strength meter offers robust, all-encompassing performance and is compatible with analog and digital television and radio channels. It measures frequencies between 5 and 870 MHz with a frequency accuracy of $+50 \times 10^{-6}$ and a temperature range of $20^{\circ}\text{C} + 14^{\circ}\text{C}$. This S110/S110D CATV signal strength meter for measuring television signal quality because it has a measuring range of 5 to 120 dBuV with a measuring accuracy of +2 dB and a carrier-to-noise measurement range of 20 to 50 dB for a signal input range of greater than or equal to 85 dBuV with an accuracy of +3 dB at a temperature of $20^{\circ}\text{C} + 14^{\circ}\text{C}$.

The type of receiving antenna used for this research is the Yagi antenna, which is a directional antenna used in telecommunication when the frequency is above 10 MHz. The frequency range of the receiving antenna is between 10–870 MHz for channels of 1– 69 UHF and VHF with a gain of 20 ± 3 dB, a noise coefficient factor of about 2 dB and an impedance of 75Ω .

The NTA channel 12 in Owerri, Imo State, Nigeria, which broadcasts at a frequency of 224.25 MHz, is the transmitting station of interest in this research. It is situated at Chief Achike Udenwa Avenue, Akanchawa, New Owerri Road, Owerri, Imo State, Nigeria. It is one of the most viewed television channels in Imo state, Nigeria because it is the sole federal government-owned TV channel there. The parameters of the NTA channel 12 Owerri transmitter are shown in Table 2.

Table 2. Transmitting parameters of nta channel 12 owerri transmitting station

Serial No.	Transmitting parameters	Description
1	Base station frequency	189.25 MHz
2	Transmission Type	Rohde & Schwarz 5 KW
3	Base station transmitting power	2.6 KW
4	Signal power transmitted	57.1 dB $I? V$
5	Base station channel	Channel 12
6	Height of transmitting antenna	230 m
7	Transmitting antenna gain	30.02 dB
8	Base station position	Long. 6.50° N Lat 7.15° E
9	Receiving antenna orientation	Omni-directional
10	Height of receiving antenna	5 → m

1.3 Empirical path loss model

The major emphasis of propagation models has typically been on predicting the strength of the received signal, with the distance (d) between the transmitter and receiver being the most important factor. Path loss is the decrease or attenuation in power density of a radio wave as it travels across space. In order to effectively plan and optimize radio networks in various propagation settings, a number of empirical path loss models have been developed. This session discusses some of the few existing empirical path loss models that were used in this investigation.

1.3.1 Free-space path loss model

The simplest and most common empirical path loss model, the free-space model, simply considers frequency (f) and distance (d). Given that there are no barriers or atmospheric influences during free-space transmission, the path loss is given by

$$P_r = P_t G_t G_r \left(\frac{\lambda}{4\pi d}\right)^2 \quad (1)$$

where P_r = receive power, P_t = transmit power, G_t = gain of transmitter, G_r = gain of receiver, and d is the transmitter and receiver distance. The free-space path loss model in Equation 1 can be expressed as follows [16]:

$$L_{FS} = 32.45 + 20\log_{10}d(Km) + 20\log_{10}f(MHz), \quad (2)$$

where f = frequency in MHz and distance in Km

1.3.2 Walfisch-Ikegami propagation model

A different name for it is the empirical COST-Walfisch-Ikegami propagation model. In this model, only the buildings on the vertical plane were considered. However, this model is thought to be quite accurate, particularly in urban settings. The Cost 231 Walfisch-Ikegami model consists of three essential components, which are shown below [17].

$$L = L_0 + L_{rts} + L_{msd} \quad (3)$$

L_0 is the free space path loss which is represented by $L_0 = 32.5 + 20\log d + 20\log f$

The roof-top-to-street (rts) diffraction and scatter loss term is given by:

$$L_{rts} = -16.9 - 10\log 10^w + 10\log 10^f + 20\log 10^{(H_{roof} - H_m)} + L_{cri}$$

and the component of multi-screen diffraction loss is given by:

$$L_{msd} = L_{bsh} + ka + kd \log 10^d + kf \log 10^f + 9 \log 10^b$$

When there is a line-of-sight path between the transmitter and the receiver in a specific region, that is, when the source transmitting appliance is below the roof, the following equation can be used [17]:

$$L_b = 42.6 + 25 \log 10^d + 20 \log 10^f \quad \text{for } d \geq 0.020 \text{ Km} \quad (4)$$

The path loss estimates for the Cost 231 Walfisch-Ikegami model were computed in this study using equation 4.

1.3.3 The Cost Hata model

The path loss model broadens the urban Hata model, which is based on the Okumura model, to a wide frequency range of roughly 2 GHz. For frequency ranges between 800 and 2000 MHz, this model utilizes experimental and descriptive techniques to calculate transmission loss in an urban environment. The path loss equation for the COST 231 Hata Model is as follows [18]:

$$L = 46.3 + 33.9 \log f - 13.82 \log h_B - a(h_r) + (44.5 - 6.55 \log h_b) \log d + C \quad (5)$$

According to the Hata Model for urban areas, C is equal to zero for medium cities and suburban areas and three for metropolitan areas. L is the median path loss in dB, f is the transmission frequency in MHz, h_B is the base station antenna height in meters, d is the link distance in kilometers, h_r is the receiver station antenna effective height in meters, and $a(h_r)$ is the receiver station antenna height correction factor. For sub-urban and rural areas, $a(h_r) = [1.1 \log(f) - 0.7]h_r - 1.56 \log(f) - 0.8$ and for urban areas, $a(h_r) = 3.20[\log 10(11.75h_r)]^2 - 4.97$; for $f > 400$ MHz

1.3.4 Okumura's model

One of the most frequently applied signal prediction models in urban areas is Okumura's. This type is suitable for distances of 1 to 100 kilometers and frequencies of 150 to 1920 MHz (but it is typically modified up to 3000 MHz). It is appropriate for base station antenna heights between 30 and 1000 meters. Equation 5 shows how the model can be stated [19]:

$$L = L_{FSL} + A_{mu} - G_{hte} - G_{hre} - G_{area} \quad (6)$$

where G_{hte} is the base station antenna height gain factor, G_{hre} is the mobile antenna height gain factor, and G_{area} is the gain due to environmental type. L is Okumura's path loss in decibels (dB), L_{FSL} is propagation loss in free space (dB), and A_{mu} is the median attenuation in relation to free space.

1.3.5 Egli model

The Egli model is a geographic model for electromagnetic waves (EM) propagation. This model was developed using accurate data from television (TV) transmissions on the VHF and UHF bands in a plethora of different locations. The expression for the Egli path loss model is shown in equation 7 [20].

$$L = 117 + 40 \log d + 20 \log f - 20 \log (H_T - H_R) \quad (7)$$

1.4 Model validation and verification

To assess how well the developed and theoretical propagation models fit with the observed path loss, four different statistical tools were used to evaluate and validate the models. The four statistical techniques employed in this study were mean error (ME), standard deviation (SD), root mean square error (RMSE), and standard deviation error (SDE). A better fit for urban and suburban environments, respectively, is indicated by RMSE values of 6 to 8 and less than 15 [21]. The more closely the values of ME, SDE, SD, and even

RMSE converge to zero, the better the model fits the observed variables [22; 23]. The statistical tool's equations are as follows:

$$RMSE = \sqrt{\frac{1}{n} \sum_{i=1}^n (PL_m - PL_c)^2} \tag{8}$$

$$ME = \frac{1}{n} \sum_{i=1}^n (PL_m - PL_c) \tag{9}$$

$$SDE \text{ or } I?_e = \frac{I?}{\sqrt{n}} \tag{10}$$

and $\sigma = \sqrt{\frac{\sum (x_i - \mu)^2}{n}}$ (11)

where $I?_e$ is the SDE, $I?$ is the standard deviation and n is the number of the given sample. PL_m is the measured path loss value at a transmitter – receiver’s distance (da) and PL_c is the empirical prediction path loss model.

2. Results and discussion

2.1. Results

Figures 1 and 2 depict graphs of the signal strength and signal path loss (SPL), respectively, for the signals generated by NTA channel 12 Owerri along the five different routes examined in Imo State, Nigeria.

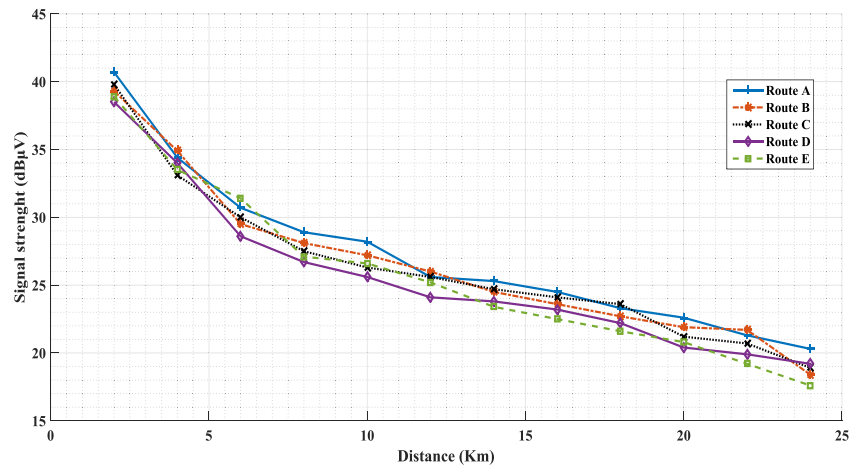


Fig. 1. NTA channel 12 Owerri signal strength along different routes in Imo State, Nigeria

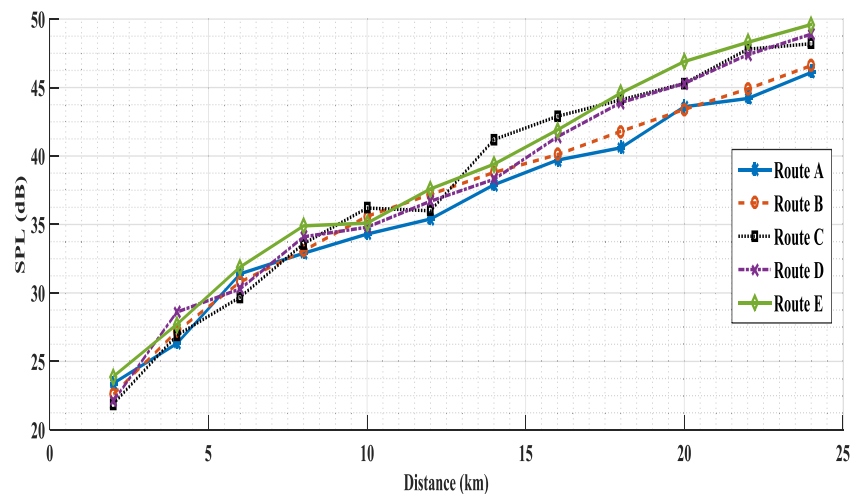


Fig. 2. NTA channel 12 Owerri path loss along different routes in Imo State, Nigeria

The path loss, which is defined as the difference between the total power transmitted and the total power received at a specific location, was calculated using the measured signal strength values while taking into account the measured power transmitted by the NTA channel 12 transmitter, which is 57.1 dBm.

In order to develop a mathematical path loss model that can accurately predict the path loss values of signals generated by NTA channel 12 Owerri, all the different path loss values for all the investigated routes were thoroughly analyzed, taking the path loss specified in figure 2 into consideration. Equation 14, which is the developed path loss model, was developed based on detailed analysis of the observed path loss values, keeping in mind the fundamental equation of path loss in equation 12 and also the basic equation of the straight-line graph shown in equation 13.

$$\text{Path loss, } L_s(\text{dB}) = L_p + 10n \log \frac{d_1}{d_0} \quad (12)$$

where, L_s = path loss, L_p = reference path loss, n = path loss exponent, d_1 = distance between the transmitter and the receiver.

$$y = mx + c \quad (13)$$

2.2 Path loss modeling

The path loss induced by NTA channel 12 in Owerri, Imo State, Nigeria, was predicted using a regression propagation model. The values of the path loss exponents were explicitly computed for each condition and used in the proposed model to characterize the television signal propagation as well as the distance breakpoint. Equation 14 shows the path loss model that was created, which is adequate for predicting the NTA signals' attenuation with distance in the Imo state of Nigeria.

$$PL = M_n + A e \log d_a + K \quad (14)$$

where $K = A e \log d_r + S$

M_n is the signal path loss value at a reference distance from the transmitter, which is considered to be 1 km from the transmitter of the base station, PL is the signal path loss value, A is the constant value of the logarithm's coefficient, which is 20, e is also known as the path loss proponent or exponent, d_r is the reference distance from the transmitter's antenna, which is assumed to be 1 km, d_a is the actual distance (in kilometers) between the transmitter and the receiver and S is the corrective factor that takes into account the loss brought on by obstructions, including scattering, interference, dispersion, and absorption etc.

The values of M_n and e varies depending on the base station's transmitter and the environment being investigated. The values for the path loss predicting model parameters for NTA channel 12 in Owerri, Imo State, Nigeria investigated are $M_n = 18$ and $e = 0.96$. The path loss exponent value e at the breakpoint for a particular site was obtained from the measured path loss by linear regression. The calculated path loss model in equation (14) was developed by using the appropriate values e , M_n , and S for a giving d_a . An application software was developed for the predicting path loss model to correctly estimate the signal path loss in the different locations of signal strength measurements. Given the uncertainty of applying the path loss model, the application software had to be designed to quickly and easily determine the signal path loss values for NTA 12 Owerri, Nigeria. Figure 3 displays a snapshot of the graphic user interface for the software program that was developed.

The application software is run to provide an output in both tabular and graphical form if the required data is supplied into the model developed. The graph of the developed path loss against distance for the NTA channel 12 Owerri base station under investigation is shown in Figure 3.

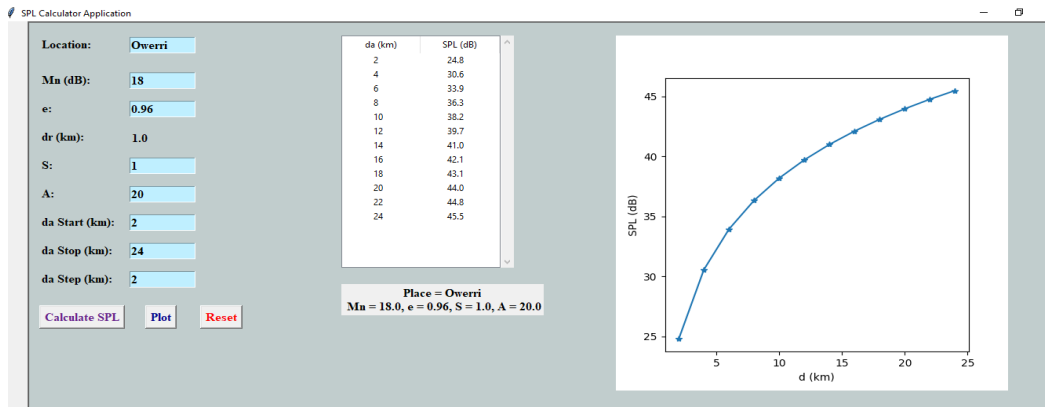


Fig. 3. Graphic user’s interface of the developed signal path loss model’s application software

2.3 Comparative analysis between measured path loss and developed model’s path loss

Path loss values from the developed model were compared to the path loss value of route A for the NTA channel 12 Owerri base stations, as shown in figure 4. The ME, Standard Deviation (SD), RMSE, and the standard deviation error (SDE) described in equation 9–11 are the statistical tools used to validate the developed path loss propagation model. Table 3 lists the results of each statistical tool that was used to validate and confirm the applicability of the developed path loss model in the investigated environments and to predict NTA channel 12 Owerri signals' path loss.

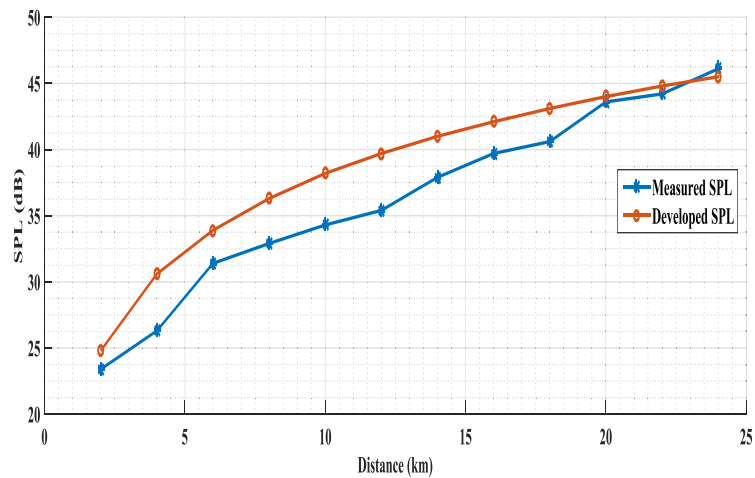


Fig. 4. Comparison of measured path loss values with the calculated path loss values for NTA Owerri in Imo State, South-Eastern, Nigeria.

Table 3. Statistical parameters of the developed path loss values for NTA channel 12 Owerri base station

S/N	RMSE	ME	SD	SDE
1	2.8056	2.3500	6.300	1.8187

All the statistical tools used in this study to validate the performance of this developed prediction model also show that the calculated path loss developed is accurate and very suitable for Distance (km) predicting path loss values of NTA channel 12 Owerri signal in the South-Eastern region of Nigeria.

2.4 Comparative analysis of different path loss models with measured values and developed path loss models' values

This section compares the measured path loss values for the base station under investigation with the suggested model values, measured values, and five other conventional existing empirical path loss models stated in equations 1–7. The relationship between measured field values, proposed model values, and some existing empirical path loss models is depicted in Figure 5. The prediction errors of the different models under consideration as well as the measured field values were estimated based on the path loss comparisons in figure 5. Table 4 displays the outcomes of each statistical tool that was used to analyze the errors of the various prediction models using measured data.

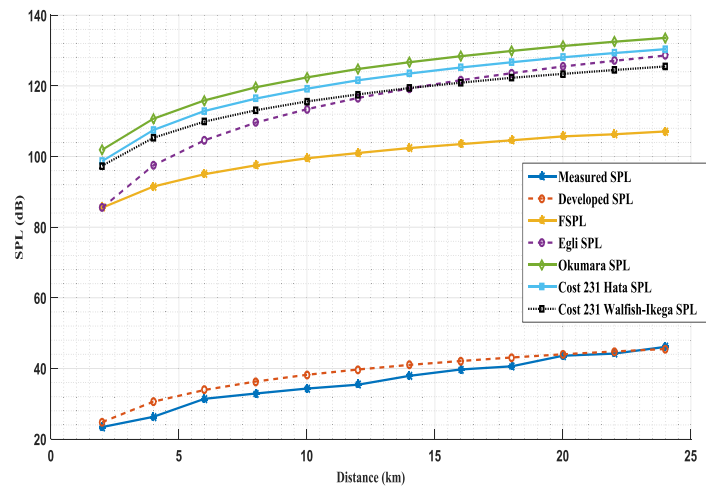


Fig 5. Comparison of some empirical path loss models with measured and developed models' path loss values for NTA Owerri in Imo State, Nigeria.

Table 4: Error analysis of the different prediction models with measured values

Statistical tools	FSPL	Egli	Okumura	Cost-231 Hata	Cost W-L
RMSE	63.67	78.33	86.88	83.69	79.95
MSE	63.65	78.09	86.83	83.64	79.93

2.5 Performance of NTA signals Owerri in Imo State, Nigeria.

In this work, the performance of the NTA signals under study was also examined. The purpose is to evaluate the effectiveness of the NTA signals received at a specified location or distance. Equation 15 provides the expression to determine the performance or quality for the NTA signals under study at a particular distance [29].

$$P (\%) = \frac{TST (dB)}{TSR (dB)} \times 100\% \quad (15)$$

When the overall performance of the signals is between 71 and 100%, the performance of the signals is considered excellent, and when the quality is between 51 and 70%, the performance of the signals is very good. The signal performance is deemed good and fair when the efficacy of the received signals is between 31 and 40%, and 41 and 50%, respectively. The performance of television signals ranging from 0 to 30% is regarded as being relatively low, making the audience who receives them feel very uneasy [24]. Table 5 shows the outcomes of the performance studies of NTA channel 12 Owerri signals evaluated at a particular distance. The findings show that NTA Owerri performs poorly at a distance of 18 km away from the base transmitting station.

Table 5. Performance analysis of the different NTA signals

Distance (km)	2	4	6	8	10	12	14	16	18	20	22	24
Signal performance (%)	59.0	53.9	45.0	42.4	39.9	38.0	33.6	30.5	28.9	23.6	22.6	19.3

2.6 Discussion of results

The received signal intensity levels were measured along the different routes in Imo State, Nigeria, where signal strength measurements were taken at intervals of 2 km, ranging from 2 km to 24 km. Inconsistent and irregular signals were eliminated by taking the average received signal at each measurement point. Equation 16 was used to calculate the path loss in decibels from the measured receive signal strength values [25]. According to [26], path loss is the difference in decibels between the power that is transmitted and the power that is received. It also refers to the attenuation of signals due to the influence of topography, atmospheric characteristics, and other elements like absorption, interference, diffraction, scattering, etc.

$$SPL = TSPT - TSSR, \quad (16)$$

where SPL is the signal path loss, TSSR is the total signal strength received and TSPT is the total signal power transmitted.

Figure 2 show the variation of the measured path loss with distance for the NTA channel 12 Owerri base station under investigated. The figure show that the path loss measured for the NTA channel 12 Owerri signals propagation increases with distance along the different routes of signal strength measurements. Figure 2 shows that, for a 2 km distance, the path loss for paths A, B, C, D, and E is, respectively, 33.7, 34.5, 35.2, 35.0, and 33.2 decibels. Path loss values for the same routes at a distance of 4 km are 30.8, 29.9, 30.2, 28.5, and 29.4 km, while at a distance of 6 km, they are 25.7, 26.3, 27.4, 26.8, and 25.2 km, respectively, in Imo State. This illustrates how signal path loss increases with increasing base station transmitter and receiver distance. For all of the investigated routes, an increasing trend in signal path loss was observed. It therefore implies that the signal strength drops off as the distance increases along any path of signal propagation.

For the purpose of predicting the path loss induced by NTA channel 12 Owerri, Imo state in South East, Nigeria, a linear propagation model was developed. The developed path loss model's results were plotted in equation 4 and show comparable patterns to the measured values, suggesting that the path loss increases with the line-of-sight distance between the base station and the television reception station with fairly little dispersion. Attenuation and dispersion become more pronounced and erratic after the breakpoint distance, but the attenuation still fits the surroundings of transmitter base stations. To determine the effectiveness of the developed path loss model in predicting path loss for the NTA channel 12 Owerri station in the different research locations, the values from the developed path loss model were compared with those from the field measurement for route A as shown in figure 5. The figure demonstrates that the predicted path loss values are quite similar to the measured path loss values and that they both exhibit the same distance-dependent incremental trends. The computed path loss model developed is accurate and extremely suited for estimating path loss values of NTA channel 12 signals in the Imo State of Nigeria, as shown by RMSE and the other statistical tool utilized in this study to validate the performance of this prediction model. For the base station under investigation, the calculated path loss's RMSE value, which is less than 8 dB, demonstrates how well the model predicts route loss in the surroundings taken into account. The maximum RMSE values for urban and suburban areas are 8 and 15 respectively for any model to be assumed to be true for predictions.

Figure 5 shows the comparison of path loss values for measured values, produced model values, and other models' values for the NTA channel 12 Owerri base stations in Imo state, Nigeria. Other empirical models, compared to the proposed model, which, on the whole, predicted the path loss accurately, overestimated the measured path loss value by roughly 85.5 dB, demonstrating a lower degree of agreement with the measured route loss values. When compared to the observed and calculated path loss values across the whole research area, the free space path loss (FSPL) model came the closest of all the empirical path loss models. However, the Okumura and Cost-231 Hata models, which projected path loss of over 101.9 dB and 98.7 dB, respectively, in all the research locations, had the biggest prediction difference from the real path loss. Though they all overestimated the path losses, FSPL made a superior prediction overall when compared

to the others. The prediction errors of the various models under consideration were calculated based on the path loss comparisons in Figure 6. For the base station taken into consideration, the mean error, the root-mean square error, the standard deviation, the standard deviation error, and the measured path loss values have been calculated as functions of distance. Table 5 displays the findings of each statistical tool that was used to analyze the errors of the different prediction models considering measured data. The difference between the measured and predicted losses for each of the models was used to compute the mean error. The results of the various statistical tools presented in table 5 affirm that the free space path loss (FSPL) model is closer to zero and therefore closer to the values of the proposed and observed path loss models. Nevertheless, in the analyzed context, the FSPL is still unsuitable to estimate route losses.

Conventional path loss models are incorrect and inappropriate for use with the NTA station under examination in this study area. For forecasting NTA channel 12 Owerri path loss, path loss models developed by other researchers for different regions and television stations were also ineffective. This led to the development of the model that you see here. The developed model performed flawlessly and was demonstrated to be quite effective for the research area and similar terrain when tested in this scenario. This generated model, in contrast to other empirical models developed by other researchers, can estimate path loss over a considerable distance exceeding 24 km. Path loss models are difficult for end users to employ because of their confusing nature due to their mathematical complexity. Thus, it has become absolutely essential to create an application software for the developed model that will allow users to quickly compute the path loss values of the developed model by inputting the pertinent variables into the application software. In summary, the model developed in this study is easy to use, efficient, reliable, appropriate, and scalable, especially in the study areas and on terrain that is similar to that of the terrain.

Conclusion

This study was conducted to develop a path loss model for NTA channel 12 Owerri and evaluate its performance in Imo State, Nigeria. Signal strength measurements were made during different hours of the day and months, from October 2021 to May 2022. In this study, the measured data was used to create a path loss model for NTA Owerri in South-East Nigeria and to evaluate signal quality in terms of efficiency.

The model developed in this study is easy to use, efficient, reliable, appropriate, and scalable, especially in the study areas and on terrain that is similar to that of the terrain. The findings show that NTA Owerri performs poorly at a distance of 18 km away from the base transmitting station. The results also show that the other conventional empirical models considered in this study overestimated the path loss of NTA channel 12 Owerri signals. Recommendations were made based on the results obtained from this study.

Recommendation

The proposed models are recommended for usage in the research areas and other places with comparable topographical features to ensure the best planning of the transmitted power efficiency and network design. Additionally, in order to ensure that their customers get signals well beyond 18 kilometers, it is also recommended that NTA Aba's management raise their power output to about 30 kW.

Acknowledgement

We would like to thank Department of Physics staff members, particularly the Chief Technologies in Communication Laboratory of the Department of Physics, University of Calabar, Calabar, Nigeria, for their encouragement and support throughout the course of this research. We would also like to express our heartfelt gratitude to the management of NTA channel 12, Owerri, for their technical assistance and for making relevant study information available.

References

- 1 Agboje O.E., Ibhaze A.E., Idowu-Bismark O.B. Performance Analysis of Wireless Mobile Network. *Intern. Journal of Applied Engineering Research*, 2016, Vol. 11, No. 8, pp. 6058 - 6062.
- 2 Zreikat A., Djordjevic M. Performance Analysis of Path loss Prediction Models in Wireless Mobile Networks in Different Propagation Environments. *Proc. of the 3rd World Congress on Electrical Engineering and Computer Systems and Science*, Rome, Italy, 2017, Vol.103, pp.VMW XXX-1-VMW XXX-8. doi: 10.11159/vmw17.103
- 3 Iwuji P.C., Emeruwa C. Influence of Atmospheric Parameters on Terrestrial Television Signals in South-Eastern Nigeria. *Journal of Scientific and Engineering Research*, 2022, Vol. 9, No. 3, pp. 61 - 71.

- 4 Adediji A.T., Ismaili M., Mandeep J.S. Variation of radio field strength and radio horizon distance over three stations in Nigeria. *Journal of Atmospheric and Solar-Terrestrial Physics*, 2014, Vol. 109, pp. 1 - 6, doi: 10.1016/j.jastp.2013.12.006
- 5 Gordon O., Ozuomba S., Kalu C. Determination of the dominant fading and the effective fading for the rain zones in the ITU-R P.838-3 recommendation. *European Journal of Mathematics and Computer Science*, 2015, Vol. 2, No. 2, pp. 17 - 29.
- 6 Darr M.J., Zhao L. A Model for Predicting Signal Transmission Performance of Wireless Sensors in Poultry Layer Facilities. *Iowa State University Digital Repository*, 2008, Vol. 51, No. 5, pp. 1818 – 1827, doi: 10.13031/2013.25297
- 7 Abiodun I.C., Ukhurebor K.E. Comparison of 1800MHz Frequency Bands Path Loss Measurements with Conventional Models in Osun State, Nigeria. *Current Applied Science and Technology*, 2021, Vol. 22, No. 2, pp. 1 – 16. doi:10.55003/cast.2022.02.22.005
- 8 Jawhly T., Tiwari R.C. The special case of Egli and Hata model optimization using least-square approximation method. *SN Applied*, 2020, Vol. 2, No. 1296, pp. 1 – 10. doi: 10.1007/s42452-020-3061-0
- 9 Mollel M.S., Kisangiri M. Optimization of Hata-model based on measurements data using least square method: a case study in Daras-Salaam, Tanzania. *Intern. Journal of Computer Application*, 2014, Vol. 102, No. 4, pp. 35 - 39, doi: 10.5120/17806-8630/
- 10 Oke M.O., Raji R.A. Exponential Models of Signal Strength of a Television Station in Nigeria. *Intern. Journal of Mathematics and Statistics Studies*, 2014, Vol. 2, No. 1, pp. 45 - 54.
- 11 Popoola I.S., Misra S., Atayero A.A. Outdoor Path Loss Predictions Based on Extreme Learning Machine. *Wireless Personal Communications*, 2018, Vol. 99, No. 7, pp. 441–460. doi: 10.1007/s11277-017-5119-x
- 12 Iwuji P.C., Bassey D.E. Investigation of the Effect of Atmospheric Temperature on Signal Strength Generated by FM Transmitter in Imo State, Nigeria. *Intern. Journal of Science and Research*, 2018, Vol. 7, No. 6, pp. 82 – 85. doi: 10.21275/ART20183068
- 13 Chima A.I., Onyia A.I., Udegbe S.U. The Effects of Atmospheric Temperature and Wind Speed on Uhf Radio Signal; a Case Study of ESUT Community and Its Environs in Enugu State. *IOSR Journal of Applied Physics*, 2018, Vol. 10, No. 2, pp. 83 – 94. doi: 10.9790/4861-1002018390
- 14 Otuonye A., Nwakanma C.I., Obi N. An E-gov model for Imo State, Nigeria. *Intern. Journal of the Trans African University and Research Development Network*, 2012, Vol. 1, No. 1, pp. 122 – 136.
- 15 Onoja U.S., Nweze I.E., Agbo M.O., Nnamani P.O., et.al. Evaluation of bacteriological quality and essential elements in commercially bottled/packaged water produced and marketed in Southeastern Nigeria. *African Journal of Microbiology Research*, 2015, Vol. 9, No. 15, pp. 138 – 149. doi: 10.5897/AJMR2014.7201
- 16 Tonga D.A. Path Loss Propagation Model Prediction for GSM Mobile Networks in Nigeria. *Proc. of First Intern. Conference Information Technology, Communication and Computing*, Bhopal, M.P., India, 2017, pp 1 – 8.
- 17 Sharma H.K. Sahu S., Sharma S. Enhanced Cost 231 W.I. Propagation Model in Wireless Network. *Intern. Journal of Computer Applications*, 2011, Vol. 19, No. 6, pp. 36 – 42. doi: 10.5120/2363-3103
- 18 Deme A., Dajab D., Nyap D.C. Computer Analysis of the COST 231 Hata Model and Least Squares Approximation for Path Loss Estimation at 900MHz on the Mountain Terrains of the Jos-Plateau, Nigeria. *Computer Engineering and Intelligent Systems*, 2013, Vol. 4, No. 9, pp. 39 – 48.
- 19 Obota A., Simeon O., Afolayan J. Comparative Analysis of Path Loss Prediction Models for Urban Macrocellular Environments. *Nigerian Journal of Technology*, 2011, Vol. 30, 3, pp. 50-59
- 20 Akanni A.O., Oliseloke A.N. Validation of Egli Model and Estimation of Pathloss Exponent of a Radio Signal at VHF Band in Hilly Terrain. *Intern. Journal of Research and Innovation in Applied Science*, 2020, Vol. V, No. ix, pp. 95-100.
- 21 Akinbolati A., Ajewole M.O. Investigation of path loss and modeling for digital terrestrial television over Nigeria. *Heliyon*, 2020, Vol. 6, pp. 1-14. doi: 10.1016/j.heliyon.2020.e04101
- 22 Nasir F., Adeseko A.A., Yunusa A.A. On the study of empirical pathloss models for accurate prediction of TV signal for secondary users. *Progress in Electromagnetic Research B*, 2013, Vol. 49, pp 155 - 176.
- 23 Blaunstein N., Censor D., Katz D. Raio propagation in rural residential aras with vegetation. *Progress in Electromagnetic Research*, 2013, Vol. 40, pp. 131 - 153.
- 24 Shoewu O.O., Akinyemi L.A., Basorun O.O., Alao W.A. Performance analysis and efficiency of television broadcast transmitting signals in Lagos environs: A case study of LTV 8. *Journal of Advancement in Engineering and technology*, 2018, pp. Vol. 6, No. 2, pp. 1 – 6. doi: 10.5281/zenodo.1217081
- 25 Perez F.F., Espineira M.P. *Modeling the Wireless Propagation Channel, a simulation approach with Matlab*. A John Willey and Sons Publication Ltd, University of Vigo, Spain, 2008, pp. 8-32.
- 26 Faruk N., Ayeni A.A., Adediran Y.A. On the study of empirical path loss models for accurate prediction of TV signal for secondary users. *Progress in Electromagnetic Research B*, 2013, No.49, pp.1-5. doi:10.2528/PIERB13011306

DOI 10.31489/2023NO2/99-105

UDC 620.178.179.119

FEATURES OF MECHANICS DESTRUCTION TRIBOUNITS AT DIFFICULT DYNAMIC LOADING

Tsyganov V. V.

Zaporizhzhia Polytechnic National University, Zaporizhzhia, Ukraine, tsyganov705@gmail.com

The mechanics of contact destruction tribounits at a friction in the conditions of difficult dynamic loading is considered. Possibility of mathematical description of complex damage knots friction is shown, intensities of wear taking into account the features of forming superficial layer at a contact. Methodology of calculation superficial durability and longevity of tribounits is presented and the examples of practical estimation of this interdependence are shown. The model of destruction surface at a friction with a different dynamic loading is offered, methods of estimation wearproofness on the change of the structural state of superficial layer by a tribospectral method and the electron work function.

Keywords: wearproofness, tribounits, superficial layer, structural state, loading

Introduction

Presently results of researches in area of wear materials in especially heavy kinds mechanical and thermal loading, that carry dynamic character, does not allow with the high degree of authenticity to choose (or to work out) one or another structurally-technological measures that is sent to the increase of longevity wares. It is caused, foremost by the kinds of realization researches that often fall short of the real kinds of exploitation of the friction pair, as greater part of details tribounits works in the conditions of difficult dynamic loading related to the vibrations operating in various directions, which influences on unstable synergetic processes.

Processes of friction and wear, and also destruction of superficial layers of tribounits is determined by dynamic character loading in a contact, by amplitudes of the mutual moving, creating the specific kinds of pin co-operation [1]. In particular, in the process of exploitation the kinds of shock with slippage (two-component loading) and shock are possible with slippage in two mutually perpendicular directions (three-component loading). Such complex of kinds loading causes the difficult tense state of superficial layers of contacting pairs. It results in limitations of possibility application of general's theory friction, and also most the results of experimental researches [2]. Decision of contact task of mechanics destruction tribounits, that is exploited in the conditions of difficult dynamic loading, maybe within the framework tribofatigue based on model of account correlation processes mechanical (volume) destruction and friction fatigue.

Obviously, that at the contact kinds of loading the superficial layers of material are damaged stronger, than deep. At a repeated loading fatigue, the microcracks appear on a surface even in default of the contact loading with disposition in active planes slippage in that are situated maximal tensions of shear [3]. It is possible to distinguish four successive stages of processes in material in accordance with the features of deformation and destruction of materials at a tiredness: strengthening of material from the increase of density dislocations in local volumes to the critical value; conception and development of submicroscopic cracks; development of microcracks to the sizes macrocracks; development and confluence of macrocracks to the separation of elements surface.

The characteristic features of basic structural elements of material determine the accumulation of defects, resulting in formation of microcrack. The initial structure of the deformed material changes substantially under the action of the repeated impulsive loading. Undersurface zone (in depth from a few units to hundreds micrometres) is the plastic deformed layer of material with a certain size and orientation of the crystallites.

Correlation of mechanical properties and parameters of structure resulted in work [3], shows that resistance to fragile destruction depends not only on the size of grain but also from the size of block mosaic.

Thus, the size of grain does not determine mechanical properties of metal simply. The conclusion is made about the determining influence of the degree of misorientation on the fracture resistance of the metal.

1 Theoretical part

Taking into account that greater part of tribounits work in the kinds of difficult three-component dynamic loading: shock and slippage in two mutually perpendicular directions, investigated wearproofness of tribounits of flat details at the oscillating differently directed slippage with the shock loading (Fig.1). Studies were conducted on the specially worked instruments allowing realizing a difficult contact loading and test samples in the kinds of close to the natural.

Researches by means of electronic microscope allowed to set that as a result of plastic flow the developed cellular structure oriented along direction of friction is formed in superficial layers [4]. Destruction by the verges of cells is initiated, perpendicular to direction of slippage, and a primary crack passes along these verges. Therefore, at the relative slippage of surfaces the origin of the differently oriented cracks is possible. Especially in case of friction with slippage in two mutually perpendicular directions.

In general case formation and growth of microcracks at a cyclic loading substantially depend both on the structural state of material and from the number of cycles of loading of N . For description of development microstructure of short cracks the equation presented in work is applicable [5]:

$$\frac{db}{dN} = C(\Delta\gamma)^m (d - b), \quad (1)$$

where b – a depth of crack; $\Delta\gamma$ – a scope of deformation shear; d – a characteristic size of element structure; C and m – the experimentally determined constants of material.

It ensues from this equation, that as far as the increase of crack to the size of grain its speed diminishes up to a zero. At tensions higher of limit of endurance a crack is not stopped, and only slows the growth or can stop on any time.

Thus, character of accumulation of deformations at the action of the repeated impulsive and pulsating loading is approximately identical [6]. So, at a shock loading dependence of contact deformation on the number of cycles carries nonlinear character with three areas: on the first area - there is contact deformation the stage of strengthening (approximately to $N = 20$); on the second area a slow accumulation of contact deformation is with approximately permanent speed ($N = 10^3 \dots 10^4$); there are a considerable growth of deformation and intensive destruction of surface on the third area.

It is set [1], that a wear at a shock loading is a nonlinear function from the number of cycles and normal tension:

$$W = C N^n \sigma^m \quad (2)$$

where C , n , m – coefficients.

Thus normal tension σ and maximal contact pressure are determined by the power of a shock, which in turn depends on speed, geometry of contact and properties of material.

Cyclic tensions result in the origin of fatigued damage both on a surface and on some depth. The phenomenon of superficial fatigue is corollary of normal collisions of microroughness, that result in an origin under the roughness of tangent tensions operating on the depth of order of heights ledges (micrometers). Under a ledge maximal tangent tension operates:

$$\tau'_m = (E' / \pi^2) \varphi \quad (3)$$

where E' - the reduced modulus of resiliency; φ – an angular coefficient of ledge.

Obviously, that microscopic (second kind) maximal tangent tensions really can be reason of formation embryonic cracks under a surface. A general case over calculated scheme of vertical superficial and horizontal cracks at a friction with a three-component dynamic loading is presented in a Fig. 2.

A surface is loaded with normal variable tension of $q(z)$ at influence of shock loading and tangential tensions τ_x and τ_y at the oscillating slipping in two mutually perpendicular directions of samples. Taking into

account probability of substantial influence of speed moving to the size of coefficient friction, the contact area between the two bodies is determined by the following conditions:

$$\begin{cases} \tau_{xy} = -q(z)\sqrt{k_x^2 + k_y^2} + (E'_m / \pi^2)\rho \\ \sigma_z = -q(z) \end{cases} \quad (4)$$

where k_x and k_y – coefficients of friction on the axis of x and y .

Material in a superficial layer it is possible to examine in the first approaching as resilient. In case of fragile destruction necessary and sufficient is a force criterion – a coefficient of intensity tensions K that quantitatively characterizes the field of tensions at the top of crack.

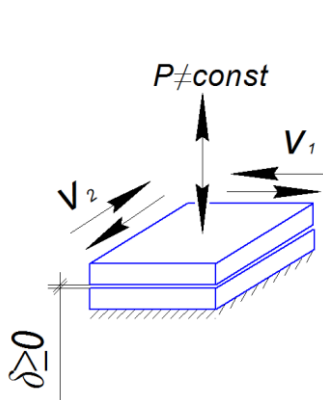


Fig. 1. Layout of the three-component loading of tribounits of flat parts.

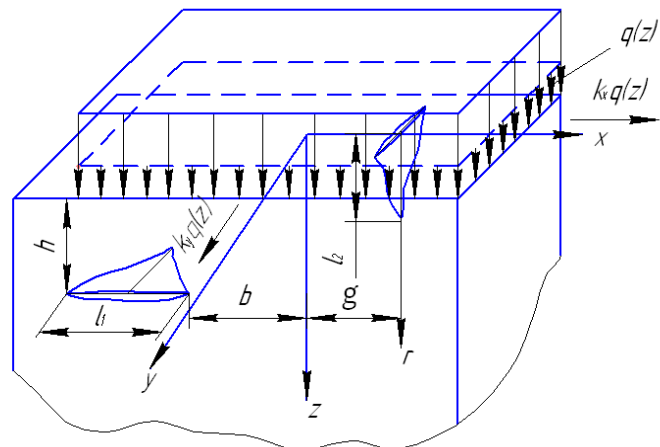


Fig. 2. Scheme of locations horizontal and vertical cracks at a friction with a three-component dynamic loading.

When calculation coefficient K a crack will attain the critical value will begin to spread. The linear resilient mechanics of destruction and force criterion the destructions worked out for fragile bodies are applicable, if the size of zone of plasticity does not exceed 1/10 thicknesses of sample.

Therefore, for the examined case the coefficients of intensity of tensions are determined [6]:
for a horizontal crack

$$\begin{cases} K_I(-b-l_1) = \lim_{x \rightarrow (-b-l_1)} \sqrt{2[x - (-b-l_1)]} \sigma_z(x, h) \\ K_{II}(-b-l_1) = \lim_{x \rightarrow (-b-l_1)} \sqrt{2[x - (-b-l_1)]} \tau_{xy}(x, h) \\ K_I(-b) = \lim_{x \rightarrow (-b)} \sqrt{2[x - (-b)]} \sigma_z(x, h) \\ K_{II}(-b) = \lim_{x \rightarrow (-b)} \sqrt{2[x - (-b)]} \tau_{xy}(x, h) \end{cases} \quad (5)$$

for vertical crack

$$\begin{cases} K_I(l_2) = \lim_{z \rightarrow l_2} \sqrt{2(z-l_2)} \sigma_x(g, z) \\ K_{II}(l_2) = \lim_{z \rightarrow l_2} \sqrt{2(z-l_2)} \tau_{xy}(g, z) \end{cases} \quad (6)$$

Using the apparatus of singular integral equation the decision of task about the resilient is possible and maximum equilibrium of flat plastins weakentd by the system of the arbitrarily oriented rectilinear cracks of longitudinal change, i.e. determinations of the tensely-deformed state of surfaces at a friction.

The decision of contact task of mechanics destruction tribounits, which is exploited in the conditions of difficult dynamic loading, is indissolubly related to strength and deformation properties of superficial layer. It is thus necessary to take into account connection of ledges of actual contact with the structural state of superficial layer and origin of the equilibrium roughness, related to the uneven making of fragments, formation of microkinks, them unorientation. The model of superficial layer appears as the located by chance fragments (crystallites), which possessing the certain level of durability and differ in direction glide planes conditionally shown by different direction of shading areas. The corresponding model of structural organization and destruction of superficial layer at a friction under conditions of multicomponent dynamic loading is presented in a Fig. 3. Reverse slippage (one-component dynamic loading) results in drawing out of fragments. Taking into account forming here comparatively big on a size fragments the got particles of wear are large.

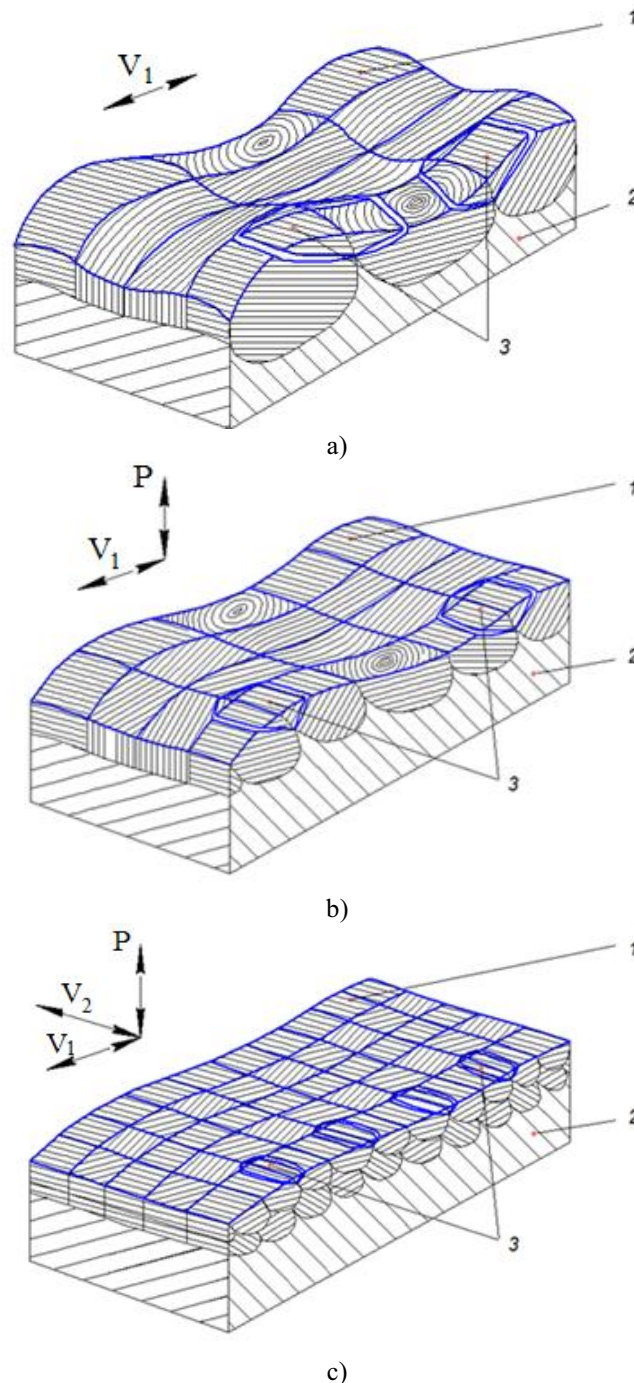


Fig. 3. Model of destruction of surface at a friction with a multicomponent dynamic loading:
 a) one-component; b) two-component; c) three-component.
 1 – fragments of superficial layer; 2 – a basic layer; 3 – particles of wear

For their separation enhanceable energy is required, that is accompanied by insignificant speed of wear (Fig. 3a). The got equilibrium roughness is considerable, especially in transversal direction and characterized by the presence of longitudinal scratches.

Adding to the reverse slippage of shock loading (two - component loading) results in diminishing of size fragments and their strength, increase of is uniform strength of superficial layer, that assists diminishing of particles wear and decline of equilibrium roughness (Fig. 3b). Speed of wear increases here. A three-component loading is characterized by shredding of fragments with formation of superficial layer high uniform strength and homogeneity (Fig. 3c). Shredding the fragmentation of the surface layer and reducing their strength facilitates the separation of wear particles. Fine wear particles, appearing in great numbers, result in high-rate of wear. At the same time, a low equilibrium roughness is formed, both in longitudinal and in transversal directions.

As the preliminary conducted researches showed [7], a difficult three-component loading (shock are possible with slippage in two mutually perpendicular directions) promotes intensity of wear materials by comparison to a wear at a two-component loading (shock and longitudinal slippage) to 2,5 times due to the change of strength and size of fragments superficial layer. With the increase amplitude of the transversal slippage a from 0 to 0,2 mm, the roughness of surface goes down in transversal direction in 1,3 - 10 times; longitudinal - in 1,3 - 2 times. Conditions are being created for forming of fragments superficial layer with the relatively easy passing of dislocation through crystallites to their borders. It assists the decline of level external tensions necessary for the action of mechanism rotary plasticity in analysable structures. As a result, a superficial layer appears with more even texture, which by an enhanceable wear is accompanied.

The change of character loading causes the change of the state of superficial layer and, as a result, change of wearproofness tribounits. Possibility to determine wearproofness by changing of the structural state of superficial layer appears. Estimating the state of superficial layer maybe on a device for sclerometric studies of materials [7], where force of friction of the diamond-pointed pyramid in the process of scanning is modulated with frequency of location crystallites, characterized by near value amplitudes as a result of change of strength on borders and inside local areas. Wherein the samples of the investigated steel or alloy with known wearproofness, state of superficial layer and kinds of loading in tribounits can be reference material.

2 Experimental part

As an example to concrete realization of method determination wearproofness and estimation of the state surface details by a tribounits tribospectral method in a Fig. 4 shows the tribograms of indenter scanning of steel samples 60S2A (C60E - AFNOR) at a two-component and three-component loading

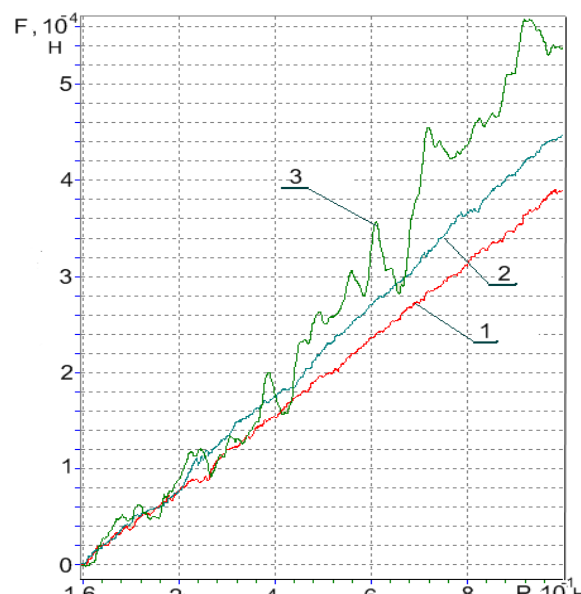


Fig. 4. Tribograms obtained in scanning of steel 60S2A samples after testing at different amplitudes of transverse slip (P is loading on an indenter): (1) $A_{trs} = 0.08$ mm; (2) $A_{trs} = 0.06$ mm; (3) $A_{trs} = 0$ mm (two-component loading).

A two-component loading in the process of tests (tribogram 3) unlike three-component with the presence of the transversal slippage (tribograms 1 and 2) results in formation of superficial layer with the structure of greater strength and heterogeneity that has fragments (crystallites) of different size with enlarged scatter of strength. Thus the change of strength superficial layer made to 35%. Taking into account the increase of wear at a three-component loading it is possible to establish, that over the increase amplitude of the transversal slippage results in diminishing of strength superficial layer, which is accompanied by the decline of size force friction indenter and decline of wearproofness.

In addition, the state of the real surface of metals is related to forming on the surface of electric dipole moments that determine the size of electrostatic barrier the electron work function (EWF). Because of the heterogeneous state of metallic surface there is a corresponding level of electrostatic barrier, qualificatory divergence of electron work function for the different areas of surface. Thus, for this surface of metal there is the characteristic energy relief conditioned by distribution of EWF on a surface [8-10]. By comparing energy relief of the standard material with the relief of the tested material, it is possible to estimate the change in the structural state of superficial layer. Measuring of EWF produced with the use of method dynamic condenser of Kelvin, in which the measurement is made from the contact potential difference arising between the measured surface and the surface of the reference sample. Thus measureable and reference sample form a flat condenser and does not contact each other, however in this case an effective exchange becomes possible by electrons under the action of difference of EWF of the used metals [7, 11, 12].

Concrete the example of realization of the offered method is presented in a Fig. 5. Investigated samples from the alloy of KhTN-61(Standard of Ukraine) at a two-component (shock with slippage) and three-component loading (slippage in two mutually perpendicular planes and shock). The condition of superficial layer samples before the friction practically identical (EWF about 4,1 eV). As a result of friction with different amplitude of the transversal slippage, the state of superficial layer of samples changed. A two-component loading ($A_{trs} = 0$) results in formation of superficial layer with a large value and increased dispersion of EWF. It is related to that the new structural state of surface, near to amorphous and, as a result, EWF increases. A friction with amplitude of the transversal slippage results in diminishing of size and dispersion of EWF, which testifies to the increase of homogeneity of the structural state of superficial layer and accompanied by the increase of wear.

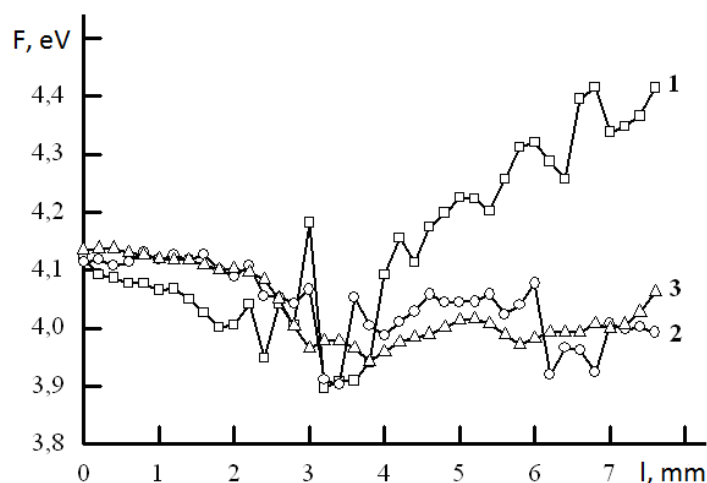


Fig. 5. Distribution electron work function along the surface of standards from the steel KhTN-61(Standard of Ukraine) after a wear with different amplitude of the transversal slippage: (1) $A_{trs} = 0$ mm; (2) $A_{trs} = 0.05$ mm; (3) $A_{trs} = 0.1$ mm.

Thus, deformation of metal at a friction with the different kinds of loading results in structural alterations of superficial layer and, accordingly, change of energy relief surface. The change of dynamics lading assists transformation of superficial layer and, as a result, change of wearproofness tribounits.

Increased number of micro cracks and enhanceable wear take place at details with homogeneous on the size of fragments a uniform strength superficial layer. The increase of the transversal slippage at a friction with a three-component loading assists formation of similar superficial layer, decline of ego of strength, to the receipt of more even micro geometry of surface that is accompanied by the decline of size and dispersion of electron work function on a surface. The degree of these changes substantially depends here chemical-

physical properties of materials and kinds of friction [7, 12, 13]. Conception of wearproofness tribosystems and tribotechnical principle of minimization wear materials is offered on the basis of the use phenomenon structural and energy adaptation of materials at a friction with the different types of loading. It's about creating of such kinds contact, when a superficial layer is formed with heterogeneous on strength and size of fragments the structural state. Thus, management possibility appears wearproofness of contacting details varying of kinds contact taking into account the features of forming superficial layer.

Conclusions

The presented models confirm actuality of mathematical description of complex damage of knots friction. The estimation of mechanics contact destruction must be produced on the basis of study behavior of superficial layers of materials in connection with the features of thermomechanical loading of tribounits in the real kinds of exploitation. In turn development of methods calculation of estimation superficial strength is necessary pre-condition of development more wearproof tribounits.

For the estimation of wearproofness steel details of tribounits at a multicomponent dynamic lading, using of complex approach of determination interconnections tribotechnical and structural properties of contacting materials is needed for the different kinds of loading. Thus, the plastic-destructive pattern of behaviour metal at a friction should be considered as physical and chemical, i.e. process that is accompanied by the complex of structural, physical and physical-chemical changes of superficial layer the deformed metal.

REFERENCES

- 1 Morozov E.M., Zernin M.V. *Contact tasks of mechanics destruction*. Moscow, 1999, 544 p. [in Russian]
- 2 Ryjov E.V. *Contact of solids at the static and dynamic loads*. Moscow, 1988, 250 p. [in Russian]
- 3 Rybakova L.M., Kuksonova L.I. *Structure and wearproofness of metal*. Moscow, 1982, 212 p. [in Russian]
- 4 Garbar I.I., Severdenko V.P., Skorynin Yu.N. Formation of foods wear at the friction of slippage. *DAN USSR*, 1975, Vol. 225, No.3, pp. 82-85. [in Russian]
- 5 Miller K.J. The behaviour of shot fatigue cracks and their initiation. *Faticue on Eng. Mat. and Struct. Part 1. A revier of the two recent books*, 1987, Vol.10, No.3, pp. 75-91.
- 6 Kolesnikov Yu.V. *Mechanics of kontakt destruction*. Moscow, 1988, 224 p. [in Russian]
- 7 Tsyganov V.V., Sheiko S. Features of engineering the wear-resistant surface of parts with the multicomponent dynamic load, *Wear*, 2022, 494-495, 204255.
- 8 Yurov V.M., Oleshko V.S. The impact of the environment on the contact potential difference of metal machine parts. *Eurasian Physical Technical Journal*, 2019, Vol. 16, No.1 (31), pp. 99 – 108.
- 9 Markov A.A. *Measuring of work exit electron at a friction*. Moscow, 1973, 28p. [in Russian]
- 10 Jarin A.L., Fishbain E.I., Shipitsa N.A. Influence of pin deformations on the size of work exit electron of surfaces. *Journal of Friction and Wear*, 1995, Vol, 7, No.3, pp. 488-504.
- 11 Tsyganov V. V., Sheiko S.P., Sakipov K.E., Kassymov S.S. Features of estimation wearproofness tribojoints by work of electron output. *Eurasian Physical Technical Journal*, 2022, Vol.19, No.3 (41), pp.78-83.
- 12 Tsyganov V., Ivschenko L., Byalik H., Mokhnach R., Sakhniuk N. Creation of wearproof eutecticum composition materials for the details of the high temperature dynamic systems. *MS and T 2019 - Materials Science and Technology 2019*, 2019, pp. 450-456.
- 13 Tsyganov V.V., Mokhnach R.E., Sheiko S.P. Increasing Wear Resistance of Steel by Optimizing Structural State of Surface Layer. *Steel in Translation*, 2021, Vol.51, No.2, pp.144-147.

FEATURES OF THE DECAY OF EXCITED STATES OF IONIC DYES IN THE NEAR FIELD OF METAL NANOPARTICLES

A.E. Kanapina¹, E.V. Seliverstova¹, N.Kh. Ibrayev¹, N.A. Derevyanko², A.A. Ishchenko²

¹Institute of Molecular Nanophotonics, E.A. Buketov Karaganda University, Karaganda, Kazakhstan, asselkanapina@mail.ru

²Institute of Organic Chemistry of the National Academy of Sciences of Ukraine, Kiev, Ukraine

The influence factor of silver nanoparticles on the intramolecular processes of deactivation of the electronically excited state of polymethine dyes (PD) of different ionicity has been studied. It has been demonstrated that the optical density for cationic 1 and anionic 2 dyes does not change under the action of the plasmon field of Ag nanoparticles. Whereas an increase in absorbance by almost 18% was observed for neutral dye 3. A decrease in the enhancement in fluorescence intensity in the series of anionic–cationic–neutral dyes was registered upon addition of Ag nanoparticles to their solutions. The fluorescence lifetime practically does not change for all PDs under study. Data processing within the framework of the model of the influence of a plasmonic nanoparticle on radiative transitions in a dye molecule showed that the values of plasmon-enhanced rates of radiative decay of molecules decreases from neutral to cationic and, finally, to anionic dye. The rates of energy transfer from PD to plasmonic nanoparticles decrease in the reverse sequence of dyes, i.e. anionic-cationic-neutral PD. This is expressed in a decrease in the proportion of neutral dye molecules that were deactivated by fluorescence.

Keywords: polymethine dye, ionicity, localized plasmon resonance, silver nanoparticles, plasmon-enhanced fluorescence.

Introduction

Over the last few decades, the phenomenon of localized plasmon resonance (LPR) of metal nanoparticles (NPs) has become a universal tool for studying the optical and electronic properties of various organic compounds [1, 2]. The LPR phenomenon is associated with the interaction of light and electrons on the NPs surface, which leads to strong oscillations of the electric field near the NPs. Such fluctuations are expressed in a significant increase in the local electromagnetic field around the NPs [3], which can be used for various applications, such as sensing, visualization, and energy conversion.

The size and shape of NPs play a decisive role in the LPR effect, since they determine the resonant frequency and strength of the plasmon resonance. The properties of the environment can also affect the LPR effect, for example, the refractive index of the environment or the presence of other molecules can change the plasmonic properties of metal NPs.

The application of plasmonic NPs of metal is currently very wide and ranges from optical technologies to biomedical applications and photovoltaic devices [2, 4]. In particular, they can be used in the development of optoelectronic devices [4, 5], nanolasers [6, 7], and photodynamic therapy [8, 9]. It was shown [10] that the addition of metal NPs to the active medium of dye lasers can lower their generation threshold. Also, in the presence of gold or silver NPs, the performance of solar [11-13] and photocatalytic [14-16] cells can be significantly increased.

Fluorophores located near the metal NPs can demonstrate both enhancement and quenching of luminescence. The magnitude and sign of the plasmonic effect of metal NPs depends on such factors as the distance between the fluorophore molecule and the plasmonic NP, the mutual orientation of their transition dipole moments, the permittivity of the medium, etc.

During the interaction between plasmonic NPs and a dye molecule, an electro-dipole interaction occurs [3, 17]. Due to the strong local electric field created by plasmonic NPs, the characteristics of the electronically excited states of organic fluorophores could be changed. This is expressed in the modification of the rates of intramolecular and intermolecular transitions with the participation of dye molecules [18, 19]. In this regard, it is reasonable to assume that the plasmonic effect of metal NPs will also depend on the ionicity of the dye.

Currently, there are practically no studies were found on the effect of the dye ionicity on the effectiveness of its interaction with plasmonic NPs. Meanwhile, the charge of metal NPs should have a strong effect on the charged molecule of dye. In this work, polymethine dyes (PDs) of various ionicity were selected: 1 – cationic, 2 – anionic, 3 – neutral dyes [20], the structural formulas of which are shown in Fig. 1.

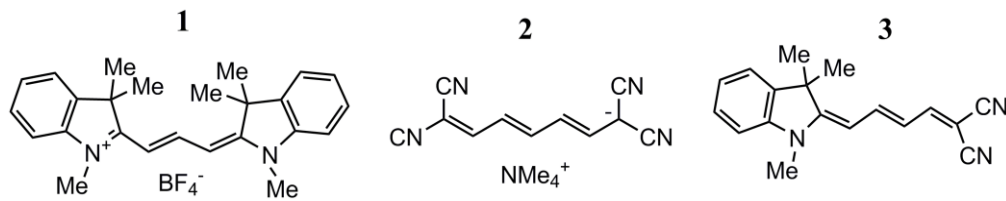


Fig.1. Structural formulas of PDs with different ionicity

1 Experimental part

For the study, solutions of PD with a constant concentration (C) of dye 1, 2, or 3 equal to 10^{-5} mol/L were prepared in ethanol. Silver NPs were used as plasmonic NPs. Their content in PDs samples was varied from $5 \cdot 10^{-13}$ to 10^{-12} mol/L.

Ag NPs were synthesized by laser ablation method. As the metallic silver target with 99.999% grade placed in ethanol (3 mL) was used. Ablation was carried out with an LQ 215 laser ($\lambda_{\text{gen}}=532$ nm, $E_p=90$ mJ, $\tau=10$ ns), with a wavelength of 532 nm and a pulse repetition rate of 20 Hz. The ablation process was lasted for 10 minutes.

Zetasizer 90S (Malvern) was used to determine the size of the obtained nanoparticles. Measurements showed that the average radius of the synthesized Ag NPs is equal to 31 ± 9 nm (Fig. 2a). According to the Mira 3MLU (Tescan) scanning electron microscope, they have a spherical shape (Fig. 2b). Zeta potential of Ag NPs is equal to -17.33 mV (ZetaPALS, Brookhaven).

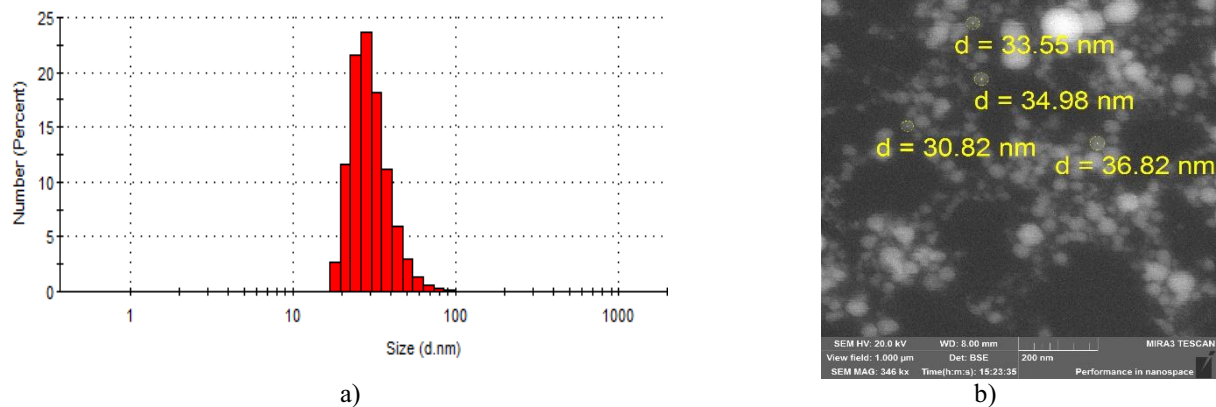


Fig. 2. Size distribution (a) and SEM image (b) of Ag NPs in ethanol.

Absorption spectra were registered on a Cary-300 spectrophotometer (Agilent), and fluorescence spectra of the samples were obtained with Eclipse spectrofluorimeter (Agilent).

The fluorescence duration of PDs molecules were measured with the TCPC system (Becker&Hickl). For the photoexcitation of solutions, lasers with picosecond pulse duration and a generation wavelength of 532 or 640 nm were used. Fluorescence decay kinetics was processed using the SPCImage program (Becker&Hickl). The fluorescence lifetime was estimated using the formula [21]:

$$I(t) = \sum_{i=1}^n \alpha_i \exp(-t/\tau_i) \quad (1)$$

where τ_i – is the decay time, α_i – is the amplitude (contribution fraction) of i -th component ($\sum_i \alpha_i = 1.0$) and t – is the time.

Spectral-luminescence measurements were carried out at atmospheric pressure and room temperature. To obtain reliable data, all measurements were carried out at least 3 times, and the obtained data were averaged.

2 Results and discussions

The absorption bands of dyes 1, 2 or 3 (curves 1, 2, or 3, respectively) and their fluorescence (curves 1', 2', or 3', respectively) without the addition of NPs, as well as the absorption spectrum of NPs in an undiluted solution (curve Ag NPs, concentration of NPs is $C_{Ag}=1.5 \cdot 10^{-10}$ mol/L) are shown in Fig. 3a. The maximum of the absorption spectrum of Ag NPs is located at 405 nm, and its absorption band has a significant overlap with the absorption and fluorescence bands of the PDs under study. On Fig. 3b the fluorescence decay kinetics of dyes 1 and 2 are shown.

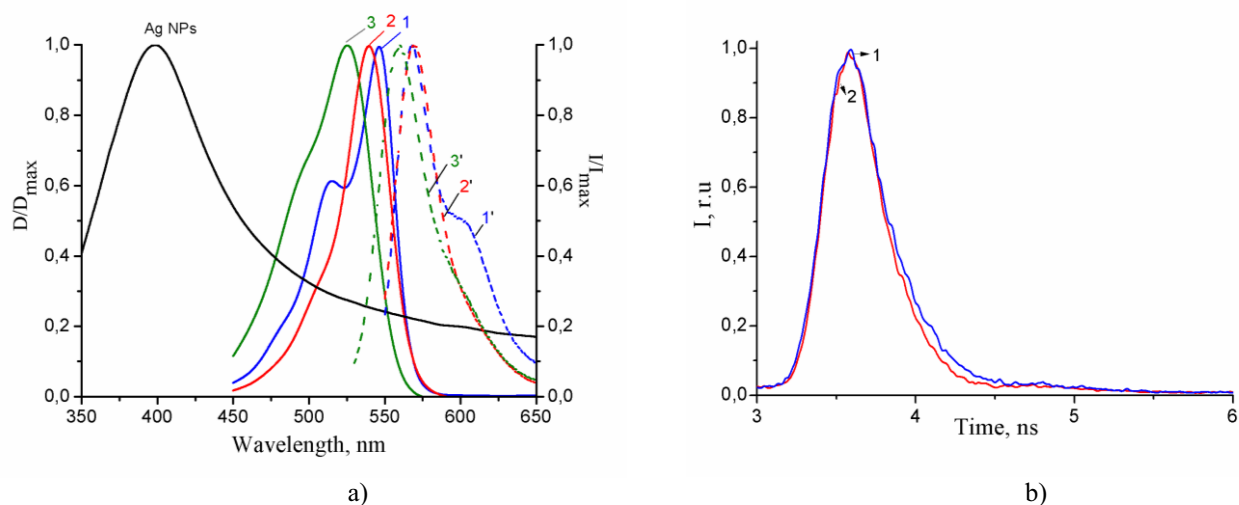


Fig. 3. (a) Normalized spectra of absorption (1, 2, 3, solid curves) and fluorescence (1', 2', 3', dashed curves) of dyes 1 (1, 1', blue), 2 (2, 2', red), 3 (3, 3', green) at $C=10^{-5}$ mol/L without addition of NPs and absorption spectrum of Ag NPs (Ag NPs curve, black); (b) decay kinetics of fluorescence for dyes 1 and 2.

It was found that no changes in the spectral characteristics of the PDs under study were observed upon addition of plasmon NPs. The absorptivity (D) did not change for 1 and 2 dyes when Ag NPs were added (Table 1, Fig. 4).

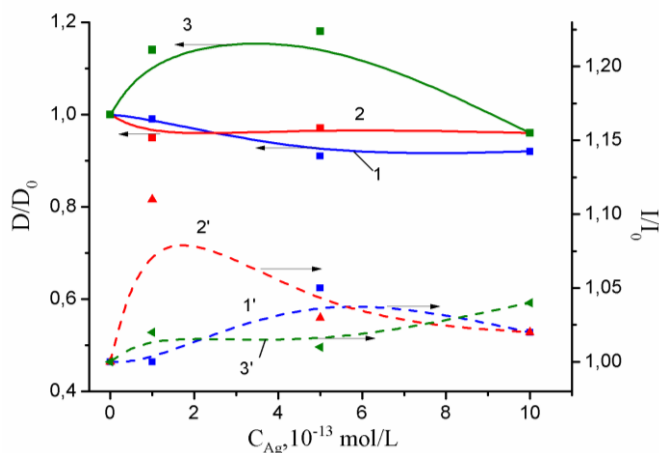


Fig. 4. Effect of Ag NPs concentration (C_{Ag}) on optical density (1, 2, 3, solid curves) and fluorescence intensity (1', 2', 3', dashed curves) of dyes 1 (1, 1', blue), 2 (2, 2', red) and 3 (3, 3', green)

For neutral dye, an increase in the D of solutions by almost 18% is observed (Table 1) upon the plasmon effect of Ag NPs. The observed increase in the absorptivity may be result of growth in the excitation rate and the transition of the dye 3 molecules to the S_1 -state [22, 23]. Fluorescence becomes more intense for all dyes when Ag NPs were added to their solutions. The concentration of Ag NPs (C_{Ag}) on the order of $\sim 10^{-13}$ mol/L is the most suitable for both cationic dye 1 and anionic dye 2. Further growth in C_{Ag} leads to the reducing of the fluorescence intensity. It is noteworthy that the largest enhancement in the fluorescence intensity is observed for PD 2 and the smallest for PD 3. At the same time, fluorescence lifetime τ_f practically was not changed (Table 1). For neutral PD 3, no noticeable changes in fluorescence intensity and lifetime were registered.

Table 1. Spectral-luminescent parameters of 1, 2 and 3 dyes at different concentrations of silver NPs*

Silver concentration, mol/L	$\lambda_{\text{abs max}}$, nm	D	D/D ₀	$\lambda_{\text{fl max}}$, nm	I, r.u	I/I ₀	τ_f , ns	τ/τ_0
1 (cationic) dye								
0	546	1.450	1.000	568	280	1.000	0.290	1.000
$1 \cdot 10^{-13}$	546	1.440	0.990	568	279	1.000	0.286	0.986
$5 \cdot 10^{-13}$	546	1.320	0.910	568	292	1.050	0.287	0.989
$1 \cdot 10^{-12}$	546	1.330	0.920	568	284	1.020	0.285	0.983
2 (anionic) dye								
0	540	1.230	1.000	569	287	1.000	0.253	1.000
$1 \cdot 10^{-13}$	540	1.170	0.950	569	319	1.110	0.251	0.992
$5 \cdot 10^{-13}$	540	1.190	0.970	569	295	1.030	0.250	0.996
$1 \cdot 10^{-12}$	540	1.180	0.960	569	294	1.020	0.248	0.988
3 (neutral) dye								
0	525	0.630	1.000	560	157	1.000	0.245	1.000
$1 \cdot 10^{-13}$	525	0.720	1.140	560	160	1.020	0.243	0.992
$5 \cdot 10^{-13}$	525	0.740	1.180	560	159	1.010	0.241	0.983
$1 \cdot 10^{-12}$	525	0.600	0.960	560	158	1.000	0.230	0.938

*where, $\lambda_{\text{abs max}}$ – is the wavelength of the absorption maximum, D – is the optical density, $\lambda_{\text{fl max}}$ – is the wavelength of the fluorescence maximum, I – is the fluorescence intensity and τ_f – fluorescence lifetime.

The mathematical model used in [18, 23] was used to analyze the data obtained. Calculations have shown (Table 2) that the w_{sp}^0 fluorescence rate of PD in the absence of Ag NPs decreases in the series of 1–2–3 dyes. Since the radiation decay rate w_{sp}^0 depends on the third power of the radiative transition frequency ω , the observed difference in the value of w_{sp}^0 is a consequence of a decrease in the frequency ω in the series of dyes 3–2–1 (Table 1). However, large values of the transition dipole moment were obtained for molecules 1 and 2, which causes a greater value of w_{sp}^0 for them. This is also clearly noticeable for the dependence of the plasmon-enhanced fluorescence rate w_{sp} , where its values decrease in the series of 1–3–2 dyes.

Table 2. Values of the estimated oscillator strength f , transition dipole moments p , plasmon-enhanced fluorescence rate of dye molecules w_{sp} , fluorescence rate of PD molecules without the metal NPs w_{sp}^0 , FRET rate $U(\omega|\mathbf{r})$ from PD to Ag NPs

Dye	p , D	I/I_0^*	w_{sp}^0 , s^{-1}	w_{sp} , s^{-1}	$w_{\text{sp}}/w_{\text{sp}}^0$	$U(\omega \mathbf{r})$, s^{-1}
1 (cationic)	11.70	1.05	$2.3 \cdot 10^8$	$3.50 \cdot 10^9$	14.90	$0.35 \cdot 10^9$
2 (anionic)	11.80	1.11	$2.2 \cdot 10^8$	$3.26 \cdot 10^9$	14.80	$0.24 \cdot 10^9$
3 (neutral)	10.70	1.04	$2.1 \cdot 10^8$	$3.30 \cdot 10^9$	15.70	$1.60 \cdot 10^9$

Thus, the value of the transition dipole moment p is one of the main parameters that has influence on the magnitude of the plasmonic effect of metal NPs on a fluorophore molecule. Calculations showed that the

maximum enhancement in the radiative decay rate w_{sp}/w_{sp}^0 of fluorophore molecule is observed for a neutral dye and it was equal to 15.7 times. However, due to the fact that the spectrum of the fluorescence band of PD 3 has a large overlap with the absorption spectrum of Ag NPs, the effect of fluorescence enhancement is leveled by the process of energy transfer (FRET) from dye molecules to metal NPs.

As were shown in [23, 24], FRET from dye molecules to NPs is a competing process with respect to fluorescence. For dye molecules 1 and 2, the rate $U(\omega|\mathbf{r})$ is about 5–6 times lower than for neutral dye 3 that results in the growth of the fraction of molecules that decay through fluorescence. The values of w_{sp} for dyes 2 and 3 have similar values. Whereas the FRET rate $U(\omega|\mathbf{r})$ to Ag NPs for dye 2 has the lowest value. In turn, this leads to large fluorescence enhancement factors observed in the experiment.

Conclusion

The role of the ionicity of the dye in the efficiency of their interaction with plasmonic NPs of silver is considered.

It has been demonstrated that the optical density for cationic 1 and anionic 2 dyes does not change with the addition of Ag NPs. Whereas for neutral dye 3, an increase in absorbance by almost 18% is observed, which is a consequence of an increase in the rate of excitation of PD3 molecules from the S_0 state to the S_1 state.

At the same time, the plasmonic effect of Ag NPs has a greater effect on the fluorescence of the anionic dye. It was found that under the action of LPR of silver NPs, the fluorescence intensity increases in the series of dyes 3–1–2 (neutral–cationic–anionic). In this case, the duration of the luminescence of the considered dyes remains almost constant.

Consideration of the obtained experimental results within the framework of the model of the influence of a plasmonic NPs on radiative transitions in a dye molecule showed that the values of plasmon-enhanced rates of molecules fluorescence decrease with the transition from neutral to cationic and, finally, to anionic dye.

The rates of energy transfer from PDs to plasmon NPs decrease in the reverse sequence of dyes, i.e. anionic–cationic–neutral PD. The plasmon Ag NPs synthesized in this work and the anionic dye for which the greatest intensity enhancement was recorded have a negative charge. Therefore, it can be concluded that this prevents the PD 2 molecules from approaching the Ag NPs at the distances necessary for effective energy transfer from the dye 2 to the Ag NPs, which results in the observed greatest increase in fluorescence.

The results obtained can serve as a scientific basis for the development of new methods of plasmon modulation of signals in devices of molecular photonics, photovoltaics, photocatalysis and detectors. The ability to control the conditions of such interaction will allow us to form and study new phenomena and properties associated with the «light-matter» interaction.

Acknowledgments (or Funding)

The work was carried out within the framework of the research project AP14870117 funded by the Ministry of Science and Higher Education of the Republic of Kazakhstan

REFERENCES

- 1 De Mol N.J., Fischer M.J.E. (editors), *Surface plasmon resonance*. Methods and protocols. New York, Springer Science, 2010, 286 p.
- 2 Homola J. *Surface plasmon resonance based sensors*. Springer series on chemical sensors and biosensors, Series 4, Berlin, Springer Science, 2006, 252 p.
- 3 Geddes C.D., Lakowicz J.R. Metal enhanced fluorescence. *J. Fluoresc.*, 2002, Vol. 12, pp. 121–129, doi:10.1023/A:1016875709579
- 4 Ranjan R., Esimbekova E.N., Kirillova M.A., Kratasyuk V.A. Metal-enhanced luminescence: Current trend and future perspectives – A review. *Anal. Chimica Acta*, 2017, Vol. 971, pp. 1–13. doi:10.1016/j.aca.2017.03.051
- 5 Seliverstova E.V., Ibrayev N.K., Zhumabekov A.Z. The Effect of silver nanoparticles on the photodetecting properties of the TiO₂/graphene oxide nanocomposite. *Opt. Spectrosc.*, 2020, 128, pp.1449–1457, doi:10.1134/S0030400X20090192

- 6 Balykin V.I. Plasmon nanolaser: current state and prospects. *Phys. Usp*, 2018, Vol. 61, pp. 846–870. doi:10.3367/UFNr.2017.09.038206
- 7 Wang D., Wang W., Knudson M.P., Schatz G.C., Odom T.W. Structural engineering in plasmon nanolasers. *Chem Rev*, Vol. 118, 2018, pp. 2865–2881. doi:10.1021/acs.chemrev.7b00424.
- 8 Xu Y., Tan Y., Ma X., Jin X., Tian Y., Li M. Photodynamic therapy with tumor cell discrimination through RNA-targeting ability of photosensitizer. *Mol*, 2021, Vol. 26, No. 19, pp. 5990. doi:10.3390/molecules26195990
- 9 Chen Y., Yu Z., Meng X., *et al.* Localized surface plasmon resonance improves transdermal photodynamic therapy of hypertrophic scars. *Nano Res*, Vol.15, 2022, pp. 4258–4265, DOI:10.1007/s12274-021-4067-7
- 10 Ibrayev N., Afanasyev D., Ishchenko A., Kanapina A. Influence of silver nanoparticles on the spectral-luminescent and lasing properties of merocyanine dyes solutions. *Laser Phys. Lett*, 2021, Vol. 18, No. 8, pp. 085001. doi:10.1088/1612-202X/ac0e3f
- 11 Morfa A., Rowlen K., Reilly T., *et al.* Plasmon-enhanced solar energy conversion in organic bulk heterojunction photovoltaics. *Appl. Phys. Lett*, 2008, Vol. 92, No.1 pp. 013504-013504-3. doi:10.1063/1.2823578
- 12 Puspitasari R., Budiarti H., Hatta A., Koentjoro S., Risanti D. Enhanced dye-sensitized solar cells performance through novel core-shell structure of gold nanoparticles and nano-silica extracted from lapindo mud vulcano. *Procedia Eng*, 2017, Vol.170, pp. 93-100. doi:10.1016/j.proeng.2017.03.018
- 13 Ibrayev N., Seliverstova E., Omarova G., Ishchenko A. Sensitization of TiO₂ by merocyanine dye in the presence of plasmon nanoparticles. *Mater Today: Proc*, 2021, Vol. 49, pp. 2464–2468. doi:10.1016/j.matpr.2020.11.424
- 14 Chen Y.S., Chao B.K., Nagao T., Hsueh C.H. Effects of Ag particle geometry on photocatalytic performance of Ag/TiO₂/reduced graphene oxide ternary systems. *Mater. Chem Phys*, 2020, Vol. 240, pp. 122216. doi:10.1016/j.matchemphys.2019.122216
- 15 Vasilaki E., Georgaki I., Vernardou D., Vamvakaki M., *et al.* Ag-loaded TiO₂/reduced graphene oxide nanocomposites for enhanced visible-light photocatalytic activity. *Appl. Surf. Sci*, 2015, Vol. 353, pp. 865-872. doi:10.1016/j.apsusc.2015.07.056
- 16 Ibrayev N.Kh., Zhumabekov A.Zh., Seliverstova E.V. Photoelectric properties of TiO₂-GO+Ag ternary nanocomposite material. *Eurasian J. Phys. Funct. Mater*, 2020, Vol.4, No. 3, pp. 261-267. doi: 10.29317/ejpfm.2020040309
- 17 Seth M., Morton D., Silverstein W., Jensen L. Theoretical studies of plasmonics using electronic structure methods. *Chem. Rev.*, 2011, Vol. 111, pp. 3962–3994. doi: dx.doi.org/10.1021/cr100265f
- 18 Kucherenko M.G., Kislov D.A. Plasmon-activated intermolecular nonradiative energy transfer in spherical nanoreactors. *J. Photochem. Photobiol. A*, 2018, Vol. 354, pp. 25–32. doi:10.1016/j.jphotochem.2017.10.020
- 19 Kucherenko M.G., Nalbandyan V.M. Absorption and spontaneous emission of light by molecules near metal nanoparticles in external magnetic field. *Phys. Procedia*, 2015, Vol. 73, pp. 136–142. doi:10.1016/j.phpro.2015.09.134
- 20 Kulinich A.V., Derevyanko N.A., Ishchenko A.A. Synthesis and spectral properties of malononitrile-based merocyanine dyes. *Russ. Chem. Bull*, 2005, Vol. 54, No.12, pp. 2820–2830. doi:10.1134/S1070363212040172
- 21 Becker W. *The bh TCSPC Handbook*, Sixth Edition, Becker&Hickl, GmbH, 2014, 466 p.
- 22 Anger P., Bharadwaj P., Novotny L. Enhancement and quenching of single molecule fluorescence. *Phys. Rev. Lett*, 2006, Vol. 96, pp. 113002–113006. doi:10.1103/PhysRevLett.96.113002
- 23 Seliverstova E., Ibrayev N., Omarova G., Ishchenko A., Kucherenko M. Competitive influence of the plasmon effect and energy transfer between chromophores and Ag nanoparticles on the fluorescent properties of indopolycarbocyanine dyes. *J. Lumin*, 2021, Vol. 235, pp. 118000. doi:10.1016/j.jlumin.2021.118000
- 24 Novotny L., Hecht B. *Principles of Nano-Optics*, Cambridge University Press, NY, 2006.

MINIATURE HIGHLY SENSITIVE ELECTRON SPECTROMETER FOR THE ANALYSIS OF CORPUSCULAR FLUXES

Saulebekov A.O.¹, Kambarova Zh.T.², Omarova G.S.²

¹ Kazakhstan branch of Lomonosov Moscow State University, Astana, Kazakhstan

² E.A. Buketov Karaganda University, Karaganda, Kazakhstan, kambarovazht@gmail.com

The work is devoted to the theoretical development of miniature highly sensitive electron spectrometer for the analysis of the composition of corpuscular flows in a wide range of measured particle energies. The mirror type axially symmetric energy analyzer in the spectrometer is constructed on the basis of an electrostatic octupole-cylindrical field and has a long-focal-length distance. The focusing properties of the scheme have been calculated, and the luminosity and resolving power of the device have been evaluated. As part of a set of equipment for spacecrafts, the proposed device will allow to determine the composition of charged particles in unsteady flows in interplanetary space. Also when designing the device there is a possibility to combine several methods of analysis (for example, with mass-spectrometric methods), which will successfully complement each other, which will provide high information content of joint analysis. This tendency is observed in the creation of space research complexes, which, as a rule, include several independent methods of analysis.

Keywords: electron spectrometer, energy analysis, energy analyzer, electrostatic mirror, corpuscular-optical system.

Introduction

The main instruments used to study the processes in cosmic plasma are energy and mass analyzers of charged particle beams. Energy analyzers are based on the principle of separation of particle by their energy and recording their spectra. This makes it possible to obtain information on various particle parameters, including their velocity, energy, angular distribution, and composition. Energy analyzers are used in various space experiments. Energy analyzers are used to study the solar wind, magnetosphere, near-Earth space plasma and other areas of space physics. Many spacecraft, including satellites, probes and stations, are equipped with energy analyzers to make detailed measurements and collect data on charged particles in near-Earth space. The use of energy analyzers in space research is increasing the understanding of physical processes in the space environment.

Energy analyzers of the cylindrical mirror type have found wide application in the study of resonance phenomena in gases, in spectroscopy for chemical analysis, for obtaining spectra of secondary electrons, photoelectrons, auto electrons, Auger-electrons, as well as in space research, in the study of interaction of atomic particles with the surface of a solid body and plasma diagnosis. The cylindrical mirror analyzer has become a basic element of electron spectrometers of various purposes, produced in the near and far abroad by leading instrumentation companies [1,2].

Work [3] presented a description of a novel electrostatic optic that is designed to offer a 2π sr instantaneous field of view for characterizing space plasmas. The system comprises a series of concentric toroidal electrodes that create multiple independent channels for energy selection. The charged particles undergo deflection towards a shared planar imaging detector. The complete three-dimensional distribution function of charged particles is obtained through a single energy sweep. The resolution of the optics, both in terms of angle and energy, is determined by several factors. These factors include the number of toroidal electrodes, the radii of curvature of the electrodes, the spacing between them, and the angular aperture of the channels. The numerical simulations presented in this study demonstrated the performance of an initial implementation of the proposed concept, which is suitable for various space plasma physics applications. The preliminary version of this three-dimensional plasma analyzer has the capability to cover energy ranges from a few electron volts (eV) up to 30 kiloelectron volts (keV), typically with a channel-dependent energy resolution varying from 10% to 7%. The angular acceptance of the system is dependent on the incident

particle's direction and ranges from 3° to 12° .

In work [4], a novel type of space plasma spectrometer, known as the wide field of view plasma spectrometer, was introduced. This spectrometer provides a field of view greater than 1.25π sr, while requiring fewer resources compared to traditional methods. The enabling component can be likened to a pinhole camera, where an electrostatic energy-angle filter is positioned at the image plane. The energy-per-charge of the particles is controlled by adjusting the bias voltage applied to the filter plate in relation to the pinhole aperture plate. For a given bias voltage, charged particles from different directions are focused by different angles to different locations. Particles with appropriate locations and angles can transit the filter plate and are measured using a microchannel plate detector with a position-sensitive anode. By employing a single high-voltage power supply, it becomes possible to achieve comprehensive coverage of both energy and angle, leading to significant resource savings. Additionally, this setup enables measurements to be conducted at rapid timescales.

In the study described in work [5], a novel approach was introduced for measuring plasmas with exceptionally high energy resolution. This was accomplished by combining a top-hat Electrostatic Analyzer (ESA) with an internally positioned Retarding Potential Analyzer (RPA). In situations where high resolutions are unnecessary, RPA can be grounded, allowing the instrument to function as a conventional, versatile plasma analyzer solely utilizing ESA.

A wide-field-of-view electrostatic analyzer has been designed specifically for the L5 mission, offering all-sky coverage [6]. The prototype model of this analyzer has been calibrated using a ground-based facility. The results exhibit a satisfactory agreement with the numerical model calculations, showcasing the analyzer's capability for space plasma measurements on board 3-axis stabilized spacecraft, such as the L5 mission.

The design of the analyzer proposed in work [7] is capable of measuring plasma characteristics in a solid angle of 2π sr in one act of data registration. The all-sky spectrometer of hot cosmic plasma comprises two stages: the first stage involves an original conical lens design, which transforms an extremely broad inflow of particles into a narrow cone-shaped beam; the second stage employs a hexapole-cylindrical configuration functioning as an energy analyzer for the narrow cone-shaped flow. The work outlines the calculations and simulations conducted to assess the proposed analyzer, utilizing original numerical and approximate analytical methods for designing electron and ion optical systems. The main device parameters are computed and presented.

This paper [8] proposes a long focal-length axially symmetric hyperbolic energy analyzer. The work has represented results of calculation of analytic parameters of energy analyzer with an axis-ring type of focusing. The design features of energy analyzer are described and the results of its experimental examination are given.

The study of work [9] involves the computation of the equipotentials of cylindrical octupoles with both symmetric and antisymmetric planes. Additionally, the calculation and analysis of equipotential portraits are performed for electrostatic axially-symmetric octupole-cylindrical fields. The analysis considers various weight contributions from the cylindrical field and circular octupole components.

The electron-optical scheme of the axially-symmetric electrostatic energy analyzer based on octupole-cylindrical mirror is proposed in work [10]. "Ring-ring" type third-order angular focusing scheme of the energy analyzer is found. This proposed analyzer demonstrates both compactness and high corpuscular-optical parameters. The instrumental function of the device has been built.

The concept proposed in this article involves utilizing axial symmetric multipole-cylindrical fields in the design of the energy analyzer. A key requirement for this energy analyzer is to have long-focal-length distance, enabling the use of multiple analysis methods and accommodating additional devices, such as mass analyzers. By employing several analysis methods, it becomes possible to overcome the limitations associated with individual methods and obtain a more comprehensive understanding of the investigated corpuscular fluxes.

The paper proposes the results of numerical modeling electron-optical scheme of the octupole-cylindrical energy analyzer. Miniature highly sensitive electron spectrometer of charged particles can be built on the basis of the proposed scheme of the energy analyzer.

The modeling of scheme of energy analyzer was performed using the CAE "Focus" numerical simulation software for electron optics systems [11,12].

1 Modeling of the octupole- cylindrical energy analyzer scheme

The potential of the electrostatic octupole-cylindrical field is described in the coordinate system r, z by the following expression:

$$U(r, z) = \mu \ln r + \omega U_{oct}(r, z), \quad (1)$$

where

$$U_{oct}(r, z) = \frac{1}{4!} z^4 + \frac{1}{2} z^2 \left\{ \frac{1}{4} (1 - r^2) + \frac{1}{2} \ln r \right\} + \frac{1}{64} r^4 + \frac{1}{16} r^2 - \frac{1}{8} \ln r \left[\frac{1}{2} + r^2 \right] - \frac{5}{64}, \quad (2)$$

is circular octupole, μ is the coefficient specifying the weight contribution of the cylindrical field $\ln r$, ω is the weight component of the circular octupole.

Based on the simulation results, the "axis-ring" type second-order angular focusing regime in the electron-optical scheme of the energy analyzer in the case of a point distant source on the symmetry axis is found. At the same time, the coefficient specifying the weight contribution of the cylindrical field $\ln r$ $\mu = 2$, the weight component of the circular octupole $\omega = 1$. Fig.1 shows a scheme of second-order angular focusing of "axis-ring" type of the energy analyzer at $\mu = 2$, $\omega = 1$ in the case of a point distant source of charged particles on the symmetry axis.

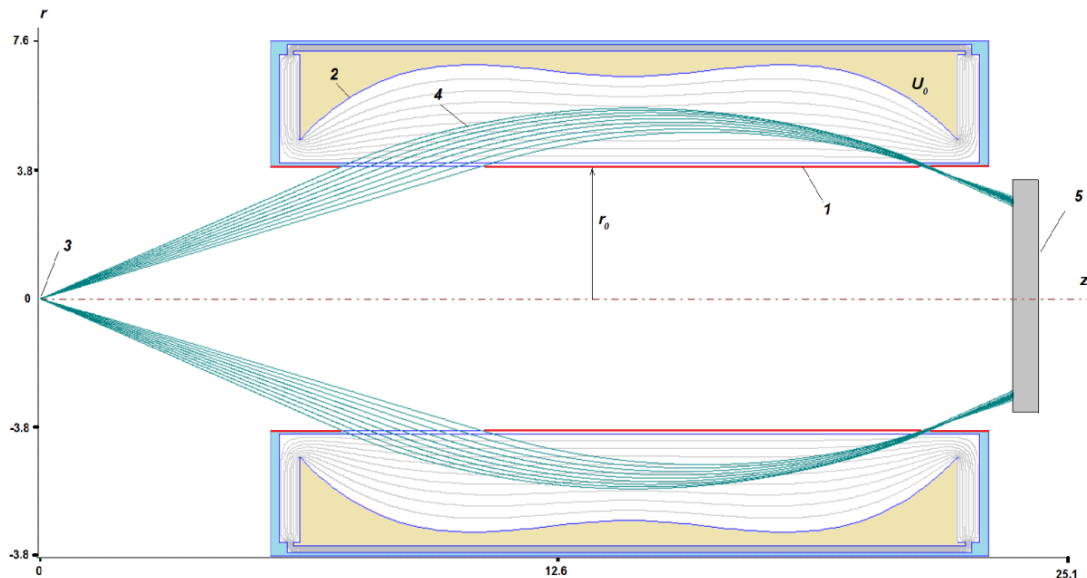


Fig.1. Regime of "axis-ring" type angular focusing in the electron-optical scheme of the energy analyzer based on the octupole-cylindrical field in the case of a point distant source on the symmetry axis: 1 - inner grounded cylindrical electrode, 2 - outer deflecting electrode, 3 – point source, 4 - charged particle beam, 5 - a position-sensitive detector

The octupole-cylindrical field is formed in the space between the cylindrical inner electrode (1), which is under the ground potential, and the outer electrode with a curvilinear profile (2), on which the deflecting potential U_0 is applied.

According to Fig. 1, particles (4) from a point source (3) enter to the analyzing field area of the analyzer through the entrance slit, then reflected from the outer deflecting electrode (2), they pass through the exit slit and are focused into ring image near the surface of the inner cylindrical electrode (1). Then they are registered by the a position-sensitive detector (5).

This scheme provides a long-focal-length distance. Distance from the point distant source to the energy analyzer, i.e. the optimal position of the point distant source relative to the left edge of the entrance aperture $Z(\text{source}) = -1.45 r_0$. The potential of the outer deflecting electrode is equal to 1. The ratio of kinetic energy of the charged particle to the outer electrode potential is $E/V=3.4$ $E[\text{eV}]/U[\text{V}]=3.4$. The range of initial

entrance angles of particles into the analyzer is $24^\circ \pm 4^\circ$. The linear energy dispersion of device is 5.65. All dimensions are expressed in conventional units.

From the calculations it was found that the scheme is capable of collecting particles from sources of small size. Calculations carried out for the case of an extended source showed that even in this case it is possible to obtain regime with a third order focusing. The extended source is in the form of a disk with a diameter $d=0.026 r_0$. In the calculations, the extended source is divided into 10 equal parts, each of which will be a point source. The Figure 2 a,b show the scheme "axis-ring" type angular focusing in the energy analyzer in the case of an extended source (a) and magnified view of an extended source (b).

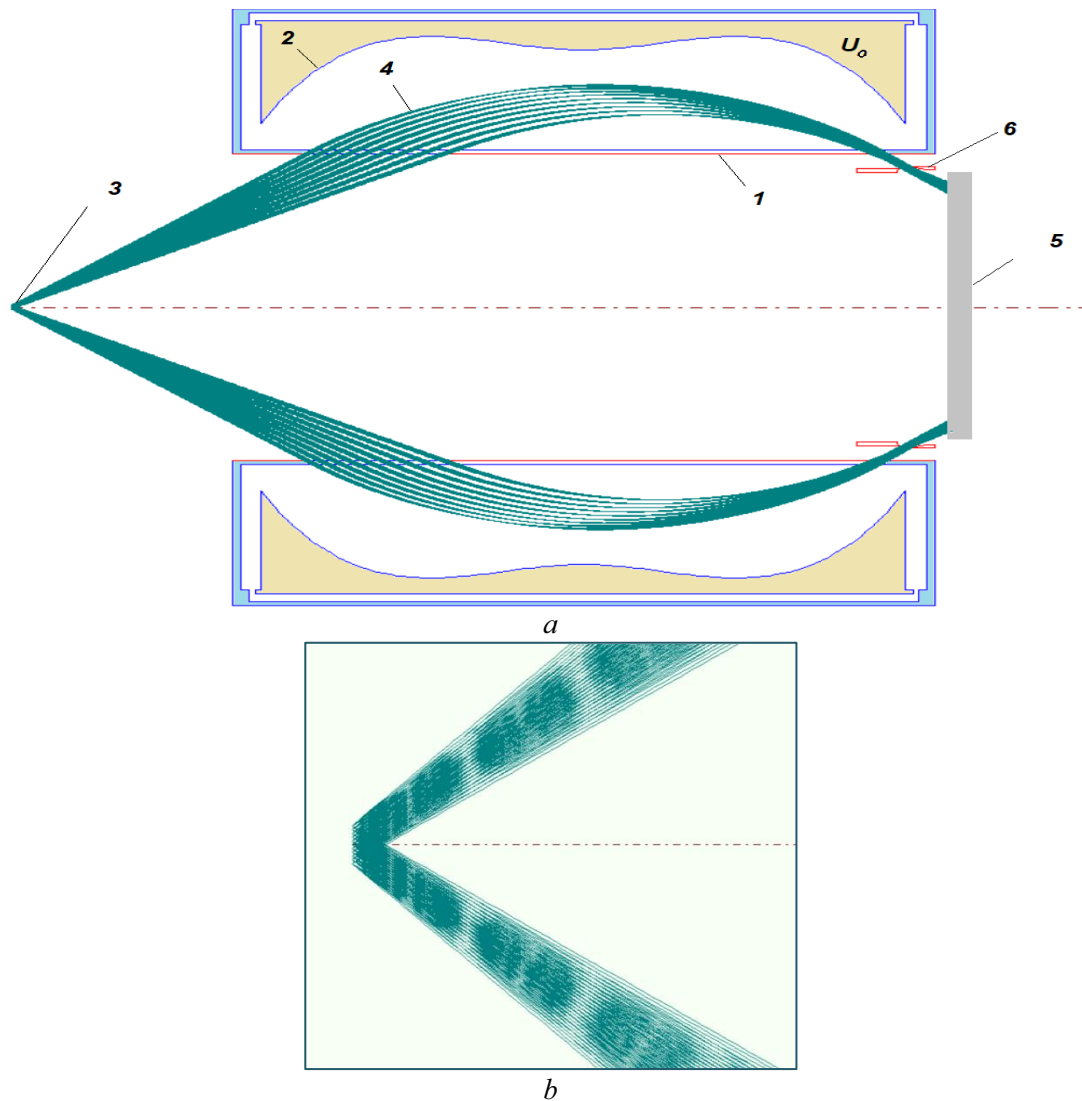


Fig.2. a - "Axis-ring" type angular focusing in the energy analyzer in the case of an extended source: 1 - inner grounded cylindrical electrode, 2 - outer deflecting electrode, 3, b - extended source source, 4 - charged particle beam, 5 - a position-sensitive detector, 6 – exit diaphragm

2 Calculation and analysis of the parameters of the system

Energy response of the energy analyzer was calculated for the cases of point and extended sources. Particles with different polar and azimuthal angles were summed.

To calculate the energy response for the case of point distant source, the exit aperture was placed near the surface of the inner cylindrical electrode. The range of initial particle entrance angles is 20° - 28° , the range of initial energies (more precisely, E/V) is 3.366-3.434 (or $\Delta E=3.4 \pm 1\%$). Exit diaphragm width is $0.0077 r_0$ (where r_0 is radius of inner cylindrical electrode).

To calculate the energy response for the case of extended source (size of source $d=0.026 r_0$), the exit aperture was placed near the surface of the inner cylindrical electrode. The range of initial particle entrance angles is 20° - 28° , the range of initial energies (more precisely, E/V) is 3.23-3.57 (or $\Delta E=3.4\pm 5\%$). Exit diaphragm width is $0.084 r_0$.

Figure 3 shows the energy response of the energy analyzer for the configurations of point and extended sources. Relative energy resolution of the system is defined as the ratio $\Delta E/E$, where ΔE represents the full width at half maximum (FWHM) of the energy distribution curves, and E corresponds to the mean energy of the detected particles.

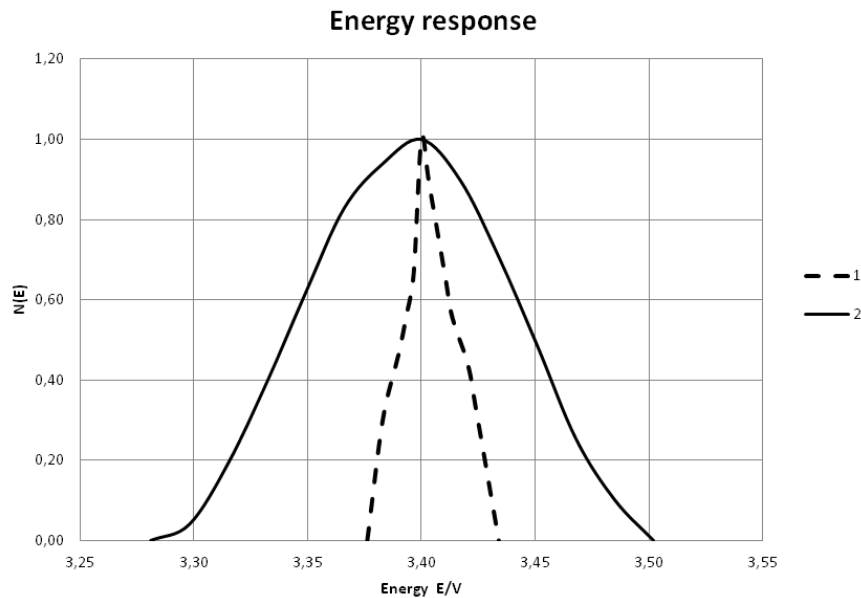


Fig.3. Energy response of the energy analyzer:
1 - for scheme with point source, 2 – for scheme with extended source.

The relatively high energy resolution is higher for the case of point distant source, reaching 0,59 % for “axis-ring” type angular focusing regime. The relatively energy resolution for case of extended source has a lower energy acceptance with 3.29% for “axis-ring” type angular focusing regime.

Table 1 presents the results of numerical calculation of the focusing properties of the octupole-cylindrical energy analyzer for the “axis-ring” angular focusing regime.

Table 1. Focusing properties of the octupole-cylindrical energy analyzer

Parameter	Point source	Extended source
Focusing order	2	3
Central angle of focusing	24°	24°
X_{foc} , coordinate of the focus point	22.78	21
Y_{foc} , coordinate of the focus point	3.3	4
Reflection parameter, P	1.0	0.8
Long-focal-length distance	$1.45 r_0$	$1.45 r_0$
$\Delta E/E$ (FWHM), %	0.59	3.29
Luminosity, $\Omega/2\pi$, %	5.67	5.67
Linear energy dispersion, D	5.65	5.65
The total length of the electron-optical scheme, $l = L/r_0$	5.87	5.87

The luminosity of the corpuscular-optical device is equivalent to the geometric solid angle Ω of the particle collection. Luminosity of the energy analyzer for “axis-ring” type angular focusing regime is $\Omega/2\pi=5.67\%$.

The analyzer proposed in this work has the best resolution compared to the classical cylindrical mirror energy analyzer, and has the long-focal-length distance and small device dimensions.

Conclusion

A scheme of the energy analyzer with a large focal-length distance, which can be applied for spatial combination with the instruments to provide alternative research methods, was found. On the basis of the proposed numerical model of the energy analyzer can be designed miniature electron spectrometer for the energy analysis of corpuscular fluxes. The developed scheme of the energy analyzer satisfies all basic requirements, such as small dimensions of the analyzer (compactness), high focusing properties. The relatively high energy resolution of the analyzer allows a detailed analysis of the particle distribution function.

Acknowledgements

The research was supported by Ministry of Science and Higher Education of the Republic of Kazakhstan, Grant number AP09058188

REFERENCES

1. Zashkvara V.V., Ashimbaeva B.U., Bylinkin A.F. The spectrograph regime in the energy analyzer of two cylindrical mirrors. *Zhurnal Technicheskoi fiziki - Technical Physics*, 1988, Vol.58, Issue 10, pp.2021-2025. [in Russian]
2. Zashkvara V.V., Ashimbaeva B.U. Cylindrical mirror analyzer with adjustable angular focusing. *Journal of Electron Spectroscopy and Rel. Phen.*, 1998, Vol.94, pp.89 – 96.
3. Morel X., Berthomier M., Berthelie J.-J. Electrostatic analyzer with a 3-D instantaneous field of view for fast measurements of plasma distribution functions in space. *J. Geophys. Res. Space Physics*, 2017, Vol. 122, pp. 3397–3410. doi:10.1002/2016JA023596
4. Skoug, R. M., Funsten H. O., Möbius E., et al. A wide field of view plasma spectrometer. *J. Geophys. Res. Space Physics*, 2016, Vol. 121, pp. 6590–6601. doi:10.1002/2016JA022581
5. Collinson G.A., Chornay D.J., Glöcker A., et al. A hybrid electrostatic retarding potential analyzer for the measurement of plasmas at extremely high energy resolution. *Review of Scientific Instruments*, 2018, Vol. 89, 113306.
6. Miyake W., Yamazaki A. Calibration Experiment of All-sky Electrostatic Analyzer. *Journal of the National Institute of Information and Communications Technology*, 2004, Vol.51 (1/2), pp.171-181.
7. Kambarova Zh.T., Saulebekov A.O., Trubitsyn A.A. The all-sky spectrometer of hot cosmic plasma. *The Astronomical Journal*, 2022, Vol. 164, No. 2, pp.47 (1-10). doi:10.3847/1538-3881/ac7561
8. Gurov V.S., Trubitsyn A.A., Grachev E.Yu. Long focal-length axially symmetric hyperbolic energy analyzer of charged particles. *Radiotekhnica – Radiotechnics*, 2016, № 8, pp. 74-79. [in Russian]
9. Kambarova Zh.T., Saulebekov A.O., Kopbalina K.B., Tussupbekova A.K., Saulebekova D.A. About the possibility of creating an efficient energy analyzer of charged particle beams based on axially-symmetric octupole-cylindrical field. *Eurasian Physical Technical Journal*, 2021, Vol.18(2), pp. 96–102.
10. Kambarova Zh.T., Saulebekov A.O., Kopbalina K.B. The electron-optical scheme of the energy analyzer of small-sized electron spectrometer. *Abstracts of 20th International Conference on Radiation Physics and Chemistry of Condensed Matter Methods, instruments and equipment for physicochemical studies (EFRE 2022)*, 2022, pp. R5-P-003102.
11. Trubitsyn A., Grachev E., Gurov V., Bochkov I., Bochkov V. CAE “FOCUS” for Modelling and Simulating Electron Optics Systems: Development and Application. *Proceedings of SPIE*, 2017, Vol. 10250, pp. 102500V-1 – 102500V-7. doi: 10.1117/12.2256570
12. Sautbekova, Z.S., Trubitsyn, A.A. FOCUS CPM Software for trajectory analysis of real axially symmetric electrostatic mirrors: Methods and Algorithms. *Eurasian Physical Technical Journal*, 2022, Vol. 19(3), pp. 91–96.

DOI 10.31489/2023NO2/118-126

UDC 539; 535.37

ENHANCING PHOTOMETRIC PERFORMANCE OF YAG:Ce CERAMICS: INVESTIGATING THE ROLE OF ANNEALING IN RADIATION-ASSISTED SYNTHESIS

Zhilgildinov Zh.S.¹, Lisitsyn V.M.², Karipbayev Zh.T.^{1*}, Tulegenova A.T.³, Alpyssova G.K.^{4*},
Mussakhanov D.A.¹, Zhunusbekov A.M.¹

¹L.N. Gumilyov Eurasian National University, Astana, Kazakhstan, karipbayev_zht_1@enu.kz

²National Tomsk Polytechnic University, Tomsk, Russia

³Al-Farabi Kazakh National University, Almaty, Kazakhstan

⁴E.A Buketov University, Karaganda, Kazakhstan gulnur-0909@mail.ru

Ceramic samples of cerium-doped yttrium aluminum garnet (YAG:Ce) were successfully synthesized utilizing a high-powered electron flux field with a considerable energy level of 1.4 MeV and a power density of 23 kW/cm². The ceramics were formed in a remarkable time span of just one second from a specifically prepared mix of yttrium, aluminum, and cerium oxides. The process of radiation-assisted synthesis of ceramics within radiation flux fields fundamentally deviates from the methodologies commonly employed today. Analyzed diffraction patterns closely align with those documented for YAG:Ce crystals, both in peak position and proportion. Furthermore, every sample consistently demonstrated a space group symmetry of Ia-3d. The luminescence and excitation spectra of ceramics synthesized in this study closely resemble those of YAG:Ce ceramics produced by other methods and YAG:Ce - based phosphors. The luminescence bands exhibit high efficiency, and the intensity ratios of the UV bands vary among the studied phosphors. The ceramics' radiation-to-luminescence conversion efficiency was found to be impressive, achieving scores of 0.57 and 0.48 in the industrial phosphors SDL 4000 and YAG-02, respectively. It was also observed that an increase in quantum efficiency of the samples could be achieved via high-temperature annealing. High conversion efficiency underscores the potential of the outlined luminescent ceramics synthesis method.

Keywords: synthesis, YAG:Ce ceramics, structure, radiation-assisted synthesis, luminescence.

Introduction

Phosphor materials play a crucial role in various modern technologies, particularly in the fields of lighting and display systems. These materials possess the unique ability to convert energy from one form into another, most commonly transforming ultraviolet (UV) or high-energy visible light into lower-energy visible light [1-4]. Among the numerous phosphor materials available, Ce³⁺ - doped luminescent phosphors have emerged as a promising candidate for a range of applications [5-10]. In particular, cerium-doped yttrium aluminum garnet (YAG:Ce) phosphor ceramics are innovative materials that evolve from the base compound of YAG, doped with cerium (Ce) ions. This insightful fusion results in an exceptional transformation of the YAG crystal structure, thereby birthing a highly efficient phosphor material that boasts distinct optical properties.

Notably, the luminescent characteristics of YAG:Ce phosphor ceramics can be deliberately customized. This is achieved by expertly manipulating certain aspects of the synthesis process, as well as the relative concentrations of the cerium dopant. By making these strategic alterations, the optical properties of the resultant ceramic material can be attuned to cater to a plethora of specific application requirements.

Such versatility and customizability empower these phosphor ceramics to function in a wide range of sectors. From lighting technologies to imaging devices, from signal amplification in telecommunications to their application in medical imaging, the YAG:Ce phosphor ceramics, with their unique properties, can be fine-tuned to meet diverse requirements, reinforcing their appeal and utility in numerous technological innovations [10]. YAG:Ce based phosphor ceramics demonstrate promising potential for applications in light-emitting diodes (LEDs)[11-13] and scintillators[14-16]. These multicomponent systems often require high-temperature and lengthy synthesis processes, which can result in inconsistent material quality. Consequently, ongoing research is focused on refining and discovering new synthesis techniques. The

growing interest in YAG:Ce phosphor ceramics is primarily driven by their potential use in energy-efficient lighting technologies, such as light-emitting diodes (LEDs). The exceptional conversion efficiency, thermal stability, and color-rendering properties of YAG:Ce phosphor ceramics make them an ideal choice for the generation of white light in LEDs.

Apart from widely-used solid-phase reactions [13], various alternative methods are being explored, such as laser ablation [17], sol-gel [18], hydrothermal [19], coprecipitation [20], and combustion [21]. One promising approach involves synthesizing ceramics within high-power radiation fluxes. Studies have demonstrated that MgF₂-based luminescent ceramics can be synthesized using high-power electron fluxes [22], and we previously showed that YAG:Ce ceramics can also be synthesized in this manner [23]. The spherical ceramic samples obtained, up to 7mm in size, exhibited luminescence upon UV excitation in the spectral region characteristic of YAG:Ce phosphor ceramics.

This paper presents the results of synthesizing YAG:Ce ceramics radiation-assisted method, along with an analysis of the material's structural and luminescent properties.

1 Materials and Research Methods

The synthesized test samples were two series of ceramics different in composition with a batch content: Y₂O₃(55%) + Al₂O₃(43%) + Ce₂O₃(2%) (YAG) and Y₂O₃(52%) + Al₂O₃(40%) + Ce₂O₃(2%) + Gd₂O₃(6%) (YAG:Ce, Gd). The initial experimental outcomes reveal that the synthesis of YAG:Ce ceramics within a radiation-assisted method is heavily influenced by the precursor prehistory of the components used in the synthesis process. Particularly, the history of the aluminum oxide powders employed exerts significant impact on the synthesis results.

Given this key finding, we chose to utilize three distinct types of alumina powders procured from different suppliers to ascertain the synthesis variance. These powders were sourced from Hefei Zhonghang Nanotechnology Development Co. Ltd. in China, marked as A with the product specification ZH-Al₂O₃-01; Labor Farma in Kazakhstan, denoted as B and classified under ChDA TU 6-09-426-75; and lastly, Chemical Reagents Plant in Russia, labelled as C and also conforming to the qualification ChDA TU 6-09-426-75.

It is important to note that the constituent dispersion of these powders was varied, leading to different experimental conditions and thereby potentially impacting the synthesis outcomes of the YAG:Ce ceramics. Hereafter, phosphors of two series (YAG and YAG:Ce, Gd) made using alumina of different prehistory are indicated by numbers in accordance with Table 1.

Table 1. Designation of ceramic samples

	Sample No.	Composition	Manufacturer Al ₂ O ₃
YAG:Ce	1	Al ₂ O ₃ (43%) + Y ₂ O ₃ (55%) + Ce ₂ O ₃ (2%)	A
	2	Al ₂ O ₃ (43%) + Y ₂ O ₃ (55%) + Ce ₂ O ₃ (2%)	B
	3	Al ₂ O ₃ (43%) + Y ₂ O ₃ (55%) + Ce ₂ O ₃ (2%)	C
YAG:Ce, Gd	4	Al ₂ O ₃ (40%) + Y ₂ O ₃ (52%) + Ce ₂ O ₃ (2%) + Gd ₂ O ₃ (6%)	A
	5	Al ₂ O ₃ (40%) + Y ₂ O ₃ (52%) + Ce ₂ O ₃ (2%) + Gd ₂ O ₃ (6%)	B
	6	Al ₂ O ₃ (40%) + Y ₂ O ₃ (52%) + Ce ₂ O ₃ (2%) + Gd ₂ O ₃ (6%)	C

Oxide powder samples were sintered using high-power electron flux to form YAG:Ce phosphor ceramics. Stoichiometric powders were poured into a 5mm-deep copper crucible with an area of up to 40x120 mm². The crucible was exposed to a high-intensity electron flux that was transmitted from a vacuum state to atmospheric pressure via a differential vacuum pumping system. This electron flux was generated by the ELV-6 accelerator, housed at the Institute of Nuclear Physics of the Siberian Branch of the Russian Academy of Sciences (INP SB RAS). The electron flux carried a substantial energy of 1.4 MeV and had a power density of 23 kW/cm². An electron beams systematically scanned the surface of the powder held within the crucible, moving at a steady speed of 1 cm/s. The cross-sectional density of the electron beam displayed a Gaussian distribution and had a diameter measuring 7 mm at its proximity to the charge surface.

This scanning process ensured that every point on the surface of the crucible was evenly exposed to the electron flux for a duration of 1 second, allowing for a controlled and systematic experiment. After exposure,

the mixture rapidly solidified, forming ceramic samples that were plate-like or spherical in shape. Up to 10 different-sized samples were formed in each crucible. After a single irradiation, the crucible was cooled, and the samples were removed. The samples were then annealed at a temperature of 1650°C for 8 hours. This article presents the research conducted before and after the annealing process.

The luminescence quantum yield (QE) of the synthesized ceramics was measured using an FLS1000 PL spectrometer (Edinburgh) and an integrating sphere (120mm diameter) in the 250-870 nm range. QE measurement involved two stages: 1) measuring the scattered radiation (i.e., outgoing radiation) and the radiation range of the empty integrating sphere; 2) repeating the measurements with the sample placed inside the sphere. The program calculated the QE from the received data. The samples were excited at 450 nm, with a calculation range for QE of 438.5 - 461.8 nm (excitation) and 467.9 - 740.0 nm (luminescence). QE measurements were taken from both the inner and outer sides of the annealed and unannealed samples. The samples exhibited a porous inner surface and a smooth outer surface.

2 Results and discussion

The synthesized samples included plate-like structures with diameters up to 3 cm and thicknesses of around 3 mm, as well as spherical cavities ranging in diameter from 0.5 to 1.5 cm with wall thicknesses of approximately 1.5 mm. These cavities were filled with porous ceramics. Images of samples 2 and 4 are presented in Figure 1. The color of the synthesized samples varied from yellow-green to yellow, depending on the history of the alumina powders used. These samples were fragile, prone to cracking upon impact, and exhibited hardness levels comparable to corundum. Refer to Figure 1 for photographs of the samples.

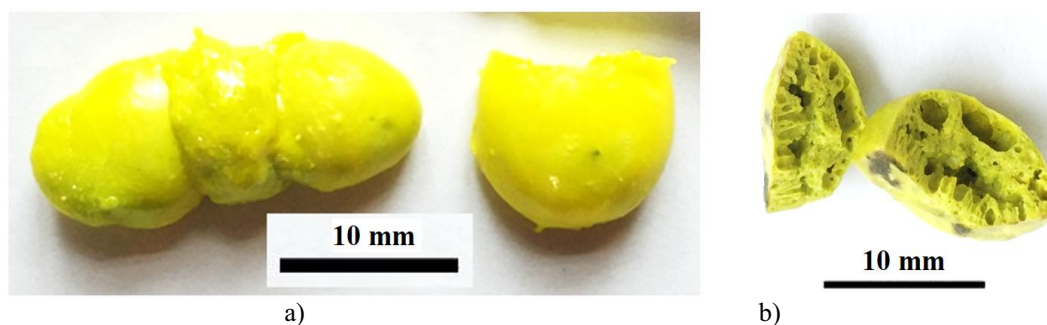


Fig. 1. Photographs of ceramic sample 2 (a- inside, b- outside).

For the study, ceramic samples were mechanically ground into particles with sizes smaller than 1 mm. Figure 2 presents photographs of sample 4, captured using a microscope after exposure to chip radiation at $\lambda=450$ nm and illumination from an incandescent lamp, along with images taken by an MD300 digital camera.

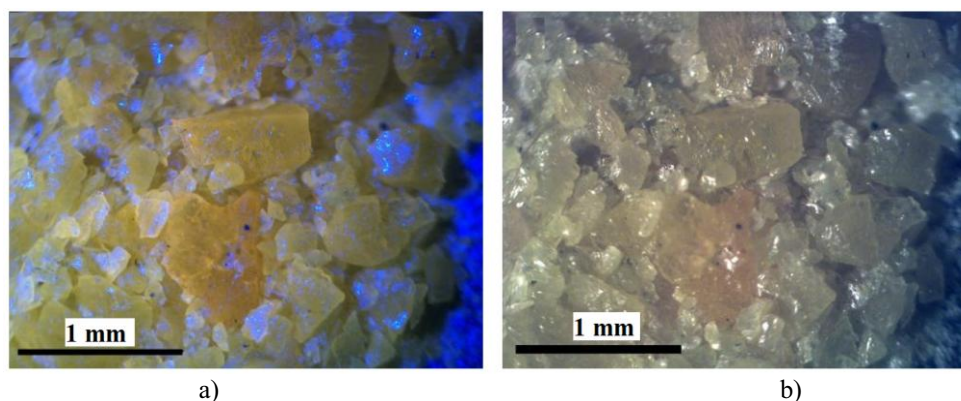


Fig. 2. Photograph of the powder prepared from sample 4 exposed to chip radiation with $\lambda=450$ nm (a) and an incandescent lamp (b).

Exposure to chip radiation resulted in intense luminescence in the yellow region, with a portion of the chip radiation scattering on cleavage planes. Some particles displayed flat, cleaved boundaries, suggesting a tendency towards crystalline structure formation. The sample morphology was examined utilizing a Quanta3D 200i scanning electron microscope (SEM) manufactured by FEI Company in the USA. In Figure 3, SEM images displaying the cleavage site for YAG:Ce and Gd (sample 4) are presented.

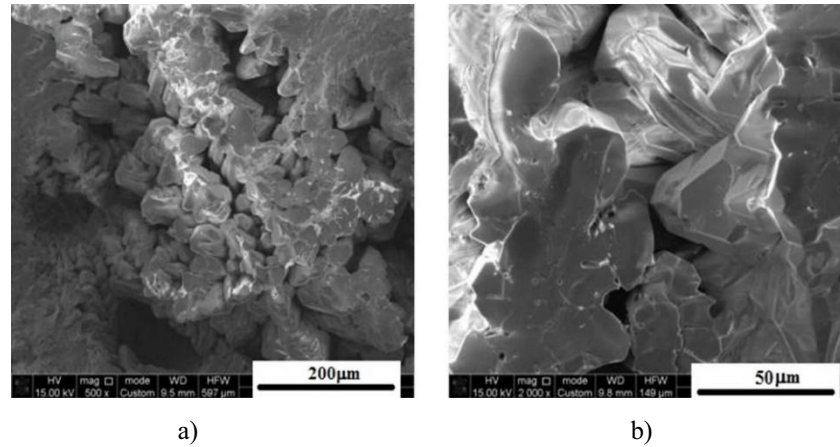


Fig 3. SEM images of the cleavage site for sample 4 (YAG:Ce, Gd) at different magnification

SEM images of the cleavages show that ceramic samples are soldered particles with sizes of $\sim 10\text{--}50$ μm . Most of the particles are in the form of melt. Particles with a well-defined faceting observed indicate the formation of microcrystals. To analyze the structure of the synthesized YAG:Ce and YAG:Ce, Gd ceramics, a Rigaku Miniflex 600 X-ray diffractometer was employed. The resulting data were then compared with ICSD standards, specifically PDF-2 Release 2016 RDB 00-066-0538 (YAG) and PDF-2 Release 2016 RDB 00-06-0291 (YAG:Ce, Gd). Figure 4 showcases the XRD measurement outcomes for YAG:Ce and YAG:Ce, Gd, displaying the XRD patterns for phosphors 2 and 5. The spectra indicate the positions of the spectral lines.

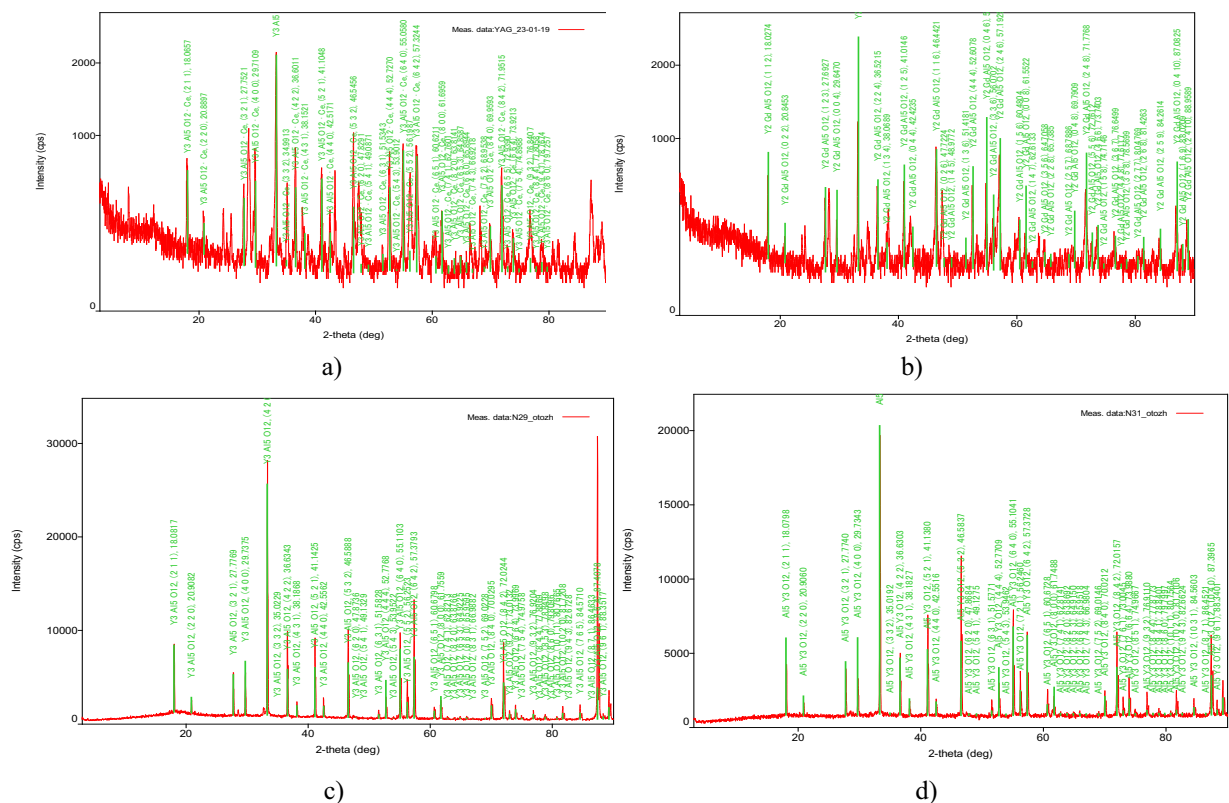


Fig. 4. XRD spectra for before annealing – YAG:Ce (a) and YAG:Ce, Gd (b), after annealing YAG (c) and YAG:Ce, Gd (d) ceramic powders

The size of crystallites is often determined using X-ray diffraction (XRD) through the Scherrer equation. This method computes crystallite sizes based on the full width at half maximum (FWHM) of the diffraction peak, the wavelength of the X-ray radiation used, and the Bragg angle. Following the synthesis of ceramics under the influence of intense radiation flux, the samples typically exhibit an inherent level of defects. Subjecting these samples to high-temperature annealing decreases defect density while enhancing crystallinity.

This improvement is mirrored in the parameters of the crystal structure, which draw closer to their standard values. The study, however, does not prioritize providing numerical evaluations of structural distortions. Additional data on the structure of ceramic samples are presented in Table 2.

Table 2. Parameters of the crystal lattice and crystallites of YAG:Ce and YAG:Ce, Gd phosphors

Sample	Compound	Lattice parameters (a,b,c), Å	Crystallite size (nm)		
		before annealing	after annealing	before annealing	after annealing
YAG:Ce	(Al ₂ O ₃ (43%) + Y ₂ O ₃ (55%) + Ce ₂ O ₃ (2%))	a=12.0234 b=12.0234 c=12.0234	a=12.007477 b=12.007477 c=12.007477	47.24	92.7
YAG:Ce, Gd	Al ₂ O ₃ (40%) + Y ₂ O ₃ (52%) + Ce ₂ O ₃ (2%) + Gd ₂ O ₃ (6%)	a=12.0546 b=12.0546 c=12.0546	a=12.008721 b=12.008721 c=12.008721	81.32	116.7
YAG (ICSD)	Y ₃ Al ₅ O ₁₂	a=12.0062 b=12.0062 c=12.0062	Unit Cell Data Source: Single Crystal.		

The diffraction patterns presented in Figure 4 correspond closely to the known positions and peak ratios associated with YAG:Ce crystals. It's evident that all samples demonstrate characteristics of the Ia-3d space symmetry group. As shown in Table 2, the substitution of Ce³⁺ ions with Gd³⁺ ions result in an increase in the lattice parameter by 0.031 Å. The enlargement of the average lattice parameter due to Gd³⁺ incorporation leads to a red shift in the luminescence band caused by Ce³⁺ ions [24]. High-temperature annealing demonstrates better conformity with the YAG standard (Space group: 230: Ia-3d; Phase: Y₃Al₅O₁₂, in accordance with the ICDD data sheet (PDF-2 Release 2016 RDB) – 230: Ia-3d) and enhanced crystallinity of the ceramics, as seen in Figure 4 (c) and (d).

3 Luminescent properties of synthesized ceramics

PL spectra of the phosphors were measured using Agilent Cary Eclipse and Solar CM2203 fluorescence spectrophotometers. Figure 5 presents the luminescence spectra results for the ceramic samples when excited at 450, 340, and 270 nm wavelengths. The spectrum shape remains consistent regardless of the excitation wavelength (a and b). Two broad luminescence bands at 520 and 580 nm are attributed to the ⁵D₀→⁴F_{5/2}, ⁴F_{7/2} transitions [25]. The luminescence and excitation spectra of ceramics synthesized in this study closely resemble those of YAG:Ce ceramics produced by other methods [26-27] and YAG:Ce-based phosphors [27-30].

When samples are excited by radiation at 270 nm, additional luminescence is observed in the UV spectral region, with bands at approximately 320, 370, and 415 nm. These bands can also be detected in commercial phosphors [31] under the same excitation conditions. The UV luminescence bands exhibit high efficiency, and the intensity ratios of the UV bands vary among the studied phosphors. Figure 5d depicts the locations of the luminescence band maxima for all the samples studied under excitation in the region of 450 nm.

Interestingly, the luminescence band maxima positions in the Gd³⁺-enriched phosphors (samples 4-6) tend to shift toward the long-wavelength spectral area, as compared to phosphors 1-3. This trend is consistent with the well-established understanding regarding the influence of the modifier [24]. It's worth highlighting that the overall shape of the luminescence spectra in the range of 480-700 nm remains unaffected by the method of excitation.

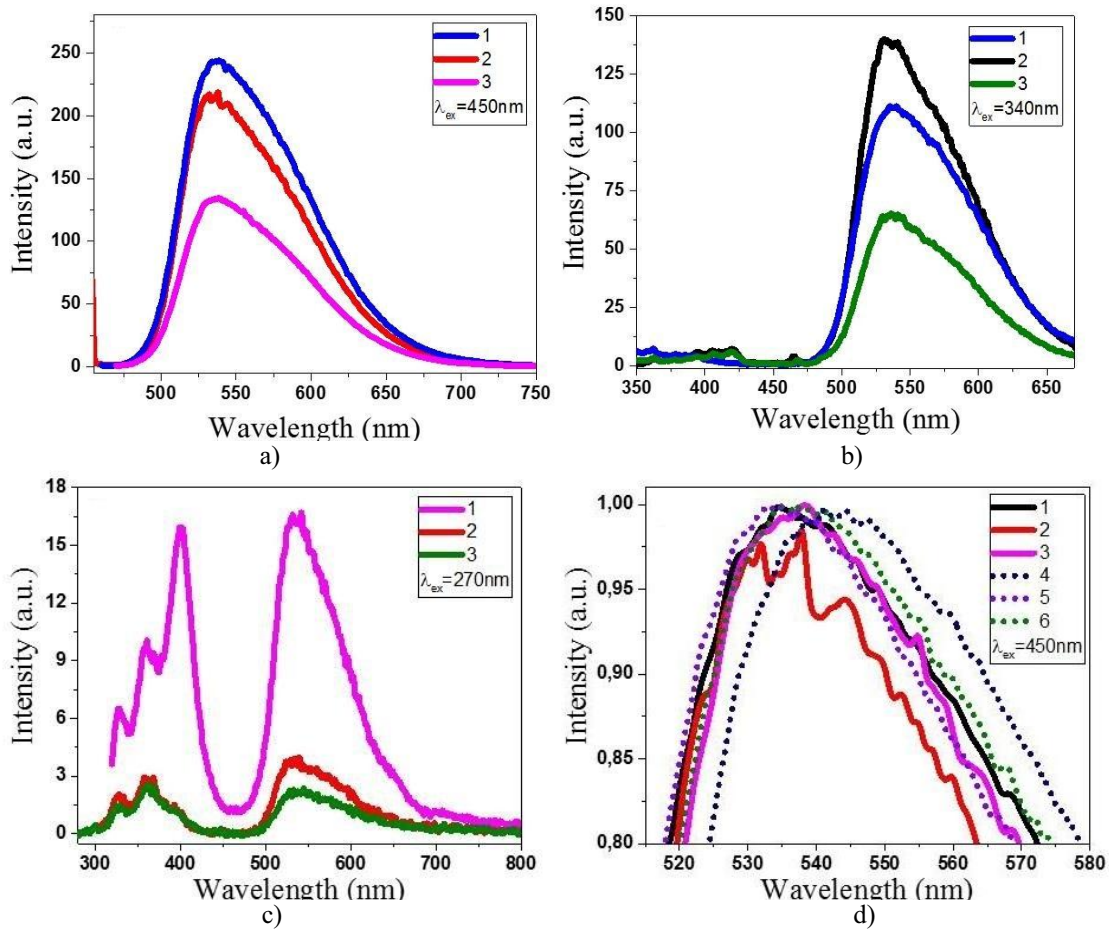


Fig 5. Luminescence spectra of the synthesized samples upon excitation at: a) 450 nm, b) 340 nm, c) 270 nm, d) 450 nm.

The luminescence spectra obtained from the pulverized samples of the synthesized ceramics, when excited by chip radiation at 450 nm and 365 nm, as well as by a laser of 337 nm wavelength measured using an AvaSpec-2048 spectrophotometer, are fundamentally consistent with those illustrated in Figure 5. Figure 6 showcases the outcomes of luminescence spectrum measurements for synthesized samples 1-3 under 540 nm excitation. The form of these excitation spectra is notably characteristic of YAG:Ce phosphors. The emergence of two excitation bands for Ce^{3+} at 460 nm and 340 nm are a consequence of the $^4\text{F}_{5/2} \rightarrow ^5\text{D}_0$ and $^5\text{D}_1$ transitions, respectively [27].

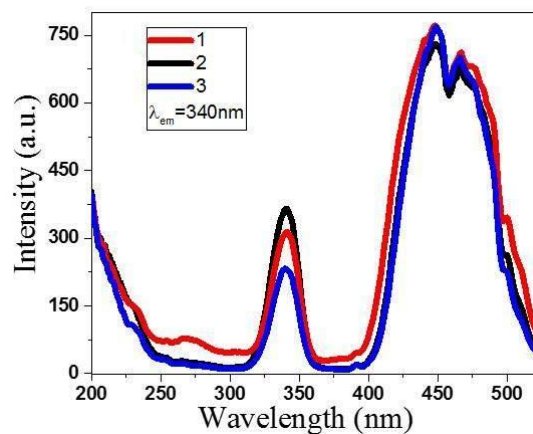


Fig. 6. Luminescence spectra of the synthesized samples excited in the region of 540 nm measured before (a) and after (b) high-temperature annealing.

Effective luminescence can also be excited by radiation with wavelengths shorter than 300 nm. As the wavelength decreases, luminescence steadily increases in the 550 nm region. When excited by 450 nm laser pulses, a nanosecond component prevails in the luminescence decay kinetics in the 550 nm region. Its characteristic time spans from 56 to 60 ns in samples 1, 2, 4, and 5. In samples 3 and 6, the characteristic time ranges from 40 to 52 ns. During these periods, the luminescence intensity decreases by two orders of magnitude within 300 ns. The nanosecond decay component is a distinctive feature of photoluminescence in YAG:Ce phosphors. In order to expediently ascertain the radiation-to-luminescence conversion efficiency, we employed a specific method. By maintaining a constant spatial relationship between the excitation source and the phosphor, we can infer that the conversion efficiency is directly proportional to the observed brightness. When dealing with a luminous object exhibiting a Lambertian distribution (L), its brightness is directly connected to luminosity (M) and the light flux projected into the hemisphere (Fv), as described by the following relationships:

$$F_v = MS = 2\pi LS \quad (1)$$

where S is the luminous surface area. The surface area of the phosphor, whose luminance is being gauged, is determined by the brightness meter's telescopic system and remains consistent throughout the measurement process.

There exists a relationship between the radiation flux (Fe) and the light flux (Fv) emanating from the phosphor, as expressed by the following equation:

$$F_e = F_v \frac{1}{683} \frac{\int_0^\infty \varphi(\lambda) d\lambda}{\int_0^\infty v(\lambda) \varphi(\lambda) d\lambda} \quad (2)$$

For phosphors of the same type, for example, YAG:Ce, we can assume that their radiation spectra $\varphi(\lambda)$ are similar. In this case, the ratio of the radiation fluxes Fv1 and Fv2 of sources with similar emission spectra: $\varphi_1(\lambda) = \varphi_2(\lambda)$, the Lambertian distribution of luminance and equal luminous surface areas, is equal to:

$$\frac{F_{e1}}{F_{e2}} = \frac{F_{v1}}{F_{v2}} = \frac{M_1 S}{M_2 S} = \frac{L_1}{L_2} \quad (3)$$

Hence, for a specific system of phosphors with analogous emission spectrums ($\varphi_1(\lambda)=\varphi_2(\lambda)$), there exists a direct proportionality between the radiation flux and the luminance. Given a stable spatial configuration of the measurement system components, which includes the excitation source, the phosphor, and the brightness meter, the ratio of brightness corresponds to the ratio of efficiencies in the radiation-to-luminescence conversion. Brightness evaluations were performed utilizing a CS-200 Chroma meter. Commercial phosphors SDL 4000 (from NPO Platan, Russia) and YAG 02 (from GrandLux Optoelectronic Co. Intematix Corporation, PRC), with their attributes detailed in [30], served as reference samples for brightness measurement, and thereby, the calculation of phosphor efficiency. Luminescence was excited by LED radiation with a wavelength of 450 nm. Measurements were conducted for powdered ceramic samples and industrial phosphors placed in washers, with the spatial location of the stand components remaining constant during measurements. No specific pattern was observed regarding the impact of high-temperature annealing on the brightness of ceramics. The outcomes of the measurements are showcased in Table 3.

Table 3. Measurement results for brightness L of the synthesized phosphors upon excitation with $\lambda_{ex}=450$ nm.

Sample number	L, cd/m ² $\lambda_{ex}=450$	
	before annealing	after annealing
1	201	193
2	143	179
3	201	235
4	205	176
5	160	188
6	188	200
SDL 4000 (Reference)	360	
YAG – 02 (Reference)	422	

The data shows that brightness of the synthesized phosphors is approximately twice lower than that of industrial phosphors. High temperature annealing increases QE of samples. The Table 4 provides data on the brightness observed for commercial reference phosphors.

Table 4. Brightness of reference phosphors

Sample number		QE, %	
		before annealing	after annealing
2	inside	25.8	35.6
	outside	24.20	43.7
6	inside	37.70	39.4
	outside	39.2	56.1
SDL 4000 [23]		40.4	

Conclusions

The study results indicate that high-power fluxes of hard radiation can be employed for synthesizing YAG:Ce-based ceramics. Activated Ce^{3+} and modified Gd^{3+} ceramics with sizes up to 1.5 cm^3 were produced. XRD analysis revealed a YAG:Ce crystalline phase in samples 1-3 and an additional YAG:Ce, Gd phase in samples 4-6. The properties of the radiation-assisted synthesized samples bear a striking resemblance to those of ceramics. The spectral-kinetic properties of luminescence and excitation found in ceramics, correspond closely to those seen in YAG:Ce and YAG:Ce, Gd phosphors produced using traditional techniques. The conversion efficiency from radiation to luminescence is notably high, attaining values of 0.48 and 0.57 in the reference commercial phosphors YAG-02 and SDL 4000, respectively. This high conversion efficiency underscores the potential of the outlined luminescent ceramics synthesis method.

It's significant to highlight the broad spectrum of conversion efficiencies observed in samples with diverse precursor histories, especially those involving aluminum oxides of varying sources. To enhance the production of ceramics exhibiting high emissive qualities, future research should explore the correlation between luminescent properties and factors such as precursor quality, dopant concentration, modifier, pre-treatment of the mixture, among others.

The process of radiation-assisted synthesis of ceramics fundamentally deviates from the methodologies commonly employed today. This process is governed not solely by temperature, but also by a high ionization density. The irradiation modes used result in an energy output of $11 \times 10^{23} \text{ eV/cm}^3$ during a 1-second exposure to the flux. The generation of one electronic excitation under intense radiation necessitates energy corresponding to 2-3 band gap energy. Consequently, throughout the synthesis duration, approximately $5.5 \times 10^{22} \text{ cm}^{-3}$ electronic excitations (which include electrons, holes, and electron-hole pairs) are produced within 1 cm^3 of the materials employed (Y_2O_3 , Al_2O_3 , Gd_2O_3 , Ce_2O_3), which possess an average band gap of 10 eV. The decay of electronic excitation generates intermediate radiolysis products – radicals with a lifetime of around 10^{-6} s , which significantly increase the efficiency of solid-state reactions and enhance mixing of the batch components. At this level of electronic excitation density, reaction efficiency between charged components is considerably higher than solid-phase synthesis.

Acknowledgments

This research has been funded by the Science Committee of the Ministry of Education and Science of the Republic of Kazakhstan (Grant No. AP14870696).

This research has been funded by the Russian Science Foundation of the Russian Federation. (Grant No. 23-73-00108).

REFERENCES

- 1 Ueda J., Tanabe S. Review of luminescent properties of Ce^{3+} -doped garnet phosphors: New insight into the effect of crystal and electronic structure. *Optical Materials*, 2019. Vol.1. pp. 100018. doi:10.1016/j.omx.2019.100018
- 2 Pankratov V., Popov A.I., Shirmane L., et al. Luminescence and ultraviolet excitation spectroscopy of SrI_2 and $\text{SrI}_2:\text{Eu}^{2+}$. *Radiation Measurements*, 2013. Vol. 56, pp. 13-17. doi:10.1016/j.radmeas.2013.02.022
- 3 Chernov S.A., Trinkler L., Popov A.I. Photo- and thermo-stimulated luminescence of CsI-Tl crystal after UV light irradiation at 80 K. *Radiation Effects and Defects in Solids*, 1998. Vol. 143 (4), pp. 345-355. doi:10.1080/10420159808214037
- 4 Elsts E., Rogulis U., Bulindzs K., et al. Studies of radiation defects in cerium, europium and terbium activated oxyfluoride glasses and glass ceramics. *Optical Materials*, 2015. Vol. 41, pp. 90-93. doi:10.1016/j.optmat.2014.10.042

- 5 Pankratov V., Popov A.I., Kotlov A., Feldmann C. Luminescence of nano- and macrosized $\text{LaPO}_4\text{:Ce,Tb}$ excited by synchrotron radiation. *Optical Materials*, 2011. Vol.33 (7), pp. 1102-1105. doi:10.1016/j.optmat.2010.12.019
- 6 Polissadova E., Valiev D., Vaganov V., et al. Time-resolved cathodoluminescence spectroscopy of YAG and YAG:Ce³⁺ phosphors. *Optical Materials*, 2019. Vol. 96, pp. 109289. doi:10.1016/j.optmat.2019.109289
- 7 Karipbayev Z.T., Lisitsyn V.M., Mussakhanov D.A., et al. Time-resolved luminescence of YAG:Ce and YAGG:Ce ceramics prepared by electron beam assisted synthesis. *Nuclear Instruments and Methods in Physics Research, Section B: Beam Interactions with Materials and Atoms*, 2020. Vol. 479, pp. 222-228. doi:10.1016/j.nimb.2020.06.046
- 8 Sidorenko A.V., Bos A.J.J., Dorenbos P., et al. Storage properties of Ce³⁺ doped haloborate phosphors enriched with ¹⁰B isotope. *Journal of Applied Physics*, 2004, Vol. 95 (12), pp. 7898-7902. doi:10.1063/1.1719260
- 9 Platonenko A., Popov A.I. Structural and electronic properties of $\beta\text{-NaYF}_4$ and $\beta\text{-NaYF}_4\text{:Ce}^{3+}$. *Optical Materials*, 2020. Vol. 99, pp. 109529. doi:10.1016/j.optmat.2019.109529
- 10 Karipbayev Z.T.; Lisitsyn V.M.; Golkovski M.G.; Zhilgildinov Z.S., et al. Electron Beam-Assisted Synthesis of YAG:Ce Ceramics. *Materials*, 2023. Vol. 16, pp. 1-11. doi:10.3390/ma16114102
- 11 Narukawa Y., Ichikawa M., Sanga D., Sano M., Mukai T. White light emitting diodes with super-high luminous efficacy. *J. Phys. D Appl. Phys.*, 2010. Vol.43, pp. 354002. doi:10.1088/0022-3727/43/35/354002
- 12 George N.C., Denault K.A., Seshadri R. Phosphors for solid-state white lighting. *Annu. Rev. Mater. Res.*, 2013, Vol. 43, pp. 481–501. doi:10.1146/annurev-matsci-073012-125702
- 13 Ye S., Xiao F., Pan Y.X., et al. Phosphors in phosphor-converted white light-emitting diodes: Recent advances in materials, techniques and properties. *Mater. Sci. Eng. R Rep.*, 2010, Vol.71, pp. 1–34. doi:10.1016/j.mser.2010.07.001
- 14 Yoshikawa A., et al. Crystal growth and scintillation properties of multi-component oxide single crystals: Ce:GGAG and Ce:La-GPS. *J. Lumin.*, 2016, Vol.169, pp. 387–393. doi:10.1016/j.jlumin.2015.04.001
- 15 Osipov V.V., Ishchenko A.V., Shitov V.A., et al. Fabrication, optical and scintillation properties of transparent YAG:Ce. *Opt. Mater.*, 2017, Vol.71, pp.98–102. doi:10.1016/j.optmat.2016.05.016
- 16 Kucera M., Nikl M., Hanus M., Onderisniva Z. Gd³⁺ to Ce³⁺ energy transfer in multi-component GdLuAG and GdYAG garnet scintillators. *Phys. Stat. Solidi (RRL)*, 2013, Vol.7, pp. 571–574. doi:10.1002/pssr.201307256
- 17 Choe J.Y. Luminescence and compositional analysis of Y₃Al₅O₁₂:Ce films fabricated by pulsed-laser deposition. *J. Mat. Res. Innovat.*, 2002, Vol.6, pp. 238-241. doi:10.1007/s10019-002-0204-4
- 18 Murai S., et al. Scattering-based hole burning in Y₃Al₅O₁₂:Ce³⁺ monoliths with hierarchical porous structures prepared via the sol-gel route. *J. Phys. Chem: C*, 2011, Vol.115, pp. 17676–17681. doi:10.1021/jp204594c
- 19 Hakuta Y., et al. Continuous production of phosphor YAG:Tb nanoparticles by hydrothermal synthesis in supercritical water. *Materials Research*, 2003, Vol.38, pp. 1257-1265. doi:10.1016/S0025-5408(03)00088-6
- 20 Vasilica Țucureanu, et al. Effect of process parameters on YAG:Ce phosphor properties obtained by co-precipitation method. *Ceramics Intern.*, 2020. Vol. 46, pp. 23802-23812. doi:10.1016/j.ceramint.2020.06.156
- 21 Huczko A. Fast combustion synthesis and characterization of YAG:Ce³⁺ garnet nanopowders. *Phys. Status Solidi B*, 2013, Vol.250, pp. 2702–2708. doi:10.1002/pssb.201300066
- 22 Lisitsyn V., et al. Luminescence of the tungsten-activated MgF₂ ceramics synthesized under the electron beam. *Nuclear Inst. and Methods in Physics Research*, 2018, Vol.435, pp. 263–267. doi:10.1016/j.nimb.2017.11.012
- 23 Lisitsyn V.M., et al. YAG based phosphors, synthesized in a field of radiation. *IOP Conf. Series: Journal of Physics: Conf. Series*, 2018, Vol.1115, pp. 052007. doi:10.1088/1742-6596/1115/5/052007
- 24 Alpyssova G., Lisitsyn V.M., Karipbayev Zh.T. et al. Luminescence of cerium doped yttrium aluminumgarnet ceramics synthesized in the field of radiation flux. *Eurasian phys. tech. j.*, 2021. Vol. 18, №3(37), pp. 37-42. doi 10.31489/2021No3/37-42
- 25 Hongling Shi, et al. Luminescence properties of YAG:Ce, Gd phosphors synthesized under vacuum condition and their white LED performances. *Optical Materials Express*, 2014, Vol.4(4), pp.649-655. doi:10.1364/OME.4.000649
- 26 Zorenko Y., Voznyak T., Gorbenko V., et al. Luminescence properties of Y₃Al₅O₁₂:Ce nanoceramics. *J. Lumin.* 2011, Vol.131, pp. 17–21. doi:10.1016/j.jlumin.2010.08.015
- 27 Dorenbos P. 5d-level energies of Ce³⁺ and the crystalline environment. IV. Aluminates and «simple» oxides. *J. Lumin.* 2002, Vol.99, pp. 283–299. doi:10.1016/S0022-2313(02)00347-2
- 28 Munoz-Garcia A.B., Barandiaran Z., Seijo L. Antisite defects in Ce-doped YAG (Y₃Al₅O₁₂): First-principles study on structures and 4f-5d transitions. *J. Mater. Chem.*, 2012, Vol. 22, pp. 19888–19897. doi:10.1039/C2JM34479C
- 29 He X., Liu X., Li R., et al. Effects of local structure of Ce³⁺ ions on luminescent properties of Y₃Al₅O₁₂:Ce nanoparticles. *Sci. Rep.*, 2016, Vol.6, p. 22238. doi: 10.1038/srep22238
- 30 Lisitsyn V., Lisitsyna L., Tulegenova A., et al. Nanodefects in YAG:Ce-Based Phosphor Microcrystals. *Crystals*, 2019, Vol.9 p.476. doi:10.3390/cryst9090476.

DOI 10.31489/2023NO2/127-137

UDC 53; 537.5; 539.5; 533.9; 539.5; 62; 620.9

MOLECULAR DYNAMIC SIMULATION OF PLASMA MATERIAL INTERACTION TO CALCULATE THEORETICAL SPUTTERING YIELD

Pahsa Alper

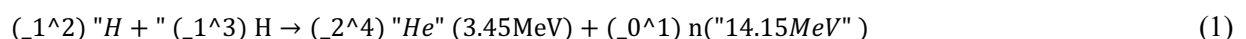
Graduate School of Natural and Applied Sciences, Ankara Yıldırım Beyazıt University, Ankara, Türkiye;
165106407@ybu.edu.tr

In a fusion reaction two light nuclei, Deuterium and Tritium merge to form a single heavier nucleus Helium. However, two positive nuclei repel each other. In order to merge two nuclei they need to have very high velocities. High speed means, high temperature. For the reaction it is significant for a nuclei to keep at 100 million °C temperature. At this temperature D and T atoms form a plasma. In order the reaction to take place, the plasma temperature must be conserved or plasma should not be cooled. Tokamak reactors are designed to confine the plasma in a magnetic field. Thus, the cooling of the plasma is prevented by hitting the reactor walls. Plasma density and temperature must be at a certain level in order to initiate the reaction and to ensure continuity. During the reaction process, positive and negative ions escaping from the magnetic field environment interact with Tokamak walls and cause deformation. This causes the plasma wall to deteriorate over time and the release of neutrons to the environment. Plasma-Wall interaction is one of the most important problems that cause interruption of fusion in Tokamak reactors. The materials which most resistant to ion corrosion in the plasma wall are graphite, beryllium, aluminium and tungsten. In this work, plasma-material interaction is studied theoretically physical and chemical erosion caused by the plasma interactions of different wall material samples (graphite, aluminium and Tungsten) used in the fusion reactor and investigated with the Monte Carlo method with molecular dynamics.

Keywords: Plasma, Nuclear Fusion, Molecular Dynamics, Sputtering Yield, Monte Carlo

Introduction

Today, the increasing world population, rapid industrialization and the need for high-tech have made electrical energy very important. Fossil resources have been used to obtain electrical energy for many years. However, since fossil fuels are depleted over time, alternative energy sources are needed for energy production. In recent years, the issue of utilizing renewable energy sources such as sun, wind, tides, waves, geothermal and biomass has gained importance [1-3]. Although electrical energy can be obtained from sources such as sun and wind, other energy sources are also needed due to problems of cost, continuity and storage. One of solution to generating electricity without using fossil fuels is the nuclear energy. Conventional nuclear power plants are based on the fission reaction. These types of reactors, which are generally based on the decomposition of unstable uranium nuclei into more stable nuclei, are the subject of debate in many aspects; such as both finding nuclear fuel and storing nuclear waste. On the other hand, combining two light elements as a result of a nuclear reaction to form a heavier element is called "fusion". A huge amount of energy is released as a result of fusion, also known as the nuclear reaction. A typical fusion reaction is the reaction between deuterium and tritium, which are isotopes of hydrogen. The following reaction equation is a atomic molecular form to specify the total energy produced in nuclear fusion:



However, the fusion reaction, which is also a nuclear reaction, is not as easy as a chemical reaction. For the reaction to occur, the repulsive force between the two positively charged nuclei must be overcome. For this issue, isotopes (D and T) must approach close to each other with very high kinetic energies. This energy must be at least 0.7 MeV. A temperature of about 3×10^9 K is needed for isotopes to have this kinetic energy. If a sufficient number of D and T nuclei are found together and this initial temperature is reached, the fusion reaction then going to be started. This is one of the most important problems in realizing the fusion reaction. On the other hand, scientists have developed two different techniques to overcome this situation. One of them is to confine deuterium and tritium to a small area spatially and initiate the reaction with a high-energy

laser, and the other is to carry out the reaction by trapping these isotopes in a magnetic field. A fusion energy reactor can be designed by utilizing the kinetic energies of the neutrons released as a result of this reaction. The most well-known of these reactors is the Tokamak reactor. In the Tokamak reactor, the plasma is trapped in the magnetic field environment to prevent its cooling.

In the Tokamak reactor, the uncharged neutrons, each of which has an energy of 14.15 MeV, are separated from the magnetic field environment. However, these neutrons can be slowed down by a cooling liquid (e.g. water). Electric energy can be obtained by operating turbines with the water vapor obtained as a result of slowing down the neutrons released in a reactor in the liquid. Since neutrons slowed in this way lose most of their energy in the process. Even if they hit the reactor wall, they cannot make the wall radioactive. Some neutrons can be used to create artificial Tritium by interacting with it. On the other hand, He cores, each of which has an energy of 3.5 MeV, are also produced in the Tokamak reactor [4-14]. This energy of helium nuclei can be used to maintain the temperature of the plasma. A Tokamak reactor is a torus (tube) shaped device. As a result of the appropriate arrangement of the magnets, the reaction is ensured by being trapped in the plasma magnetic field environment, and it is prevented from contacting the reactor wall and cooling. However, while the plasma is moving in the magnetic field, some high-energy He ions escape from the magnetic field environment and hit the reactor wall, and some of them escape from the environment due to the secondary magnetic field and hit the reactor wall again. Although most of the He ions are discharged from the divertor, some of them cannot be prevented from hitting the reactor wall. These fugitive He ions sometimes cause the reactor wall to erode and the Tokamak to collapse in the long run. Because of this process the plasma wall to deteriorate over time and the release of neutrons to the environment. This causes neutronic, thermal, radiative and thermomechanic stress load on the walls of the nuclear fusion reactor. Interface management between the plasma and the wall structures of the nuclear reactor is essential.

The main results of the confinement, like H mode is based on efficient management of the controlled interface. There are many mechanisms occur in the wall structures of the nuclear fusion reactor, for instance adsorption of large quantities of gas particles issued by the plasma, fast particles in the plasma cause erosion and heat flux on the surface of the walls. These mechanisms result plasma radiation to lose large amount of temperature and type of impurities that affect the plasma. This process creates the plasma wall to deform over time to release neutrons into the environment [15-16]. Interaction between the reactor walls and plasma is important factor in designing a fusion reactor. Since plasma induced erosion can seriously shorten the life time of the reactor wall components [17-18].

The interaction of the plasma with the reactor walls has been one of the critical issues in the development of the fusion energy reactor, as plasma-induced wear can severely limit the lifetime of the wall components. There are many interactions that cause plasma with reactor walls. One of them is the divertor segment of the Tokamak fusion reactors. Generally nuclear fusion reactor such as Tokamak type of geometry has a output door called divertor to take of the He out of the plasma. Innovation on the material fusion wall materials research is progressing day by day and understanding the plasma and wall interaction are the central topics in nuclear fusion research under the plasma diagnostic and plasma material interaction literature. Produced fusion artifacts such as fusion ash from He must be cleaned out of plasma. As the He cleans off then the He contacts the divertor walls of the nuclear fusion reactor wall. This mechanism cause divertor and the nuclear fusion walls deform over time and to release neutrals into the environment. Graphite, Beryllium, Molybdenum, Steel and Tungsten are resistant materials against the erosion processes in Tokamak reactors. Tungsten is the most resistant material against plasma with high atomic number and melting point [19-20].

In experimental reactors such as ITER or DEMO, He ash accumulation measurements are stated in recent studies. Observations shows that the effects of the alpha particle concentration on plasma process is studied and the computations are done as in zero dimensional power and particle balance equations so that the He fusion reactions and they reach to the optimal condition. Literature observations stated that He as the as of the deuterium-tritium reaction cannot be avoided in Tokamak fusion reactors. Experimental reactors such as ITER and DEMO shows the low activation materials such as steels SiC ceramic composites and vanadium alloys are tried in nuclear wall materials. There are many new investigations related to diagnostic tools and measurement techniques to measure the deformation amount in the wall materials existed in research. The measured value of the affect of the plasma material interactions is mainly found by the energy (temperature) of the plasma, the charge density of the plasma and the mass density of the material. Since the plasma material interactions are all concentrated on various complex and multifaceted atomic and plasma processes. For instance, materials crystal structures physiology affects the molecular bounds of the plasma

particles to create new artifacts during the nuclear fusion operation. During the plasma material interaction nuclear fusion reactor complex processes are existed such as neutralization, desorption, reflection, dust, cavities, sputtering, H/He trapping, interstitials, vacancies inside the material crystal structures, bubbles, dislocations, co-depositions and neutron damaging. These mechanisms must be simulated separately to understand the physics behind the system. Modeling and simulating the plasma material interaction in Tokamak reactors are easy and cheap way to design and build fusion reactors by linking the experimental gaps. Extrapolation of plasma material interaction in literature experiments to the relevant duration of operations in commercial fusion reactors and plasma material interaction results on fusion performances to commercial fusion reactors must be shown. Plasma material interaction in Tokamaks involve complex material and plasma interaction which exists on time and space scales spanning over several orders of magnitude. It is also comprehensive to model and simulate the plasma material interactions in Tokamak to solve a hierarchy of material and plasma models coupling. In order to solve the complex occasions fast computers to compute high performance calculations. In literature multiscale modelling, continuum fluid model, quantum mechanics model, lattice Boltzmann, Brownian Dynamics, Kinetic Monte Carlo and Molecular Dynamics with Monte Carlo are existed as a context in plasma material interactions [21].

In this study, physical erosion, chemical erosion and sputtering rates of Be, Al, C and W used to meet plasma in Tokamak reactor against neutron and He ions were calculated using molecular dynamic Monte Carlo simulation model. This method is effective and efficient when compared with the above mentioned methods. It is easy to establish the borders of the modelling context and time efficient in calculations in the molecular structure when performing the executions in the computer simulation. For this, Python-based OMFIT (One Modeling Framework for Integrated Tasks) and ASE (Atomic Simulation Environment) programs were used. In this context, the open code software ASE Monte Carlo simulation package program was used to examine the interaction of neutron (H+) and He(+) with Be, Al, C and W. As a result of the study candidate materials of the reactor wall, physical sputtering yields, chemical sputtering yields, back scattering yield and total sputtering yield and radiation enhanced sublimation (RES) were calculated.

1 Methods

1.1 Calculation of Total Sputtering Yield

One of the most important concepts in plasma-wall interaction is sputtering yield. Sputtering yield can be defined as the number of particles removed per particle falling on the wall.

$$Y = \frac{\text{NumberofParticlesRemoved}}{\text{NumberOfIncomingIons}} \quad (2)$$

Incoming ion atoms interact with the target atom and cause it to break, as well as being held by the target. Therefore, sputtering depends on both the properties of the incoming ion (energy, mass and kinetic energy) and the properties of the target atoms (atomic mass, surface binding energy, surface texture, crystal orientation). If the kinetic energy of the bombardment particle is greater than the lattice displacement energy of the target atoms, surface damage will occur. The lattice displacement energy is the energy required to move the target atom one atomic distance from its original position.

The above yield of sputtering yield is a very general statement. When evaluated more comprehensively, the sputtering yield also depends on the bombardment energy (E_0), the angle of incidence of the incoming ions. A series of elastic scattering is also possible if the electronic stimulation of the target is neglected. Sputtering yield, taking into account elastic collisions and recoil atoms in the target

$$Y(E_0, \theta_0) = \beta \alpha N S_n(E_0) \quad (3)$$

It can be expressed as Here, β is a factor that defines the properties of the target (such as surface binding energy, crystal orientation). N is the atomic density at the target, α is the correction factor defined as the ratio of the mass of the target atoms to the mass of the incoming ions, and S_n is the nuclear arrest cross section is expressed as [22]. From the literature Yamamura to calculate the sputtering yield under normal incoming conditions is given as:

$$(E) = 0.42 \frac{a^* Q K S_n(\epsilon)}{U_s [1 + 0.35 U_s S_e(\epsilon)]} \left[1 - (E_{th}/E)^{1/2} \right]^{2.8} \quad (4)$$

1.2 Molecular Dynamics and LAMMPS Method

As part of the simulation studies, Molecular Dynamics calculations were performed using the Large Scale Atomic/Molecular Massively Parallel Simulator (LAMMPS) open source code package program. Molecular Dynamics consists of solving classical Newton's equations for N atoms in a predefined simulation cell. According to classical Newton's equations i. force acting on the atom and the position of the atom is defined as:

$$F_i(t_0) = m_i \ddot{r}_i(t_0) = -\frac{\partial U}{\partial r_i(t_0)} \quad (5)$$

$$r_i(t_0 + \Delta t) = r_i(t_0) + \dot{r}_i(t_0)\Delta t + \frac{1}{2}\ddot{r}_i(t_0)[\Delta t]^2 + \dots \quad (6)$$

The interaction potential (U) between atoms was calculated with the embedded-atom model (EAM).

The surface of the simulation cell (100) was bombarded with an ion beam of 1-5 keV. The ion beam was placed 10 Å above the top layer (on the z-axis) and an initial kinetic energy was given. The bombardment simulation was repeated for 2000 times steps with 0.01 fs time steps, and the bombardment simulation was repeated 60 times as a function of the kinetic energy of the ions. Physical sputtering yield values were calculated by counting neutral atoms 5 Å above the target surface. In numerical application, physical sputtering yield and chemical erosion yield are calculated with the generalized equations obtained by using data obtained as a result of Monte Carlo simulation with empirical equations.

1.3 Monte Carlo Method

Monte Carlo Method is a simulation method that determines the state of a system consisting of N particles and in a constant volume V at any temperature T. The Monte Carlo method is based on the numerical solution of a problem that models the motion of objects interacting with their surroundings, taking into account the body-body or body-environment interactions. Partition function in classical physics, is defined as [23]:

$$Q = c \int dp^N dr^N \exp[-H(r^N, p^N)/k_B T] \quad (7)$$

Here, r^N is the coordinates of the N particle, and p^N is the momenta. H is the Hamiltonian of the system. By using Monte Carlo technique in plasma surface interaction, physical sputtering yield and chemical erosion yield are calculated numerically. Then, analytical expressions are fitted to the numerical data obtained for practical applications. Physical sputtering yield based on experiment and Monte Carlo numerical data:

$$Y^{fiz}(E_0) = Q S_n(\epsilon) \left[1 - \left(\frac{E_{th}}{E_0} \right)^{\frac{2}{3}} \right] \left(1 - \frac{E_{th}}{E_0} \right)^2 (\cos \alpha)^{-f} \exp\left[-f \left(1 - (\cos \alpha)^{-1} \right) \cos \alpha_{opt} \right] \quad (8)$$

It is given with Here, Q and threshold energy are feet parameters. E_0 is the energy of the incident particle.

2 Results and Discussion

Using the equations given in Method section, the total sputtering yield of H, He and D ions from Be, C, W and Al surfaces, which are the materials used as plasma countering materials in the Tokamak reactor, were calculated. Sputter yield calculated as a function of the kinetic energy of H, He and D ions are given in Fig 1, Fig 2 and Fig 3. In the H, D and He-wall interactions, the atom sputtering yield of W was lower than that of Be, C (Graphite) and Al. W is used as wall material in the Diverter part (the part where He and excess heat are discharged) in Tokamak reactors. Although the probability of splitting atoms from W for these isotopes seems very low from the figures, it is thought that H and He ions are held on the W surface, and even high-energy H ions penetrate into the W and cause diffusion. The solubility of H in W is very low and it occupies the tetrahedral crack regions. He atoms, on the other hand, have self-trapping properties as they settle in these regions of W. In this way, the accumulation of H and He ions in W affects all mechanical and physical properties of W. On the other hand, atom sputtering yield from Be was found to be the highest in the 0-1000 eV kinetic energy range.

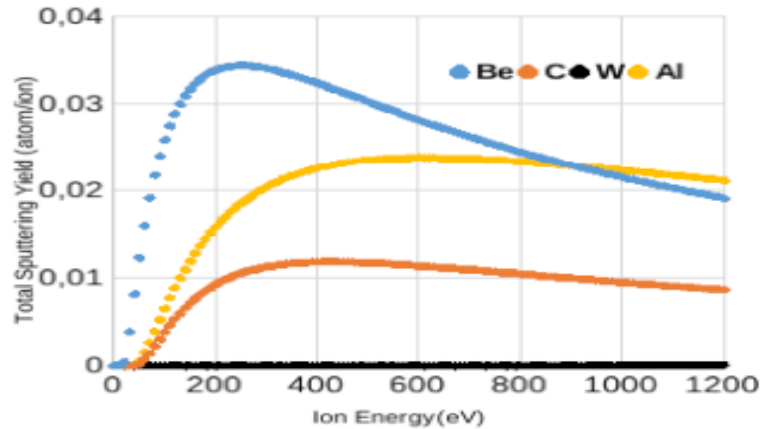


Fig 1. Atom sputtering yield of H from Be, C (Graphite), W and Al surfaces

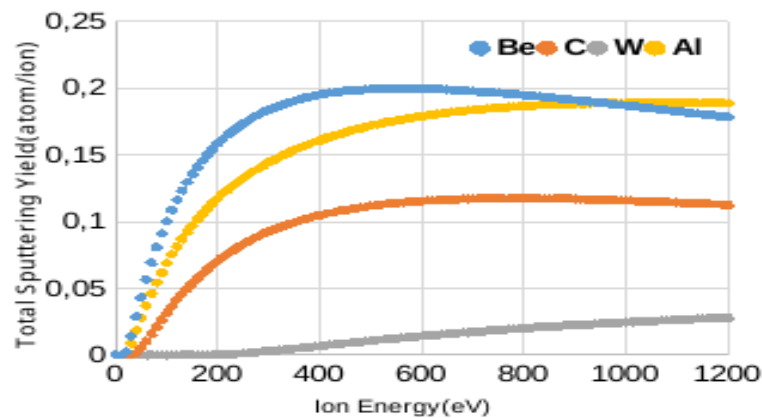


Fig 2. Atom sputtering yield from He's Be, C (Graphite), W and Al surfaces

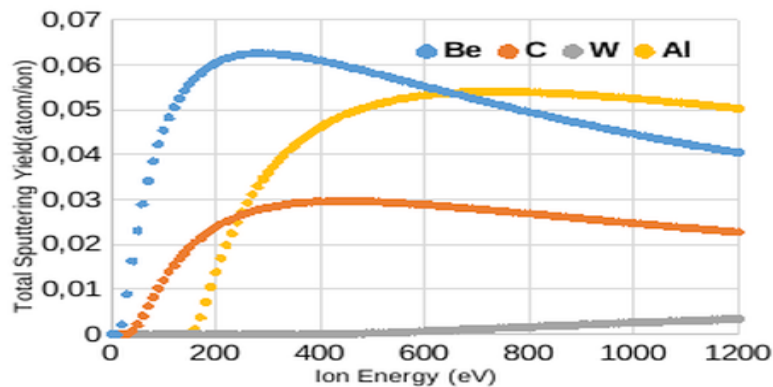


Fig 3. Atom sputtering yield from D's Be, C, W and Al surfaces

From the plotted graphs of the theoretical calculation resultant graphs between Fig-1, Fig-2 and Fig-3 most minimum sputtering yield affected atom can be seen as the bombardment of Ion Energy increased of H, He and D is determined as W. This fact is also similar in the experimental studies of the [24], W is selected as the main wall material in the design of the ITER demo reactor. Since the design of the ITER is now build as monoblock W plates that is placed in the reactor wall. It is already tested to the hot plasma and W gave the most resistive material among the other materials. As the heat in the plasma increases as can be seen in the Fig-1, Fig-2 and Fig-3 sputtering effects which is calculated as total sputtering yield already provide W is the most featured material.

In applications of material development mechanisms given in [24] also states the diamond can be used with W by mixing them to resist against the hot plasma. This is because diamond (C) or graphite is the highest melting point after W. However, since it is low atom numbered material it cannot be used alone. As

can be seen from sputtering yield graphs H, He and D ion plasma energies, C showed the most resistive case as in sputtering yield when compared to the W.

When we consider Be, it is a candidate material for good thermal loading and minimize radiation losses of the sputtered plasma atoms from H, He or D. However, from the graphics of the sputtering yield theoretical works it is third material with the highest sputtering yield in Fig-1, Fig-2 and Fig-3. In [24] states the experimental works show that Be has low melting point and its high toxicity. This means it cannot be used purely in the long run in the plasma facing material for future. For this reason Be is mixed with other metals such as Titanium and Vanadium. The last material Al is the soft metal crystal which has the higher sputtering yield in Fig-1, Fig-2 and Fig-3 with the minimum atomic number. It is affected by H, He and D plasma ions. Al is not used alone in the nuclear fusion reactors. It is mixed with different alloys. It has the lowest melting point when compared to Be and W. It is specified in [24] studies and Bronze is mixed with Al to be used ITER blanked design experiments. Since pure Al cannot resist against the hot plasma in the long duration process of nuclear fusion.

In the literature, there are several open-coded computer programs that examine the plasma-wall interaction in Tokamak reactors. In the research study, the current package programs and the related literature were examined in detail. Especially Python-based OMFIT (One Modeling Framework for Integrated Tasks) and ASE (Atomic Simulation Environment) programs have been found to be suitable for the purposes of the study. In this context, the ASE package program, which is an open source code software, was modified to examine the H-W interaction and it was determined whether the Lennard Jones and Morse potentials were suitable for the H-W interaction with test studies. Fig 4 and Fig 5 show the minimum energy paths and diffusion barriers calculated by the Nudged elastic band (NEB) method using these potentials for the H-Al interaction. It has also been observed that the diffusion barrier for the Morse potential is high and there is a potential well on the minimum energy path. A high diffusion barrier means that it is difficult for incoming ions to eject atoms from the target up to the diffusion threshold.

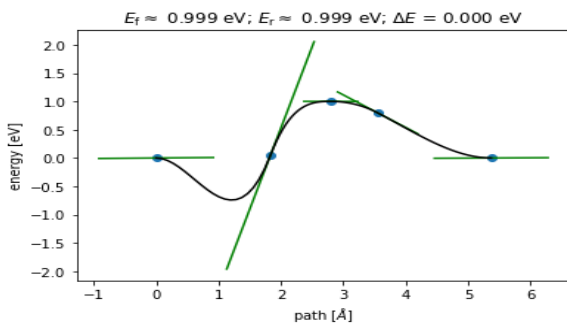


Fig 4. Diffusion barrier obtained by NEB method using Morse potential in H-Al interaction

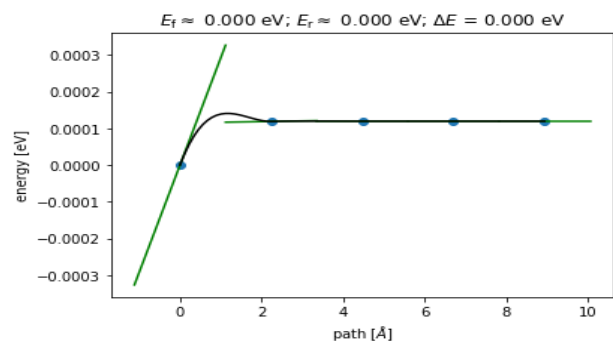


Fig 5. Diffusion barrier obtained by NEB method using Lennard-Jones potential in H-Al interaction

Nudge Elastic Band of the H and Al interaction is also computed in Fig 4 and Fig 5 by using the Lennard Jones and Morse Potentials. It can be seen that the potential threshold energy to eject an atom a high diffusion barrier energy need to be passed for each candidate material that will be used in the nuclear fusion reactor design. That means if the candidate materials are studied in [24], it must be also known the barrier energies also a criteria for selecting the plasma facing materials.

For graphite bombarded with H, D, T and He ions, the physical sputtering yield values calculated using the sputtering yield calculation using Molecular Dynamics, LAMMPS and Monte Carlo processes stated in Method section as a function of kinetic energy, incidence angle and plasma temperature are given in Fig 6, Fig 7 and Fig 8, respectively.

Fig 9 gives the change of chemical erosion yield depending on ion energy. In studies in the literature on graphite, the chemical erosion yield is generally calculated only for the low energy region. Therefore, no peak around 300 eV was observed. This peak indicates that the chemical erosion of the target material is maximum at this energy. It was observed that the chemical erosion caused by deuteron at an energy value of 300 eV was the highest. As can be seen from the figures, the physical sputtering yield increases as the mass of the bombardment ion increases in all four cases. For physical sputtering, this is to be expected.

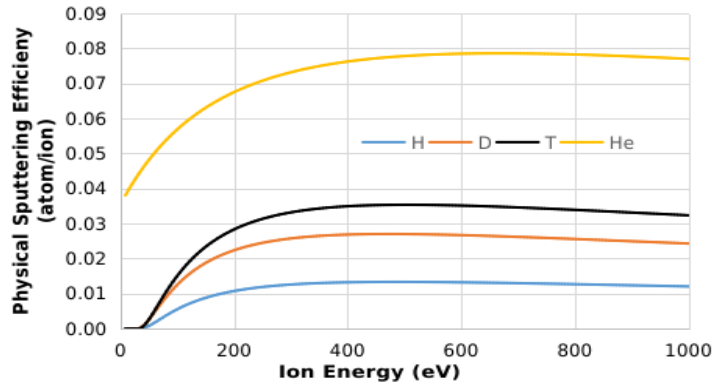


Fig 6. Variation of physical sputtering efficiency depending on the energy of H, D, T and He ions

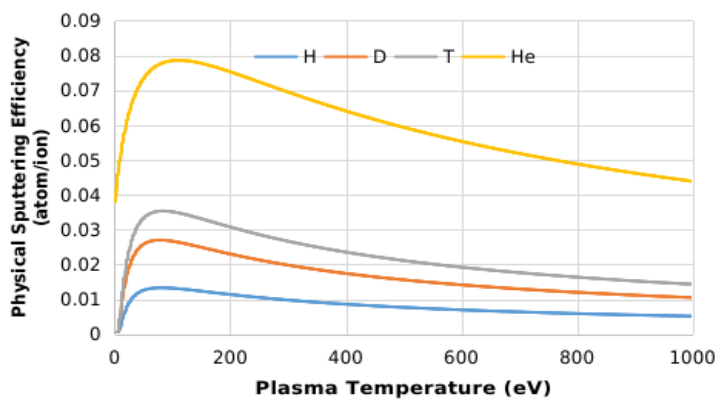


Fig 7. Variation of physical sputtering efficiency depending on the plasma temperature

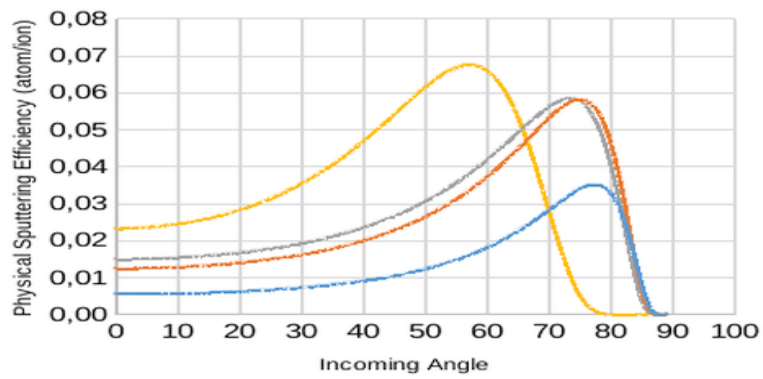


Fig 8. Variation of physical sputtering yield with plasma temperature

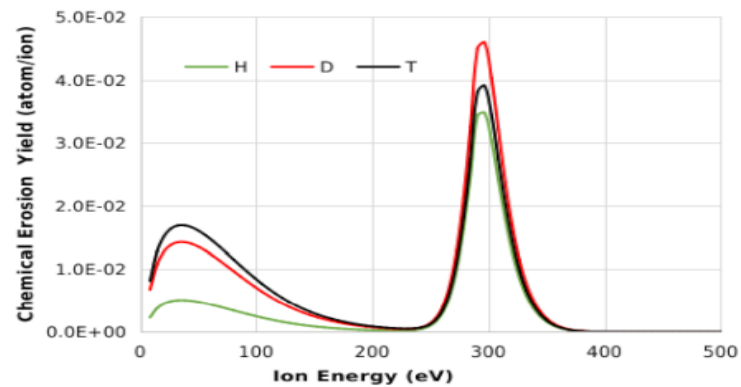


Fig 9. Variation of physical sputtering yield with the angle of incidence of ions

On the other hand, the maximum of the physical sputtering yield was observed for all three hydrogen isotopes at the same location, while the maximum sputtering yield for the He ion was observed at a lower angle. From the graphs depending on the energy and temperature, it was observed that the target material was subjected to a strong physical sputtering up to a certain energy value and then the physical sputtering became stable. When evaluated according to the angle of incidence, it is seen that the physical sputtering yield is maximum when the ions come to the target surface at an angle of 50-80 degrees.

While the physical sputtering yield was generally calculated in the literature studies, in this study, chemical erosion, back scattering, RES (Radiation Enhanced Sublimation) yield and thermal evaporation yield were also calculated using the PSI open source code based on the Kinetic Monte Carlo simulation method. For this purpose, an ion beam consisting of 1013 ions was sent to the graphite surface and chemical erosion, back scattering yield, RES yield and temperature increase in the target material were calculated using the Yamamura technique. Fig 10 The variation of the back scattering yield depending on the ion energy is given. Since low energy ions can be back scattered by ESP (electron stopping power), it is expected that the back scattering yield is high at low temperatures of the plasma and decreases with increasing temperature.

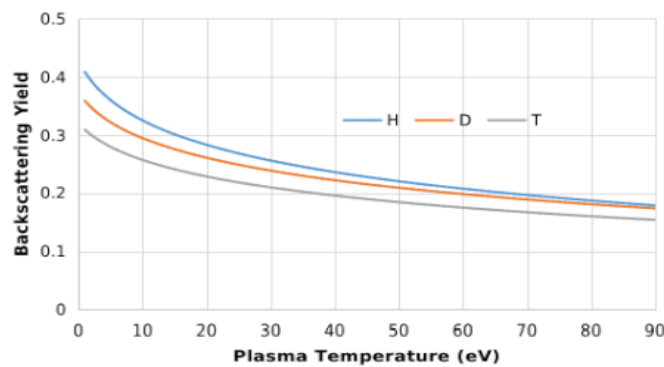


Fig 10. Variation of back scattering yield with temperature of H, D and T ion plasma

The variation of RES yield with the temperature of the graphite target is given in Fig. 11. Radiation enhanced sublimation (RES) is unique to the graphite material and is the result of increasing the ratio of the number of graphite (C) atoms emitted to the number of ions in the plasma beam when graphite reaches high temperatures.

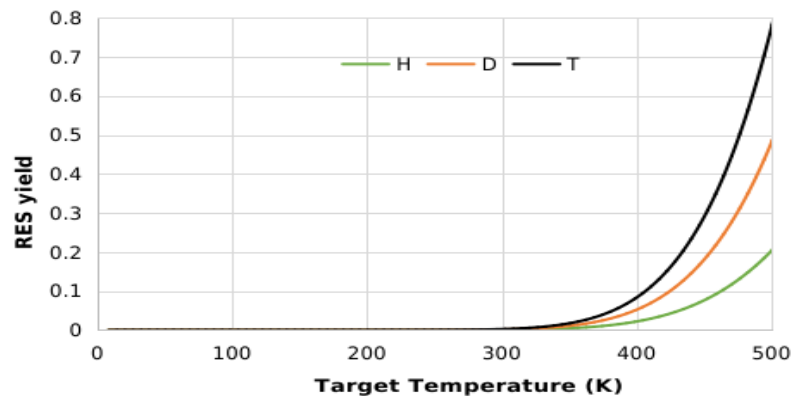


Fig 11. Variation of RES yield with temperature of graphite target

Fig 12 shows the temperature change in the graphite target depending on the energy of the ions. As seen in the figure, the increase in the energy of the plasma beam causes a non-linear increase in the temperature of the target material. In addition, it can be seen that the increase in the number of ions is very important in increasing the temperature of the target material. In the case of 1012 ions, the temperature increase on the target surface is in the range of 300-500 K, while in the case of 1013 ions, the temperature increases up to 3000K.

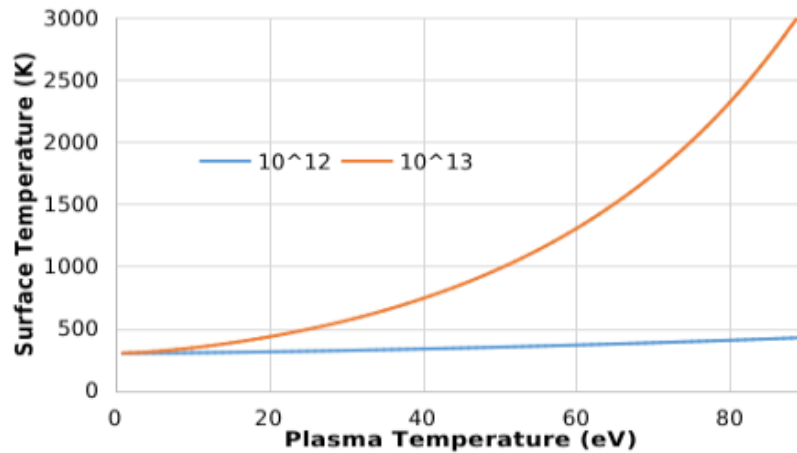


Fig 12. Variation of back scattering yield with temperature of H, D and T ion plasma

Fig. 13 shows the evaporation flux depending on the increase in ion energy. As can be seen from the figure, while the evaporation flux for all ions up to 430 eV is quite low, it is seen that after this energy the flux increases again after a significant peak. Evaporation flux is the number of atoms ejected from the target surface. In the study, it was planned to experimentally measure the ion density in the tube and the number of atoms detached from the target. For this, it is planned to use Langmuir probe. However, due to the increase in the exchange rate, the Langmuir probe was abandoned and it was decided to calculate it by simulation. As seen in the figure, while no atoms were removed from the surface until the threshold energy of 430 eV, atoms began to be snatched from the surface due to this threshold temperature. Especially after this energy value, the sudden rupture of more than 10^{14} atoms from the surface shows that a rapid erosion starts in the material after this energy.

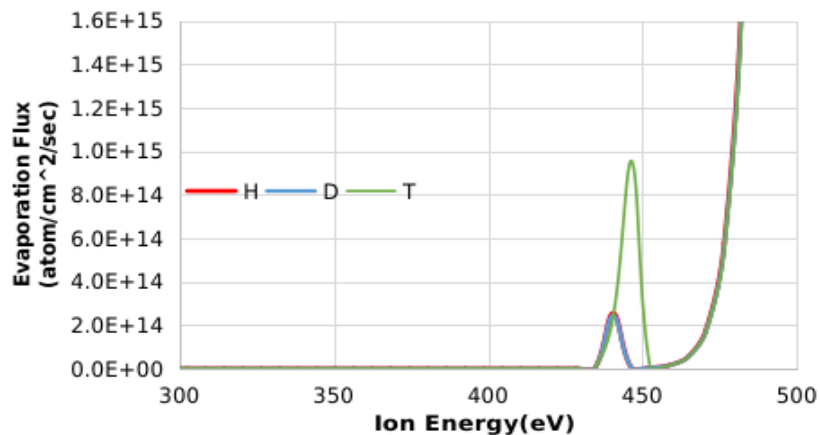


Fig 13. Variation of the evaporation flux in the target due to the change in ion energy

Calculations made within the scope of the study were performed on the Dell Power Edge R740 Rack Server. Chemical sputtering is observed in the materials which is known for the best graphite/diamond (C) atoms. Beside graphite/diamond (C) atoms are affected by the hot plasma H, He and D ions by physical sputtering, it is also known that graphite/diamond (C) atoms are also affected in chemical sputtering path too. In the next part of the theoretical studies, graphite/diamond (C) atoms are bombarded with H, He, D and T plasma ions. Plasma temperature, incoming angle, ion energy, backscattering graphics are calculated in Fig 6 to Fig 13. In study [24] diamond or graphite is mentioned with the highest melting point. However, it has the lowest atom number. That means barrier energy of graphite/diamond (C) material is very low to eject from its crystal structure. Especially H, D and T plasma ions can make chemical bounds with the ejected graphite/diamond (C) atom. In order to prevent this phenomena, graphite/diamond (C) materials are alloyed with other materials such as W to increase the resistance to the hot plasma interaction.

Conclusion

In the study, the interactions of H, D and He ions and Al, C, Be and W, which are used as plasma meeting materials in Tokamak reactors, were investigated using molecular dynamics and Monte Carlo simulation techniques. From the molecular dynamics simulation results, it was seen that the material with the lowest total sputtering yield was W. This result shows that the material with the highest radiation resistance that can be used in the reactor is Tungsten (W). Calculations of physical sputtering yield, chemical erosion yield, radiation-enhanced sublimation calculations were performed as a result of the interaction of H, D, T and He ions with graphite (C). The results showed that the physical sputtering yield and chemical erosion yield of He cores were the highest. It has also been observed that the surface temperature changes depending on the plasma density (ion number) and the number of atoms detached from the surface increases very rapidly after a threshold value of the plasma energy (approximately 450 eV). For instance, research in Joint European Torus (JET) experiment Be and W mix is used in the vacuum reactor wall. In that occasion researchers observe Be has good heat conductivity, strong gettering, high tolerance for plasma impurity and low nuclear activation. However, as the experiments progress erosion and tritium retention based on H is observed. Because of this plasma purity is also affected. In some of the experimental reactors Graphite is also used as first wall material. But Graphite adsorbs and traps too much H fuel from the plasma into its crystal structure. Generally, engineers use Tungsten material as a selection because it has the highest melting point and extremely resistant to heat because of melting point is high. Inner reactor wall of the tokamak is upgraded from graphite to beryllium. Graphite makes new molecular bounds with the H and test in JET reactor in 2011. Beryllium is excellent in thermal and mechanical properties for the fusion reactor. In ITER reactor it is considered to be Tungsten material on the wall material and Beryllium in the divertor regions of the Tokamak reactor walls. Aluminum is selected as a replacement against the Beryllium in the divertor regions of the Tokamak reactors. It is cheap and easy to supply to the reactor designers. However, its metal structure is affected by He highly in its crystal structures. All of the body of the crystal structure in the Al is transform into the cheese type of formation after the He interaction. Its melting point is also low when compared to all three materials Be, C and W. These observations are also made in the molecular dynamic models of the study. Tungsten showed low sputtering yield affection in the model, then Be and after Al and C showed the similar graphic values. When the calculation results are evaluated together, it has been concluded that Tungsten (W) is the most suitable material for facing with H, D and He ions in Tokamak reactors, but Tungsten (W) has high Tritium retention and it is appropriate for the components to face Tritium to be made of Aluminum (Al) or Graphite (C).

Acknowledgement

This work is supported by the Scientific and Technological Research Council of Turkey (TUBITAK) under grant number 118F052.

REFERENCES

- 1 Malo, M., Morono, A., Hodgson, E.R. Plasma Etching to Enhance the Surface Insulating Stability of Alumina for Fusion Applications. *Nuclear Materials and Energy*, 2016, Vol.9, pp. 247 – 250. doi: 10.1016/j.nme.2016.05.008
- 2 Bachmann, C., Aiello, G., Albanese, R., et al. Initial DEMO Tokamak Design Configuration Studies. *Fusion Engineering and Design*, 2015, Vol. 98-99, pp. 1423 – 1426. doi: 10.1016/j.fusengdes.2015.05.027
- 3 Brooks J.N., Hassanein A., Koniges A., et al. Scientific and Computational Challenges in Coupled Plasma Edge/Plasma-Material Interactions for Fusion Tokamaks. *Contrib. Plasma Phys.*, 2014, Vol.54, pp. 329 – 340. doi:10.1002/ctpp.201410014
- 4 Giroud C., Maddison G.P., Jachmich S., et al. Impact of Nitrogen Seeding on Confinement and Power Load Control of a High-Triangularity JET Elmy H-Mode Plasma with A Metal Wall. *Nuclear Fusion*, 2013, Vol.53(11), pp. 113025. doi: 10.1088/0029-5515/53/11/113025
- 5 International Atomic Energy Agency, (Anonymous). Lifetime Predictions for The First Wall and Blanket Structure of Fusion Reactors. *Proceedings of a Technical Committee Meeting. Karlsruhe*, 1985.
- 6 Ivanova-Stanik I., Zagórski R. Mitigation of the Divertor Heat Load in DEMO Reactor by Impurity Seeding. *Journal of Nuclear Materials*. 2013, Vol.463, pp. 596-600. DOI: 10.1016/j.jnucmat.2014.11.105
- 7 Kripner L. *Distribution of power fluxes to plasma-facing components of a Tokamak due to edge-localized modes*. Master Thesis, Faculty of Mathematics and Physics, Charles University, Prague, 2016
- 8 Eckstein W., Preuss R. New Fit Formulae for the Sputtering Yield", *Journal of Nuclear Materials*, 2003, 320, pp. 209 – 213.

- 9 Muyuan L., Jeong-Ha Y. Cracking Behavior of Tungsten Armor under ELM-Like Thermal Shockloads II: A Revised Prediction for Crack Appearance Map. *Nuclear Materials and Energy*, 2016, Vol.9, pp. 598-603. doi:10.1016/j.nme.2016.02.001
- 10 Nakano T., Asakura N., Kubo H. The JT-60 team. Contribution of Ne Ions to Radiation Enhancement in JT-60U Divertor Plasmas. *Journal of Nuclear Materials*, 2013, Vol.438, pp. S291-S296.
- 11 Nordlund K. Atomistic Simulations of Plasma-wall interactions in Fusion Reactors. *Physica Scripta*, 2006, Vol.124, pp. 53-57.
- 12 Pitts R.A., Carpentier S., Escourbiac F., et al. Physics Basis and Design of The ITER Plasma-Facing Components. *Journal of Nuclear Materials*, 2011, Vol.415, pp. S957-S964.
- 13 Pitts R.A., Carpentier S., Escourbiac F., et al. A full tungsten divertor for ITER: Physics issues and design status. *Journal of Nuclear Materials*, 2013, Vol.438, pp. S48-S56.
- 14 Philipps V. Tungsten as Material for Plasma-Facing Components in Fusion Devices. *Journal of Nuclear Materials*, 2011, Vol.415, pp. S2-S9.
- 15 Rapp J., Temmerman D.G., Van Rooij, et al. Plasma Facing Materials Research for Fusion Reactors at Fom Rijnhuizen. *Proceeding of the 15th Intern. Conf. on Plasma Physics and Applications. Romania Journal of Physics*, 2011, Vol.56, pp. 30 – 35.
- 16 Rasinski M., Kreter A., Torikai Y., Linsmeier Ch. The Microstructure of Tungsten Exposed to D Plasma with Different Impurities. *Nuclear Materials and Energy*, 2017, Vol.12, pp. 302-306.
- 17 Reiser J., Rieth M. Optimization and Limitations of Known DEMO Divertor Concepts. *Fusion Engineering and Design*, 2012, Vol.87, pp. 718 – 721.
- 18 Roth J., Tsitron E., Loarte Th., et al. Recent Analysis of Key Plasma Wall Interactions Issues for ITER”, *Journal of Nuclear Material*, 2009, 390-391, pp. 1 – 9.
- 19 Stork D., Agostini P., Boutard J.L., et al. Developing Structural, High-Heat Flux and Plasma Facing Materials for A Near-Term DEMO Fusion Power Plant: The EU Assessment. *Journal of Nuclear Materials*, 2014, Vol.455, pp. 277 – 291.
- 20 Stork D., et al. Assessment of the EU R&D programme on DEMO structural and high-heat flux materials, final report of the materials assessment group. *Technical Report. EFDA*, 2012, Vol.12, pp. 52.
- 21 You J.H., Visca E., Bachmann Ch., et al. European DEMO divertor target: Operational requirements and material-design interface. *Nuclear Materials and Energy*, 2016, Vol.9, pp. 171-176.
- 22 Guping D., Tingwen X., Yun L. *Proceeding of the 6th SPIE Intern. Symposium on Advanced Optical Manufacturing and Testing Technologies: Advanced Optical Manufacturing Technologies*, 2012, Vol. 841604
- 23 Voter A.F. *Introduction to Kinetic Monte Carlo Method. Theoretical Division*. Los Alamos National Laboratory, Los Alamos. 2007, pp. 1 – 2.
- 24 Motevalli N., Dashtban M., Maleki. Determination of optimum conditions in ITER tokamak by using zero-dimensional model. *Indian Journal of Physics*, 2020, Vol.94, pp. 1-7.

SUMMARIES	ТҮСІНІКТЕМЕЛЕР	АННОТАЦИИ
<p>Расулов З.Н., Усанов Д.Н., Войнаш С.А., Маликов В.Н., Карнаухов А.И., Ишков А.В., Фадеев Д.А. Молибден мен ниобий бөлшектерін жасау процесінде металдың бұзылуы Беттік-белсенді қасиеттеріне ие жабындылардың және аэротермоакустикалық өңдеудің Мо және Nb –дің қалыптаулық қабілетіне, кристалдық тордың механикалық қасиеттері мен микробұрмалануына әсері қарастырылған. Кристалдық тордың иілімділігін арттыру және микробұрмалануын азайту арқылы мұндай технологияларды пайдалану кезінде сорғышпен алынған бұйымдардың сапасын жақсарту анықталған. Құралдың беттік модификациясы деформацияланған Nb-нің 2 және 3 типті кернеулерін кеміту және оның қалыптылығын, сонымен бірге жартылай фабрикаттар мен дайын бұйымның сапасын жақсарту арқылы кристалды тордың микрооблыстарындағы бұрмалануды азайтады. Мо және Nb-дің төмен қалыптылығы иілімділік пен тұтқырлықты кемітетін тақташа және үшкір пішінді нәзік фазалардың болуымен байланысты. Nb үшін қосымша теріс фактор - 40-50 мкм-ге дейінгі дәндердің болуы болып табылады. Кілт сөздері: жабындылар, молибден, ниобий, микроқұрылым, аэротермоакустикалық өңдеу, деформациялылық.</p>	<p>Расулов З.Н., Усанов Д.Н., Войнаш С.А., Маликов В.Н., Карнаухов А.И., Ишков А.В., Фадеев Д.А. Разрушение металла в процессе изготовления деталей из молибдена и ниобия Рассмотрено влияние покрытий, обладающих поверхностно-активными свойствами и аэротермоакустической обработки на штампуемость Мо и Nb, механические свойства и микроискажения кристаллической решетки. Установлено улучшение качества изделий, получаемых вытяжкой при использовании этих технологий за счет повышения пластичности и уменьшения микроискажения кристаллической решетки. Модификация поверхности инструмента снижает искажение в микрообластях кристаллической решетки, уменьшая напряжения 2 и 3 рода деформированного Nb и улучшая его штампуемость и качество полуфабрикатов и готового изделия. Низкая штампуемость Мо и Nb связана с наличием хрупких фаз пластинчатой и острогранной формы, снижающих пластичность и вязкость. Для Nb дополнительным негативным фактором является наличие зерен размером до 40-50 мкм. Ключевые слова: покрытия, молибден, ниобий, микроструктура, аэротермоакустическая обработка, деформируемость.</p>	<p>Расулов З.Н., Усанов Д.Н., Войнаш С.А., Маликов В.Н., Карнаухов А.И., Ишков А.В., Фадеев Д.А. Разрушение металла в процессе изготовления деталей из молибдена и ниобия Рассмотрено влияние покрытий, обладающих поверхностно-активными свойствами и аэротермоакустической обработки на штампуемость Мо и Nb, механические свойства и микроискажения кристаллической решетки. Установлено улучшение качества изделий, получаемых вытяжкой при использовании этих технологий за счет повышения пластичности и уменьшения микроискажения кристаллической решетки. Модификация поверхности инструмента снижает искажение в микрообластях кристаллической решетки, уменьшая напряжения 2 и 3 рода деформированного Nb и улучшая его штампуемость и качество полуфабрикатов и готового изделия. Низкая штампуемость Мо и Nb связана с наличием хрупких фаз пластинчатой и острогранной формы, снижающих пластичность и вязкость. Для Nb дополнительным негативным фактором является наличие зерен размером до 40-50 мкм. Ключевые слова: покрытия, молибден, ниобий, микроструктура, аэротермоакустическая обработка, деформируемость.</p>
<p>Хайралиев С.И., Кайшубаева Н., Канаева С.Д., Bergander M. J., Джундибаев В.Е. Кедір-бұдыр беттердің статикалық үйкеліс коэффициенті. Қазіргі таңда машина жасау және кейбір басқа құрылымдар үшін құрғақ үйкеліс қондырғыларын жобалау процесі барған сайын қиынға түсуде, бұл конструкторларды мұндай жұмысқа көбірек күш салуға мәжбүр етеді. Орындалатын жұмыстардың айтарлықтай күрделенуі екі жанасатын беттердің кедір-бұдырлылықтың кездейсоқтық сипатымен байланысты және бұл жағдай конструкторларды бар мәселелерді шешудің жаңа жолдарын іздеуге мәжбүр етеді. Берілген жұмыста кедір-бұдырлылығы сфералық беттермен модельденетін екі кедір-бұдырлы бөлшектің жанасуының өзара әрекеттесуі қарастырылған. Ұсынылған үйкеліс жұбының моделі қарастырылатын беттер арасында әрекет ететін жанасатын кедір-бұдырлы беттердің өзара әрекеттесу күштерін бағалауға мүмкіндік береді. Бұл жұмыста қарастырылған денелердің кедір-бұдыр беттерімен салыстырмалы қозғалысын/сырғанауын бастауға қабілетті сыртқы күшпен әсер еткенде жанасатын денелердің өзара әрекеттесуі қарастырылғанын атап өткен жөн. Кілт сөздері: кедір-бұдыр бет; аналитикалық модельдеу; кедір-бұдыр беттердің статикалық өзараәрекеттесуі.</p>	<p>Хайралиев С.И., Кайшубаева Н., Канаева С.Д., Bergander M. J., Джундибаев В.Е. Коэффициент трения покоя шероховатых поверхностей. В настоящее время процесс проектирования узлов сухого трения машиностроения и некоторых других конструкций становится все более трудоемким, что вынуждает конструкторов прилагать все больше усилий в этой работе. Существенное усложнение выполняемых работ придает случайный характер шероховатости обеих контактирующих поверхностей и это обстоятельство заставляет конструкторов искать новые пути решения существующих проблем. В данной работе рассматривается контактное взаимодействие двух шероховатых деталей, шероховатость которых моделируется сферическими поверхностями. Предложенная модель пары трения позволяет оценить силы взаимодействия соприкасающихся шероховатых поверхностей, действующих между рассматриваемыми поверхностями. Следует подчеркнуть, что в данной работе рассматривается взаимодействие контактирующих тел с приложенной внешней силой, способной начать относительное движение/скольжение рассматриваемых тел с шероховатыми поверхностями. Ключевые слова: шероховатая поверхность; аналитическое моделирование; статическое взаимодействие шероховатых поверхностей.</p>	<p>Хайралиев С.И., Кайшубаева Н., Канаева С.Д., Bergander M. J., Джундибаев В.Е. Коэффициент трения покоя шероховатых поверхностей. В настоящее время процесс проектирования узлов сухого трения машиностроения и некоторых других конструкций становится все более трудоемким, что вынуждает конструкторов прилагать все больше усилий в этой работе. Существенное усложнение выполняемых работ придает случайный характер шероховатости обеих контактирующих поверхностей и это обстоятельство заставляет конструкторов искать новые пути решения существующих проблем. В данной работе рассматривается контактное взаимодействие двух шероховатых деталей, шероховатость которых моделируется сферическими поверхностями. Предложенная модель пары трения позволяет оценить силы взаимодействия соприкасающихся шероховатых поверхностей, действующих между рассматриваемыми поверхностями. Следует подчеркнуть, что в данной работе рассматривается взаимодействие контактирующих тел с приложенной внешней силой, способной начать относительное движение/скольжение рассматриваемых тел с шероховатыми поверхностями. Ключевые слова: шероховатая поверхность; аналитическое моделирование; статическое взаимодействие шероховатых поверхностей.</p>

Narjis Zamil Abdulzahra

Тотыққан кеуекті кремнийге жағылған лазерлік күйдірілген бор нанобөлшектерінің аса жоғары магниттік кедергісі.

Берілген зерттеуде лазерлік күйдірудің тотыққан кеуекті кремнийге (n-B/PSiO₂) жағылған нанобордың электрлік және магниттік қасиеттеріне әсері және оның спинтроникада қолдану әлеуеті зерттелген. Nd: YAG лазері n-B жұқа қабықшаларын әртүрлі энергиялар кезінде күйдіру үшін қолданылған. Лазер энергиясының артуы дәннің өлшемдерін ұлғайтып, оның құрылымын ретке келтіреді. Ол сондай-ақ дәндердің жаңа шекаралары мен екінші ретті фазалардың пайда болуына байланысты беттің кедір-бұдырлығын арттырды. Материалдың электрлік қасиеттеріне тікелей және кері токтың жоғарылауымен лазерлік күйдіру және күйдіру температурасының жоғарылауымен меншікті электр кедергісінің артуы әсер етті. Сонымен қатар зерттеу лазер температурасының жоғарылауымен материалдың магнит кедергісінің артуын көрсетті, бұл кремний диоксидінің жұқа қабаты арқылы туннельдік инъекциямен байланысты және магнит өрісіндегі күйдірілмеген n-B/PSiO₂ салыстырғанда 7 есе жоғары болуы мүмкін. Зерттеуде материалдар дәнінің өлшемі мен құрылымын олардың физикалық және электрлік қасиеттері үшін бақылаудың маңыздылығы көрсетілген. Одан басқа, n-B/PSiO₂ –нің электронды қасиеттері мен магнит өрісіндегі заряд тасымалдаушылардың тәртібі туралы түсінік берілген.

Кілт сөздері: аса жоғары магниттік кедергі, лазерлік күйдіру, нанобор, тотыққан кеуекті кремний, электрлік қасиеттер, магниттік қасиеттер, спинтроника қосымшалары.

Narjis Zamil Abdulzahra

Сверхвысокое магнито-сопротивление лазерно-отоженного наночастиц бора, нанесенного на окисленный пористый кремний.

В этом исследовании изучается влияние лазерного отжига на электрические и магнитные свойства нанобора, нанесенного на окисленный пористый кремний (n-B/PSiO₂), и его потенциал для применения в спинтронике. Лазер Nd: YAG использовался при различных энергиях для отжига тонких пленок n-B. Увеличение энергии лазера увеличило размер зерна и сделало его структуру более упорядоченной. Это также увеличило шероховатость поверхности из-за образования новых границ зерен и вторичных фаз. На электрические свойства материала также повлиял лазерный отжиг с увеличением прямого и обратного тока и увеличением удельного электрического сопротивления при повышении температуры отжига. Исследование также показало, что магнитосопротивление материала увеличивается с увеличением температуры лазера, что связано с туннельной инъекцией через тонкий слой диоксида кремния, и может быть до 7 раз выше, чем у неотожженного n-B/PSiO₂ в магнитном поле. В исследовании подчеркивается важность контроля размера и структуры зерна материалов для их физических и электрических свойств. Кроме того, он дает представление об электронных свойствах n-B/PSiO₂ и поведении носителей заряда в магнитном поле.

Ключевые слова: сверт высокое магнито-сопротивление, лазерный отжиг, нанобор, окисленный пористый кремний, электрические свойства, магнитные свойства, приложения спинтронике.

Алқадери Л.А., Юрченко А.В., Мохаммед Ж.А.-К., Нешина Е.Г.

Кептіру жүйесінің өнімділігін арттыруға арналған температура мен ылғалдылықты бақылау және мониторингінің автоматтандырылған жүйесі

Температура мен салыстырмалы ылғалдылық азық түлік тағамдарының сапасын сақтау және жақсарту үшін кептіру процестеріндегі бақылаудың негізгі параметрлері болып табылады. Бұл мақсатқа жету үшін әртүрлі климаттық аймақтардың қоршаған орта талаптарына және кептірілген өнімнің түріне сәйкес жылу мен кептіру ағындарын қамтамасыз ететін автоматты басқару жүйесі әзірленіп құрастырылды. Датчиктермен бірге басқару жүйесі кептіру камерасының температурасы мен ылғалдылығын берілген параметрлер бойынша онлайн режимінде реттеуге мүмкіндік береді. Сәулелену тым аз немесе жоқ болғанда немесе кептірудің жоғары жылдамдығы қажет болған жағдайда, резервтік электр жылытқышына қосымша ретінде электр қозғалтқышы бар желдеткіштің көмегімен қыздырылған ауа ағыны жасалуы мүмкін. Желдеткіш кептіру камерасының қажетті температурасына байланысты энергия тиімділігін арттыру үшін ендік-импульстік модуляциялау технологиясымен жылдамдығын автоматты түрде өзгертеді. Arduino Uno тақтасындағы басқару жүйесі күн кептіргішіне салынған, содан кейін сынақтар өткізіледі. Сынақ нәтижелері дисплейде көрсетіледі. Басқару жүйесі қоршаған ортаның температурасын 40-тан 60 °C-қа дейін және салыстырмалы ылғалдылықты 10-нан 20% - ға дейін ұстап тұруға бейімделген. Кептіру ортасын басқарудағы тиімділігін көрсететін эксперименттік дәлелдерге сәйкес, жүйе әртүрлі климаттық аймақтар мен кептіру өнімдері үшін икемді шешім болып табылады. Бұл жүйе энергияны үнемдей алады, себебі ол азық-түлік тағамдарының айналасындағы температура 60 °C-тан төмен болған кезде ғана жұмыс істейді.

Кілт сөздері: күн кептіргіші; температура мен ылғалдылықты бақылау; Arduino UNO; электр желдеткіші; резервтік жылытқыш; бақылау жүйесі, баспа тақталары.

Алкахдери Л.А., Юрченко А.В., Мохаммед Ж.А.-К., Нешина Е.Г.

Автоматизированная система контроля и мониторинга температуры и влажности для повышения производительности системы сушки

Температура и относительная влажность являются ключевыми параметрами контроля в процессах сушки для сохранения и улучшения качества пищевых продуктов. Для достижения этой цели была разработана и построена автоматическая система управления, обеспечивающая потоки тепла и сушки в соответствии с требованиями окружающей среды различных климатических зон и видом высушиваемого продукта. Система управления в сочетании с датчиками позволяет в режиме онлайн регулировать температуру и влажность сушильной камеры по заданным параметрам. Когда излучение слишком мало или отсутствует, или когда требуется высокая скорость сушки, поток нагретого воздуха может создаваться с использованием вентилятора с электродвигателем в дополнение к резервному электрическому нагревателю. Вентилятор автоматически изменяет свою скорость с помощью технологии широтно-импульсной модуляции для повышения энергоэффективности в зависимости от требуемой температуры сушильной камеры. В солнечную сушилку встраивается система управления на плате Arduino Uno, после чего проводятся испытания. Результаты теста отображаются на дисплее. Система управления была настроена на поддержание температуры окружающей среды в пределах от 40 до 60 °С и относительной влажности в пределах от 10 до 20 %. Система является гибким решением для различных климатических зон и сушильных продуктов, согласно экспериментальным данным, демонстрирующим ее эффективность в управлении средой сушки. Наконец, эта система может экономить энергию, потому что она работает только тогда, когда температура вокруг пищи ниже 60 °С.

Ключевые слова: Солнечная сушилка; контроль температуры и влажности; Arduino UNO; электрический вентилятор; резервный нагреватель; система наблюдения, печатные платы

Клименко В.Н., Супрун Т.Т.

Украинада енгізу үшін синтетикалық жаңартылатын метан өндіру технологияларын талдау

Синтетикалық жаңартылатын метанды алу үшін метанаңия технологиялары қарастырылған. Каталитикалық және биологиялық метанаңия әдістерін қолдану мүмкіндіктері талданды. Метанаңия технологияларын енгізу жаңартылатын энергия көздерін тиімді пайдалана отырып жүзеге асырылады. Әр түрлі елдерде синтетикалық жаңартылатын метан өндіруге арналған Power to Gas концепциясы қарастырылған. Ағымдағы жобаларда алынған метанаңия процестерін зерттеудің кейбір нәтижелері ұсынылған. Синтетикалық жаңартылатын метанды өндіру үшін метанаңия технологияларын енгізудің әлемдік тәжірибесі Украина үшін үлгі бола алады.

Кілт сөздері: синтетикалық жаңартылатын метан, метанаңия процестері, Power to Gas концепциясы, жаңартылатын энергия көздері.

Клименко В.Н., Супрун Т.Т.

Анализ технологий производства синтетического возобновляемого метана для внедрения в Украине

Рассмотрены технологии метанаңии для получения синтетического возобновляемого метана. Проанализированы возможности применения методов каталитической и биологической метанаңии. Внедрение технологий метанаңии осуществляется с эффективным использованием возобновляемых источников энергии. Рассмотрена концепция Power to Gas для производства синтетического возобновляемого метана в разных странах. Представлены некоторые результаты исследований процессов метанаңии, полученные в текущих проектах. Мировой опыт внедрения технологий метанаңии для производства синтетического возобновляемого метана может быть примером для Украины.

Ключевые слова: синтетический возобновляемый метан, процессы метанаңии, концепция Power to Gas, возобновляемые источники энергии.

Усенков Р. А., Коханова С. Я., Трушин М. В.

Оқшауланған тұтынушылардың инженерлік жүйелерінің жұмыс істеуі үшін баламалы энергия көздерін пайдалану

Жеке тұрғын үйдің жұмыс істеуі үшін қажет болатын көптеген инженерлік жүйелердің жұмысы баламалы энергияның нақты көздеріне тәуелді, оларды пайдалану дәстүрлі қазба энергия ресурстарын тұтынуын айтарлықтай төмендетуі мүмкін. Баламалы энергия көздерін пайдаланатын инженерлік жүйелерге арналған ғылыми жұмыстарға шолу жасалды. Оқшауланған тұтынушыларға берілетін жылу және электр энергиясын алу үшін энергиялық қондырғының бірнеше сұлбалары құрастырылды. Жұмыс істеу үшін күннің сәулеленуін қолданатын стационарлық техникалық күн жүйесін жобалау кезінде энергиялық қондырғының орналасуы, ғимараттың төбесіндегі күн қабылдағышының көлбеу бұрышы және оның көкжиекке оңтайлы көлбеу бұрышының мәндері анықталды. Су ағынының қысымын пайдаланатын электр энергиясын өндіретін шағын портативті су электр станциясының сұлбасы құрастырып әзірленді. Жылытылатын ортаны жылыту үшін жануарлар қорасынан шығарылатын ауаның жылуын пайдаланатын термотоңазытқыш қондырғысы әзірленді.

Кілт сөздері: баламалы энергия көздері, гидроэнергетика, жылу, термосалқындатқыш қондырғы, температура, жылытылатын орта.

Усенков Р.А., Коханова С.Я., Трушин М.В.

Использование альтернативных источников энергии для функционирования инженерных систем обособленных потребителей

Работа многих инженерных систем, необходимых для функционирования отдельно стоящего жилого здания, зависит от конкретных источников альтернативной энергии, использование которых может значительно снизить потребление традиционных ископаемых энергоресурсов. Дан обзор научных работ, посвященных эксплуатации инженерных систем с использованием альтернативных источников энергии. Было разработано несколько схем энергетического оборудования для получения тепловой и электрической энергии, подаваемой изолированным потребителям. При проектировании стационарной технической солнечной системы, использующей для работы солнечное излучение, были определены места расположения всего энергетического оборудования, угол наклона солнечного приемника на крыше здания и значения его оптимального угла наклона к горизонту. Была разработана схема небольшой переносной гидроэлектростанции, которая вырабатывает электрическую энергию, используя давление, создаваемое потоком воды. Разработана тепловая холодильная установка, которая использует тепло воздуха, удаляемого из стойла для животных, для нагрева нагреваемой среды.

Ключевые слова: альтернативные источники энергии, гидроэнергетика, тепло, термохолодильная установка, температура, нагреваемая среда

Jaddoa Ameer A., Mahdi Mahmoud M., Hamad Karema A.

Иракта гибриді күн коллекторлар сұлбасының тиімділігін бағалау

Берілген зерттеуде Ирактағы қоршаған ортаның сипаттамаларын электрлік, жылу және эксергетикалық тиімділік тұрғысынан бағалау ұсынылған. Зерттеу 2022 жылдың мамырында Багдадтың бір аймағында жүргізілген. Маңызды сәт - жылу тасымалдағыштың массалық тұтынуы есебінен жүретін фотоэлектрлік қондырғылардан жылуды бұру процесі болып табылады. Эксперименттік зерттеулер оқшауланған жағдайларда фотогальваникалық элементтің бетінен жылу энергиясын жұтылуы кезінде және су салқындатқыш қондырғыны қолдану арқылы жүргізілген. Нәтижелер 0,2 кг/с массалық тұтыну кезінде жүйенің максималды орташа жалпы тиімділігі 22% деңгейінде тіркелгенін көрсетті. Нәтижесінде, бүкіл жүйенің тиімділігін арттыру және өтелу мерзімін қысқарту үшін тиімді күн фотоэлектрлік жылу жүйелерін жасауға болады.

Кілт сөздері: күн энергиясы, энергия және эксергия, гибриді күн фотоэлектрлік коллекторы.

Jaddoa Ameer A., Mahdi Mahmoud M., Hamad Karema A.

Оценка эффективности схемы гибридных солнечных коллекторов в условиях ирака

В этом исследовании представлена оценка характеристик окружающей среды в Ираке с точки зрения электрической, тепловой и эксергетической эффективности. Исследование проводится в мае 2022 года в столичном районе Багдада. Существенным моментом является процесс отвода тепла от фотоэлектрических установок, который происходит за счет массового расхода теплоносителя. Экспериментальные исследования проводились при поглощении тепловой энергии с поверхности фотогальванического элемента в изолированных условиях и с использованием водоохлаждаемой установки. Результаты показали, что при массовом расходе 0,2 кг/с максимальная средняя общая эффективность системы была зафиксирована на уровне 22%. В результате рекомендуется, чтобы для сокращения периода окупаемости и для повышения эффективности всей системы можно было разработать эффективные солнечные фотоэлектрические тепловые системы.

Ключевые слова: солнечная энергия, энергия и эксергия, гибридный солнечный фотоэлектрический коллектор.

Тлеубергенова А.Ж., Дюсембаева А.Н., Танашиева Н.К., Миньков Л.Л., Мұхамедрахим А.Р.

Құрамалы қалақшалы жел энергетикалық қондырғысының аэродинамикалық тарту күшін зерттеу

Берілген мақалада желдің ауыспалы жылдамдығы жағдайында жұмыс істейтін көлденең айналу осі бар жел энергетикалық қондырғысы қарастырылған. Осы мақсатта айналмалы құрамалы қалақшалары бар жел энергетикалық қондырғысының макеті жасалды. Эксперименттер барысында цилиндрге қатысты қозғалмайтын қалақшаның орналасу бұрышы 0°-тан 60°-қа дейін, 15° қадаммен өзгерді. Ауа ағынының жылдамдығы 3-тен 12 м/с-қа дейін өзгерді. Ауа ағынының жылдамдығынан жел энергетикалық қондырғының айналу жиілігін өзгерту бойынша эксперимент нәтижелеріне талдау жүргізілді. Қозғалмайтын қалақшаның орны өзгерген кезде (0°, 15°, 30°, 45°, 60°) тарту күшінің мәні ауа ағынына қатысты тікелей пропорционалды түрде өзгереді. Ауа ағынының жылдамдығының жоғарылауымен жел доңғалағының айналу жиілігі сызықты түрде өседі. Қозғалмайтын қалақша 60° бұрышта орналасқан кезде, ауа ағынының максималды жылдамдығы 12 м/с болғанда, тарту күшінің мәні 2,06Н жеткені анықталды. Цилиндр мен қозғалмайтын қалақша сияқты құрамалы екі көтеру күшін біріктіріп қолдану арқылы тарту күшінің артуы байқалады. Алынған нәтижелер құрамалы қалақшалы жел энергетикалық қондырғысының тәжірибелік үлгілерін жасау кезінде пайдалы болып табылады.

Кілт сөздері: жел энергетикалық қондырғы, ағын жылдамдығы, құрамалы қалақша, Т-1-М аэродинамикалық құбыр, тарту күші, айналу жиілігі.

Тлеубергенова А.Ж., Дюсембаева А.Н., Танашева Н.К., Миньков Л.Л., Мұхамедрахим А.Р.

Исследование аэродинамической силы тяги ветроэнергетической установки с комбинированными лопастями

В данной статье рассмотрена ветроэнергетическая установка с горизонтальной осью вращения, работающая в условиях переменных скоростей ветра. Для данной цели был изготовлен макет ветроэнергетической установки с вращающимися комбинированными лопастями. В ходе выполнения экспериментов угол расположения неподвижной лопасти относительно цилиндра изменялся от 0° до 60° , с шагом 15° . Скорость воздушного потока варьировался, от 3 до 12 м/с. Проведен анализ результатов эксперимента по изменению частоты вращения от скорости воздушного потока ветроэнергетической установки. При изменении положения неподвижной лопасти (0° , 15° , 30° , 45° , 60°) значение силы тяги меняется относительно воздушного потока прямо пропорционально. С ростом скорости воздушного потока, частота вращения ветроколеса растет линейно. Установлено, что при расположении неподвижной лопасти под углом 60 градусов, при максимальной скорости воздушного потока 12 м/с значения силы тяги достигла 2,06 Н. За счет комбинированного использования двух подъемных сил, таких как цилиндра и неподвижной лопасти, наблюдаются повышенные значения силы тяги. Полученные результаты являются полезными при создании опытных образцов ветроэнергетической установки с комбинированными лопастями.

Ключевые слова: ветроэнергетическая установка, скорость потока, комбинированная лопасть, аэродинамическая труба Т-1-М, сила тяги, частота вращения.

Ермаханова А.М., Кенжегулов А.К., Мейірбеков М.Н., Самсоненко А. И, Байсериков Б.

Шыны- және арамидті эпоксидті композиттердің радиомөддірлігі мен диэлектрлік өткізгіштігін зерттеу

Арамид-эпоксидті композиттер аэроғарыштық заманауи аппараттардың конструкцияларында кеңінен қолданылады. Олар керемет механикалық қасиеттерге ие ғана емес, сонымен қатар толқындарды тасымалдауға арналған радиомөддір материалдар болып табылады. Бұл жұмыста вакуумдық инфузия әдісімен арамидті-эпоксидті композит және шыныталшық радиомөддірлік пен диэлектрлік өткізгіштікті салыстырмалы зерттеу жүргізу үшін жасалды. Зерттелген материалдардың радиомөддірлігі 1-6 ГГц жиілік диапазонында бос кеңістікте өлшеу әдісімен бағаланды. Радиомөддірлік нәтижелері бойынша арамид-эпоксидті композит шыныталшыққа қарағанда электрмагниттік толқынның жоғалуына аз ұшырайды. Диэлектрлік өткізгіштігін өлшеу кезінде арамид-эпоксидті композит төмен орташа мән 2,874, ал шыны талшықта 4-ке тең екендігі анықталды.

Кілт сөздері: арамид-эпоксидті композиттер, шыныталшық, эпоксидті шайыр, радиомөддірлік, жиілік, диэлектрлік өткізгіштік.

Ермаханова А.М., Кенжегулов А.К., Мейірбеков М.Н., Самсоненко А. И, Байсериков Б.

Исследование радиопрозрачности и диэлектрической проницаемости стекло- и арамидных эпоксидных композитов

Арамидно-эпоксидные композиты широко используются для изготовления в конструкциях аэрокосмических современных аппаратов. Они обладают не только превосходными механическими свойствами, но и являются радиопрозрачными материалами для передачи волн. В данной работе были изготовлены арамидно-эпоксидный композит и стеклопластик методом вакуумной инфузии для проведения сравнительного исследования по радиопрозрачности и диэлектрической проницаемости. Радиопрозрачность исследованных материалов оценивалась методом измерения в свободном пространстве в частотных диапазонах 1-6 ГГц. По результатам радиопрозрачности арамидно-эпоксидный композит претерпевает меньше потерь электромагнитной волны, чем в стеклопластике. При измерении диэлектрической проницаемости арамидно-эпоксидный композит установлено низкое среднее значение 2,874, тогда как у стеклопластика определено равное 4.

Ключевые слова: арамидно-эпоксидный композит, стеклопластик, эпоксидная смола, радиопрозрачность, частота, диэлектрическая проницаемость.

Жанабаев З.Ж., Усипов Н.М.

Гравитациялық толқын сигналдарын информациялық-энтропиялық анықтау

GW гравитациялық толқындарының жұптасқан кара құрдымдардан табылуы GW астрономия дәуірінің басталуының белгісі болды. Дәстүрлі түрде, эксперименттік деректерден GW сигналдарын алу үшін ғылыми топтар келісілген фильтрацияның стандартты әдісін қолданады. Теориялық кутулерден тыс GW сигналдарын табуы қиындатытын белгілі сигнал үлгілері қолданылады. Сонымен қатар, қолданатын белгілі сигнал үлгілерінің санына байланысты келісілген фильтрдің есептеу құны өте жоғары болып келеді. Бұл мақалада біз теориялық сигнал шаблондарын қажет етпейтін GW сигналдарын анықтаудың жаңа информациялық-энтропиялық әдісін ұсынамыз. Біздің әдісіміздің сенімділігін көрсету үшін біз модельденген және нақты деректерді қолдана отырып талдау жасадық. Осы зерттеу барысында біз шартты информация өлшемі GW сигналдарын анықтайтынын және оны келісілген фильтрация әдісімен бірге қолдануға болатынын анықтадық.

Кілт сөздері: гравитациялық толқындар, информация-энтропия, сигналдарды анықтау, бейсызық процесс.

Жанабаев З.Ж., Усинов Н.М.

Информационно-энтропийное обнаружение сигналов гравитационных волн

Обнаружение гравитационных волн GW от пары сливающихся черных дыр ознаменовало начало эры GW-астрономии. Традиционно для извлечения сигналов GW из экспериментальных данных научные коллективы используют стандартный метод согласованной фильтрации. Используются существующие шаблоны сигналов, что затрудняет поиск сигналов GW, выходящих за рамки теоретических ожиданий. Более того, вычислительная стоимость согласованного фильтра очень высока, так как зависит от количества используемых шаблонов. В данной статье мы предлагаем новый информационно-энтропийный метод обнаружения GW, не требующий теоретического банка шаблонов сигналов. Чтобы продемонстрировать надежность нашего метода, мы провели анализ с использованием смоделированных и реальных данных. В ходе этого исследования мы установили, что наша мера условной информации обнаруживает сигналы GW и может использоваться вместе с методом согласованной фильтрации.

Ключевые слова: гравитационные волны, информация-энтропия, обнаружение сигналов, нелинейный процесс.

Iwuji P.C., Okoro R.C., Idajor J.A., Amajama J., Ibrahim A.T., Echem Ch.O.

Нигерияның IMO штатында теледидар сигналдарын тарату жолында өнімділікті талдау және шығындар моделін зерттеу.

Сымсыз желіні жоспарлауда, жиіліктерді тағайындауда және теледидар параметрлерін бағалауда тарату модельдерінің маңыздылығын асыра бағалау мүмкін емес. Климаттық жағдайлар, ғимарат құрылымы, жер бедері және т.б. тұрғысынан екі орынның бірдей болмауы кез-келген аймақ үшін жолдағы шығындарды болжау модельдерін қолдану қиындыққа соғады. Сондықтан қоршаған ортаның барлық параметрлері үшін қолданылатын таралу жолындағы шығындардың бірыңғай моделін жасау мүмкін емес. Бұл зерттеудің негізгі мақсаты - NTA 12 Owerri арнасы үшін жолдағы шығын үлгісін зерттеу және Нигерияның Имо штатындағы таңдалған бес бағыттағы қабылданған сигнал қуатының мәндері негізінде оның өнімділігін бағалау болып табылады. Жолдағы шығындардың қолайлы моделі сигнал деңгейі туралы алынған мәліметтерден алынған әрбір базалық станция үшін өлшенген жол шығындарының мәндерін сыни талдау арқылы жасалды. Жолдағы шығындардың ұсынылған моделінің мәндері басқа зерттеушілер зерттеген жолдағы шығындардың басқа эмпирикалық модельдерінің мәндерімен, сондай-ақ жолдағы шығындардың өлшенген мәндерімен салыстырылды. Нәтижелер жолдағы шығындардың ұсынылған моделі зерттелетін ортадағы 12 NTA арнасының Оверри сигнал жолындағы шығынды болжау үшін жақсы жұмыс істейтінін көрсетті, ал осы зерттеуде ескерілген басқа дәстүрлі эмпирикалық модельдер NTA 12 арнасының Оверри сигнал жолындағы шығынды орташа квадраттық 63,65 және одан жоғары шамадан қателікпен арттырды. Сонымен қатар, нәтижелер NTA Owerri базалық тарату станциясынан 18 шақырым ара-қашықтықта нашар жұмыс істемейтінін көрсетеді. Жалпы тұжырымдар зерттеу орнында және басқа ұқсас орталарда телевизиялық желінің перспективті арналарын жобалау үшін пайдалы.

Кілт сөздері: жол шығындары; теледидар; жолдағы шығын моделі; қабылданатын сигнал деңгейі, сымсыз желі

Iwuji P.C., Okoro R.C., Idajor J.A., Amajama J., Ibrahim A.T., Echem Ch.O.

Анализ производительности и разработка модели потерь на пути распространения телевизионных сигналов в штате IMO, Нигерия.

Невозможно переоценить важность моделей распространения в планировании беспроводной сети, назначении частот и оценке телевизионных параметров. Тот факт, что нет двух одинаковых мест с точки зрения климатических условий, структуры зданий, рельефа местности и т. д., делает использование моделей прогнозирования потерь на трассе для любой области чрезвычайно сложным. Поэтому невозможно разработать единую модель потерь на пути распространения, применимую ко всем параметрам окружающей среды. Основная цель этого исследования — разработать модель потерь на пути для канала NTA 12 Owerri и оценить ее производительность на основе значений мощности принятого сигнала на пяти выбранных маршрутах в штате Имо, Нигерия. Подходящая модель потерь на трассе была разработана путем критического анализа измеренных значений потерь на трассе для каждой базовой станции, которые были извлечены из полученных данных об уровне сигнала. Значения разработанной модели потерь на пути сравнивались со значениями других эмпирических моделей потерь на пути, разработанными другими исследователями, а также с измеренными значениями потерь на пути. Результаты показывают, что предложенная модель потерь на трассе хорошо подходит для прогнозирования потерь на трассе сигналов Оверри канала 12 NTA в исследуемой среде, в то время как другие традиционные эмпирические модели, принятые во внимание в этом исследовании, превышали потери на трассе сигналов Оверри канала 12 NTA со среднеквадратичной ошибкой 63,65 и выше. Кроме того, результаты показывают, что NTA Owerri плохо работает на расстоянии 18 километров от базовой передающей станции. Общие выводы полезны для проектирования перспективных каналов телевизионной сети в месте проведения исследования и в других подобных средах.

Ключевые слова: потеря пути, телевидение, модель потерь на пути; уровень принимаемого сигнала; Беспроводная сеть

Цыганов В.В.

Күрделі динамикалық жүктеме кезіндегі триботораптардың бұзылу механикасының ерекшеліктері

Күрделі динамикалық жүктеме жағдайында үйкеліс кезіндегі триботораптардың байланысының бұзылуының механикасы қарастырылған. Байланыс кезінде беттік қабаттың қалыптасу ерекшеліктерін ескере отырып, үйкелістің күрделі тораптарын, тозу қарқындылығын математикалық сипаттау мүмкіндігі көрсетілген. Триботораптардың беттік беріктігі мен төзімділігін есептеу әдісі ұсынылған және осы өзара тәуелділікті практикалық бағалау мысалдары көрсетілген. Әр түрлі динамикалық жүктемелермен үйкеліс кезінде бұзылудың беттік моделі, трибоспектрлік әдіспен және электрон шығу жұмысымен беттік қабаттың құрылымдық күйінің өзгеруі бойынша тозуға төзімділікті бағалау әдістері ұсынылған.

Кілт сөздері: тозуға төзімділік, триботораптар, беттік қабат, құрылымдық күй, жүктеме.

Цыганов В.В.

Особенности механики разрушения трибоузлов при сложном динамическом нагружении

Рассмотрена механика контактного разрушения трибоузлов при трении в условиях сложного динамического нагружения. Показана возможность математического описания сложных узлов трения, интенсивностей изнашивания с учетом особенностей формирования поверхностного слоя при контакте. Представлена методика расчета поверхностной прочности и долговечности трибоузлов и показаны примеры практической оценки этой взаимозависимости. Предложена модель поверхности разрушения при трении с различной динамической нагрузкой, методы оценки износостойкости по изменению структурного состояния поверхностного слоя трибоспектральным методом и работой выхода электрона.

Ключевые слова: износостойкость, трибоузлы, поверхностный слой, структурное состояние, нагружение.

Канапина А.Е., Селиверстова Е.В., Ибраев Н.Х., Дервянко Н.А., Ищенко А.А.

Металл нанобөлшектерінің жақын өрістегі иондық бояғыштардың қозған күйлерінің ыдырау ерекшеліктері

Күміс нанобөлшектерінің әртүрлі иондылықтағы полиметин бояғыштарының молекулаларындағы электронды қозған күйді дезактивациялаудың молекулаларлық процестеріне әсері зерттелді. Ag нанобөлшектерінің қатысуымен катионды 1 және анионды 2 бояғыштардың оптикалық тығыздығы өзгермейтіні көрсетілген. Ал бейтарап 3 бояғышының жұтылу қабілетінің шамамен 18% өсуі байқалады. Ag нанобөлшектерінің қатысуымен флуоресценция қарқындылығы анионды-катионды-бейтарап бояғыштар үшін төмендейді. Флуоресценцияның өмір сүру уақыты барлық зерттелетін полиметин бояғыштары үшін мүлдем өзгермейді. Флуоресценция қарқындылығының ең үлкен өсуі анионды бояу үшін тіркелді. Плазмондық нанобөлшек пен бояғыш молекуласының электрдипольдік өзара әрекеттесу моделі арқылы нәтижелерді талдау флуоресценция жылдамдығының плазмондық жоғарылау коэффициенттерінің бейтарап-катионды-анионды бояғыштар жағдайында төмендейтінін көрсетті. Полиметин бояғыштардан плазмондық нанобөлшектерге энергия беру жылдамдығы бояғыштардың кері тізбегінде кемиді, яғни анионды-катионды-бейтарап полиметин бояғышы. Бұл флуоресценция арқылы ыдырайтын бейтарап бояғыш молекулалар санының азаюына әкеледі.

Кілт сөздері: полиметин бояғышы, иондылық, локализацияланған плазмон резонансы, күміс нанобөлшектері, плазмон күшейтілген флуоресценция.

Канапина А.Е., Ибраев Н.Х., Селиверстова Е.В., Дервянко Н.А., Ищенко А.А.

Особенности распада возбужденных состояний ионных красителей в ближнем поле металлических наночастиц

Изучено влияние наночастиц серебра на внутримолекулярные процессы дезактивации электронно-возбужденного состояния в молекулах полиметиновых красителей (ПК) различной ионности. Продемонстрировано, что оптическая плотность для катионного 1 и анионного 2 красителей не изменяется в присутствии наночастиц Ag. Тогда как для нейтрального красителя 3 наблюдается прирост поглощательной способности почти на 18%. Интенсивность флуоресценции в присутствии наночастиц Ag уменьшается в ряду анионный-катионный-нейтральный краситель. Время жизни флуоресценции практически не изменяется для всех исследуемых ПК. Наибольший прирост интенсивности флуоресценции был зарегистрирован для анионного красителя. Анализ данных с помощью модели электродипольного взаимодействия плазмонной наночастицы и молекулы красителя показал, что коэффициенты плазмонного увеличения скорости флуоресценции убывают в последовательности нейтральный-катионный-анионный красители. Скорости передачи энергии от ПК к плазмонным НЧ уменьшаются в обратной последовательности красителей, т.е. анионный-катионный-нейтральный ПК. Это приводит к уменьшению числа молекул нейтрального красителя, распадающихся путем флуоресценции.

Ключевые слова: полиметиновый краситель, ионность, локализованный плазмонный резонанс, наночастицы серебра, усиленная плазмонной флуоресценция.

Саулебеков А.О., Қамбарова Ж.Т., Омарова Г.С.

Корпускулалық ағындардың құрамын талдауға арналған шағын жоғары сезгіш электронды спектрометр

Жұмыс бөлшектердің өлшенетін энергияларының кең ауқымында корпускулалық ағындардың құрамын талдау үшін шағын өлшемді жоғары сезгіш электронды спектрометрдің теориялық құрастыруға арналған. Спектрометрдегі айналы энергия талдағышы электрстатикалық октупольді-цилиндрлік өріске негізделген және үлкен тоғыс ара-қашықтығына ие. Сұлбаның тоғыстық қасиеттері есептелген, аспаптың жарық күші мен ажырату қабілеттілігі бағаланды. Ұсынылған аспап ғарыш аппараттарына арналған қондырғылар кешенінің құрамында планетааралық кеңістіктегі стационарлық емес ағындардағы зарядталған бөлшектердің құрамын анықтауға мүмкіндік береді. Сондай-ақ, аспапты жобалау кезінде бір-бірін сәтті толықтыратын бірнеше талдау әдістерін (мысалы, масс-спектрометриялық әдістермен) үйлестіру мүмкіндігі бар, бұл үйлесімді талдаудың жоғары ақпараттылығын қамтамасыз етеді. Бұл үрдіс, әдетте, бірнеше тәуелсіз талдау әдістерін қамтитын ғарыштық зерттеу кешендерін құру кезінде байқалады.

Кілт сөздері: электронды спектрометр, энергия талдау, энергия талдағыш, электрстатикалық айна, корпускулалы-оптикалық жүйе.

Саулебеков А.О., Камбарова Ж.Т., Омарова Г.С.

Малогабаритный высокочувствительный электронный спектрометр для анализа состава корпускулярных потоков

Работа посвящена теоретической разработке малогабаритного высокочувствительного электронного спектрометра для анализа состава корпускулярных потоков в широком диапазоне измеряемых энергий частиц. Зеркальный энергоанализатор частиц в спектрометре построен на основе электростатического октупольно-цилиндрического поля и обладает большим фокусным расстоянием. Рассчитаны фокусирующие свойства схемы, оценены светосила и разрешающая способность прибора. В составе комплекса оборудования для космических аппаратов предложенный прибор позволит определять состав заряженных частиц в нестационарных потоках в межпланетном пространстве. Также при конструировании прибора есть возможность комбинирования нескольких методов анализа (например, с масс-спектрометрическими методами), которые будут успешно дополнять друг друга, что будет обеспечивать высокую информативность совместного анализа. Данная тенденция наблюдается при создании космических исследовательских комплексов, в составе которых, как правило, входят несколько независимых методов анализа.

Ключевые слова: электронный спектрометр, энергоанализ, энергоанализатор, электростатическое зеркало, корпускулярно-оптическая система.

Жилгельдинов Ж.С., Лисицын В.М., Карипбаев Ж.Т., Тулегенова А.Т., Алтысова Г.К., Мусаханов Д.А., Жунусбеков А.М.

YAG:Ce керамикасының фотометриялық сипаттамасын арттыру: радиациялық синтезде күйдірудің рөлін зерттеу

Цериймен белсендірілген итрий-алюминий гранатының (YAG:Ce) керамикалық үлгілері энергиясы 1,4 МэВ және қуат тығыздығы 23 кВт/см² қуатты электронды ағынның өрісін қолдану арқылы синтезделді. Керамика итрий, алюминий және церий оксидтерінің арнайы дайындалған қоспасынан қысқа уақыт ішінде – небәрі бір секундта пайда болды. Радиациялық өріс ағынында керамиканың синтез процесі қазіргі кезде жиі қолданылатын әдістерден түбегейлі ерекшеленеді. Талданған дифракциялық суреттер YAG:Ce керамикалары үшін шыңдар орындары да, пропорциялары да бойынша жақын сәйкес келеді. Сонымен қатар, әрбір үлгі Іа-3d кеңістіктік топ симметриясын дәйекті түрде көрсетті. Осы зерттеуде синтезделген керамиканың люминесценция және козу спектрлері басқа әдістермен дайындалған керамиканың YAG:Ce спектрлеріне және YAG:Ce негізіндегі люминофорларға өте ұқсас. Люминесценция жолақтары жоғары тиімділікті көрсетеді, ал ультракүлгін жолақтардың қарқындылық қатынасы зерттелетін люминофорлар үшін әртүрлі. Керамикалық сәулеленуді люминесценцияға түрлендіру тиімділігі өлшеніп, SDL 4000 және YAG-02 өнеркәсіптік люминофорлары үшін сәйкесінше 0,57 және 0,48-ге жетті. Сондай-ақ үлгілердің кванттық тиімділігін арттыруға жоғары температурада күйдіру арқылы қол жеткізуге болатыны көрсетілді. Жоғары түрлендіру тиімділігі люминесцентті керамика синтезі үшін сипатталған әдістің жоғары әлеуетін атап көрсетеді.

Кілт сөздері: синтез, YAG:Ce керамикасы, құрылым, радиациялық синтез, люминесценция.

Жилгельдинов Ж.С., Лисицын В.М., Карипбаев Ж.Т., Тулегенова А.Т., Алтысова Г.К., Мусаханов Д.А., Жунусбеков А.М.

Улучшение фотометрических характеристик керамики YAG:Ce: исследование роли отжига в радиационном синтезе

Керамические образцы иттриево-алюминиевого граната, легированного церием (YAG:Ce), были успешно синтезированы с использованием мощного поля электронного потока с энергией 1,4 МэВ и плотностью мощности 23 кВт/см². Керамика была сформирована за короткий промежуток времени - всего за одну секунду -

из специально приготовленной смеси оксидов иттрия, алюминия и церия. Процесс радиационного синтеза керамики в полях радиационного потока принципиально отличается от методик, обычно используемых сегодня. Проанализированные дифракционные картины близко совпадают с задокументированными для керамик YAG:Ce, как по положению пиков, так и по пропорциям. Кроме того, каждый образец последовательно демонстрировал пространственную групповую симметрию Ia-3d. Спектры люминесценции и возбуждения керамики, синтезированной в этом исследовании, очень похожи на спектры YAG:Ce керамики, полученной другими методами, и люминофоров на основе YAG:Ce. Полосы люминесценции демонстрируют высокую эффективность, а соотношения интенсивностей ультрафиолетовых полос варьируются у исследуемых люминофоров. Эффективность преобразования излучения керамики в люминесценцию оказалась впечатляющей, достигнув показателей 0,57 и 0,48 для промышленных люминофоров SDL 4000 и YAG-02 соответственно. Было также замечено, что увеличение квантовой эффективности образцов может быть достигнуто с помощью высокотемпературного отжига. Высокая эффективность преобразования подчеркивает высокий потенциал описанного метода синтеза люминесцентной керамики.

Ключевые слова: синтез, YAG:Ce керамика, структура, радиационный синтез, люминесценция.

Alper Pahsa

Теориялық бұрқу коэффициентін есептеу үшін плазманың материалдармен өзара әрекеттесуін молекулалық-динамикалық модельдеу.

Синтез реакциясы нәтижесінде дейтерий мен тритийдің екі жеңіл ядросы бірігіп, бір ауыр гелий ядросын құрайды. Алайда екі оң ядро бір-бірін тебеді. Екі ядро бірігу үшін олардың жылдамдығы өте жоғары болуы тиіс. Жоғары жылдамдық жоғары температураны білдіреді. Реакция үшін ядролардың температураны 100 миллион °C ұстап тұруы маңызды. Бұл температурада D және T атомдары плазма түзеді. Реакция жүруі үшін плазманың температурасын сақтау керек немесе плазманы салқындатпау керек. Токамак реакторлары плазманы магнит өрісінде ұстауға арналған. Осылайша, плазманы салқындату реактордың қабырғаларына соқтығысу арқылы алдын алады. Плазманың тығыздығы мен температурасы реакцияны бастау және үздіксіздікті қамтамасыз ету үшін белгілі бір деңгейде болуы керек. Реакция процесінде магнит өрісінің ортасынан шыққан оң және теріс иондар Токамак реакторының қабырғаларымен әрекеттесіп, деформацияны тудырады. Бұл уақыт өтуімен плазмалық қабырғаның бұзылуына және нейтрондардың қоршаған ортаға шығарылуына әкеледі. Плазманың қабырғамен өзара әрекеттесуі Токамак реакторларында термоядролық синтездің үзілуіне әкелетін маңызды мәселелердің бірі болып табылады. Плазмалық қабырғадағы иондық коррозияға ең төзімді материалдар графит, бериллий, алюминий және вольфрам болып табылады. Бұл жұмыста плазманың материалмен өзара әрекеттесуі теориялық тұрғыдан зерттеледі, термоядролық реакторда қолданылатын қабырға материалдарының әртүрлі үлгілерінің (графит, алюминий және вольфрам) плазмалық әрекеттесуінен туындаған физикалық және химиялық эрозия молекулалық динамика мен Монте-Карло әдістерімен зерттелген.

Кілт сөздері: плазма, ядролық синтез, молекулалық динамика, бұрқу коэффициенті, Монте-Карло әдісі.

Alper Pahsa

Молекулярно-динамическое моделирование взаимодействия плазмы с материалами для расчета теоретического коэффициента распыления.

В результате реакции синтеза два легких ядра дейтерия и трития сливаются, образуя одно более тяжелое ядро гелия. Однако два положительных ядра отталкивают друг друга. Чтобы слиться два ядра, они должны иметь очень высокие скорости. Высокая скорость означает высокую температуру. Для реакции важно, чтобы ядра сохраняли температуру 100 миллионов °C. При этой температуре атомы D и T образуют плазму. Чтобы реакция шла, необходимо сохранять температуру плазмы или не охлаждать плазму. Токамак-реакторы предназначены для удержания плазмы в магнитном поле. Таким образом, охлаждение плазмы предотвращается за счет ударов о стенки реактора. Плотность и температура плазмы должны быть на определенном уровне, чтобы инициировать реакцию и обеспечить непрерывность. В процессе реакции положительные и отрицательные ионы, вылетающие из среды магнитного поля, взаимодействуют со стенками токамака и вызывают деформацию. Это приводит к разрушению плазменной стенки с течением времени и выбросу нейтронов в окружающую среду. Взаимодействие плазмы со стенкой является одной из важнейших проблем, вызывающих прерывание термоядерного синтеза в реакторах токамаков. Материалами, наиболее устойчивыми к ионной коррозии в плазменной стенке, являются графит, бериллий, алюминий и вольфрам. В этой работе взаимодействие плазмы с материалом теоретически изучается, физическая и химическая эрозия, вызванная плазменным взаимодействием различных образцов материалов стенок (графит, алюминий и вольфрам), используемых в термоядерном реакторе, и исследуется методом Монте-Карло с молекулярной динамикой.

Ключевые слова: плазма, ядерный синтез, молекулярная динамика, коэффициент распыления, метод Монте-Карло.

**INFORMATION
ABOUT AUTHORS**
**АВТОРЛАР ТУРАЛЫ
МӘЛІМЕТТЕР**
**СВЕДЕНИЯ
ОБ АВТОРАХ**

- Abdulzahra, N.Z.** – PhD, Department of Physics, College of Science, Al-Nahrain University, Jadriya, Baghdad, Iraq; ORCID iD:0000-0002-7655-3854; ner_ner2@yahoo.com
- Alkadhery, L.A.R.** – Master (Eng.), Lecturer, Electromechanical Engineering Department, National Research Tomsk Polytechnic University, Tomsk, Russia, ORCID ID: 0000-0003-2785-0761, 50226@uotechnology.edu.iq
- Alpyssova, G.K.** - PhD, Academician E.A.Buketov Karaganda University, Karaganda, Kazakhstan, SCOPUS Author ID: 57204979025; ORCID iD: 0000-0002-7164-2188; gulnur-0909@mail.ru
- Amajama, J.** - PhD, Associate Professor, Department of Physics, University of Calabar, Calabar, Nigeria; SCOPUS Author ID: 58091457900
- Baiserikov, B.M.** – Master, Researcher, JSC «National Center of Space Research and Technology», Almaty, Kazakhstan; Satbayev University, Almaty, Kazakhstan; SCOPUS Author ID: 58040708000; ORCID iD: 0000-0003-0804-3147; baiserik.b.91@mail.ru
- Bergander, Marek J.** – PhD, Dr. habil., Magnetic Development, Inc., Madison, USA; SCOPUS Author ID: 35619301800; ORCID iD: 0000-0002-2783-2179; mjb1000@aol.com
- Derevyanko, N.A.** – Senior Research Fellow, Institute of Organic Chemistry of National Academy of Sciences of Ukraine, SCOPUS Author ID 35428560600, ORCID 0000-0001-6474-9254; al.al.ishchenko@gmail.com
- Dyusembayeva, A.N.** – PhD, E.A. Buketov Karaganda University, Karaganda, Kazakhstan, aikabesoba88@mail.ru
- Dzhundibayev, V.E.** – Doctor of Techn. Sciences, Professor, L.N. Gumilyov Eurasian National University, Astana, Kazakhstan; Scopus Author ID: 57221819184; ORCID iD: 0000-0003-2815- 9614
- Echem, C.O.** - Researcher, Department of Physics, University of Calabar, Calabar, Nigeria
- Fadeev D.A.** – Master student, Department of General and Experimental Physics, Altai State University, Barnaul, Russia; ORCID iD: 0000-0003-3467-7506; katasonovrffi@gmail.com
- Hamad, Karema A.** – Master, Associate Professor, Teaching staff member, Electromechanical Engineering Department, University of Technology, Baghdad, Iraq; SCOPUS Author ID: 57245159900; Karema.A.Hamad@uotechnology.edu.iq
- Ibrahim, A.T.** – Researcher, Department of Physics, University of Calabar, Calabar, Nigeria
- Ibrayev, N.Kh.** – Doctor of phys.-math. sciences, Professor, Professor-Researcher, Director of the Institute of Molecular Nanophotonics, E.A. Buketov Karaganda University, SCOPUS Author ID: 9333698600, ORCID ID: 0000-0002-5156-5015; niazibrayev@mail.ru
- Idajor, J.A.** – Researcher, Department of Electrical and Electronic, University of Calabar, Calabar, Nigeria
- Ishchenko, A.A.** – Doctor of chem. sciences, Professor, Corresponding member of the National Academy of Sciences of Ukraine, Head of the department of Color and Structure of Organic Compounds, Institute of Organic Chemistry of National Academy of Sciences of Ukraine, SCOPUS Author ID 8338223800, ORCID 0000-0003-2722-3944; al.al.ishchenko@gmail.com
- Ishkov, A.V.** – Doctor of techn. sciences, Candidate of Chem. Sciences, Professor, Department of Technology structural materials and repair mashine, Altai State Agricultural University, Barnaul, Russia, SCOPUS Author ID: 6603935969; ORCID iD: 0000-0003-1637-2258; svaritrffi@gmail.com
- Iwuji, Prince C.** - PhD, Associate Professor, Department of Physics, University of Calabar, Calabar, Nigeria; SCOPUS Author ID: 57739427700; pciwuji@unical.edu.ng
- Jaddoa, Ameer A.** - PhD., Associate Professor, Head of the Energy Engineering and Renewable Energy Department, University of Technology, Baghdad, Iraq; SCOPUS Author ID: 57193803386; ORCID iD: 0000-0001-5158-1827; ameer.a.jaddoa@uotechnology.edu.iq
- Kaishubayeva, N.** – Master (Sci.), Engineer, “Rauza-PV” LLP, Astana, Kazakhstan, ORCID iD: 0009-0001-8084-3475; n.kaishubayeva@rauzapv.kz
- Kambarova, Zh.T.** - PhD, Associate Professor, Physical and Technical Faculty, E.A Buketov Karaganda University, Karaganda, Kazakhstan, ORCID ID: 0000-0001-9808-5484, SCOPUS ID: 55543382800, WoS Researcher ID: AAV-8669-2020, kamarovazht@gmail.com
- Kanapina, A.E.** – PhD student, E.A. Buketov Karaganda University, SCOPUS Author ID 57226236798; ORCID 0000-0001-7819-4667; asselkanapina@mail.ru

Kapayeva, S.D. - PhD, Associate Professor, D. Serikbayev East Kazakhstan Technical University, Ust Kamenogorsk, Kazakhstan; SCOPUS Author ID: 57194502107; Researcher ID:C-4174-2018; ORCID iD: 0000-0002-2237-6960; kapaewa_s@rambler.ru

Karipbayev, Zh.T. - PhD, L.N. Gumilyov Eurasian National University, Astana, Kazakhstan; SCOPUS Author ID: 56433531200; ORCID iD: 0000-0003-4066-1826, karipbayev_zht_1@enu.kz

Karnaukhov, A.I. – Candidate of techn. Sciences, Associate Professor, Associate Professor, Forest Engineering Department, Siberian State Aerospace University named after Academician M.F. Reshetnev, Krasnoyarsk, Russia; SCOPUS Author ID: 57979593000; ORCID iD: 0000-0002-7284-2050, karnaukhov.ai@mail.ru

Kenzhegulov, A.K. – PhD, Researcher JSC «National Center of Space Research and Technology», Almaty, Kazakhstan; Satbayev University, JSC «Institute of Metallurgy and Ore Beneficiation», Almaty, Kazakhstan; SCOPUS Author ID: 57210622996; ORCID iD: 0000-0001-7001-2654; a.kenzhegulov@satbayev.university

Khairaliyev, S.I. - PhD., Technical Director of INTEKKO L.t.d., Astana, Kazakhstan, SCOPUS Author ID: 57199743504; kh.serik@gmail.com

Klimenko, V.N. - Doctor of techn. sciences, Professor, Corresponding Member of NAS of Ukraine, Chief researcher, Institute of Engineering Thermophysics of the National Academy of Sciences of Ukraine, Kyiv, Ukraine; SCOPUS Author ID 36833344100; vnklimenko@gmail.com

Kokhanova, S.Ya. - Candidate of techn. sciences, Associate Professor, Docent, Kazan National Research Technical University named after A.N. Tupolev, Kazan, Russia; SCOPUS Author ID: 57474910400; Orcid ID: 0000-0003-3788-7285; syakokhanova@kai.ru

Lisitsyn, V.M. – Doctor of phys.- math. sciences, Professor, National Research Tomsk Polytechnic University, Tomsk, Russia; SCOPUS Author ID: 35577898600; ORCID iD: 0000-0002-2075-4796; lisitsyn@tpu.ru

Mahdi, Mahmoud M. – PhD. Associate Professor, Associate Professor, Lecture, Electromechanical Engineering Department, University of Technology, Baghdad, Iraq; SCOPUS Author ID: 57204816536; 50295@uotechnology.edu.iq

Malikov, V.N. – Candidate of techn. sciences, Associate Professor, Department of General and Experimental Physics, Altai State University, Barnaul, Russia; SCOPUS Author ID: 57217258853; ORCID iD:0000-0003-0351-4843, osys11@gmail.com

Meirbekov, M.N. – Master, Senior Researcher, JSC «National Center of Space Research and Technology», Almaty, Kazakhstan; Satbayev University, Almaty, Kazakhstan; SCOPUS Author ID: 57218282617; ORCID iD: 0000-0003-0434-9114; muhammed_91@mail.ru

Minkov, L.L. – Doctor of phys.-math. sciences, Professor, National Research Tomsk State University, Tomsk, Russia

Mohammed, J.A.-K. – PhD, Professor, Electromechanical Engineering Department, University of Technology, Baghdad, Iraq; SCOPUS Author ID: 57191737360; ORCID ID: 0000-0003-1456-6673; 50128@uotechnology.edu.iq

Mukhamedrakhim, A.R. – student, E.A. Buketov Karaganda University, Karaganda, Kazakhstan

Mussakhanov, D.A. - PhD, L.N. Gumilyov Eurasian National University, Astana, Kazakhstan; SCOPUS Author ID: 57197728253; ORCID iD: 0000-0002-1823-2526; mussakhanov_da@enu.kz

Neshina, Y.G. - Candidate of techn. sciences, Head of Department "Energy Systems", A. Saginov Karaganda Technical University, Karaganda, Kazakhstan; SCOPUS Author ID: 57191724446, ORCID ID: 0000-0002-8973-2958, 1_neg@mail.ru

Okoro, R.C. – Researcher, Department of Physics, University of Calabar, Calabar, Nigeria

Omarova, G.S. - PhD, Associate Professor, Physical-Technical faculty, E.A. Buketov Karaganda University, Karaganda, Kazakhstan; SCOPUS Author ID: 56669661100, ORCID ID: 0000-0003-2900-2168, guldenserikovna@mail.ru

Pahsa, Alper – PhD, Associate Professor, Graduate School of Natural and Applied Sciences, Ankara Yıldırım Beyazıt University, Ankara, Türkiye; SCOPUS Author ID: 57211430619; 165106407@ybu.edu.tr

Rasulov, Z.N. – Candidate of techn. sciences, Senior Teacher, Baltic State Technical University "VOENMEH" named after D.F. Ustinov, St. Petersburg, Russia; SCOPUS Author ID: 57368399300; ORCID iD:0000-0002-6966-7060; rasulov_zn@voenmeh.ru

Samsonenko, A.I. – Bachelor, Chief Engineer, SLLP «Institute of Space Engineering and technology», Almaty, Kazakhstan; ORCID iD: 0000-0002-5651-6108; anatolly.sam@yandex.ru

Saulebekov, A.O. - Doctor of phys.-math. sciences, Professor, Kazakhstan branch of Lomonosov Moscow state University, Astana, Kazakhstan, SCOPUS Author ID: 6505502480, WoS Researcher ID:ABA-6235-2020, ORCID iD: 0000-0002-6842-9263, saulebekovarm@yandex.ru

Seliverstova, E.V. – PhD, Senior Research Fellow, Institute of Molecular Nanophotonics, E.A. Buketov Karaganda University, SCOPUS Author ID: 35323255400, ORCID ID: 0000-0002-9507-8825; genia_sv@mail.ru

Suprun, T.T. - Candidate of techn. sciences, Senior Researcher, Senior Researcher of Institute of Engineering Thermophysics of the National Academy of Sciences of Ukraine, Kyiv, Ukraine; SCOPUS Author ID 6602978555; ORCID iD 0000-0002-5360-388X; suprun@secbiomass.com

Tanasheva, N.K. – PhD, Associate professor, E.A. Buketov Karaganda University, Karaganda, Kazakhstan, nazgulya_tans@mail.ru

Tleubergenova, A.Zh. – PhD student, E.A. Buketov Karaganda University, Karaganda, Kazakhstan, shymkent.a7@mail.ru

Trushin, M.V. - Candidate of biological sciences, Associate Professor, Docent, Kazan (Volga Region) Federal University, Kazan, Russia; SCOPUS Author ID: 10142619100; Orcid ID: 0000-0001-7467-011X; mtrushin@mail.ru

Tsyganov, V.V. – Doctor of techn. sciences, Academician of the Technical Sciences Academy of Ukraine, Corresponding Member of the Ukrainian Academy of Tribotechnics, Associate Professor, Zaporizhzhia Polytechnic National University, Zaporozhie, Ukraine; SCOPUS Author ID: 56712109100 ORCID iD :0000-0001-5682-7005, tsyganov705@gmail.com

Tulegenova A.T. - PhD, Al-Farabi Kazakh National University, Almaty, Kazakhstan; Scopus Author ID: 56811383700; ORCID iD: 0000-0002-5701-6674; tulegenova.aida@gmail.com

Usanov, D.N. – graduate student, Baltic State Technical University "VOENMEH" named after D.F. Ustinov, St. Petersburg, Russia; usanov@voenmeh.en

Usenkov, R.A. – PhD, Associate Professor, Docent, Kazan National Research Technical University named after A.N. Tupolev, Kazan, Russia; SCOPUS Author ID: 57204491738; Orcid ID: 0000-0002-7119-8048; RAUsenkov@kai.ru

Ussipov, N.M. - PhD student, Department of Physics and Technology, Al-Farabi Kazakh National University, Almaty, Kazakhstan; SCOPUS Author ID: 57226319348; ussipov.nurzhan@kaznu.kz

Voinash, S.A. – Leading Engineer, Research Laboratory “Intellectual Mobility”, Institute of Design and Spatial Arts, Kazan Federal University, Kazan, Russia; SCOPUS Author ID: 57194339935; ORCID iD: 0000-0001-5239-988; sergey_voi@mail.ru

Yermakhanova, A.M. – PhD, Acting Deputy Chairman of the Board, JSC «National Center of Space Research and Technology», Almaty, Kazakhstan; SCOPUS Author ID: 57203409618; ORCID iD: 0000-0002-2145-5122; a.yermakhanova@mail.ru

Yurchenko, A.V. - Doctor of techn. sciences, Professor, National Research Tomsk State University, Tomsk, Russia; SCOPUS Author ID: 55308619600; niipp@inbox.ru

Zhanabaev, Z.Zh. - Doctor of phys.-math. sciences, Professor, al Farabi Kazakh National University, Almaty, Kazakhstan; SCOPUS Author ID: 15840905700; WoS ResearcherID: B-2924-2015; ORCID iD: 0000-0001-5959-2707, zhanabayev.zeinulla@gmail.com

Zhilgildinov, Zh.S. - PhD student, Department of technical physics, L.N. Gumilyov Eurasian National University; Astana, Kazakhstan; SCOPUS Author ID: 58294243400; zhilgildinov_zhs@enu.kz

Zhunusbekov, A.M. - Candidate of phys.- math. sciences, L.N. Gumilyov Eurasian National University, Astana, Kazakhstan; SCOPUS Author ID: 6508013732; ORCID iD: 0000-0003-2052-0065; zhunusbekov_am@enu.kz

GUIDELINES FOR AUTHORS

Eurasian Physical Technical Journal (Eurasian phys. tech. j.) is a peer-reviewed open access international scientific journal publishing original research results on actual problems of technical physics and other related fields. Since 2004 «Eurasian phys. tech. j.» is published in English.

Acceptance of the manuscript for publication in the Eurasian phys. tech. j. is carried out online through website - <https://phtj.buketov.edu.kz/index.php/EPTJ>. Authors should check that their submissions meet all of the following requirements, as submissions may be returned to authors that do not comply with these guidelines.

Scientific article topic and content

A scientific article should contain the results of original scientific research previously unpublished and not intended for publication in other publications.

Manuscript of the article should contain at least 75% of the original text.

All articles are published **in English in 4 scientific areas of physics: Energy, Engineering, Materials Science, Physics and Astronomy.**

Publication Ethics and Malpractice Statement

Submission of an article to the Eurasian phys. tech. j. implies that the paper described has not been published previously, that it is not under consideration for publication elsewhere, that its publication is approved by all authors and tacitly or explicitly by the responsible authorities where the paper was carried out, and that, if accepted, it will not be published elsewhere in the same form, in English or in any other language, including electronically without the written consent of the copyright holder. In particular, translations into English of papers already published in another language are not accepted.

For information on Ethics in publishing and Ethical guidelines for journal publication see <http://www.elsevier.com/publishingethics> and <http://www.elsevier.com/journal-authors/ethics>.

The Eurasian phys.tech.j. strictly adheres the Code of Conduct of the Committee on Publication Ethics (COPE), and follows the COPE Flowcharts for Resolving Cases of Suspected Misconduct (http://publicationethics.org/files/u2/New_Code.pdf).

To verify originality, your article may be checked by the originality detection service Cross Check <http://www.elsevier.com/editors/plagdetect>.

Pre-publication process

Authors are responsible for the content of their publications. No other forms of scientific misconduct are allowed, such as plagiarism, falsification, fraudulently data, incorrect interpretation of other works, incorrect citations, etc. Authors are obliged to participate in peer review process and be ready to provide corrections, clarifications, retractions and apologies when needed. All authors of a paper should have significantly contributed to the research.

Reviewers should provide objective judgments and should point out relevant published works which are not yet cited. Reviewed articles should be treated confidentially. The reviewers will be chosen in such a way that there is no conflict of interests with respect to the research, the authors and/or the research funders.

Editors have complete responsibility and authority to reject or accept a paper, and they will only accept a paper when reasonably certain. They will preserve anonymity of reviewers and promote publication of corrections, clarifications, retractions and apologies when needed.

The acceptance of a paper automatically implies the copyright transfer to the Eurasian phys. tech. j.

All submitted papers will be sent for reviewing to leading experts in the given area.

The Editorial Board of the Eurasian phys. tech. j. will monitor and safeguard publishing ethics.

The editors reserve the right to accept or reject manuscripts.

The article and all documentation must be identified by the name of the 1st author: Akhmetov AA_et al_paper; Akhmetov AA_et al_fig.1; Akhmetov AA_et al_Cover letter; ...

The article text must be formatted according to the **Template**, font - Times New Roman, size -11 pt; line spacing-single; alignment-in width, see <https://phtj.buketov.edu.kz/index.php/EPTJ/about/submissions#authorGuidelines>

An article should consist:

Title: includes a separate line on the left the UDC index, Title of the article, information about the authors-surname and initials, name of institution, city, country, e-mail of a corresponding author. The author* who submitted an article for publication will be considered as a corresponding author.

Abstract should consist of at least 5-6 sentences, not exceeding 200-250 words without formula, references, abbreviations. An abstract is a short and powerful summary that describes the focus and subject of a research paper. It could contain the information about why the research study was done, background, what the methodology was and something about the findings of the author(s).

Keywords: at least 3-10 basic terms or short phrases used in the article.

The text should be divided on structural parts: Introduction, Main part (Theoretical part, Methods and materials or Experimental technique), Results and Discussion, Conclusions.

Conclusions: formulating main results; a comparison of the results with the existing data on this topic; assessment of scientific novelty and practical value of the results.

Acknowledgments or Funding may be shown at the end of the article text, before References.

References: a bibliographic list is compiled according to the requirements:

- Books, abstracts, patents: Surname and initials of the authors (it is enough to indicate the first three or one surnames, et al), *Title of the book* in italics, publish house or city, year and total number of pages.
- Journals, collections of papers, conference proceedings - Surname and initials of the authors (the first three are enough), the title of the article, the *Title of the journal* in italics (you can use the abbreviated title), city and / or country, year, volume, issue number, pages of the "beginning and end" (pp. ... - ...).
- Internet links also must to indicated the authors, the title and URL

The authors should represent References according to the requirements of international journals on physics, but should to consult preliminarily for standard abbreviations of journal's names. More information on references guidelines for journal publication you can see in Harvard reference system - **Ошибка! Недопустимый объект гиперссылки.**

All references must be numbered in the text (for example, [1], [2-4]) and listed in numerical order.

All abbreviations and acronyms, with the exception of obviously well-known, should be deciphered at first use in the text.

Equations in your paper have to be written using the Microsoft Equation Editor or the MathType.

Tables, numbered and titled, should be inserted into the text (Times New Roman, size - 10 pt) or have been presented as an appendix at the end of the article.

Figures should be prepared in a digital form suitable for direct reproduction. Figures shall be submitted on the separate sheets or can be included into the text.

The manuscript volume, including text, formulas, figures, bibliography, should not exceed 12 pages including tables, figures (no more than 8-10) and references (no more than 30-35) of text typed on a computer using Microsoft Word editor. The review article should not exceed 20 pages with no more than 15 figures.

List of required documents

The following files must be uploaded to the journal's website:

1. Text of the article, with pictures (*.doc);
2. Figure, Picture, Photo (fig1.jpg, fig2.pcx, ...);
3. Figure captions (*.doc);
4. A Cover letter - from a university, research institute or an organization licensed to conduct research activities, must be issued on an official letterhead and / or certified by the organization seal. The management officially confirms by this letter that the article (the title of the article and the names of the authors are indicated in English) doesn't contain any information constituting state or commercial secrets, and the article can be published in the Open Press. Authors must upload a copy of the signed Cover Letter in Pdf format to the Journal website.

It's necessary to upload by separately 2 files in English (and in Russian for authors from Russia, and in Kazakh for authors from Kazakhstan):

5. Article's data: Surname and initials of the authors, the article title, abstract, keywords.
6. Information about each co-author: full name, academic degree, academic title, place of work or study, title of organization, city, country, SCOPUS Author ID or ORCID iD; and contact details (e-mail, phone).
7. Receipt of payment. Authors should pay for the publication only after receiving notification about a positive decision of the reviewers.